Microstructural Processes Leading To Fracture In Nuclear Graphites.

Thesis

Microstructural processes leading to fracture in nuclear graphites

Neighbour, Gareth Bryan

Award date:
1993

Awarding institution:
University of Bath

MICROSTRUCTURAL PROCESSES LEADING TO FRACTURE IN NUCLEAR GRAPHITES.

Submitted by Gareth Bryan Neighbour
for the degree of PhD of the University of Bath.
1993

ProQuest LLC
789 East Eisenhower Parkway
P.O. Box 1346
Ann Arbor, MI 48106-1346

ACKNOWLEDGEMENTS

This work has been carried out as a SERC CASE project between the School of Materials Science, University of Bath and Berkeley Nuclear Laboratories (BNL) of Nuclear Electric plc, and I wish to thank both bodies for providing laboratory facilities. I would like to take this opportunity to express my sincere appreciation to the following people, to whom I am deeply indebted for their assistance in this research programme:

The Science and Engineering Research Council and Nuclear Electric plc for financial support.

Prof B. McEnaney and Mr M. G. Phillips for their constant interest and encouragement in the course of this work, and for many stimulating discussions and suggestions.

The Revd Dr M. O. Tucker for his valuable ideas, contributions and support.

Dr J. Reed, Mr D. D. Jones, Mr K. Swallow and the staff of BNL, Nuclear Electric plc for their help, encouragement and ideas where much of the success of this project lies. I am also grateful to them for making my work at BNL such a pleasant and enjoyable experience.

The staff and technicians of the School of Materials Science, University of Bath for their technical and scientific suggestions.

DEDICATION

This thesis is dedicated to my mother and father simply for their love, understanding and inspiration.

All Along the Watch Tower

"There must be some way out of here," said the joker to the thief,
"There's too much confusion, I can't get no relief.
Businessmen, they drink my wine, plowmen dig my earth,
None of them along the line know what any of it's worth."

"No reason to get excited," the thief, he kindly spoke,
"There are many here among us who feel that life is but a joke.
But you and I, we've been through that, and that is not our fate,
So let us not talk falsely now, the hour is getting late."

Bob Dylan, 1968

Read not to contradict and confute, nor to believe and take for granted, nor to find talk and discourse, but to weigh and consider.

Francis Bacon

ABSTRACT

Thermal nuclear reactors, such as Magnox and AGR, contain graphite moderator blocks in which irradiation-induced internal stresses are generated. Measurement of the internal stresses is required by the nuclear power industry and acoustic emission (AE) monitoring has been identified as a possible method. There is some evidence that a Kaiser effect occurs in graphites, *i.e.*, on stressing a graphite that has been subject to a prior stress, the onset of AE occurs at the previous peak stress. The work reported in this thesis examines the suitability of AE for this purpose. The microstructures of three nuclear graphites (PGA, IM1-24 and VNEC) were characterised qualitatively and quantitatively using optical and electron microscopy and AE was monitored during both monotonic and cyclic loading to failure in tensile, compressive and flexural test modes. For unirradiated graphites, the Kaiser effect was not found in cyclic loading, but a Felicity effect was observed, *i.e.*, the onset of AE occurred below the previously applied peak stress. The Felicity effect was attributed to time-dependent relaxation and recovery processes and was characterised using a new parameter, the Recovery ratio. It was shown that AE can be used to monitor creep strain and creep recovery in graphites at zero load. The AE-time responses from these experiments were fitted to equations similar to those used for creep strain-time at elevated temperatures. The number of AE counts from irradiated graphites were greater than those from unirradiated graphites, subject to similar stresses, due to increases in porosity caused by radiolytic oxidation. A Felicity effect was also observed on cyclic loading of irradiated graphites, but no evidence for a Kaiser effect was found for irradiated graphites loaded monotonically to failure. Thus internal stresses in irradiated graphites could not be measured using AE. This was attributed to relaxation and recovery processes that occur in the considerable time interval between removing the irradiated graphite from the reactor and post-irradiation examination. Therefore it was concluded that AE monitoring is not a suitable technique for measuring internal stresses in irradiated graphites.

MICROSTRUCTURAL PROCESSES LEADING TO FRACTURE IN NUCLEAR GRAPHITE

CONTENTS

Part A :
Introduction

CHAPTER ONE : GENERAL INTRODUCTION

Nuclear Electric plc has two series of thermal nuclear reactors to provide their power production capacity for England and Wales: the Magnox Reactor and the Advanced Gas-Cooled Nuclear Reactor (AGR). Both are gas-cooled, graphite moderated, fission reactors. The Magnox reactor started in service in the early 1950s and was joined by the AGR in the mid 1970s. The AGR is a much improved design and a development of the Magnox reactor. The CEGB, the predecessor of Nuclear Electric plc, commissioned its first civil Magnox nuclear power station in 1962 at Berkeley in Gloucestershire; it was also the first reactor in the U.K. to reach the end of its useful life and was shut down in preparation for de-commissioning in 1989. Nuclear Electric plc still has seven Magnox and five AGR power stations in operation that provide around one sixth of the electricity for the U.K.'s present needs (CEGB, 1985).

The core of a Magnox reactor, such as the one at Oldbury in Avon, consists of a structure of radially-keyed high purity graphite moderator bricks (Figure 1.1a and 1.1b) through which run about 3000 channels, each containing eight natural uranium fuel elements contained in magnesium alloy (Magnox) cans stacked on top of each other, over which the circulated carbon dioxide (CO_2) coolant flows. In addition, there are about 100 other channels for the boron steel control rods that move in and out of the graphite core to control the chain reaction by absorbing the neutrons. Heat from the controlled chain reaction is transferred to the water boilers by pressurised CO_2 gas. The hot CO_2 gases are used to produce steam at the heat exchangers to drive the turbines that, in turn, generate electricity. The whole of the core is contained within a concrete pressure vessel that is about 7 m thick above and below the reactor, and about 5 m thick at its sides. Oldbury produces up to 435 MW of electricity a day at 16,500 Volts. Fresh fuel elements are inserted in to the reactor core two or three times a week (Poulter, 1963).

The AGR mainly differs from the Magnox reactor in the fuel: uranium dioxide (UO_2) pellets, made from enriched uranium, in stainless steel cans are used. This fuel enables higher fuel ratings, higher temperatures and thus greater efficiency. Other additions to the AGR are the graphite fuel sleeves which contain the stainless steel fuel cans and which are replaced with the fuel every 5-7 years (Moore, 1971). The first AGR, Dungeness B, was ordered in 1965 but took over ten years to complete due to design changes in production. The later AGR stations have significantly different design parameters than those of Dungeness B. As experience from earlier AGR stations became available, each new AGR station design differed from the previous one. A typical AGR station consists of two reactors with a combined electrical output of 1350 MW. Each reactor consists of a pre-stressed concrete pressure vessel some 9 m thick enclosing approximately 200 tonnes of high purity graphite as the moderator. Approximately 300 vertical fuel channels run down through the roof of the pressure vessel and continue down through the graphite moderator. When the reactor is operational, 1550 MW of thermal energy is produced in both the fuel and the moderator. This heat is removed by CO_2 gas pumped up each fuel channel before reaching the heat exchangers (Patterson, 1980).

The graphite moderator serves several functions. Primarily, it slows down the fast neutrons (2 MeV) produced during fission to thermal energies (<1 eV) to maximise the efficiency of their interaction with uranium nuclei and so allowing the chain reaction to continue. However, the graphite core is also a major structural material of the reactor supporting the weight of the graphite, fuel stringers (containing eight sleeve components), coolant and other structural materials. The graphite core must also be capable of withstanding gas pressure or differential pressure, restraining forces, including forces imposed by operating or maintenance procedures and stresses arising from earthquakes. Failure of a moderator brick could cause severe problems such as the jamming of a fuel stringer in the channel, altering the coolant flow up the channel and causing the fuel to overheat with undesirable consequences, or more disastrously

blocking the insertion of control rods (Carpenter and Norfolk, 1984).

In the AGR, deformation of the moderator graphite is caused by two principal factors:- changes in dimensions and strength due to neutron irradiation and radiolytic oxidation which is corrosion when irradiated in the presence of CO_2-based coolant gases (Carpenter and Norfolk, 1984). The core is also subject to thermal gradients within the restraint structure which impose displacements. The combined effect of the deformation processes and thermal gradients leads to the build up of complex residual stresses that reduce the ability of the core to withstand external loads (Reed *et al.*, 1991). The integrity of the core is dependent upon the strength of its individual components. In principle, most components of a reactor can be replaced, but the graphite moderator cannot and therefore its integrity effectively determines the life of the nuclear reactor. For these reasons, the moderator graphite is continuously monitored by Nuclear Electric plc. In addition, if the reactor's performance deteriorates too rapidly, causing the life of the reactor to end prematurely, then this could cost hundreds of million of pounds of capital investment to be written off, as well as a loss of income.

There is a clear need for Nuclear Electric plc to monitor residual stresses within the reactor core, and various techniques have been suggested such as X-ray stress analysis, brick bore ovality measurements, slot closure of fuel sleeves and acoustic emission (Cullity, 1978; Fenn *et al.*, 1987; Prince and Brocklehurst, 1986; Critcell *et al.*, 1988; and Reed *et al.*, 1991). This technical requirement has prompted the work presented in this thesis which addresses the structure, mechanical and physical properties and acoustic emission responses from nuclear graphites. The general aims of the work are (i) to evaluate the feasibility of methods to determine residual stress by acoustic emission, and (ii) more generally to study microstructural processes that control the deformation, fracture and failure mechanisms of nuclear graphites using acoustic emission as a tool of investigation.

This thesis is divided in to four parts. Part A (Chapter One to Chapter Five) provides an introduction to graphite, its production, mechanical properties, fracture, deformation behaviour and the problems associated with graphite within the nuclear industry. Part B (Chapter Six and Chapter Seven) describes the microstructure and mechanical properties of nuclear graphites, and in particular those graphites chosen for this study. Part C (Chapter Eight to Chapter Twelve) reviews previous acoustic emission studies and describes acoustic emission experiments on the chosen nuclear graphites. Part D (Chapter Thirteen) completes the thesis and provides a discussion of the results and states the conclusions arising there from, particularly in relation to the general aims of the thesis.

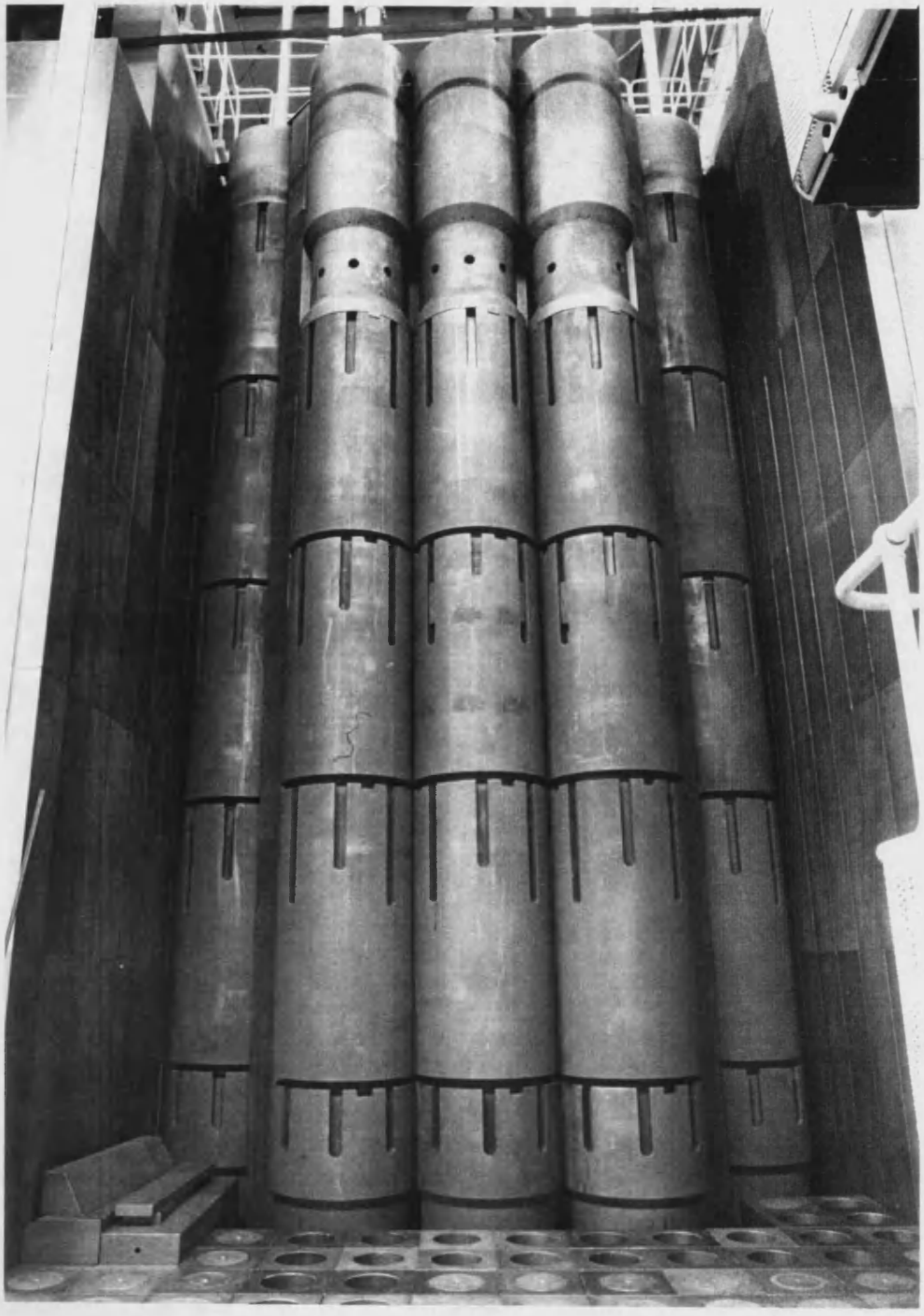

FIGURE 1.1 (a) : A typical civil Advanced Gas–Cooled Reactor graphite core (BNL Zero Energy Experimental Reactor under construction) (courtesy of Nuclear Electric plc)

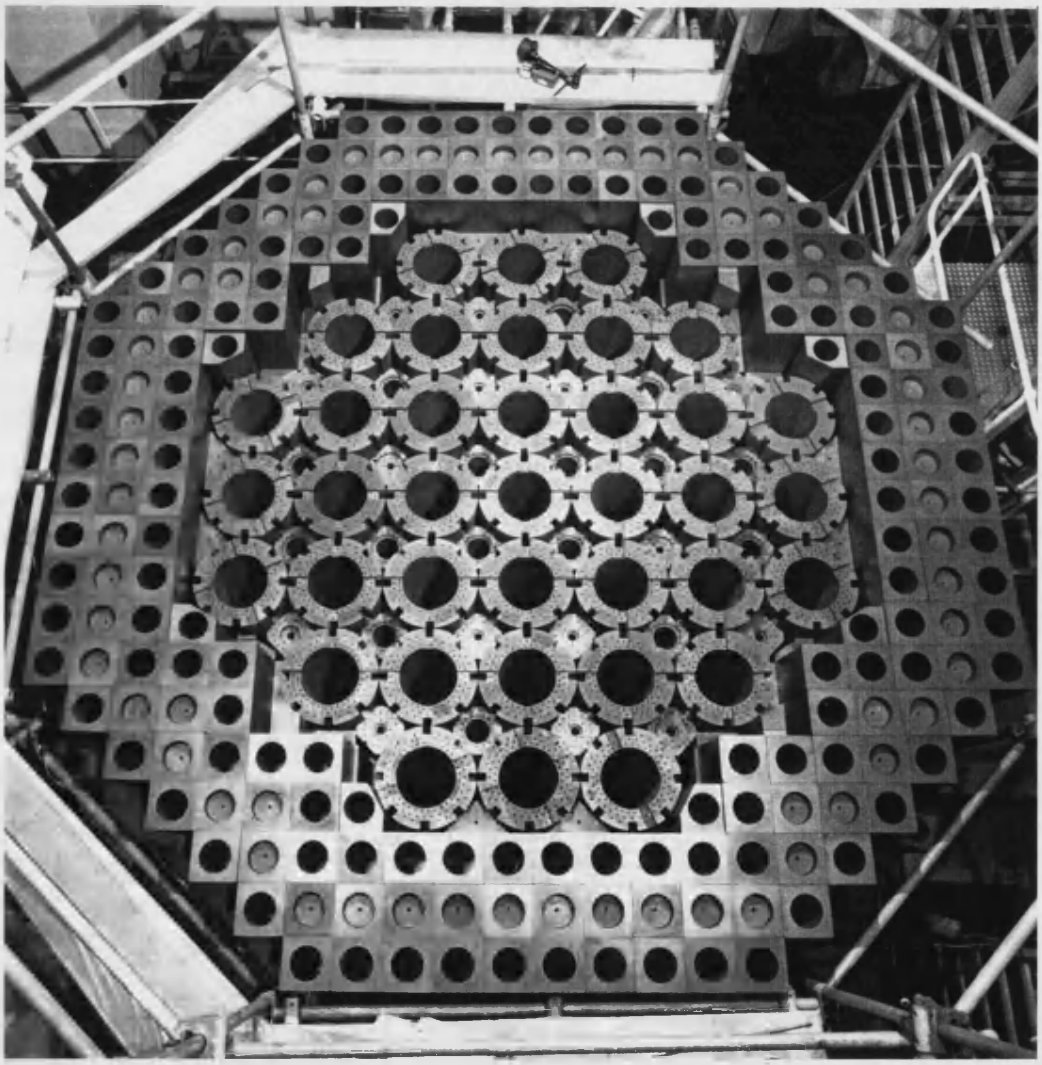

FIGURE 1.1 (b) : A typical civil Advanced Gas–Cooled Reactor graphite core (BNL Zero Energy Experimental Reactor under construction) (courtesy of Nuclear Electric plc)

CHAPTER TWO : INTRODUCTION TO GRAPHITE

Polycrystalline graphite is a complex and variable material which makes it difficult to understand completely its mechanical properties; much is unknown and much needs to be known to exploit fully these materials. Many bulk properties are derived as a result of single crystal properties and the manufacturing process. Nuclear applications are a small fraction of the possible uses for polycrystalline graphites: graphite is used as the moderator of neutrons within a nuclear reactor because of its high scattering and low capture cross sections, low atomic weight, relatively high density and low cost (Carpenter and Norfolk, 1984).

2.1 Graphite

The element carbon has the atomic number of six, an atomic weight of 12.011 and has two principal crystalline allotropes: diamond and graphite. The word "carbon" (Fr. carbone) coined by A. L. Lavoisier in 1789 is from the Latin *carbo,* meaning charcoal. The name "graphite" was proposed by A. G. Werner and D. L. G. Harsten in the same year from the Greek *graphien,* meaning "to write", and was given to the substance on account of its use for that purpose: the first lead pencils were manufactured commercially in the reign of Queen Elizabeth I in 1564 using Cumberland graphite (Newth, 1897).

Familiar forms of carbon are soot, coke, charcoal, graphite (or plumbago, popularly termed blacklead) and diamond. Natural graphite, which can be found in large quantities in Siberia, Ceylon and various parts of India, is a soft, shiny, greyish-black substance, which is smooth and soapy to touch, a good conductor of both heat and electricity and has wide uses including steelmaking, foundries, refractories, crucibles, retorts, nozzles, lubricants, brake linings, carbon products and pencils (Greenwood and Earnshaw, 1984).

2.2 Graphite Single Crystal

Figure 2.1 shows the hexagonal crystal structure of graphite (ABAB stacking sequence) which was first established by J. D. Bernal (1924). The basal planes consist of extended hexagonal arrays of carbon atoms with the interatomic distance 1.415 Å. The neutral carbon atom has six electrons, four of which are in the outer L-shell and available for bond formation: the isolated atom has the electronic configuration of $1s^2 2s^2 2p^2$. In the graphite basal plane there are three 120° co-planar bonds formed by sp^2 hybridization, while the remaining electron in the unused p_z orbital forms a π bond for a mixed role in intraplanar and interplanar bonding. The basal planes are separated by a spacing of 3.35 Å and are held together by weak van der Waals forces. The single crystal density of graphite is 2.265 g cm^{-3}. Lipson and Stokes (1943) were able to show that the rhombohedral lattice (ABCABC stacking sequence) fully accounted for the extra X-ray lines in powder photographs of natural graphite. The rhombohedral form accounts for less than 10% in natural graphite, and irreversibly converts to the hexagonal form at temperatures ~2400 K. The rhombohedral form of graphite is not present in synthetic graphite unless subjected to mechanical treatment, such as grinding (Boehm and Coughlin, 1964). In highly crystalline form, graphite shows a planar morphology and a brilliant silvery surface, while in polycrystalline forms it is dark grey, porous and soft. The graphite single crystal exhibits considerable anisotropy due to differences in properties within basal planes and across basal planes. All forms of graphite are good conductors of heat and electricity, chemically rather inert and only oxidise in air above temperatures of 450 °C (Reynolds, 1968).

2.3 Manufacture of Synthetic Graphites

Synthetic graphites are commonly manufactured by the Acheson process, which was patented in the U.S. in 1895. Most synthetic graphites are produced from a petroleum

coke "filler" and a coal-tar pitch "binder". Petroleum coke is the solid residue left after the delayed coking process and is a by-product of the petroleum industry. Petroleum coke is preferred to other cokes because it gives a high degree of crystallinity when heated to 2800-3000 °C. Coal-tar pitch is the heavy residue left from the distillation of coal-tar. It is preferred over other pitches because of its thermoplasticity, *i.e.* it is a solid at room temperature and liquid at higher temperatures (from ~160 °C). Other advantages of coal tar pitch are its high carbon content, high specific gravity, ready availability and low cost. The wide range of cokes and pitches available enables manufacturers to tailor the mechanical, chemical and physical properties of graphites to achieve their specifications. Different grades of industrial graphites are produced by modifications of conventional manufacturing methods and the description below only summarises a conventional route (Figure 2.2). Many accounts of the production of commercial graphites are published (Nightingale, 1962; Mantell, 1968; Reynolds, 1968 and Kelly, 1981).

The raw petroleum coke is calcined at temperatures up to 1400 °C for about two hours. This removes impurities and volatile hydrocarbons, stabilises the material by developing the crystal structure and effects a shrinkage before being incorporated in the formed article. The calcined coke is then crushed and screened to produce a range of particle sizes and fine flour of grains for use in the manufacture of various grades of synthetic graphites. Differences in coke shapes arises from variations in the degree of alignment of rudimentary crystals in the raw coke and determines in which way the calcined material fractures. A high degree of crystal alignment causes the material to fracture in to flake or needle shaped particles, whereas particles of less-ordered material are more nearly equi-axed in shape.

Various sizes and flours of coke particles are then mixed with a coal-tar pitch in approximately a three-to-one ratio at a temperature of ~165-170 °C at which temperature the binder viscosity is low. The mixing operation should effect a uniform

distribution of coal-tar pitch and petroleum coke filler. The mixture is then either moulded, or more commonly, extruded through a die. Some fine-grained graphites are formed by isostatic pressing. Such processes introduce a preferred orientation in the formed body (bulk anisotropy), particularly if the filler particles are needle shaped rather than spherical. For example, extrusion tends to align needle-coke filler particles in the direction of extrusion, while during moulding, particles tend to line up with their longest dimension perpendicular to the moulding force. This bulk anisotropy can be related to the anisotropy of the graphite lattice. The bulk anisotropy of extruded graphite articles usually results in compressive and tensile strengths, Young's modulus and thermal conductivities that are greater parallel to extrusion than perpendicular. The bulk anisotropy of moulded graphite articles usually results in lower strengths, electrical and thermal conductivities in the direction of the moulding force.

The moulded or extruded body, in the form of a log, is then baked at 800-1000 °C to stabilise the binder by driving off the gaseous products which inadvertently increases the porosity. It is the function of baking to convert the pitch from a thermoplastic material to an infusible solid. When the binder pyrolyzes, large quantities of hydrogen and other volatiles are evolved, allowing polymerisation and cross linking to proceed within the binder and between the binder and filler material. After baking, the material is hard and brittle and has around 25% porosity. Impregnation is then carried out with a fluid, similar to the binder, to increase the bulk density, which upon subsequent pyrolysis in a rebaking or graphitising operation will deposit secondary carbon in the voids. The green body is then re-baked before either re-impregnation or graphitisation.

The material is now ready for final graphitisation. This requires electrical heating in the absence of air to temperatures in the range 2400-3000 °C followed by slow cooling over several days. Most of the remaining hydrogen and other volatiles are removed before 1500 °C leaving only a small amount of impurity, usually of metallic origin.

Nuclear graphites are speciality grades of industrial graphites of high purity: if mineral impurities are present in the material, neutron absorption will occur and reduce efficiency. The impurity content of the final product can be reduced in the three ways. These are (i) careful attention to the purity of the raw materials; (ii) the utilisation of high graphitisation temperatures to encourage impurities to diffuse out; and (iii) the treatment with halogens. Halogens have the ability to penetrate bulk graphite, react with impurities and remove them as volatile halide salts. Fluorine is used to remove boron from industrial graphite for nuclear applications.

Nuclear graphites have densities around 1.7-1.9 g cm^{-3} compared with the theoretical single crystal density of 2.265 g cm^{-3}; the difference is attributed to porosity (~20%). Figure 2.3 illustrates schematically the principal features of a polycrystalline graphite with open and closed porosity surrounding filler particles within a binder phase. McEnaney and Mays (1989) describe various types of porosity in carbons and graphites together with their effects on properties. The pores within the filler particles are usually volumetric shrinkage cracks, formed during the carbonisation and calcination of the coke particles, that lie parallel to the basal planes of the particle and they are usually closed, *i.e.* isolated from the external surface, probably because they are sealed with binder pitch during the mixing operation of manufacture. The shrinkage cracks in the filler particles may be opened up by either thermal or radiolytic oxidation by gases. Open porosity is a series of interconnected passages that lead to the external surface of the specimen. Globular macropores in the binder phase are examples of open pores which are formed by the evolution of the volatile gases during baking stage of manufacture. Mrozowski (1956) suggested that the globular pores in the binder phase are linked by a network of fine shrinkage cracks, formed as a result of contraction on cooling from graphitisation temperatures due to the random orientation of the crystallites.

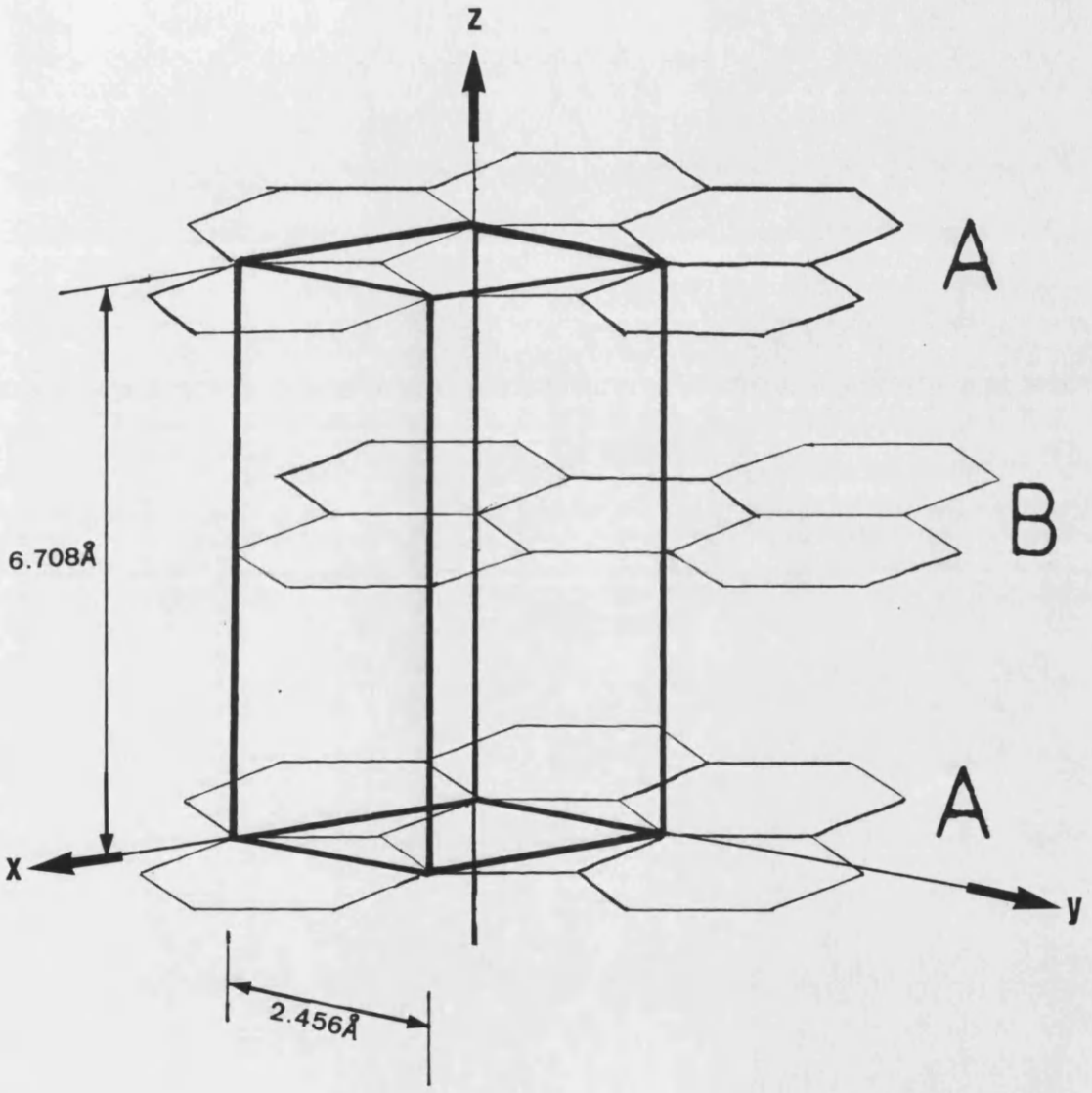

FIGURE 2.1 : The ideal graphite crystal structure with hexagonal unit cell.

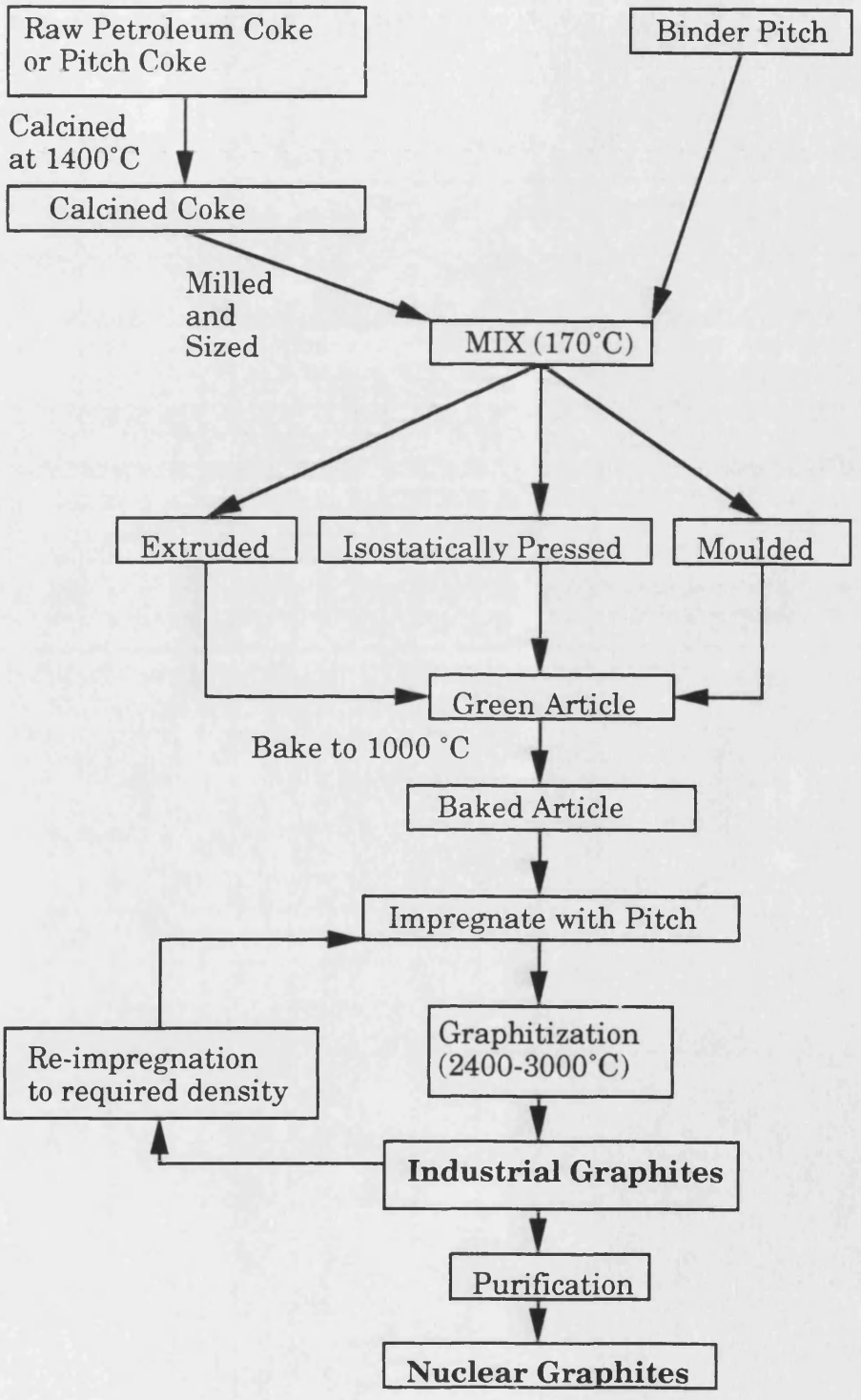

FIGURE 2.2 : Materials and processes used in graphite manufacture.

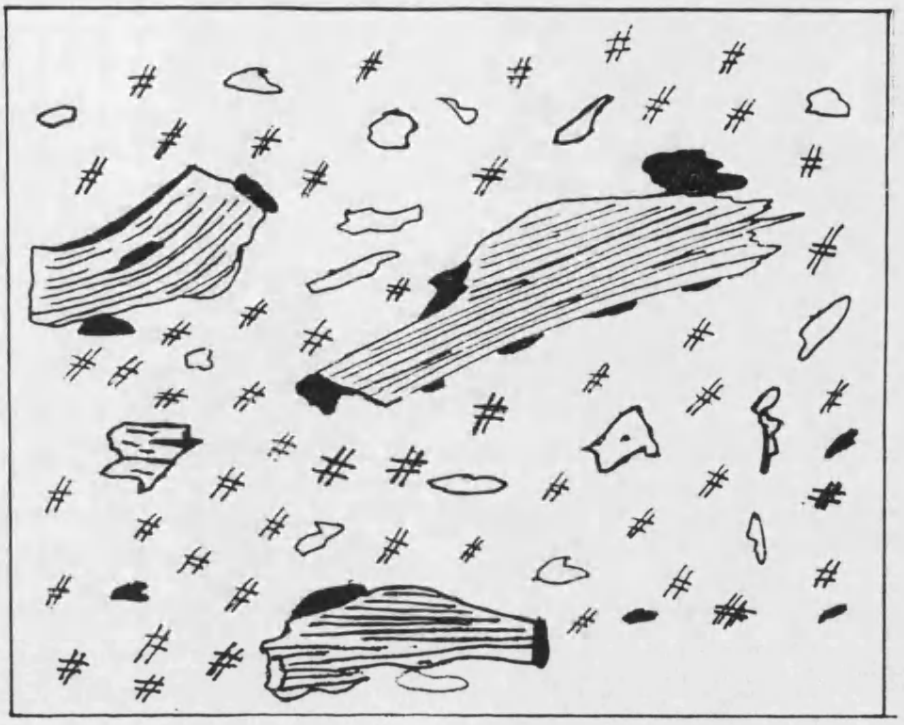

Binder phase

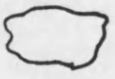

Open porosity

Closed porosity

Filler particles

FIGURE 2.3 : A schematic illustration of the microstructure of a polycrystalline graphite.

CHAPTER THREE : MECHANICAL PROPERTIES OF NUCLEAR GRAPHITES

The mechanical properties of synthetic graphites have been well documented in reviews by Taylor *et al.* (1967); Mantell (1968); Losty (1970); Brocklehurst (1977); and Kelly (1981). The graphite materials range widely in filler particle size and type, binder type, and pore structure, all of which strongly influence their properties. Table 3.1 lists the mechanical properties for a range of commercial grades of graphite, and it shows the range in mechanical properties, from grade to grade, and also in mutually perpendicular directions for some anisotropic grades, for reasons explained in Chapter Two. The nature of graphite production methods also results in variations in mechanical properties within a grade because re-produceability is not achievable from one batch to another and therefore standard deviations of 10% of the mean of graphite properties are not unusual. Usually, increases of strength and elastic modulus can be attained by reducing the porosity and/or the filler particle size. Other factors that affect mechanical properties are specimen volume, test geometry and the environment. Typical values of the total tensile strain to failure of intermediate strength materials are between 0.1 and 0.3% at room temperature (Reynolds, 1968).

3.1 Stress-Strain Behaviour of Graphites

Figure 3.1 presents a typical example of the cyclic stress-strain curve for a nuclear graphite (Nightingale, 1962). The stress-strain behaviour of polycrystalline graphite is markedly non-linear and during cyclic loading there is a permanent set at zero load, which can be recovered by thermal annealing. On re-stressing substantial hysteresis is apparent. On stress cycling between two stress limits, identical superimposed hysteresis loops are produced. During stress cycling, and on increasing peak stress, a decreasing elastic modulus is apparent. Arragon and Berthier (1958) first reported these effects for artificial graphites in compression. Losty and Orchard (1962)

reported stress-strain behaviour for a reactor graphite in both tension and compression and found that pre-compression caused the Young's modulus of a graphite to decrease, but it did not appear to affect the tensile strength. Jenkins (1962b) observed a similar non-linear stress-strain relationship in reactor graphites during cyclic loading in compression. For low stresses he proposed a mathematical relationship (without specifying any microstructural mechanism) based on a simple model of a Voigt element (friction block) backed by a spring. According to the model, polycrystalline graphites were reversibly deformed plastically on unloading due to back-stresses. The model yielded a general parabolic law of the form

$$\varepsilon = A\sigma + B\sigma^2 \qquad \text{(Initial loading)} \qquad (3.1)$$

$$\varepsilon_m - \varepsilon = A(\sigma_m - \sigma) + B(\sigma_m - \sigma)^2/2 \qquad \text{(Unloading)} \qquad (3.2)$$

$$\varepsilon - \varepsilon_0 = A\sigma + B\sigma^2/2 \qquad \text{(Re-loading to the previous maximum)} \qquad (3.3)$$

where A (=1/E, where E is Young's modulus) and B are material constants, ε, ε_m, ε_0, σ and σ_m are strain, maximum strain, permanent set at zero load, applied stress and maximum applied stress, respectively.

Seldin (1966) examined the longitudinal and transverse stress-strain curves for several grades of graphite in both tension and compression. He reported that the longitudinal stress-strain responses fitted the mathematical model of Jenkins (1962b) while transverse stress-strain responses differed in curvature. Slagle (1967) observed the deformation of SGBF graphite under tensile and compressive stresses. He noted that on increasing stress, extensive cracking occurred parallel to the layering direction in the particles, and he attributed such cracking to weak regions or flaws that occurred between the planes. He also reported that on relaxation of the applied load, some of the smaller cracks closed up, but larger cracks failed to close completely. Slagle

suggested that such behaviour would account for the experimentally observed permanent set.

Davidson and Losty (1958) and Seldin (1966) both showed that the room temperature permanent set induced by stressing a polycrystalline graphite can be removed by thermal annealing at about 1000 °C. The presence of a permanent set implies that dislocations are held away from their initial equilibrium position by some temporary pinning points, but that they retain sufficient memory of their initial state to provide a back-stress which acts during annealing. In creep studies of graphite at ambient temperature, Andrews *et al.* (1960) found that the permanent set increased linearly with logarithmic time of loading and that there was some recovery on unloading with the permanent set decreasing with time at zero stress. They declined to interpret their results in terms of the carbon structure without further investigating the dependence of the creep and recovery on the particle size, binder content and type, and heat treatment.

In his review of fracture in polycrystalline graphite, Brocklehurst (1977) suggested the non-linear stress-strain behaviour of polycrystalline graphite can be explained if the response to an applied stress is governed by a continuous carbon network which provided an elastic boundary restraint to shear deformation of the component grains. Such a mechanism can account for the memory displayed by graphites for their original state. The elastic and plastic deformation of graphites is governed by basal plane shear and slip of crystallites with the layer planes moving over each other (Davidson and Losty, 1960). Glissile dislocations within the basal plane which can provide a mechanism for such slip were identified by Amelincx *et al.* (1965). Brocklehurst accounts for the low Poisson's ratio of graphite by suggesting that crystals deform into available pore space. He continues to attribute the permanent set and hysteresis at low temperatures to the internal friction associated with interlamellar shear.

3.2 Strain Rate

Birch and Brocklehurst (1983) showed that the strength of a polycrystalline graphite is independent of strain rate. They studied the impact behaviour of a wide range of graphites, and found an absolute equivalence between the measured flexural strength and the fracture strength calculated from the energy required to cause fracture in one impact. Burchell (1986) reported a trend suggesting a reduction in strength with increasing strain rate, but attributed such decreases in strength to a possible time lag in the load-amplification circuits in the tensile testing machine. Therefore it may be concluded there is no significant loss in the graphite strength with increasing strain rate.

3.3 Effect of Pre-stress on Young's Modulus and Strength

Oku and Eto (1973) investigated the effects of compressive pre-stress on the Young's modulus, the tensile and compressive strengths of some nuclear grade graphites. Their results showed that the Young's modulus and the tensile strength of these graphites decreased as compressive pre-stress increased, whereas the compressive strength remained the same. They attributed their results to the formation and propagation of cracks in graphite. Ioka and Yoda (1990) measured the changes in resistivity, Young's modulus and flexural strength of isotropic IG-11 nuclear graphite specimens in the directions parallel and perpendicular to the compressive pre-stress axis. Figure 3.2 presents a schematic representation of their observations. The Young's modulus of the parallel specimens remained constant until subjected to a pre-stress of $0.4\sigma_c$ before decreasing abruptly (by as much as 20%) with increasing pre-stress; σ_c denotes mean compressive failure strength. However, for the perpendicular specimens, the Young's modulus remained constant until a pre-stress of $0.2\sigma_c$ before gradually decreasing with pre-stress to about -7.5% at near failure. The flexural strength of the parallel specimens increased of uniformly by ~5% until a pre-stress of $0.4\sigma_c$ before decreasing

to -5% at near failure. The flexural strength of the perpendicular specimen remained almost unchanged up to a pre-stress of $0.2\sigma_c$ before gradually decreasing with increasing compressive pre-stress to -7.5% at near failure. The change in resistivity with increasing pre-stress for parallel specimens contradicted the trend found for the flexural strength by decreasing until a pre-stress of $0.4\sigma_c$ before increasing to ~+2% change at near failure. However, for the perpendicular specimens, the resistivity rose with increasing pre-stress of $0.5\sigma_c$ before becoming constant with an abrupt change in slope at $\sim 0.4\sigma_c$.

Ioka and Yoda (1990) explained their results using a model which assumed a macroscopically isotropic graphite due to random orientation of the filler grains (Figure 3.3). The basis for the model was the change in resistivity due to the opening and closing of microcracks and pores parallel and nearly perpendicular to the loading axis, *i.e.* the increase and decrease of resistivity with pre-stress is due to the creation and closure of pore or microcracks, respectively. At low stresses, initially only those filler particles inclined at 45° to the loading axis deform plastically, whereas others deform elastically. As the stress increases, the number of filler particles that deform plastically also increases, and at even higher stresses shearing of the filler-binder interface occurs. Inherent pores and microcracks between basal planes nearly perpendicular to the loading axis would be cleaved or be shrunk during compressive loading. In the case of filler particles whose basal planes are parallel to the loading axis, delamination between basal planes is expected to occur easily since the lateral plastic flow around the grains results in resolved tensile stresses, but the grains as a whole do not deform plastically due to low shear stresses. On unloading from small stresses, these delaminations will remain due to the surrounding plastic deformation. At high stresses, the grains with basal planes nearly perpendicular to the loading axis will deform plastically. On unloading from high stresses the authors proposed two recovery mechanisms to release the elastic strain induced in the basal planes nearly perpendicular to the loading axis (i) completely reversed slips between the parallel

basal planes, and (ii) delamination between the basal planes, which is similar to the thermal stress relaxation mechanism corresponding to the formation to Mrozowski cracks (1956).

3.4 Effect of Porosity

Mrozowski (1956) proposed the creation of fine shrinkage cracks on cooling from graphitisation temperatures due to contraction of the binder, caused by angular and shearing stresses present at the boundary between adjoining crystallites. These stresses will only be relieved above the temperature (~2300-2500 °C) at which viscous creep occurs. Thus stresses built up on cooling will remain locked or "frozen" in the material. The existence of these frozen-in stresses is partly responsible for the temperature dependence of the mechanical strength for graphites.

Typical synthetic graphites have fractional porosities of around 20%. The material contains a spectrum of pores, from small microcracks to large voids. Porosity affects mechanical properties such as strength and elastic modulus, since it reduces the volume of the solid within which the stresses are distributed. Also pores can act as sites for local stress concentration which can initiate failure, especially if they have a high aspect ratio. Pickup *et al.* (1986) showed for two graphites, PGA and IM1-24, that the mechanical properties such as fracture toughness, dynamic elastic modulus and the fracture strength decreased with increasing porosity (resulting from thermal oxidation) which can be described by empirical exponential equations. They found that the most significant change in the microstructure of the graphites upon oxidation is the development of narrow, slit shaped cracks in the binder phase, as well as the opening up of the closed porosity within the filler particles.

3.5 Deformation Mechanisms and Microstructure

Extensive reviews of deformation mechanisms in carbons and graphites have been carried out by Jenkins (1973); Brocklehurst (1977); and Kelly (1981). Jenkins (1962a) describes the fracture of a petroleum coke nuclear graphite which has slowly been bent until failure. Fracture proceeded preferentially along striations within the highly oriented structure of the filler particles, particularly under shear, at angles to the direction of maximum strain. Cracks travelled between pores and isolated cracks appeared before major fracture. Jenkins (1962a) concluded that the material deforms mainly by interlamellar slip and fracture within the filler particles, which are inhibited by less well-oriented binder, suggesting that crack propagation is considerably more difficult than crack initiation. Taylor *et al.* (1967) observed in graphites with petroleum coke fillers and coal-tar pitch binders that cracks were initiated at pores and branched out; the fracture path linked the initiated cracks and tended to include the larger pores. They further observed crack branching and that secondary cracks ahead of the main advancing crack ran back to meet it. They also noted that advancing cracks were deflected around spherical coke particles.

Experimental observations of fracture have been described by Pickup *et al.* (1986) and Burchell (1986). In flexural tests, cracks start to appear at one third of the maximum deflection. These cracks lie either in regions of well-oriented binder phase material or along the interfaces between the filler particles and the binder. They note that there are many subcritical defects or crack fronts which occur randomly on numerous planes within the sample. The subcritical cracks increase in size and density as load increases and eventually some of them connect with each other. At high load, one crack will suddenly grow rapidly to interlink with others on its passage across the section of the specimen, leading eventually to failure. The path of the crack tends to be linked to a narrow volume of material running parallel to the plane of the maximum tensile stress.

Burchell *et al.* (1986a) and Burchell *et al.* (1987) made qualitative and quantitative studies of fracture in several polygranular graphites, ranging from a fine-textured, strong, aerospace graphite to a coarse-textured, weak, electrode graphite subject to flexural loading, by observing dynamic crack propagation with an optical microscope. They identified that porosity had three roles in the fracture process; (i) initiating cracks from favourably oriented pores; (ii) assisting crack propagation by attracting advancing cracks in well-aligned domains; and (iii) arresting crack propagation by attracting cracks into unfavourably oriented mosaics, which resist crack growth. They observed microcrack initiation in regions of binder phase where there is extensive basal plane alignment. On increasing stress, cracks link with one another to produce a coherent defect. Failure occurs when such a defect reaches a critical length. They showed that the cleavage of domains occurred at stresses well below the fracture stress, whereas areas of mosaics only cleaved at stresses approaching the fracture stress. Filler particles with good basal plane alignment are highly susceptible to microcracking and cleaved at low stresses, facilitated by calcination cracks which lie parallel to the basal planes. An advancing crack may propagate through a well aligned filler particle taking advantage of the easy cleavage path. For needle-coke graphites with filler particles that are preferentially oriented parallel to the tensile stress, the dominating features of the fracture surface are cleaved, needle coke grains lying parallel to the fracture surface. In the case of Gilsocarbon filler particles, cracks were observed to propagate circumferentially through the outer part of the "onion skin" array of the calcination cracks and parallel to the basal plane alignment, creating "cusps and domes" in the fracture surface. Filler-binder interfaces were subjected to crack initiation and propagation and in the case of poorly aligned filler particles the interfaces attracted advancing cracks, due to residual stresses created on cooling from graphitisation.

Fracture surfaces, for most graphites, are less smooth in the binder phase than in the filler particles. This difference is due to the poor alignment of the basal planes in the binder phase. As Brocklehurst (1977) explained, the fracture energy for the cleavage

of basal planes is less than the energy required to propagate cracks in non-basal plane directions, and therefore the crack front in the binder phase is tortuous as it attempts to follow the poor alignment of basal planes.

Polycrystalline graphites subjected to tensile and flexural stresses usually fail to produce a granular fracture surface normal to the applied maximum stress. Brocklehurst (1977) describes the tensile fracture process as the development and increase in density of microcracks as the applied stress increases until a critical crack size is reached followed by catastrophic failure. Similar specimens subjected to compressive stress usually result in shear type failure with the fracture plane at an angle to the applied stress direction. Taylor *et al.* (1967) report an angle of 35° in some reactor graphites. They proposed that this type of fracture process results from the linking of microcracks which form in high stress regions, and lie on the same inclined plane. After initiation, they then stabilise, rather than propagate as a single critical crack as in tensile failure. Failure under compression can be visualised as the linking of cracks along a plane of maximum net shear stress. However, Greenstreet *et al.* (1969) reported that the failure of EGCR-AGOT graphite subjected to an applied longitudinal compressive stress resulted from longitudinal tensile cracks. They attributed such behaviour to an increasing compressive strain where the transverse strain reached the tensile failure strain and a longitudinal break resulted. After an initial crack is nucleated, the crushing action of the loading mechanism tended to destroy the evidence of the actual failure mode.

Grade	Application	Source	Forming Method	Bulk Density gcm-3	Young's modulus/GPA //or⊥to forming axis	Strength(MPa)		
						tensile	compression	flexure
AGSR	General purpose	UCAR	Extruded	1.58	9.45/5.31	7.58/5.24	30.06/27.3	15.31/9.86
AGW	Electronic Anodes	UCAR	Extruded	1.68	11.65/6.07	8.43/6.14	31.37/31.43	15.86/11.61
AGOT	Nuclear	NCC	Extruded	1.7	10.27/7.65	9.93/8.69	41.30/41.09	16.55/13.58
PGA*	Nuclear	BAEL/AGL	Extruded	1.7	11/6	10/6	30/30	14/9
IM1-24*	Nuclear	BAEL/AGL	Moulded	1.8	10/10	22	85	33
SM2-24*	Nuclear	BAEL/AGL	Moulded	1.7	8.0/8.5	12	47	19
ATJ*		NCC	Moulded	1.75	8/10	10/12	59/57	25/28
ZTA*		USA	Hot pressed	1.95	6/18	8/28	80/50	17/37

TABLE 3.1 : Mechanical properties of common graphites (Mantell, 1968 and *Brocklehurst, 1976).

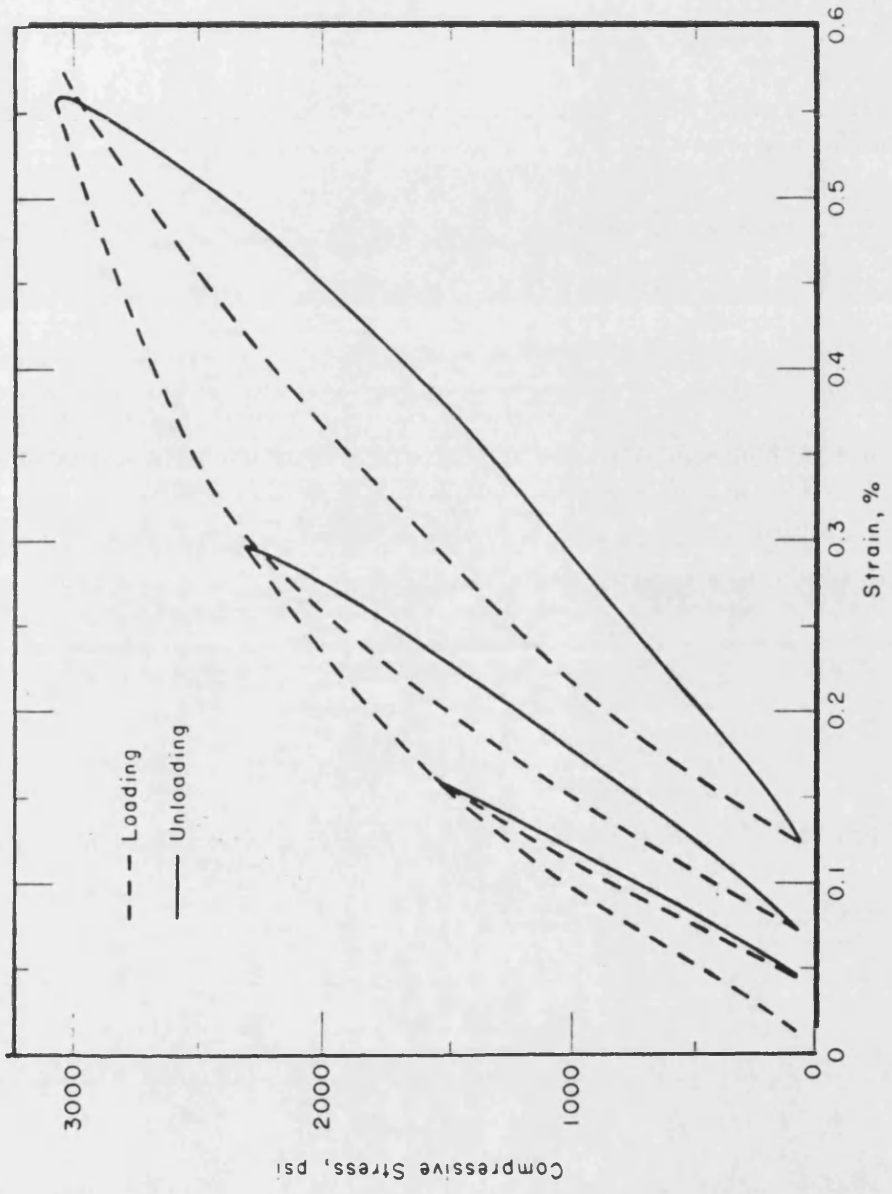

FIGURE 3.1 : A typical compressive stress-strain curve for a nuclear graphite (Nightingale, 1968).

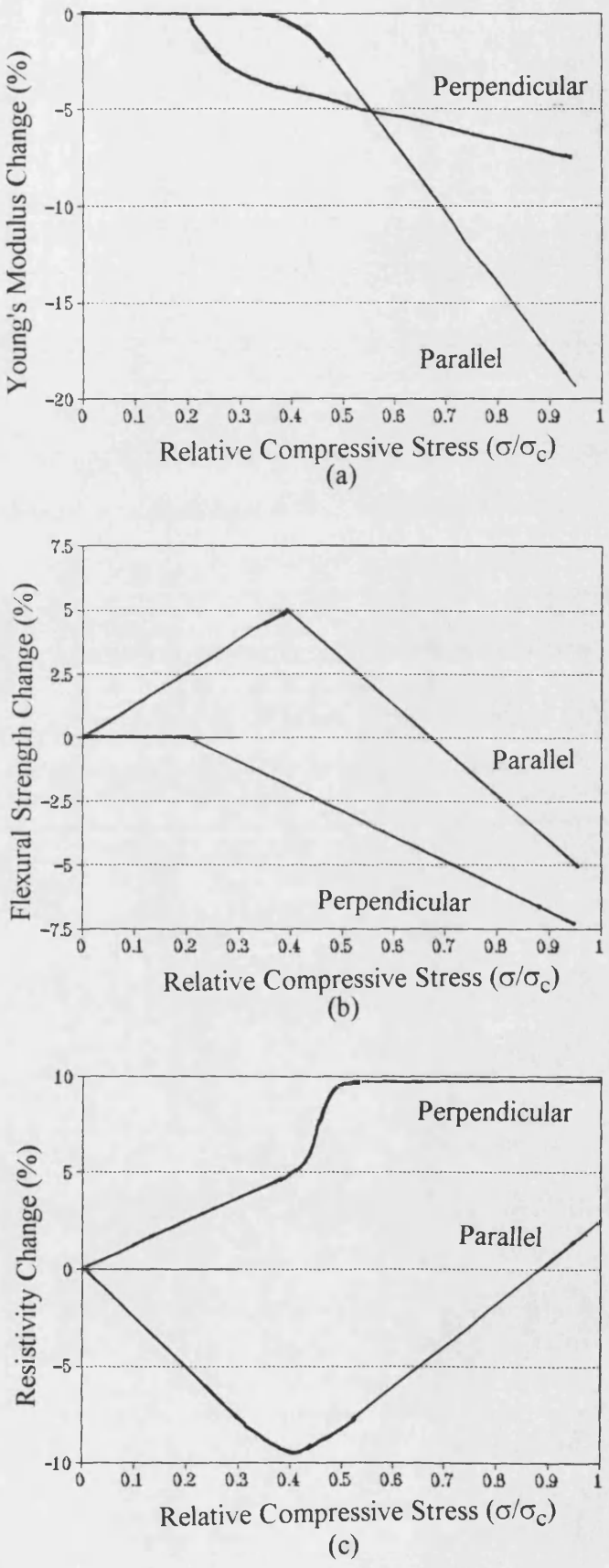

FIGURE 3.2 : Schematic representation of Ioka and Yoda (1990) observations.

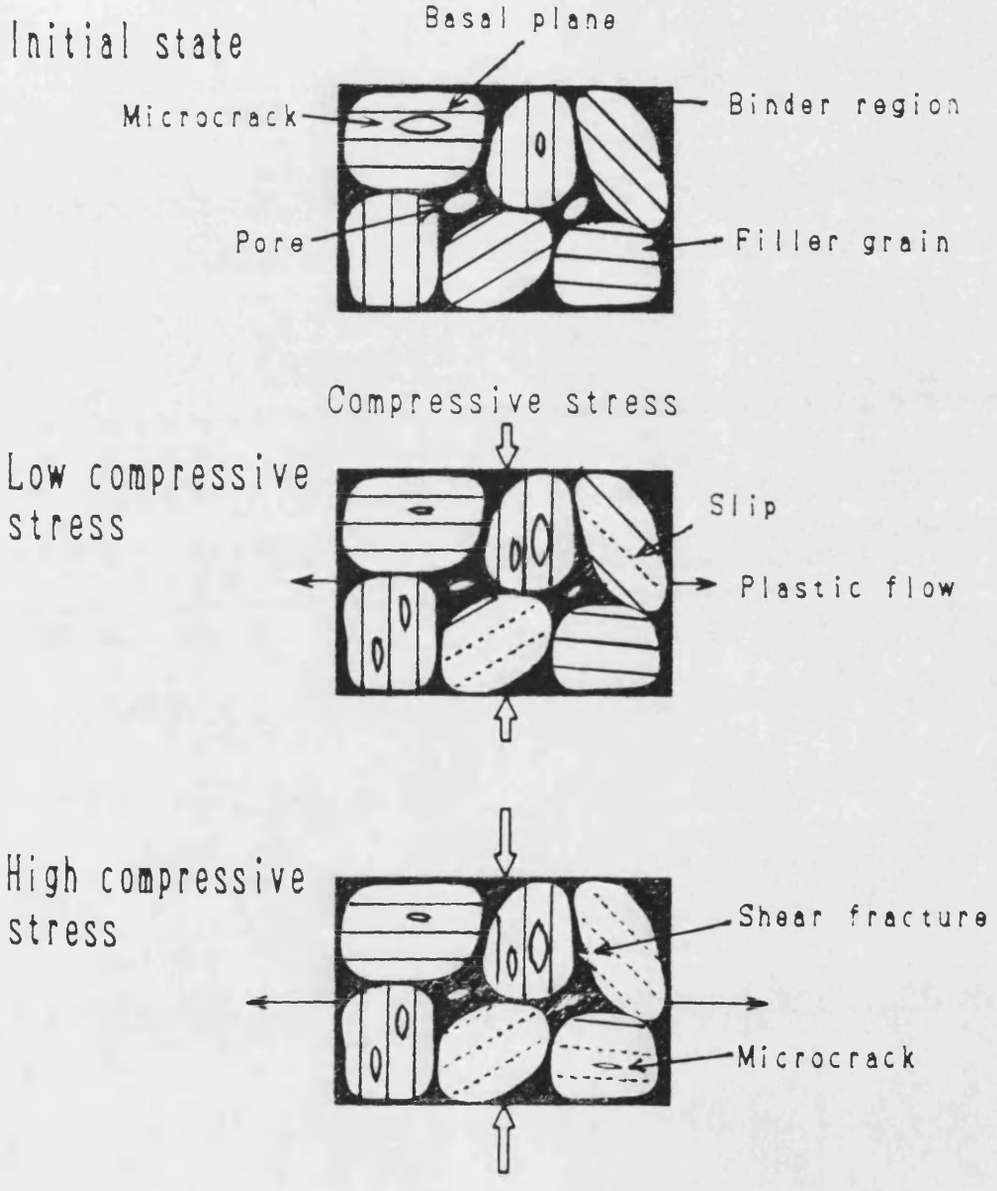

FIGURE 3.3 : Model for the mechanism of compressive deformation of an isotropic graphite (Ioka and Yoda, 1990).

CHAPTER FOUR : REVIEW OF FRACTURE IN NUCLEAR GRAPHITES

4.1 Fracture Mechanics

Fracture mechanics is a vast field, and its basic principles have been summarised (Knott, 1973). The application of fracture mechanics to graphite is a relatively small area which is summarised in this chapter. Fracture and mechanical behaviour models are essential for predicting the life of graphite components, especially for a reactor core, and are generally used in designing new components. They are based on two approaches: (i) the global energetical balance in creating two new surfaces, or (ii) the stress fields surrounding a sharp crack. In both cases a critical condition defines fracture and the failure of a component.

4.1.1 Energetical Approach to Fracture Mechanics

Fracture mechanics owes its beginning to Griffith (1920) who attributed the discrepancy between the theoretical and the observed tensile failure strengths of glass to the presence of microcracks, around which a strong stress concentration arose when the solid was stressed. Griffith treated his observations using a thermodynamic balance of surface energy necessary for the creation of two new surfaces. He postulated for a stable propagating crack, that the strain energy released is just sufficient to provide the increase in surface energy necessary to propagate the crack. He derived the formula for the failure strength, σ_f, for plane stress, *i.e.* $\sigma = 0$ in the thickness direction, as

$$\sigma_f = (2\gamma_s E/\pi a)^{1/2} \qquad (4.1)$$

where γ_s is the surface energy, E is the Young's Modulus and a is the crack length. For plane strain, *i.e.* zero strain in the thickness direction, the equation is altered by dividing the modulus by $(1-\nu^2)$ where ν is the Poisson's ratio. For most synthetic

graphites, $\nu \approx 0.2$, and thus the term $(1-\nu^2)$ is usually ignored, since it approximates to unity. The Griffith's equation (equation 4.1) shows that the stress necessary for crack propagation varies inversely with the square root of the crack length. The strength of a brittle material is therefore determined by the size of the largest crack before loading.

Orowan (1955) and Irwin (1958) independently developed Griffith's relationship further by taking account of the occurrence of plastic flow in the material. They showed that during crack propagation it is possible for a small amount of plastic deformation to occur requiring extra energy, γ_p. It can be shown that the surface energy plus the energy expended in plastic deformation is equivalent to the critical strain energy release rate, G_c, commonly called the fracture toughness (*e.g.* Anderson *et al.*, 1990), *i.e.*

$$G_c = 2(\gamma_s + \gamma_p) \qquad (4.2)$$

thereby modifying the Griffith relationship to

$$\sigma_f = (EG_c/\pi a)^{1/2} \qquad (4.3)$$

Nakayama (1965) considered the direct measurement of effective surface energies from the load-deflection curves for brittle heterogeneous materials, and provided a mathematical criterion of stable crack growth from a notched specimen (Figures 4.1 and 4.2). The effective surface energy is defined as the work done to create unit area of a new fracture surface. He noted for stable crack growth that the elastic stored energies in the specimen plus the apparatus must be less than the energy required to complete the fracture process, and that the additional external work required is supplied by the moving crosshead. However, if the stored energies are greater than that required the complete the fracture process, then the fracture mode is catastrophic and the excess energy is consumed by other forms of energy, such as the kinetic

energies of the fragments.

Tattersall and Tappin (1966) described a method for measuring the work of fracture from the load-deflection curve similar to that described by Nakayama (1965), but used a rectangular bar with a notch having an isosceles triangular cross-section. The apex of the triangle was used to initiate controlled crack grow at the notch and to limit plastic flow for the more ductile materials. The work of fracture is defined as the work done to create unit area of a new fracture surface over the entire fracture process. They considered various materials, including a reactor graphite, which typically gave a work of fracture of ~100 J/m^2.

Davidge and Tappin (1968) examined the effective surface energy from load-deflection curves in flexural loading of single edged notched beams (SENB) of four brittle materials; alumina, polymethylmethacrylate, glass and polycrystalline graphite. They calculated the effective surface energy at the initiation of fracture using an analytical method and a compliance method, and then compared these values with the work of fracture. They concluded that the effective surface energy at the initiation of fracture from both methods gave consistent values for all materials. For the polycrystalline graphite (PGA), the effective surface energy was less than the work of fracture due to subsidiary cracking as the fracture process proceeded. For PGA graphite, they found that the work of fracture decreased with increasing notch depth (from unnotched to a notch to depth ratio of 0.9) from 227 to 84 J/m^2. They attributed this phenomenon to the tortuous crack path and the secondary cracks that open up during the fracture process. Thus crack propagation is more difficult than crack initiation.

Polycrystalline graphite has been shown to demonstrate plastic deformation (*e.g.* Sakai *et al.*, 1983, described §4.2.1). Pickup *et al.* (1986) described polycrystalline graphites as non-ideal brittle materials, suggesting the extent of non-ideality will vary with graphite type from fine to coarse-textured graphites. They defined a non-dimensional,

non-ideality parameter, κ, which quantifies the deviation from ideal brittle behaviour. For an ideal material, the effective surface energy, $2\gamma_f = G_{Ic} = K_{Ic}^2/E$, but for a non-ideal material

$$2\gamma_f = K_{Ic}^2/E + \kappa (K_{Ic}^2/E) \qquad (4.4)$$

where E is the elastic modulus and K_{Ic} is the critical stress intensity factor (described in §4.1.2). The second term, $\kappa (K_{Ic}^2/E)$, represents the contribution to $2\gamma_f$ from crack branching and other sub-critical events. For two graphites, PGA and IM1-24, the authors found κ to be 0.56 and 0.19, respectively, indicating that fracture of PGA deviates more from ideal brittle behaviour than compared to IM1-24.

4.1.2 Stress Intensity Approach to Fracture Mechanics

The premise that the intensity of the stress or strain fields surrounding a crack-tip may be uniquely described in terms of the stress intensity factor, K, a function of applied stress and the crack length, is the concept of Linear Elastic Fracture Mechanics (LEFM). LEFM considers the case for a perfectly elastic and brittle material; as soon as a crack initiates, it grows and propagates in a catastrophic manner. However, the critical stress intensity factor can often give misleading results due to excessive plasticity at the crack tip. The stress intensity factor is derived by considering the stress distribution ahead of a sharp crack tip, and is given by the formula

$$K = \sigma a^{1/2} Y(a/w) \qquad (4.5)$$

where σ is the applied stress, a is the crack depth, and Y is a geometrical function of a/w where w is the depth of the specimen. The magnitude of K depends on the structural geometry and the loading system.

Brocklehurst (1977), in his review, discusses K_{Ic} determination and inherent flaw size

for a range of graphites. The inherent flaw size is the calculated size of an inherent crack in a material that effectively increases the machined notch by a constant amount, and it is estimated from comparing tests on unnotched and notched specimens (see Chapter Seven). He noted that in previous studies, that many authors calculated a effective flaw size that corresponded to observable microstructural features, such as the maximum grain or pore size. In the same review, he presented results from his own studies of SENB tests on IM1-24 graphite, and showed that K_{Ic} ranged from 1.4 to 1.5 $MNm^{-3/2}$ with no significant differences for a/w ratio between 0.1 to 0.5. The inherent flaw size ranged from 0.25 to 0.4 mm, which is similar to the filler particle size.

Rose (1985) reported K_{Ic} values for curved and straight beam specimens of unirradiated pitchcoke graphite using the polynomial function for SENB specimens derived by Srawley and Gross (1976). He concluded that in reporting fracture toughness data of graphites, the calculated K_{Ic} had to take account of the inherent flaw size. Rose (1985) also found K_{Ic} to be independent of notch depth for $a/w > 0.3$, and obtained a value of K_{Ic} of 1.20 ± 0.15 $MNm^{-3/2}$ with an additional crack length of 0.6 mm below the machined notch. However, Allard *et al.* (1991) measured crack growth resistance curves on anthracite-based carbons materials and recommended that the a/w ratio should be between 0.3 and 0.7. For deep notch depths, they found edge effects distorted the results, since the crack growth resistance is much higher at the specimen rear surface due to the increased size of the process zone.

4.2 Models of Failure for Synthetic Graphites

No single theory has been developed for polycrystalline graphites that has adequately described all the circumstances of possible fracture. This is not surprising considering the complexity of the graphite microstructure. In situ, the nuclear materials must withstand shock loading, internal stresses, corrosion, neutron-induced hardening and

dimensional changes. As stated earlier, there is a need for a model to predict mechanical behaviour of graphite components, such as moderator bricks and fuel sleeves, for design and life-prediction purposes. A model should be able to predict mechanical behaviour and deformation under various stress states, and among other things it should also be able to predict acoustic emission responses. Only recently has a model been emerging that is able to predict semi-quantitatively acoustic emission responses from static loading (McLachlan, 1992).

4.2.1 Early Failure Models

The simplest model for graphite is based solely on fracture mechanics in which the failure of a component is to due to stress concentrations caused by the presence of crack-like defects. The failure criterion is that a Griffith crack is placed at its most damaging position in a stressed specimen (Tucker *et al.*, 1986). Graphites have an abundance of crack-like defects and therefore the derived critical crack size may be representative of the material. This critical crack size may be the combination of weak crystallites and pores, typical of the microstructure, *i.e.* it differs for each grade of graphite. Therefore, fracture will be characterised by microstructural features which give rise to a critical crack size.

Weibull (1951) first proposed a statistical model for brittle failure that described the survival probability $P_S(V_0)$ as the fraction of identical samples, each of volume V_0, which survive loading to a tensile stress, σ, such that

$$P_S(V_0) = \exp\left[-\left(\sigma / \sigma_0\right)^m\right] \qquad (4.6)$$

where σ_0 is simply the tensile stress that allows 37% of samples to survive, and m is the Weibull modulus which is determined empirically using best fit curve methods. The lower the value of m, the greater variability in strength. Having determined m, it is in theory possible to predict the dependence of strength upon specimen volume. The

strength of a material is dependent upon the flaw size distribution within its volume. A large sample will fail at a lower stress than a smaller sample, on average, because it has a higher probability that will contain a large flaw. This suggests that there is a volume dependence of the strength, which may be described by the Weibull theory. The probability that a batch of n samples all survive the stress σ is simply $[P_s (V_0)]^n$. If all these n samples were stuck together to give a single sample of volume $V = nV_0$, then its survival probability would still be $[P_s(V_0)]^n$. So

$$P_s (V) = [P_s (V_0)]^n = [P_s (V_0)]^{V/V_0} \quad (4.7)$$

Taking logs on both sides and rearranging gives

$$P_s (V) = \exp [V/V_0 \ln P_s (V_0)] \quad (4.8)$$

If eqn. 4.6 is inserted in eqn. 4.8 then

$$P_s (V) = \exp [-V/V_0 (\sigma/\sigma_0)^m] \quad (4.9)$$

which describes the volume dependence on the survival probability for a specimen of volume, V. Brocklehurst (1977) reported that the Weibull theory failed to give any consistent values of m as a material parameter for graphites. He stated that the Weibull theory strictly only applies to brittle, linear-elastic materials, and since that graphites show non-linearity in their stress-strain behaviour it is not surprising that the theory does not conform to experimental data.

Buch (1976) proposed a fracture model for polycrystalline graphite which related tensile strength to microstructural features. He considered a model for polycrystalline graphite consisting of cubical grains bonded together to form a bulk body. Each cubical grain contained a plane of weakness oriented to the applied stress that

corresponded to the basal plane of a graphite crystallite. As the applied stress increased, the density of microcracks, or cracked cubical grains, within the material was assumed to increase. The material failed when the number of adjacent microcracks reached a critical size for catastrophic crack growth. Porosity was incorporated into the model by considering pores as randomly distributed pre-cracked grains.

Buch's model was extended with some success by Rose and Tucker (1982). They considered a three dimensional array of cubic blocks of uniform size representative of the particle size of graphite. Each block contained a randomly oriented crystalline structure where only basal plane cleavage occurs. Pores are treated as blocks of zero cleavage strength. When a load, σ, is applied, the cubic block only fails when the resolved tensile stress on the cleavage plane exceeds a critical value. If two adjacent blocks have failed the intervening boundary between the blocks is also considered to have failed forming a contiguous crack extending across both particles. For a loaded specimen, the cracks are assumed to develop on planes normal to the axis of principal stress. Cracked blocks are treated as delaminated square regions of the plane shown in Figure 4.3. The specimen fails when enough adjacent blocks within a plane have cleaved to form a defect large enough to fail as a brittle Griffith's crack. The probability of failure of the specimen is then the probability that any one of the planes contain such a critical defect.

A detailed review of six fracture models was presented by Tucker *et al.* (1986), applying each model to a comprehensive range of experimental data for several graphite grades. The six models were (i) the Weibull theory; (ii) the Rose/Tucker model; (iii) the fracture mechanics model; (iv) the critical strain energy density criterion; (v) the critical stress criterion, and (vi) the critical strain criterion. The first three models have been discussed previously. The last three models treated the graphite as an elastic continuum, and failure was assumed to occur when the maximum

stress, maximum strain or elastic strain energy density reached a critical value for a region of tensile stress. Tucker *et al.* (1986) found these three models were unsuccessful in describing graphite failure behaviour. The Weibull theory predicted successfully the effects relating to volume rather than microstructure, but was inferior to the Rose/Tucker model and the fracture mechanics model. It was concluded that the models based explicitly on microstructural detail were more successful than those considering the material as a continuum.

Polycrystalline graphite has demonstrated complicated irreversible deformation processes and non-linear stress-strain behaviour during mechanical testing. Papers published in recent years have classified polycrystalline graphite as an elastic-plastic material (Sakai *et al.*, 1983; Oku *et al.*, 1986; Sakai *et al.*, 1988; Allard *et al.*, 1991; and Barinov and Shevchenko, 1992). A non-linear fracture toughness parameter from Elasto-Plastic Fracture Mechanics is not currently available due to mathematical difficulties. However, by simulating the effects of plastic deformation within the context of elastic analysis and using global energy principles, the fracture behaviour may be characterised by extending the concepts of LEFM to obtain a crack growth resistance parameter. For controlled crack growth, the global energy balance at each instant of crack growth approximates to

$$\partial W/\partial A = \partial(U_e + U_p)/\partial A + \partial\Gamma/\partial A \qquad (4.10)$$

where ∂A denotes the increment of the cracked surface area, U_e is the elastic stored energy, U_p is the plastic energy dissipated, and W and Γ are the work done by the external force and the surface energy required by the new cracked surface, respectively. Therefore, the energy available for crack extension must be

$$\partial W/\partial A - \partial(U_e + U_p)/\partial A \qquad (4.11)$$

which represents the part of the work done by the external force which is not consumed in the elastic-plastic deformation, *i.e.* the crack driving force. Thus a non-linear fracture toughness parameter, G_c', can be defined as

$$G_c' = \partial[W-(U_e + U_p)]_c/\partial A \qquad (4.12)$$

For the case of linear elastic solids, $U_p \equiv 0$, G_c' will reduce to the elastic fracture toughness parameter, the strain energy release rate, G_c. A measure of crack growth resistance, R, may now be defined as

$$R = \partial(W - U_e)_c/\partial A \qquad (4.13)$$

Crack growth resistance curves, or R curves, are used to characterise the fracture behaviour over the whole fracture process. These curves relates the crack growth resistance to the extent of crack growth, and are usually calculated graphically from load-crack opening displacement curves for steady state incremental crack growth for cyclic loading of typically SENB specimens. Using this "elasto-plastic" analysis, and for the isotropic polycrystalline graphite Toyo Tanso IG-11, Sakai *et al.* (1983) determined the elastic and plastic components of the fracture energy, he found that 38% of the total fracture energy was consumed as plastic energy. Allard *et al.* (1991) characterised very coarse anthracite-based carbon materials using R curves (Figure 4.4) and noticed three main stages: (i) an initial increase in fracture energy corresponding to the growth of a process zone before the onset of a macrocrack; (ii) a constant value of crack growth resistance corresponding to a critical process zone size which moves with steady state crack growth as the fracture process proceeds, and (iii) a further increase in the crack growth resistance corresponding to the interaction of the process zone with the specimen rear surface.

4.2.2 The McLachlan Model

The McLachlan model (McLachlan *et al.*, 1989 and McLachlan, 1992) is the latest one developed from the original Buch model (1976) and fracture mechanics. The model takes account of microstructural features such as porosity, that initiates crack growth, and the polycrystalline mosaic that inhibits crack propagation. The elastic-plastic model divides the pore population, of various geometries and sizes, into active and passive defects. Under applied stress, only active pores will initiate cracks, passive pores remain intact and only take an active part in affecting material properties, but may assist crack propagation in attracting the crack tip. At the boundary of an active pore, the criterion for crack initiation is such that the stress, quantified using the concept of stress intensity factor, must reach a critical value. The crack propagates with little resistance from porosity and suitably oriented inter-crystalline boundaries. A crack opening is not assumed to be a continuous, but is generally connected by sheared crystallites (see Figure 4.5). As the applied stress increases, the stress intensifies around the crack tip until a critical value before the crack front moves further into the material. The model only assumes the crack can be arrested by crystallites intersecting the crack tip (see Figure 4.5), opposing the inter-crystalline shear, and effectively "pinning" the advance of the crack tip. The pinning crystallite is only assumed to fail by cleavage of the basal plane, and the stress required to do this depends on the orientation of the crystallite to resolved forces. The probability of failure of the pinning crystallite can be calculated from the crystallite orientation distribution of the within the material. Thus the probability of a crack propagating includes a function of the probability of a single adjacent pinning crystallite fracturing and the actual number of such crystallites on the crack edge. The propagation of a crack through polycrystalline graphite may be represented by a sequence of incremental crack edge advances. Each advance is of probable length between neighbouring pinning crystallites. Therefore, each active pore has a probability that it will initiate a crack that eventually leads to failure after following the appropriate sequence of incremental advances. It also has a probability of total arrest after a series of incremental steps.

Hence, it is possible to resolve for a specimen an overall probability of its failure as a function of applied stress. Each pore has an associated probable volume greater than its unstressed value as the applied stress increases. The model uses failure probabilities and behavioural changes, such as pore volume changes, to predict stress related physical properties, such as strain hysteresis and acoustic emission.

The model may be used to predict acoustic emission responses. Only two types of microstructural mechanisms are considered that give rise to acoustic emission: (i) the creation of an open crack from failure of a number of crystallite and inter-crystallite boundaries, and (ii) the deformation of the grains within the plastic region by shear of inter-crystalline boundaries or of the basal planes of their constituent crystallites. By associating a number of events with the failure a crystallite or inter-crystalline shear in the proximity of the crack edge, and also the opening of the surface area created by the crack advance, the AE event count is derived. In both cases, the number of AE events generated is associated with the volume of the material deformed. The cumulative AE event count predicted is therefore the total number of AE events from both of these two sources for the entire fracture path plus all other subcritical cracking and plastic deformation for arrested crack propagation routes (Figure 4.6).

For cyclic loading up to the point of previous maximum stress, the model assumes that the AE generated from the opening of a crack, *i.e.* those from failure of a crystallite or inter-crystalline boundary will not be re-generated. However, those from deformation of grains within the plastic region, *i.e.* shear, will be re-generated. These AE events from crystallite shearing are said to be less energetic than those of the once off events from the fracture of pinning grains and they occur from the onset of stress. Hence, in the predicted experimental AE response, some events are expected before the previous peak stress attributed to the incomplete shear of crystallites.

Experimental AE work described in Part D of this thesis supports the ideas suggested

in the McLachlan model. Experimental evidence shows the AE response to have a small amount of AE events prior to the previous peak stress, and these events are attributable to a reversible shear mechanism. Part D also attempts to quantify the amount of reversible AE events from cyclic loading in order to learn more about the recovery processes occurring in nuclear graphites.

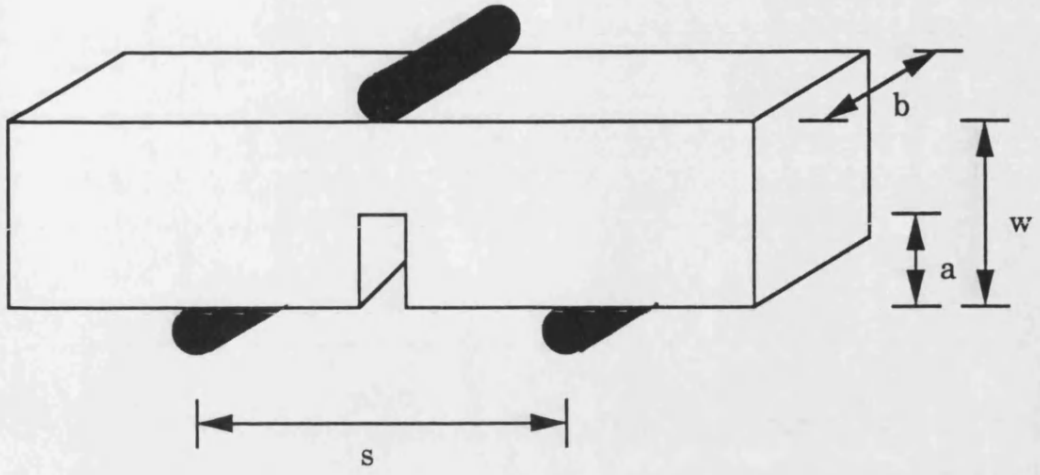

s Loadspan
b breadth
a notch depth
w specimen depth

FIGURE 4.1 : An illustration of a single-edged notched beam between knife edges.

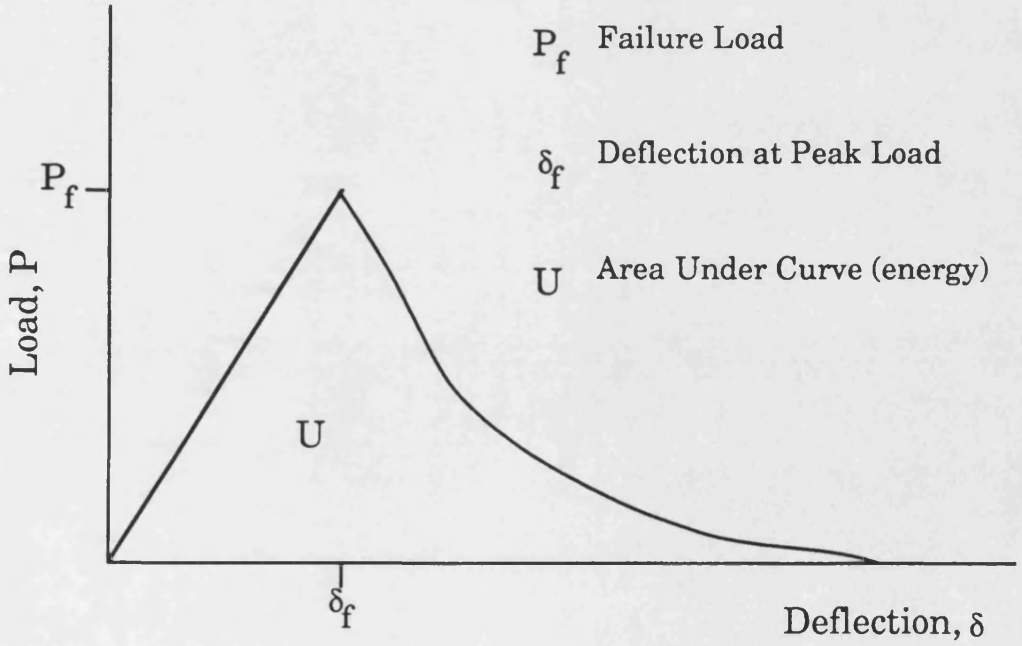

FIGURE 4.2 : An illustration of a typical load-deflection curve from controlled crack growth of a single-edged notched beam.

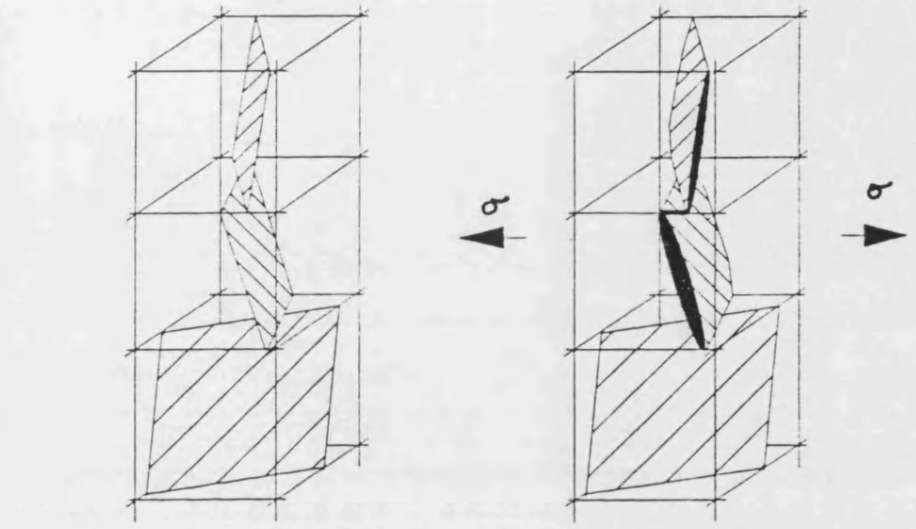

Failure Probability = Probability that enough adjacent particles are cracked to form a critical defect.

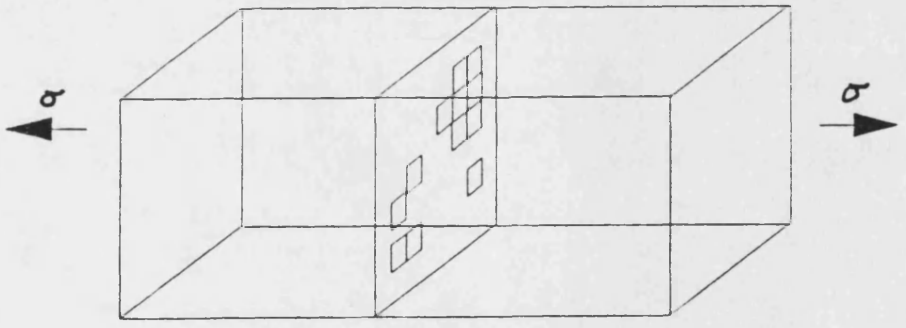

FIGURE 4.3 : The Rose/Tucker model of graphite failure (Tucker *et al.*, 1986).

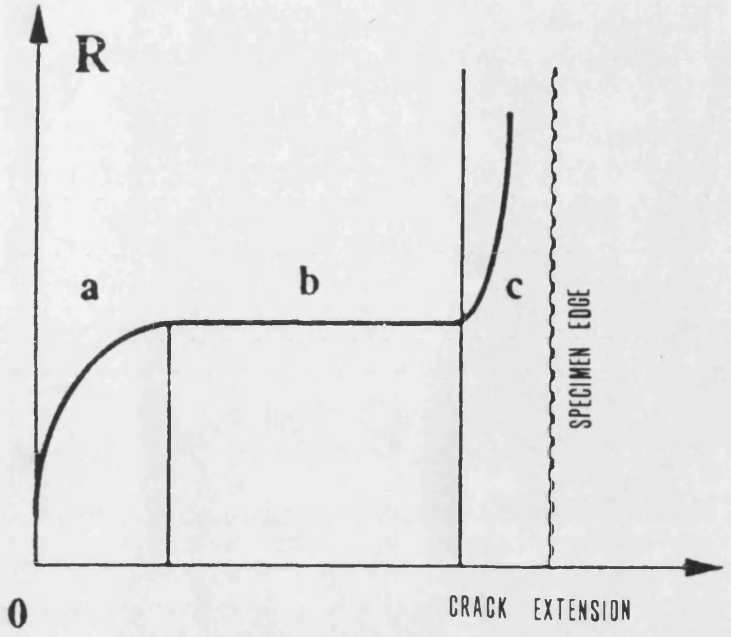

FIGURE 4.4 : A illustration of a typical R curve (Allard *et al.*, 1991).

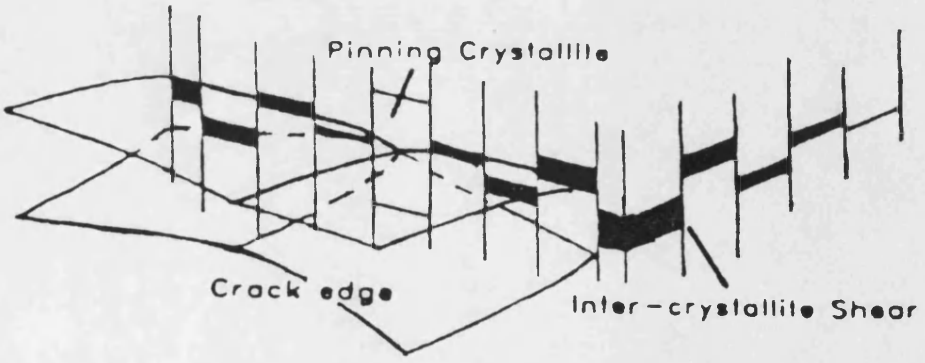

FIGURE 4.5 : The McLachlan Model (McLachlan *et al.*, 1989).

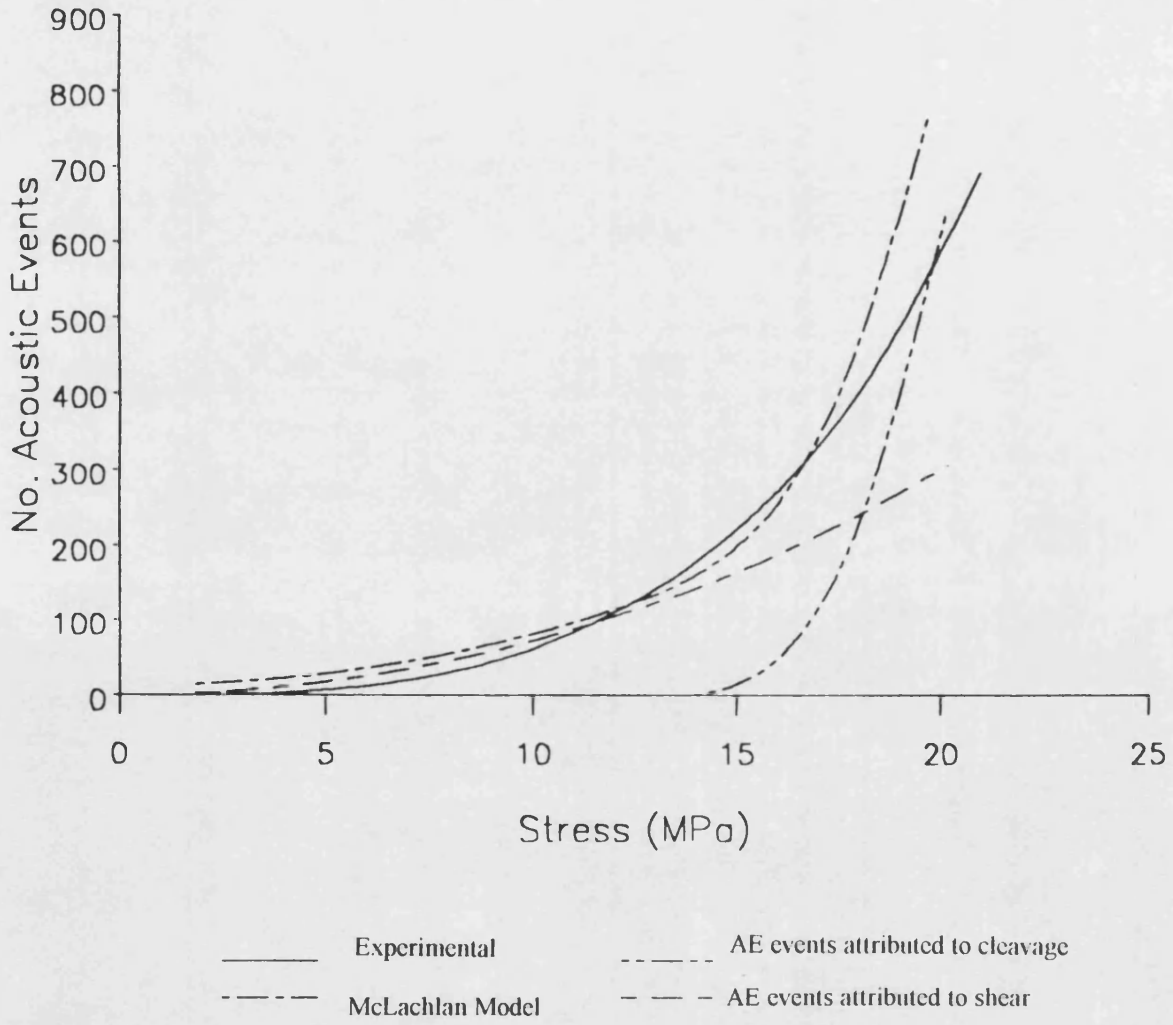

FIGURE 4.6 : Components of a predicted AE curve (McLachlan *et al.*, 1990).

CHAPTER FIVE : EFFECTS OF REACTOR ENVIRONMENT ON THE GRAPHITE MODERATOR

Amongst the materials available for use as the moderator in nuclear reactors, deuterium oxide (D_2O) is the best followed by beryllium. Graphite, although less efficient, is the moderator material chosen for the U.K. thermal nuclear reactors because it has important practical advantages. Graphite is a good moderator because of its high scattering and low neutron capture cross sections and low atomic weight. Its practical advantages are that it can be easily machined to form structural components, its mechanical stability increases with increasing temperature, it has excellent resistance to thermal shock, good thermal properties, ready availability and low cost (Carpenter and Norfolk, 1984). Throughout the life of a nuclear reactor, the graphite undergoes deformation mechanisms and changes in mechanical and physical properties, primarily due to radiolytic oxidation and differential dimensional changes due to non-uniform neutron irradiation from the fuel. These effects reduce the ability of the moderator core to withstand external loads and cause internal stresses.

5.1 Radiolytic Oxidation

Radiolytic oxidation is initiated by radiation energy (arising from neutrons and γ rays) dissipated in the CO_2 coolant. CO_2 is broken down to CO plus a range oxidising ions and free radicals, sometimes denoted collectively as "Ox". "Ox" recombines to reform CO_2 unless it impinges on a graphite surface, in which case it gasifies a carbon atom as CO. "Ox" is short lived, hence the coolant is apparently stable as CO_2. "Ox" diffuses into the surface of graphites, at most, a few micrometres before annihilation. Radiolytic oxidation therefore occurs as fast in pores of width from a few micrometres upwards as it does on an external surface. Moreover, because it enlarges the pores which then contain more gas and accessible surface, corrosion tends to accelerate with time, eventually approaching three times the original rate (Best *et al.*, 1985; Murdie *et*

al., 1986 and Wickham, 1990). The rate of reaction is determined by gamma flux, gas pressure and graphite porosity (open pore volume). This corrosion can be inhibited to an acceptable level by the use of methane (0.023% volume) and carbon monoxide (1% volume) in the coolant gas. Since radiolytic oxidation increases the porosity with time of reaction, the main effect on the moderator graphite is loss of strength and elastic modulus.

5.2 Neutron Irradiation

Fast neutrons produced in fission have energies of about 2 MeV. Moderation of these neutrons down to thermal energies of <1 eV is caused by elastic collisions with the carbon atoms; where 25-60 eV is required to displace a carbon atom from the graphite lattice creating vacancies and interstitials. Many point defects recombine, annihilating one another, some become trapped, while others aggregate to form more complex defects which are less energetic and so are more stable. There is a balance between displacement rate, *i.e.* fast neutron flux and the defect mobility, which is related to temperature. At low temperature (<300 °C), the crystal lattice grows perpendicular to the basal planes and shrinks parallel, and overall the volume increases (Carpenter and Norfolk, 1984).

The dimensional changes caused by the displacement of atoms leads to lattice strain and Wigner energy. At temperatures above 300 °C there is little dimensional change and low Wigner energy due to much higher defect mobility. At these temperatures, interstitials are so mobile that they aggregate to large areas of the graphite lattice. Dislocation loops have been observed in graphites (Amelinckx *et al.*, 1965), and it has been suggested that these loops are formed by the collapse of adjacent lattice planes into a vacancy cluster (Kelly, 1982). As irradiation proceeds further, the atoms knocked into the interlayer positions will be subject to further displacement by the fast neutrons. If the graphite is stressed while this is happening, this secondary

displacement will free the neighbouring atomic planes to slip over one another, by a dislocation pinning-unpinning mechanism, allowing the graphite to deform plastically by what is termed irradiation creep. This phenomenon was first demonstrated in detail by Perks and Simmons (1964) but has since been studied by many other workers (*e.g.* Kelly, 1992). Irradiation creep has the beneficial effect of relieving the build up of residual stresses that arise from any non-uniform dimensional changes. It has been estimated, that on average each carbon atom in the moderator core is displaced twenty times during the life of the reactor (Carpenter and Norfolk, 1984).

Neutron irradiation causes changes in crystallinity without appreciable changes in density. Losty and Orchard (1962) irradiated specimens of a reactor graphite in the British Experimental Pile Zero (BEPO) at 60 °C, and they confirmed that changes in the crystallinity at constant density cause the modulus and strength to increase with dose (up to 10.2 x 10^{18} neutrons per cm^2) so as to maintain constant the ultimate strain energy per unit volume. Davidson and Losty (1960) explained that the increases of strength and elastic modulus of polycrystallites (irradiation hardening) were due to single interstitials knocked out of plane by neutrons, and inhibiting the motion of basal planes, *i.e.* pinning the dislocations responsible for the low C_{44} stiffness in polycrystalline graphites.

Taylor *et al.* (1967) reported that after irradiation the stress-strain relation becomes increasingly linear with increasing dose. Birch and Bacon (1983) confirmed that the compressive stress-strain curve of polycrystalline graphite becomes much more linear with increasing doses of neutron irradiation. They also showed that the Young's modulus and strength also increase with neutron dose up to ~6 x 10^{18} neutrons per cm^2 before becoming constant. However, they also showed that upon subsequent thermal annealing (>400 °C) the fracture strength returned to its unirradiated value.

Tucker and Wickham (1990) reviewed the operation of the AGR and the effects of

neutron irradiation on polycrystalline graphites. The interstitial carbon atoms cause the crystallites to grow perpendicular to the basal plane (c axis) and shrink parallel to the plane (a axis) without any significant volume change in the individual crystallites. The initial effect on the structure is a closure of crack-like fine pores parallel to the crystallite basal planes (with large pores remaining relatively unaffected), and contraction of the crystallites in the direction parallel to the basal planes causing an initial shrinkage in the bulk polycrystalline graphite. Effectively, some of the differential thermal contraction during cooling after graphitisation is being reversed. In this way the individual crystallite growth is accommodated but polygranular material as a whole shrinks. The process reverses (*i.e.* expansion occurs) when the pores are unable to accommodate new growth. New internal stresses build up within the material to the point where microcracks and fresh pores begin to appear, when the polycrystalline material begins to expand. The irradiation dose at which this shrinkage occurs is dependent upon the degree of radiolytic oxidation that has occurred.

Norfolk *et al.* (1986) also review the initial shrinkage of the graphite core, and the eventual "turn-back" which occurs when the material begins to expand eventually beyond its original dimensions. Turn-back of AGR moderator core usually occurs around 15 Effective Full Power Years (EFPY); the design life being 25.5 EFPY. Radiolytic oxidation may delay "turn-back" by the creation of extra porosity. Figure 5.1 presents a semi-quantitative picture of a typical turn-back curve, where the dimensional changes in an AGR brick decrease initially with neutron dose and then turn-back later in life. Point A to B represents pore closure due to c-axis growth but no pore generation; B to F represents unaccommodated c-axis axis growth and undelayed pore generation; B to C represents transient pore generation due to radiolytic oxidation accommodating new c-axis growth and delaying turn-back; C to D represents steady state pore generation from the prising apart of the structure from unaccommodated crystal growth; and B to E represents the theoretical case of unlimited pore closure.

5.3 Reactor Environment and Internal Stresses

The strength of graphite decreases in the presence of moisture from the atmosphere. Orowan (1949) states that adsorption from the atmosphere diminishes the surface energy and thus, according to the Griffith formula (eqn. 4.1 in Chapter Four), reduces strength. Logsdail (1968) reported for PGA graphite that the flexural strength decreased as much as 40% by the physical adsorption of water vapour. Vitovec and Stachurski (1972) showed also that the strength of a polycrystalline graphite increased in *vacuo* by as much as 40% for Speer Carbon Co. RC4 and between 15-30% for POCO AXF-Q1. Boey and Bacon (1986) measured the room temperature failure stress and strain for three graphites at atmospheric pressure and at 600 psi. In all cases, at 600 psi, they noted a decrease between 2 and 7% in failure stress and a larger decrease in failure strain between 13 and 18%. They demonstrated that if specimens had the same probability of failure at different pressures, the strengths are lower at 600 psi than at atmospheric pressure. At 600 psi, all specimens had a higher stiffness which they attributed to the reduction in volume of closed porosity caused by the pressurising fluid penetrating the open pores. They related the decrease in the strength with pressure to a reduction in strain energy density with pressure. That is, the reduction in strain at failure is greater than that required to offset the increase in Young's modulus for a constant strain energy criterion. Jones and Reed (1991) found the strength of unirradiated graphite in reactor coolant environment (approximately 40 bar pressure, 400 °C and 200-400 vpm H_2O) to be greater than those found at ambient temperature in the open laboratory. They concluded that any measurement in the open laboratory will lead to a pessimistic estimate of strength in the reactor.

Substantial variations in fast-neutron flux occur radially within individual bricks, *i.e.* the bore and periphery initially shrink at different rates. This distorts the bricks and produces internal stress and consequently creep strains. The graphite moderator is

built using the radial keying concept of the individual bricks (see Figure 1.1 (a) & (b)) which should accommodate distortion and dimensional change. However, the keyways are the weakest link in the structure, and are also the most inaccessible part and so determination of the structural integrity is difficult.

Finite element analysis can calculate the expected stress at a keyway from the determined mechanical properties of a trepanned brick sample. Models can predict stresses at the bore and periphery of moderator bricks for the rest of the reactor life from the early experimental data. Figure 5.2 shows a typical example of predicted stresses at the bore and keyway throughout the life of an AGR graphite core brick. Early in life, the higher dose rate from the fuel in the bore causes faster shrinkage than in the periphery of the brick. This generates tensile hoop stresses at the bore and compressive hoop stresses at the periphery of the moderator brick. Later in life, these stresses reverse since the bore is the first to reach "turn-back" and starts to expand. This stress reversal occurs often about 17.5 EFPY, as in Figure 5.2. In addition, irradiation also affects the coefficient of thermal expansion (CTE), which initial increases and then falls with increasing fast neutron dose. Since the bore and the periphery of bricks have different irradiations, they will therefore have different CTEs. As a result, early in life, thermal contraction at shutdown will reinforce the shrinkage stresses, the combination being referred to as the internal stress. These stresses in latter life will also be reversed.

The reserve strength factor (RSF) at the keyway is a critical parameter which indicates the remaining margin against brick failure at any time, and an acceptably large value is therefore a necessary condition for continued fitness for service (Norfolk and Carpenter, 1984 and Prince and Brocklehurst, 1986). The RSF is given by

$$RSF = (\sigma_f - \sigma_s) / \sigma_a \qquad (5.1)$$

where σ_f is the strength of graphite after irradiation/corrosion, σ_s is the internal stresses and σ_a is the stress due to the applied load. Target values for RSF are 5 for normal operation, 3 for design studies of events such as earthquakes and frequent faults, *e.g.* reactor trips, 2 for infrequent faults, and 1 and 2 for safe shut-down.

The residual stress at the keyway root is the necessary parameter for determination of the structural integrity of the core using the RSF. However, as yet there is no satisfactory technique to measure internal stresses from the core as stated in Chapter One. There are several techniques currently being investigated, and acoustic emission has been identified as one possible technique. In this method, samples trepanned from the core are mechanically tested and their acoustic emission response analysed to determine the internal stress present. Hence effective monitoring of the nuclear reactor may be possible. This thesis presents a study of acoustic emission in nuclear graphites and determines the feasibility of such a technique to determine the internal stress. Part B of the thesis (Chapter Six and Seven) describes and characterises the microstructure and mechanical behaviour of the selected nuclear graphites chosen for this study. Part C (Chapters Eight to Twelve) reviews previous acoustic emission studies on polycrystalline graphites, describes the experimental programme and results, and further describes the use of acoustic emission as a tool for investigating the microstructural processes in nuclear graphites. Part D completes the thesis and provides a discussion of the results and conclusions resulting from the overall aims of the thesis.

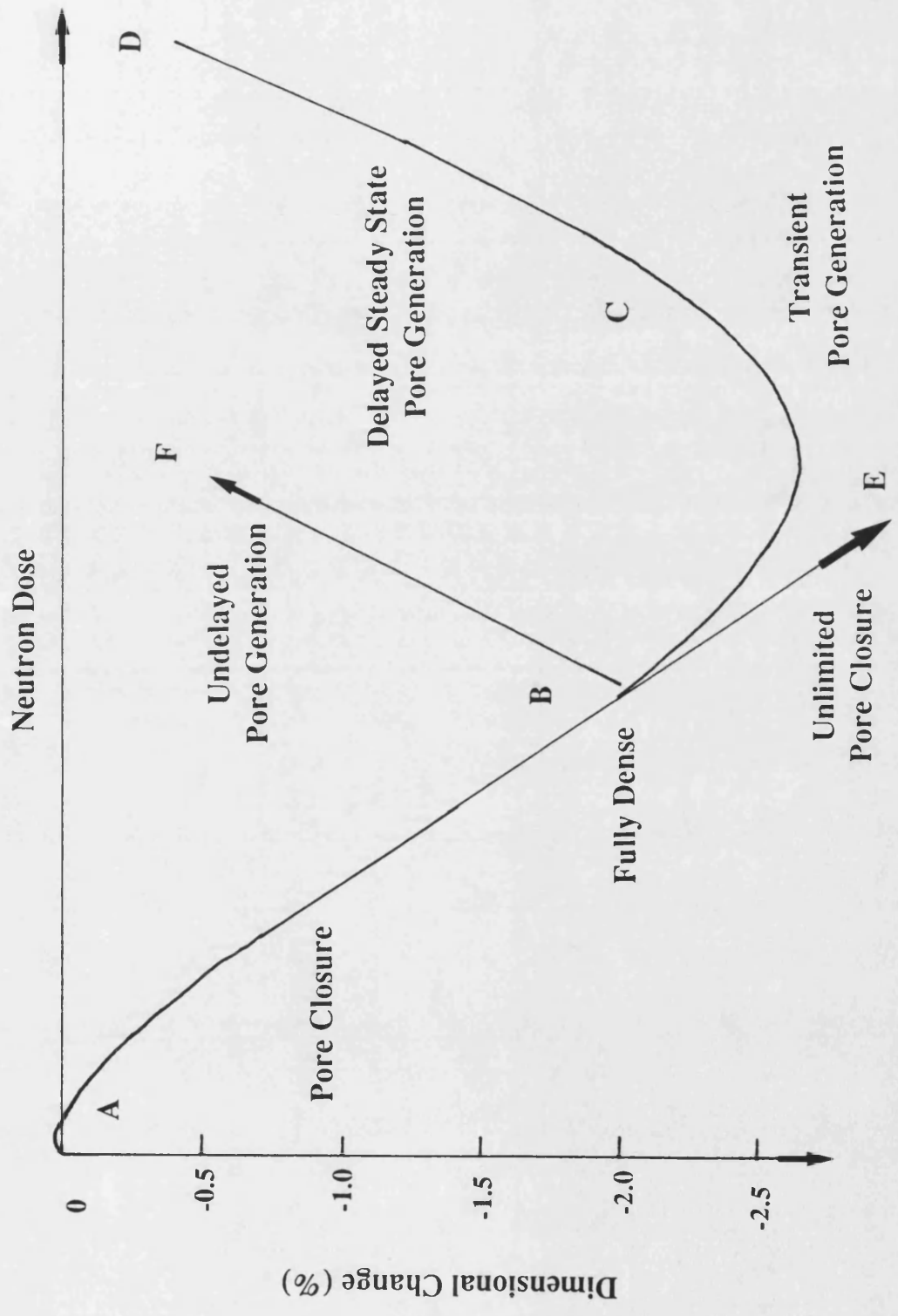

FIGURE 5.1 : The turn-back curve: the dimensional change for a moderator graphite in core life.

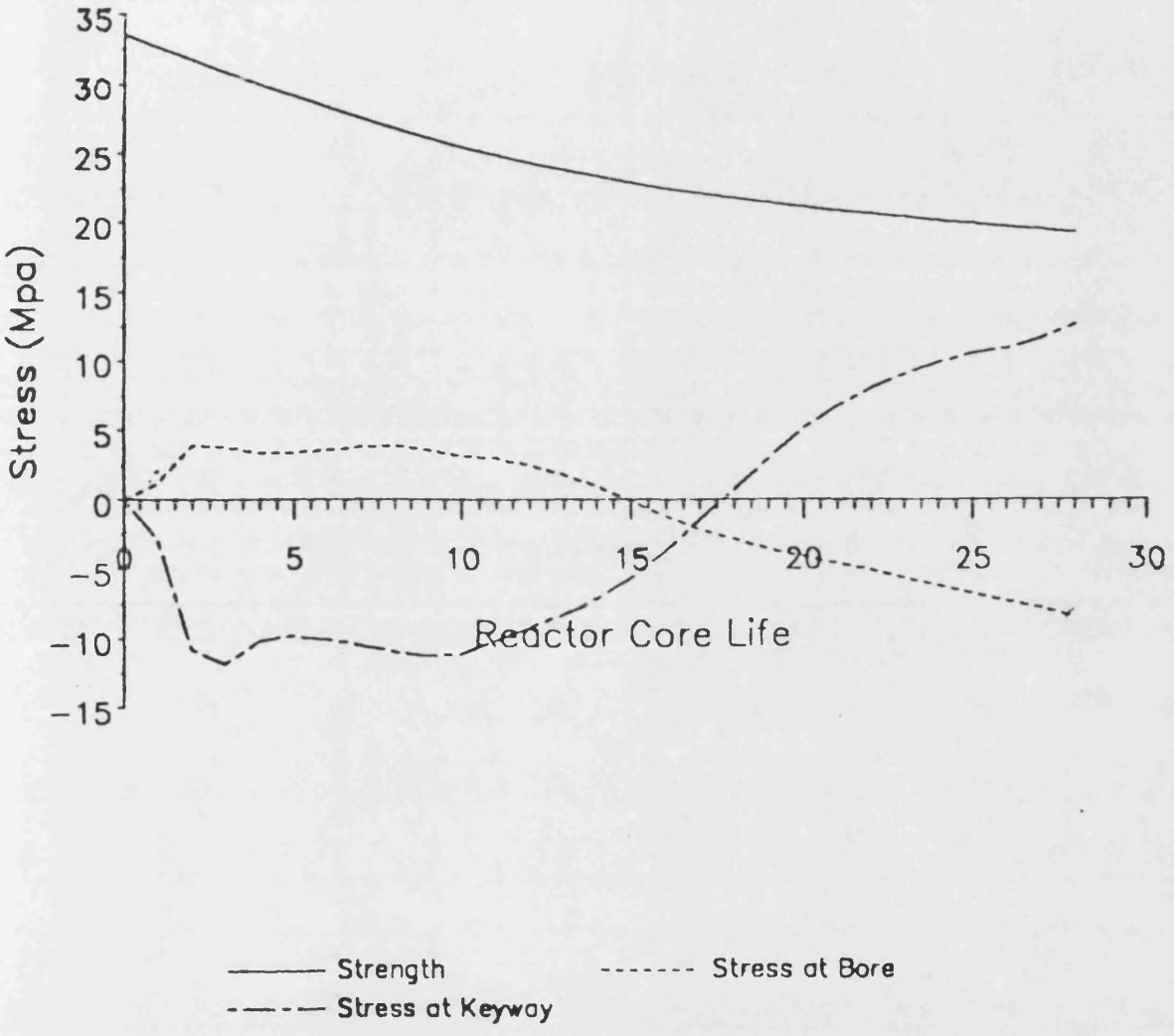

FIGURE 5.2 : The predicted residual stress pattern of moderator graphite in core life.

Part B :
Material Characterisation

CHAPTER SIX : THE MICROSTRUCTURE OF UNIRRADIATED NUCLEAR GRAPHITES

A basic understanding of the microstructure of nuclear graphites can provide evidence to explain the microstructural processes prior to failure, and hence their acoustic emission responses. This chapter considers the texture of each of the graphites selected for this study. For extruded graphites, both perpendicular and parallel directions to the extrusion axis are considered. No previous study has considered texture in both directions for two different nuclear graphites (PGA and VNEC) using polarised light microscopy, and including estimates of both filler particle and pore size distributions. No reference to the microstructure of VNEC has been found in the literature. Only scant information, such as the estimated filler particle size, is available for PGA and IM1-24 graphites (*e.g.* Tucker *et al.*, 1986). Therefore this chapter aims to compare the three graphites and to illustrate their major differences by providing, for the first time, quantitative information regarding their microstructure. It also explores the potential of an image analysis technique to provide representative quantitative information on the microstructure of nuclear graphites. Information gathered is used in later chapters to help understand the mechanical behaviour of graphites (Chapter Seven) and acoustic emission results (Chapter Ten).

6.1 Materials

Brief details of each grade of graphite used in unirradiated studies in this project are given below. However, the majority of the work in this study has concentrated on three nuclear grade graphites:- PGA, IM1-24 and VNEC, and only their microstructure is considered in this chapter.

6.1.1 Pile Grade 'A' Moderator Graphite (PGA)

PGA graphite is an extruded, medium-textured, nuclear graphite made by Anglo Great Lakes Ltd. (AGL). PGA was developed specifically for use as the moderator in the British Magnox reactor. It consists of large needle-coke filler particles (~1 mm length) within a coal-tar pitch binder and it has ~20% porosity. PGA exhibits anisotropy in mechanical properties, *e.g.* the elastic modulus in the direction parallel to extrusion is greater than in the perpendicular direction. All specimens used in this work had their longitudinal axis parallel to the extrusion direction (see Chapter Nine).

6.1.2 IM1-24 Moderator Graphite

IM1-24 graphite is a near-isotropic, moulded, moderator graphite, and the successor to PGA in the second generation of British thermal reactors (the AGRs). There are two sources of manufacture, British Acheson Electrodes Ltd. (BAEL) of Union Carbide plc and AGL, both of which use spherical Gilsocarbon filler particles (~0.5 mm diameter) and coal-tar pitch binder, and IM1-24 has ~18% porosity. IM1-24 is known to have been subjected to one impregnation and graphitised at a temperature of 2400 °C. The Gilsocarbon is produced by heat treatment of Gilsonite, a naturally occurring asphaltite which is mined in Utah, USA. The Gilsocarbon was chosen as the filler particle because of its spherical shape, in order to confer isotropy in mechanical properties and, more importantly, when subjected to neutron irradiation.

6.1.3 VNEC (Candidate) Sleeve Graphite

VNEC is made by Union Carbide plc in the United Kingdom as a candidate sleeve graphite for the AGR. It is a fine grained extruded graphite with a pitchcoke filler (~0.3 mm length). VNEC has had one impregnation before final graphitisation and it has ~18% porosity. All specimens used in this work had their longitudinal axis parallel to the extrusion direction (see Chapter Nine).

6.1.4 CAGR VFT-Pitchcoke Sleeve Graphite

This is the common grade of graphite used for the fuel sleeves in the AGR. There are two sources of manufacture, BAEL and Pechiney (SERS), both of which use VFT-Pitchcoke filler particles and a pitch binder. The graphite is extruded, then machined to produce sleeves, and therefore it is anisotropic with a density in the range 1.8-1.9 g cm^{-3} equivalent to 16-20% porosity.

6.1.5 EO4 and P2 Nittetsu Candidate Sleeve Graphites

These graphites are manufactured using Nittetsu EO4 and P2 cokes nominally in the same way as the VFT-Pitchcoke graphite sleeves. They are currently being considered as alternatives to VFT-Pitchcoke graphite as a source for sleeve graphite. The main difference between these graphites is the size distribution of the filler particles within the bulk graphite. They have a density of ~1.85 g cm^{-3} equivalent to ~18.5 % porosity.

6.2 Optical Microscopy

6.2.1 Preparation of Samples for Optical Microscopy

Each specimen for optical microscopy is prepared by mounting a graphite sample in a resin block and polishing to produce a surface that is not only scratch-free, but also optically flat. Prior to mounting in resin, each graphite specimen was cut, ultrasonically washed, degreased with acetone and dried. All samples were then mounted under vacuum in a slow setting epoxy mix (Epofix Resin HQ and Epofix Hardener HQ made by Struers Ltd. in the ratio of 15:2). The samples were then cured by placing them under pressure (30 psi) for 24 hours. A new polishing technique was specially developed for this work based on the systematic metallographic concepts and principles proposed by Bousfield (1988) and Bousfield and Bousfield (1990). For all grades of graphites, each mounted specimen was prepared using the following

polishing technique on the Buehler Motopol 12 automatic polisher with 5 psi of pressure per sample unless otherwise stated:

(i) Complementary planar grinding (150 rpm) with 240 grit SiC paper for ~15 seconds;
(ii) Contra-rotation grinding (25 rpm) with Metlap Integrity Surface (I.S.) 4 and 9 μm diamond, oil-based slurry for 10 minutes;
(iii) Complementary rotation grinding (240 rpm) with Metlap I.S. 1 and 1 μm diamond water-based slurry for 8 minutes;
(iv) Complementary rotation grinding (100 rpm) with Metlap I.S. 1 and 0.06 μm mixed oxide (SiO_2 and Al_2O_3 in pH 9.8 base) slurry for 4 minutes (7.5 psi pressure per sample);
(v) Contra-rotation polishing (100 rpm) Mastertex P.S. 7 and 0.06 μm colloidal SiO_2 suspension for 2 minutes (2.5 psi pressure per sample).

6.2.2 Optical Microscopic Examination

Various methods for studying the carbon and graphite microstructure are reviewed by Marsh (1989). The simplest method of studying the microstructure of a graphite is to use a reflected light microscope in either bright-field or polarised light (Bousfield, 1989). In this work, optical microscopy studies were carried out using an inverted stage ICM45 Zeiss polarising microscope.

Graphite is highly pleochroic and birefringent which makes the use of polarised light useful to study graphitic microstructure. The birefringence of a material (at a particular wavelength) is the difference between the two refractive indices for the ordinary (O) and extraordinary (E) rays of light entering the crystallite (Battey, 1981). In addition to the use of polarised light, a sensitive tint (1λ) plate is inserted in the microscope which shifts the colour of isotropic and extinct regions from black to first order red (the extinction colour). Optically anisotropic regions of the graphitic

structure, *i.e.* areas of strong basal plane alignment, appear coloured (yellow or blue) according to their orientation with respect to the polariser and the analyser. Each isochromatic region observed within the graphitic microstructure varies in size and colour, depending on the size and orientation in the field of common basal plane alignment. Hence, the sensitive tint plate greatly increases the ability to assess the degree of preferred orientation since basal planes orientation is indicated from one of three colours.

If an isochromatic region is rotated through 360°, two positions of maximum and minimum light intensity are passed, which appear as first order red. If there is a slight change from these positions (*i.e.* in birefringence caused by the different crystallographic orientation of the grain), the isochromatic region exhibits a different interference colour. These intermediate regions between the maxima and minima are yellow (phase difference between E and O waves $< 1\lambda$) and blue (phase difference between E and O waves $> 1\lambda$). Therefore rotation of the grain changes the interference colour from red to yellow to red to blue *etc.*. A grain may contain more than one interference colour if the crystallites within the grain have different orientations. If the crystallites are too small to be resolved by eye (<10 μm), the yellows and blues merge together to appear as a rose colour.

All polycrystalline graphites have common microscopic features. Polarised light microscopy (with sensitive tint plate) reveals the filler particles from the manufacturing process to be the largest isochromatic regions present. These regions contain hundreds and thousands of small crystallites on the order of 800 Å diameter, assembled with some long range order throughout the particle of linear basal plane orientation (Blackman, 1970). A change in the linear basal plane orientation within a filler particle would be signalled by the change in interference colour. Microscopy also shows that these filler particles are surrounded by a graphitised binder phase with a substantial amount of open and closed porosity. The demarcation between the filler particle and

the binder phase is not always clear, and often the filler-binder interface is marked by shrinkage cracks caused by cooling from graphitisation temperatures, and by porosity created from poor wetting of the binder in the mixing stage of manufacture. In addition to the binder phase, within the original pore walls, a graphitised impregnate can often be distinguished by an unusual "smooth" look at high magnifications.

The binder phase typically consists of mosaics and domains. The term mosaic is used to describe features, built up of isochromatic areas of 0.1 to 10 μm where there is common basal plane alignment of crystallites. Areas of coarse-textured common basal plane alignment of greater size, *i.e.* >10 μm upward, are termed domains (Pickup *et al.*, 1986). These domains often deviate from planarity due to shearing forces from bubble percolation, acting upon the plastic mesophase to cause a "flow-type" anisotropy. Areas of extreme distortion due to bending, folding or twisting the mesophase are known as disclinations (Pickup, 1984).

The microstructure of polycrystalline graphite contains open and closed porosity which can be classified into the following:- (i) large threadlike cracks parallel to the basal planes within the filler particle due to volumetric shrinkage of the filler particles during calcination; (ii) large oblong pores due to gas entrapment within the binder phase which form during the mixing and baking stage of manufacture; and (iii) slit-shaped pores in the binder phase which form either as a result of volumetric shrinkage on baking or anisotropic contraction on cooling from graphitisation temperatures (Mrozowski cracks). They are often found at the domain / mosaic boundaries in the binder phase and are frequently connected to gas entrapment pores (Pickup *et al.*, 1986).

6.3 Quantitative Image Analysis

Mays and McEnaney (1992) review computer-based quantitative microscopy for characterising macropores in carbon materials and conclude by summarising the advantages over rival techniques, *e.g.* mercury porosimetry, for estimating pore shapes and sizes. They review the technique of image analysis and present examples of some parameters of the geometry of macropore cross-sections. Visible features of a polished specimen larger than 1 μm, the limiting resolution of the optical microscope, can be studied using an image analysis (IA) system. IA utilises a computer to analyse digitised images captured from a camera mounted on a microscope. The captured image consists of pixels of various levels of contrast (grey levels) corresponding to different phases in the material within a square frame, or field, of 262144 pixels (for the Magiscan 2A system).

In this work, IA was carried out using a Zeiss Ultraphot Universal microscope with a Bosch TYK-91D photolens camera (Chalnicon tube) supplied by Joyce Loebl with the Magiscan 2A system. The samples used for IA studies were the same as those used for optical microscopy. The samples were illuminated by a 100 Watt variable halogen bulb controlled via a transformer to give a steady output, with no special filters attached. Each sample was viewed by a x8 objective lens, for porosity examination, and x2 objective lens, for filler particle examination, and then further magnified in both cases by 1.25 by an intermediate lens before capture by the camera (which also magnifies the image). The field area was 96.37×10^4 μm^2 and 6.510 mm^2 for porosity and filler particle measurements, respectively.

The IA system was controlled by the Magiscan 2 Menu 7.55 software which captured the image and then performed data collection tasks. No special functions for image enhancement were carried out for filler particle examination, but for porosity examination, "Mean" and "Edge" routines which improve the definition of a object

were performed automatically using a prepared routine, or interactively using a touch pen on the screen. An adaptive threshold was used to compensate for variation in light intensity across the field. The datafile was then interrogated by the Magiscan 2 Results Rev. 3.01 program using a truth qualifier, *i.e.* all objects are included.

Information on objects routinely collected in each field are enclosed area, detected area, length, breadth and perimeter. This information is written to a datafile on disk after each field is surveyed and is continuously updated. The information gathered may be displayed as tabulated data or graphically in the form of histograms. Hard copies of results and programs are obtained via an attached printer. For these studies, the data were transferred to Quattro Pro spreadsheet on a PC and the data were analysed to produce various distributions.

6.4 The Microstructure of Selected Nuclear Graphites

6.4.1 PGA Moderator Graphite

Figure 6.1 shows the general features and microstructure of PGA cut parallel to the extrusion axis under polarised light. There is a very large elongated needle-coke filler particle (N), ~2.5 mm in length, surrounded by smaller filler particles and a coarse-textured coal-tar binder phase (B). The filler particle has a uniform colour throughout emphasising the shrinkage cracks (in the direction of the basal planes), and indicating common basal plane alignment of crystallites. Cracks and pores are usually black because the light is absorbed rather than reflected. The coarse texture of PGA is indicated by the wide range of colours (*i.e.* mixtures of yellows, reds and blues) and varying sizes of isochromatic domain regions.

Figure 6.2 (a) and (b) clearly shows the pleochroism of graphite; Figure 6.2 (a) is the same region as in Figure 6.2 (b) but rotated 90° with respect to the polariser. The filler particle (N) is seen to change colour from yellow to blue via first order red as the

direction of basal plane alignment changes orientation. Large curved filler particles show a similar effect. The apparent colour of the particle changes (in sequence, yellow, red, blue or vice versa) as the basal plane alignment with the analyser and polariser changes (see Figure 6.4).

Figure 6.3 shows a small region of aligned graphitised filler particles highlighted by a strong blue colour from a section of PGA cut parallel to the extrusion axis. The longitudinal axes (perpendicular to the graphitic crystallographic axis) of the filler particles (N) are seen to be aligned, which accounts for the bulk anisotropy in mechanical properties of the graphite article. A small amount of much smaller yellow grains with their basal plane alignment normal to the blue grains are dispersed over the whole field. In addition to these particles there are optically isotropic regions coloured red.

Figure 6.4 shows a polarised micrograph of PGA cut perpendicular to the extrusion axis. The microstructure differs in two respects from a section cut parallel to extrusion; (i) the filler particles (N) are apparently shorter in length (reflecting the anisotropy of needlecoke particles); and (ii) there is also present a small number of multiple coloured "crescent" shaped filler particles (CP).

6.4.2 IM1-24 Moderator Graphite

Figure 6.5 shows the general features and microstructure of IM1-24 under polarised light. There is a large spherical Gilsocarbon filler particle (G), ~0.9 mm in diameter, enclosed in a thin mosaic region (S) giving a yellow and blue speckled appearance. The spherical Gilsocarbon filler particles consist of small contiguous crystallites which are slightly mis-aligned to form a circumferential pattern. The change in direction of crystallites with respect to the polariser on the microscope can be seen by the formation of a first order red "Maltese cross" and yellow and blue (opposite) quadrants within the Gilsocarbon particle. Within the filler particles are calcination cracks (C)

that give a characteristic "onion-skin" appearance. These fine cracks result from volumetric shrinkage during calcination and contribute mostly to closed porosity. These encapsulated Gilsocarbon filler particles are bound together within a fine textured, graphitised coal-tar pitch binder phase (B) containing open and closed porosity. There are also present fragments of large Gilsocarbon particles (F). As noted in §6.1.2, the circumferential orientation of the graphitic crystallites in the Gilsocarbon filler contributes substantially to the bulk isotropy of IM1-24, both with respect to the mechanical properties and to irradiation effects.

Figure 6.6 shows a section of binder phase (B) between two Gilsocarbon particle fragments (F) containing a variety of pores. In the intermediate regions between filler particles, there are regions of fine mosaics, shown in polarised light microscopy as a rose colour, (*i.e.* the unresolved yellow and blue colours of fine crystallites of size <10 μm). The mosaic texture of the binder phase also contributes to the bulk isotropy of IM1-24. There are also large gas-entrapment pores (E), resulting from bubble percolation of volatile gases during the baking stage of manufacture; these are open pores, *i.e.* they are accessible to the environment. Within some open pores, there are areas of impregnation (I). Figure 6.7 shows the different appearances of the impregnate (I) and the binder phase (B) in gas entrapment pores.

6.4.3 VNEC Sleeve Graphite

In many respects, VNEC can be regarded as a much finer version of PGA. The starting materials are similar, but they are much smaller and finer for VNEC. For example, the pitch-coke filler particles are about one quarter of the size of those in PGA (see §6.5). Figure 6.8 shows the general features and microstructure under polarised light of VNEC cut parallel to the extrusion axis. There is a filler particle (F), ~0.6 mm in length, surrounded by open (O) and closed (C) porosity within a fine-textured binder phase (B).

A comparison of the microstructure of VNEC cut parallel (Figure 6.8) and perpendicular (Figure 6.9) to the extrusion axis reveals no obvious indication that the maximum dimension of the filler particles and shrinkage cracks are aligned parallel to the extrusion axis. This is probably due to the small size of the filler particles. Curious features of VNEC shown in directions both parallel and perpendicular to the extrusion axis, and not obvious in the other two graphites studied, are the aligned rows of open pores (R-R' in Figures 6.8 and 6.9). These long pathways are probably escape routes created by bubble percolation of volatile gases during the baking stage of manufacture.

The fine texture of VNEC in the binder phase is revealed by the large areas of rose coloured mosaics which are interspersed with smaller areas of yellow and blue domains. Figure 6.10 shows a filler particle (F) surrounded by mosaics and domains of the binder phase. The filler particle is coloured yellow and blue, showing the change in the basal plane orientation, but surprisingly few shrinkage cracks are revealed. To the right of the filler particle is a large globular pore containing debris which may be remnants of an impregnate.

6.5 Filler Particle Size Distributions

Filler particle size distributions were determined by the IA technique described in §6.3 for three nuclear graphites PGA, IM1-24 and VNEC: for PGA and VNEC, IA parameters parallel and perpendicular to the extrusion axis were measured. Distributions in filler particle length, breadth and shape factors were collated. The length and breadth of a particle are generally referred to as the maximum and minimum dimensions of the particle, D_{max} and D_{min}, respectively. It is important to note that it is extremely difficult to obtain a complete distribution of filler particles sizes. This is because the filler is not only composed of large, easily-recognisable particles, but also small particles and flours. Many of these cannot be identified in the microstructure because they cannot be resolved from the binder. The purpose of this study is to

examine the larger, identifiable particles, because they are most likely to influence the fracture process. Each filler particle was identified by striations within the filler itself or surrounding shrinkage cracks, and measured by drawing around them using a light pen.

For each graphite, the distributions of particle dimensions (Figures 6.11 (a) & (b), 6.12 and 6.13 (a) & (b)) are shown with a tail extending to large values of the dimensions. For PGA and VNEC graphites, the largest values of D_{max} are greater in the direction parallel to extrusion. This reflects the alignment of large filler particles upon extrusion. A similar, though less-marked difference between large values of D_{min} in parallel and perpendicular directions are also found. For smaller particle dimensions the differences in the distributions between D_{max} and D_{min} and between parallel and perpendicular directions are less marked. As expected, the particle size distributions for VNEC are less skewed than those for PGA and the modes are smaller. For example, the mode of D_{max} distributions parallel to the extrusion axis are ~0.6 mm and ~0.40 mm for PGA and VNEC, respectively.

For IM1-24 (Figure 6.12), the distributions of D_{max} and D_{min} for small particles are near-Gaussian, but for D_{max} there is a tail extending to large particle sizes, thus giving overall a skewed distribution for D_{max}. For IM1-24, the mode of the D_{max} distribution is just greater than D_{min}, showing the Gilsocarbon particles are not purely spherical.

IA studies can also be used to characterise objects by their shape. Circularity, equation 6.1, characterises the shape of an object in relation to a perfect circle, *i.e.* the measured area (A) of the object is compared to its perimeter (P). If the object is a perfect circle, then its circularity would be unity, while for non-circular objects, the circularity is less than unity. The measured area of an object may be converted in to an equivalent circle diameter as in equation 6.2.

$$\text{Circularity} = 4\pi A/P^2 \quad (6.1)$$

$$\text{Equivalent Circle Diameter} = (4A/\pi)^{1/2} \quad (6.2)$$

Filler particle circularity distributions for PGA and VNEC are similar in that they are broad distributions ranging from 0.3 to 0.9. The distribution for IM1-24 (Figure 6.14) is quite different. As expected, there is a large number of Gilsocarbon particles with a circularity close to unity, as might be expected from the spherical shape (*e.g.* see Figure 6.5). However, some particles have a circularity of around 0.55, which corresponds to elongated or fragmented particles. This distribution suggests that the Gilsocarbon particles are oval rather than spherical, but it may also reflect the presence of broken Gilsocarbon particles as revealed by optical microscopy (Figure 6.6).

Graphite Grade and Orientation	Number of Observations, n	Mean D_{min} (mm)	Mean D_{max} (mm)
PGA Parallel	126	0.262 ± 0.166	0.657 ± 0.503
PGA Perpendicular	120	0.286 ± 0.141	0.516 ± 0.288
IM1-24	94	0.437 ± 0.174	0.604 ± 0.291
VNEC Parallel	119	0.203 ± 0.091	0.423 ± 0.222
VNEC Perpendicular	114	0.193 ± 0.075	0.378 ± 0.169

TABLE 6.1 : Mean D_{min} and D_{max} Values For Filler Particles (± 1 S.D.)

Table 6.1 presents summary data for mean particle sizes for each graphite from approximately one hundred observations in each case. These results provide some quantitative support for the qualitative observations presented in §6.4. Thus mean D_{max} values are in the sequence PGA>IM1-24>VNEC, as also indicated qualitatively by optical microscopy. However, unsatisfactory features of these results are the large standard deviations on measurements which render comparisons between the different measurements difficult. For example, although mean D_{max} values for PGA and VNEC show that the dimensions of the filler particles are greater parallel to the extrusion

direction than in the perpendicular direction, (as expected) the differences are not significant at the 95% confidence level. The large standard deviation result from highly skewed size distributions. The difference in the D_{min} and D_{max} values for IM1-24 support the suggestion that the Gilsocarbon filler particle is not perfectly spherical.

	Equivalent Circle Diameter / mm	
	Mean	**S. D.**
IM1-24	0.5244	0.5093
PGA Parallel	0.4494	0.5824
PGA Perpendicular	0.3747	0.4052
VNEC Parallel	0.2828	0.2705
VNEC Perpendicular	0.2512	0.2105

TABLE 6.2 : Equivalent Circle Diameters For Filler Particles (±1 S.D.)

Table 6.2 presents for each of the graphites, the values of the equivalent circle diameter, calculated from mean values of observed area and perimeter of objects, and are within the range of D_{max} and D_{min} (Table 6.1) as might be expected. The equivalent circle diameter may possibly be used as a single parameter to characterise the microstructure and the filler particle size.

6.6 Pore Size Distributions

Porosity in graphites is known to vary in a wide spectrum of sizes and shapes. Understanding porosity is crucial to understanding crack initiation and the role porosity plays in crack propagation. Many pores not only act as stress concentrators that initiate cracks but others can also attract propagating cracks. Characterising small pores may not lead to useful information, since it is mainly the larger pores that influence fracture, especially in crack initiation. However, it is important to determine the proportion of larger pores in the total porosity, so that the role of porosity in the fracture process may be clearly defined.

Pore size distributions were obtained for three nuclear graphites PGA, IM1-24 and VNEC using the image analysis system described in §6.3. In this study both open and closed pores were considered together. For PGA and VNEC, sections cut parallel and perpendicular to the extrusion axis were considered (IM1-24 is assumed to be isotropic). A magnification (x8 objective) was used that covered the whole spectrum of pore sizes that could be optically resolved. For all graphites and directions over ten thousand pores were detected by the IA system before the data were interrogated.

For all graphites, the minimum pore size detected was 1.95 μm, equal to two pixels; this is the minimum pore size that can be detected by the Magiscan IA system. Table 6.3 compares the fractional porosity determined from the IA technique to the value obtained from bulk density measurements. It should be expected that the fractional porosity derived from IA technique should approach that calculated from bulk density measurements. For PGA and VNEC, the two measurements are similar, but for IM1-24, the porosity determined using the IA technique is much less than that derived from the bulk density measurement.

Fractional Porosity / %									
	Bulk Density Measurements			**Image Analysis**					
				Parallel			**Perpendicular**		
	Mean	**S.D.**	**n**	**Mean**	**S.D.**	**n**	**Mean**	**S.D.**	**n**
PGA	23.05	0.62	10	25.00	3.49	15	19.53	3.06	21
IM1-24	19.51	0.22	10	12.63		3.42		50	
VNEC	20.05	0.71	10	18.44	3.00	20	17.92	1.79	24

Table 6.3 : Fractional Porosity From Bulk Density and Image Analysis Measurements (where n is the number or samples or fields surveyed).

There are three main reasons for discrepancies in the two techniques to measure bulk porosity: (i) limited resolution of image analysis techniques, *i.e.* bulk density measures all pores inclusive of those less than 1 μm, which are shown to exist by mercury porosimetry; (ii) image analysis is based on a two-dimensional section and to calculate a bulk porosity from a two dimensional section, it is implicitly assumed that the pores

are an isotropic array of spheres (Delesse's principle)- this is not true for pores in graphites; and (iii) for IM1-24, the density from mercury porosimetry is less than that estimated from bulk density measurements (Best *et al.*, 1985), which implies a greater proportion of micropores are present in IM1-24 than in the other graphites.

As with filler particles, the shape of pores can be characterised by their equivalent circle diameter (equation 6.2), often called the equivalent pore diameter (E.P.D.).

	Equivalent Pore Diameter / μm	
	Mean	**S. D.**
IM1-24	27.09	69.46
PGA Parallel	21.58	49.45
PGA Perpendicular	22.46	48.79
VNEC Parallel	21.13	55.00
VNEC Perpendicular	22.77	51.87

TABLE 6.4 : Mean Equivalent Pore Diameters (± 1 S. D)

Table 6.4 presents the equivalent pore diameters for observed pores from each graphite calculated from mean measured values of area and perimeter. The E.P.D. for IM1-24 shows a higher mean and standard deviation than found for the other graphites, *i.e.* much larger pores are observed in IM1-24 than in the other two graphites. This is in line with qualitative observations that can be made in optical microscopy. For example, Figure 6.5 shows a large open pore in a section of IM1-24 of a size not seen in PGA (Figure 6.4).

In all, each graphite and orientation had similar pore size distributions. For each graphite, the mode of the frequency distribution (~900 pores) was at 8 μm (equivalent to 13-14 pixels in size); this is in line with established theory (Best *et al.*, 1985). However, on average, 95% of all observed pores was less than 40 μm, but this only accounted ~38% of total porosity. In line with mean E.P.D. values (Table 6.4), the largest pore in PGA and VNEC graphites occurs between 320-360 μm, but for IM1-

24, the largest pore size was ~550 μm. Therefore, the majority of the porosity seems to be concentrated in a small fraction of the total pores.

Figures 6.15 and 6.16 present for both parallel and perpendicular directions to the extrusion axis, the pore size distribution for PGA and VNEC graphites, respectively. In each case, the cumulative porosity is plotted against the equivalent circle diameter (note: there is a change of scale at 150 μm). For both graphites, at low pore diameters, in both directions, the distributions are very similar. However, at large pore diameters, the distributions deviate. For both graphites, but particularly for VNEC, the cumulative porosity is larger in the perpendicular direction than in the parallel direction for a given pore size. Therefore, in VNEC and PGA graphites, there is evidence that pores are elongated parallel to the extrusion axis for larger diameters. Inspection of the micrographs, *e.g.* Figure 6.1, suggests that this effect is due to calcination cracks in the filler particles which are aligned in the extrusion direction. Figure 6.17 compares the pore size distribution of IM1-24 to PGA cut in the perpendicular direction. From very low pore diameters, the cumulative porosity at a given diameter is lower for IM1-24. However, for IM1-24, the pore size distribution continues up to a pore diameter of ~530 μm. Figure 6.18 compares the pore size distributions in the perpendicular direction for both PGA and VNEC graphites. Both have similar maximum pore diameters (~300 μm), but VNEC has a smaller proportion of porosity at pore sizes up to ~200 μm.

This chapter has introduced three nuclear graphites chosen for this study, and has described their microstructural features using optical microscopy. It has further attempted to describe these graphites quantitatively using an image analysis technique, and has presented for the first time, possible characteristic values describing the microstructure, *e.g.* filler particle and pore size distributions.

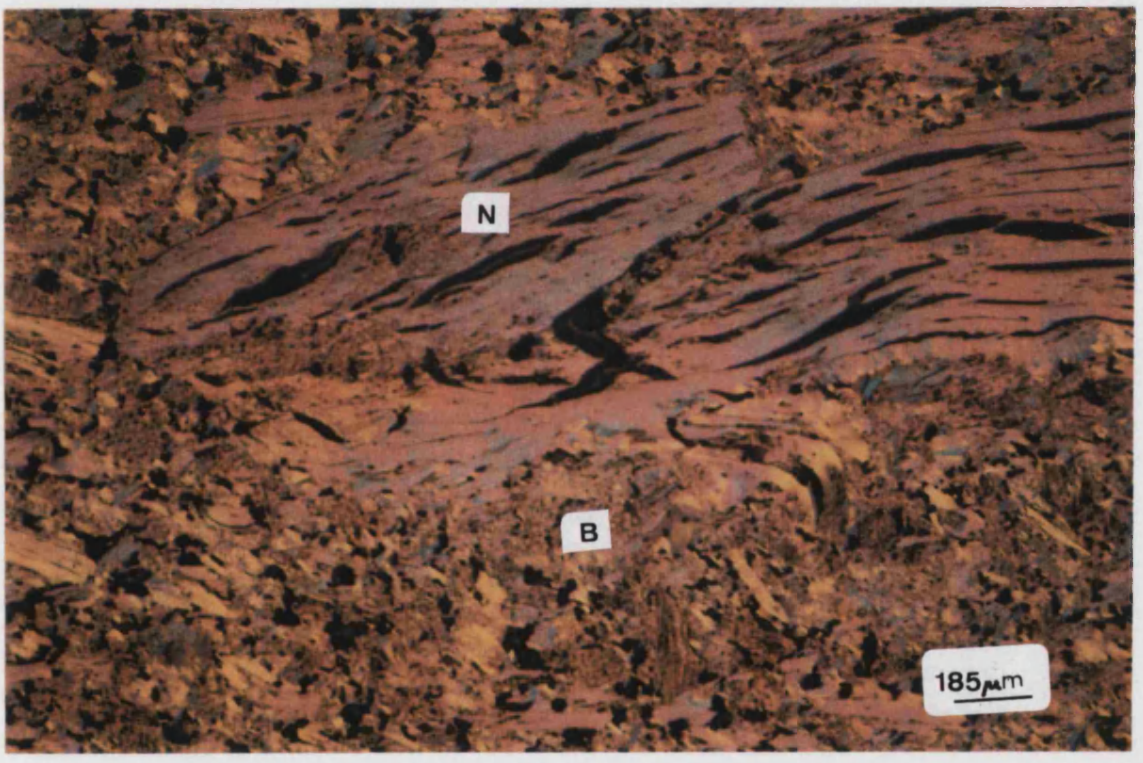

FIGURE 6.1 : A polarised light micrograph of PGA graphite cut parallel to the extrusion axis (N - Needlecoke filler particle, B- binder phase).

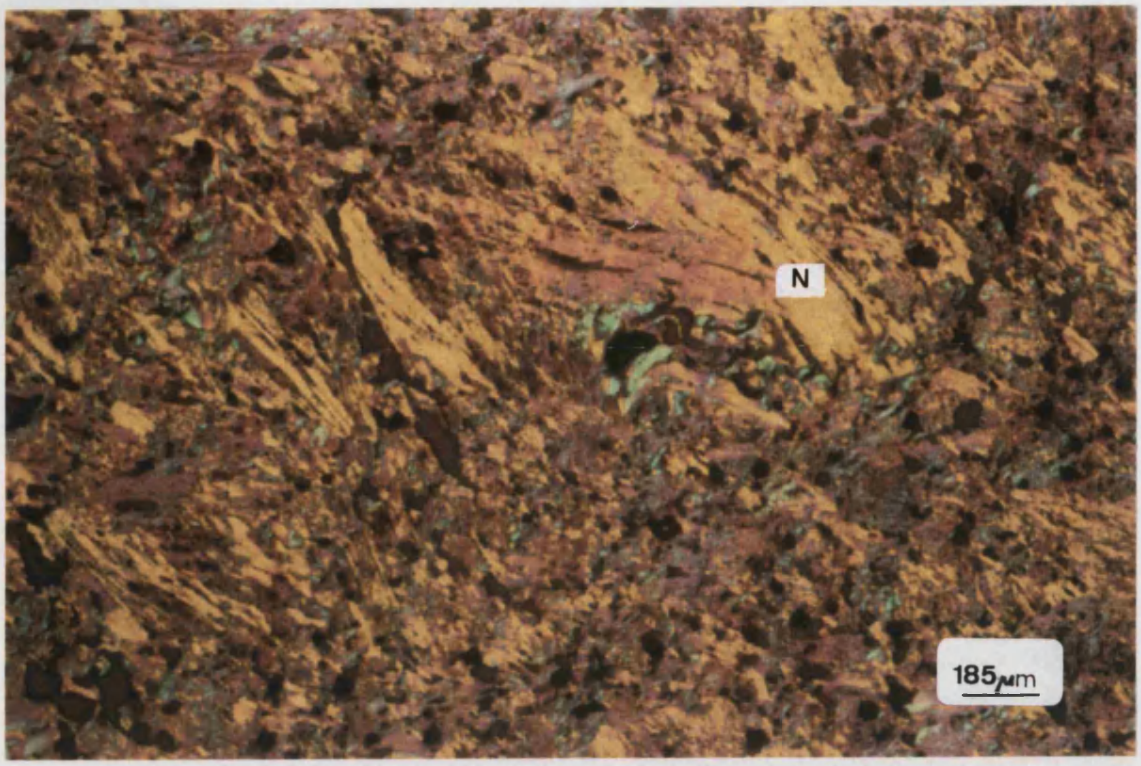

(a)

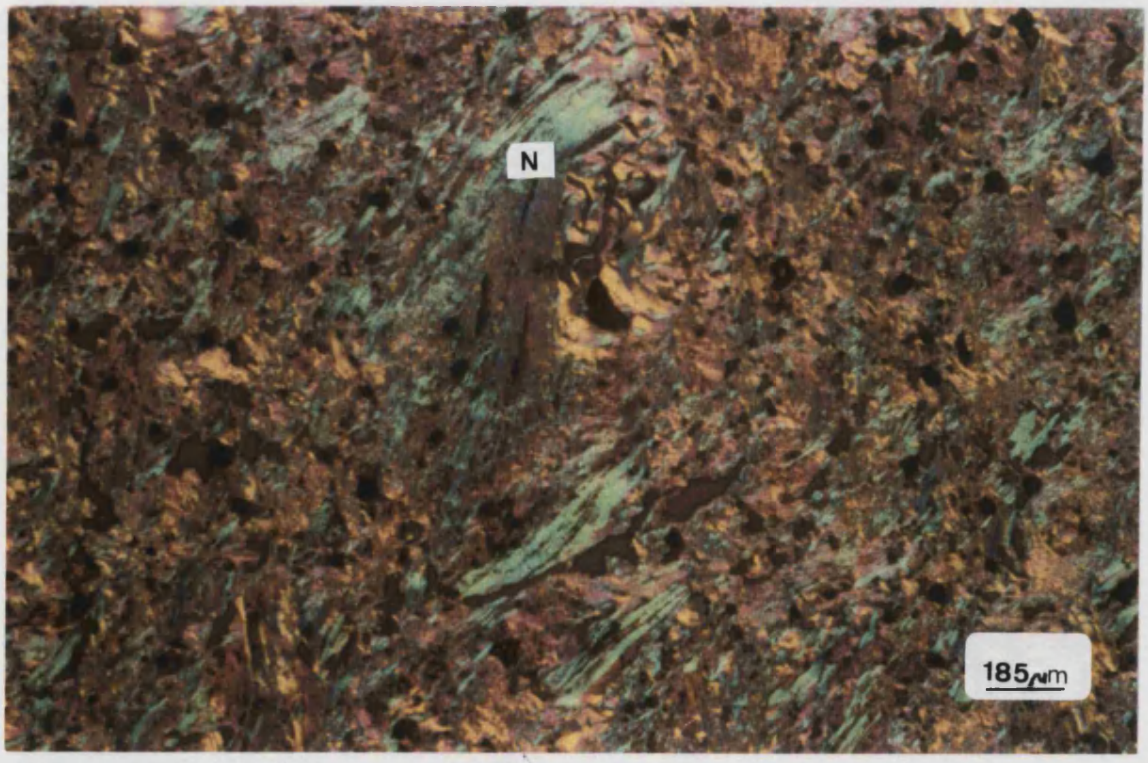

(b)

FIGURE 6.2 (a) and (b) : Polarised light micrographs of a region of PGA graphite cut parallel to the extrusion axis showing the pleochroism of graphite (Figure 6.2 (b) has been rotated 90° from the position in Figure 6.2 (a)).

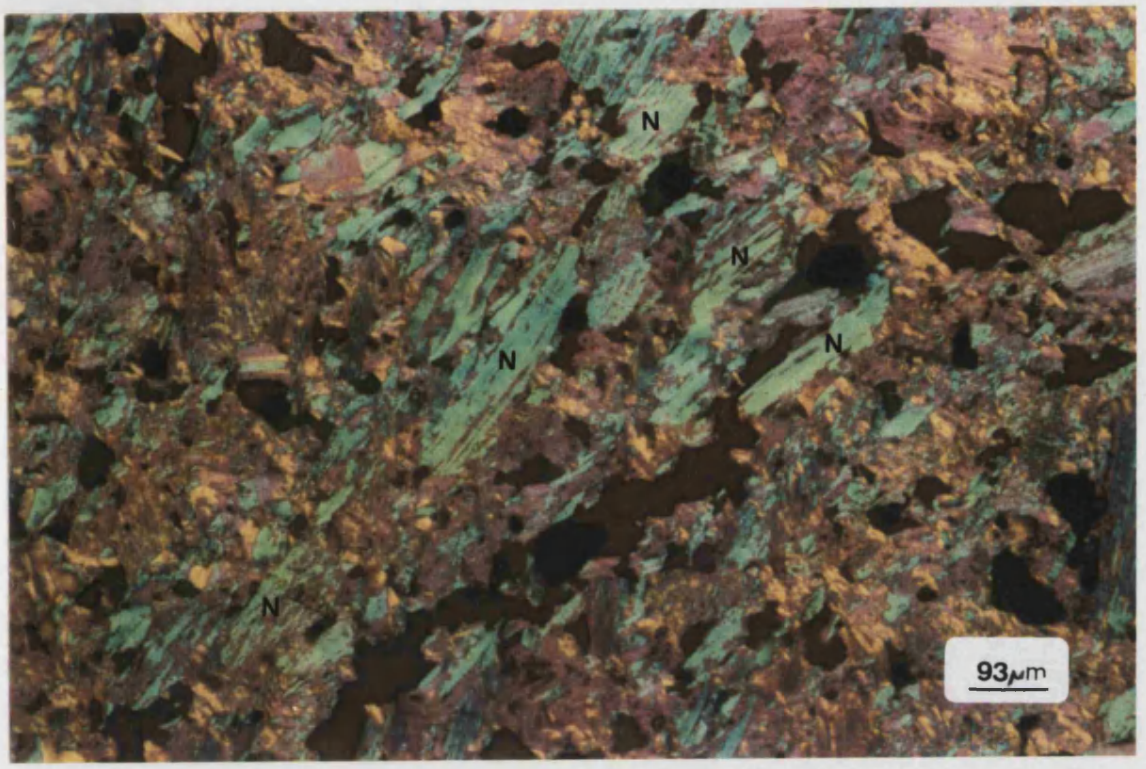

FIGURE 6.3 : A polarised light micrograph of PGA graphite cut parallel to the extrusion axis showing a small region of aligned graphitised filler particles (N).

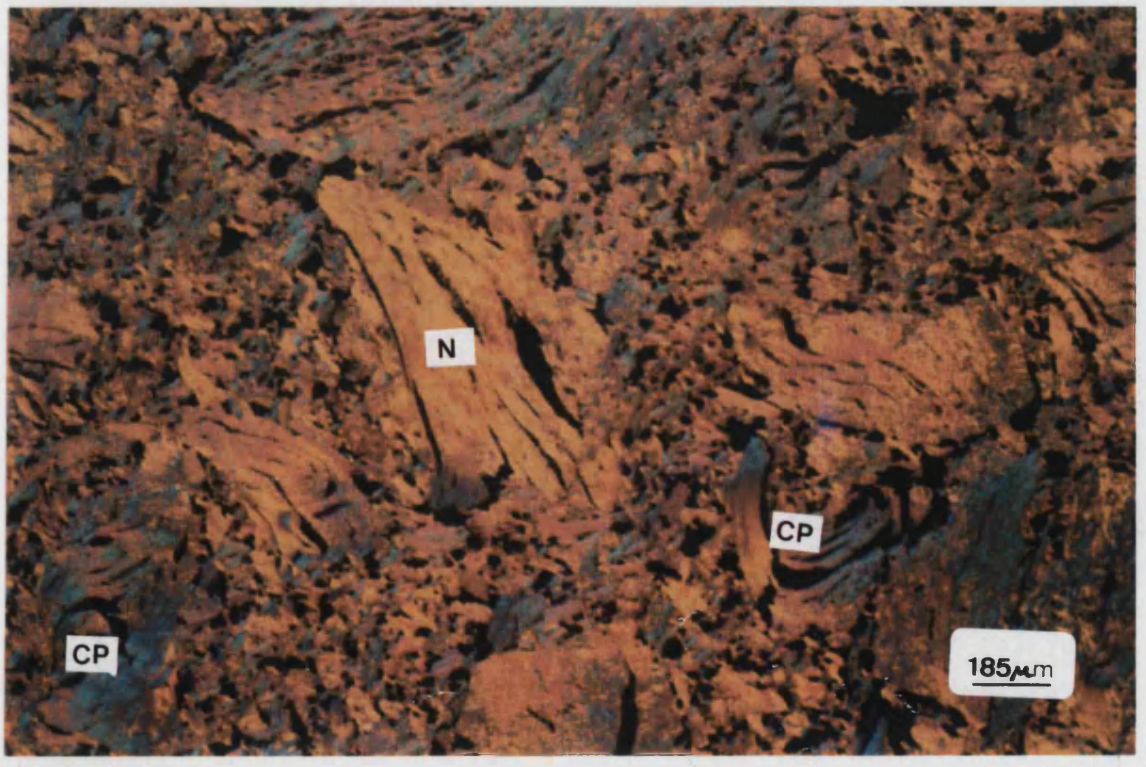

FIGURE 6.4 : A polarised light micrograph of PGA cut perpendicular to the extrusion axis showing multiple coloured "crescent" shaped filler particle (CP).

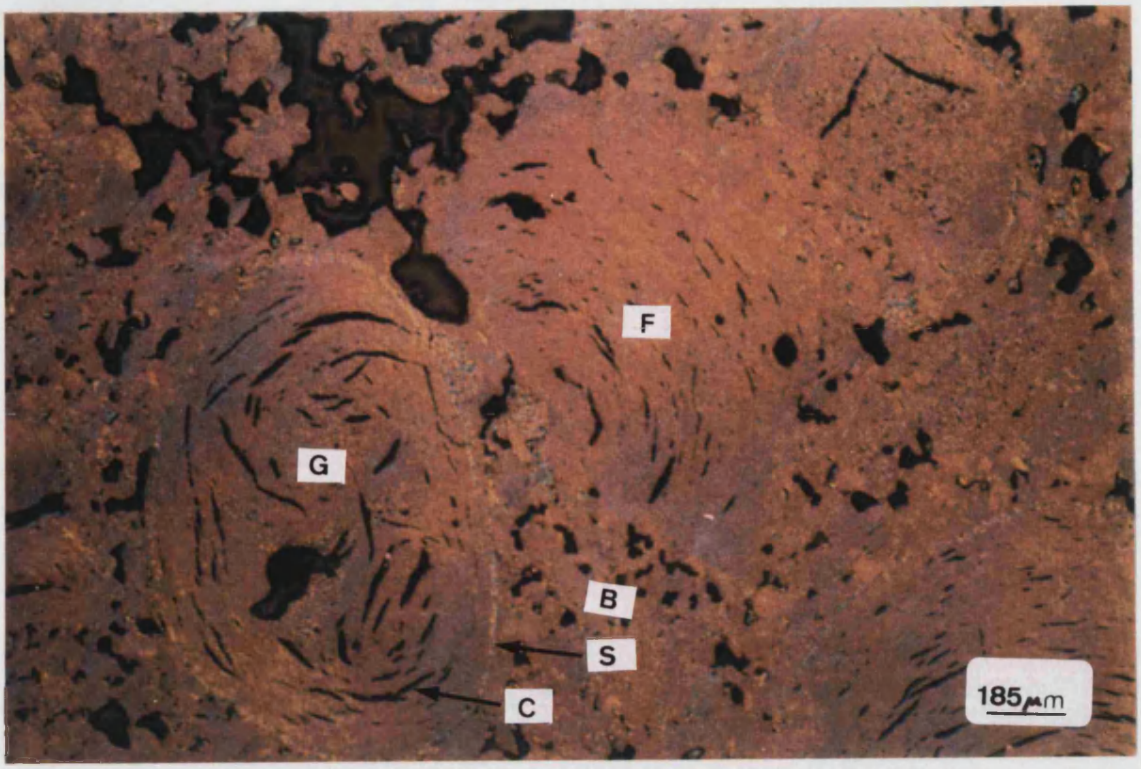

FIGURE 6.5 : A polarised light micrograph of IM1-24 (G - Gilsocarbon filler particle, S - filler particle (mosaic) speckled region, C - calcination cracks, B - binder phase, F - fragmented Gilsocarbon filler particle).

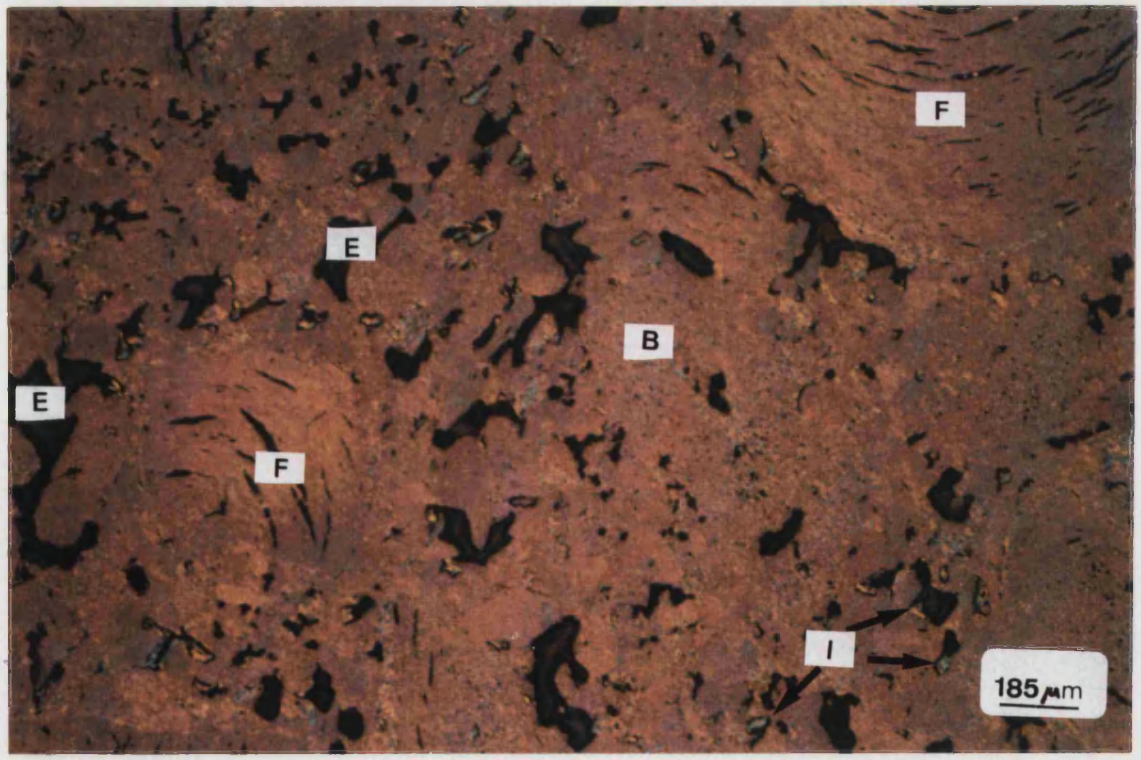

FIGURE 6.6 : A polarised light micrograph of IM1-24 graphite showing a region of binder phase between fragmented Gilsocabon filler particles (F) (E - gas-entrapment pores, I - impregnate).

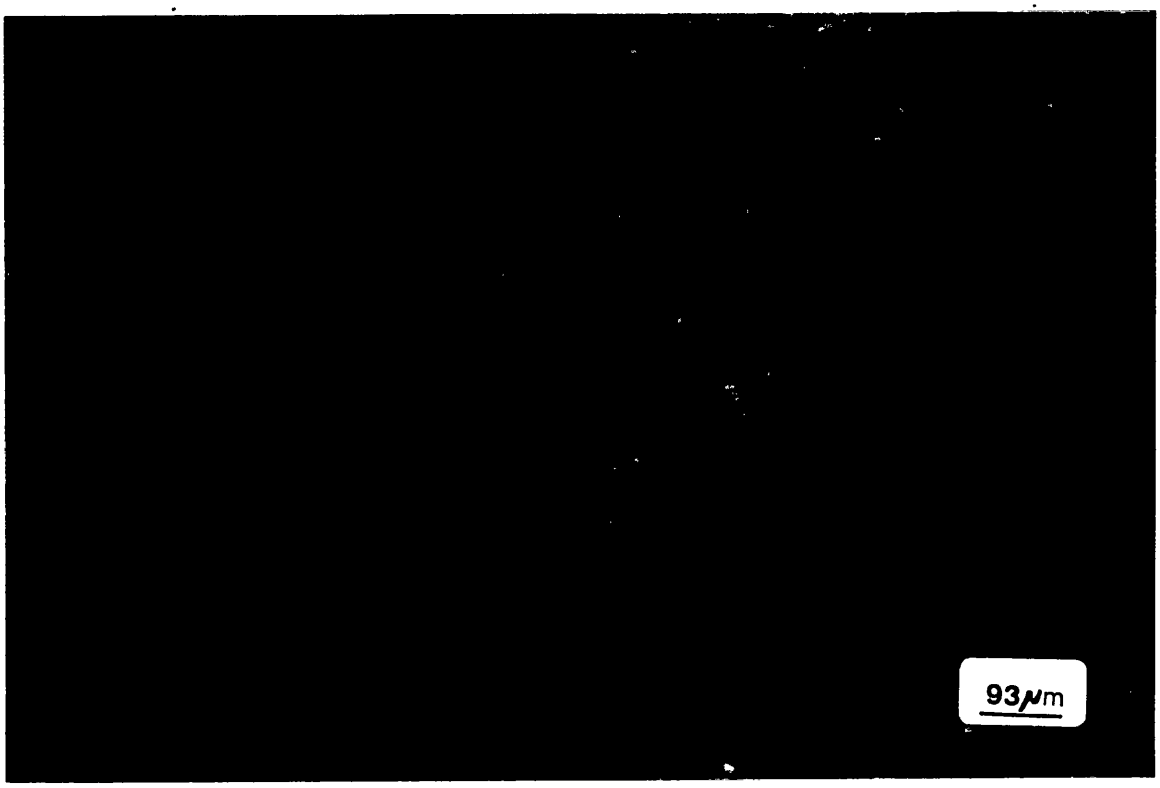

FIGURE 6.7 : A polarised light micrograph of IM1-24 graphite (I - impregnate, B - binder phase).

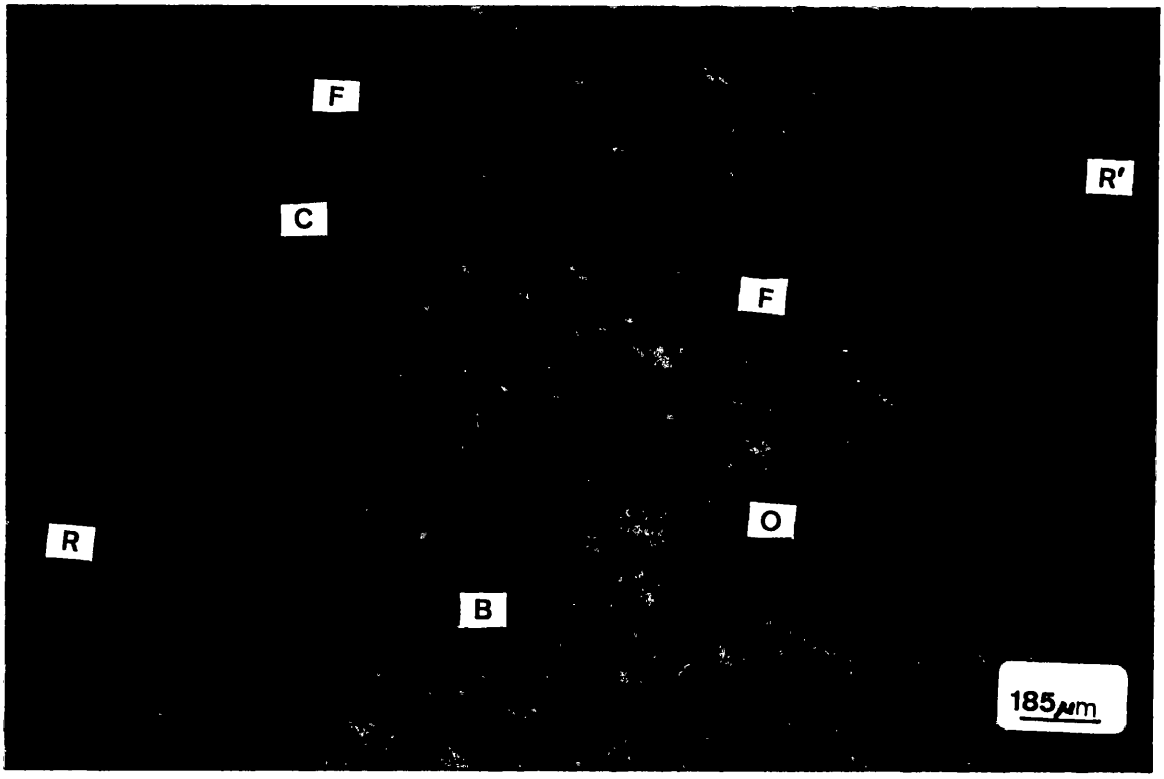

FIGURE 6.8 : A polarised micrograph of VNEC cut parallel to the extrusion axis (F - filler particle, O -open gas-entrapment porosity, C - closed porosity, B - binder phase, RR'- volatile gas escape routes).

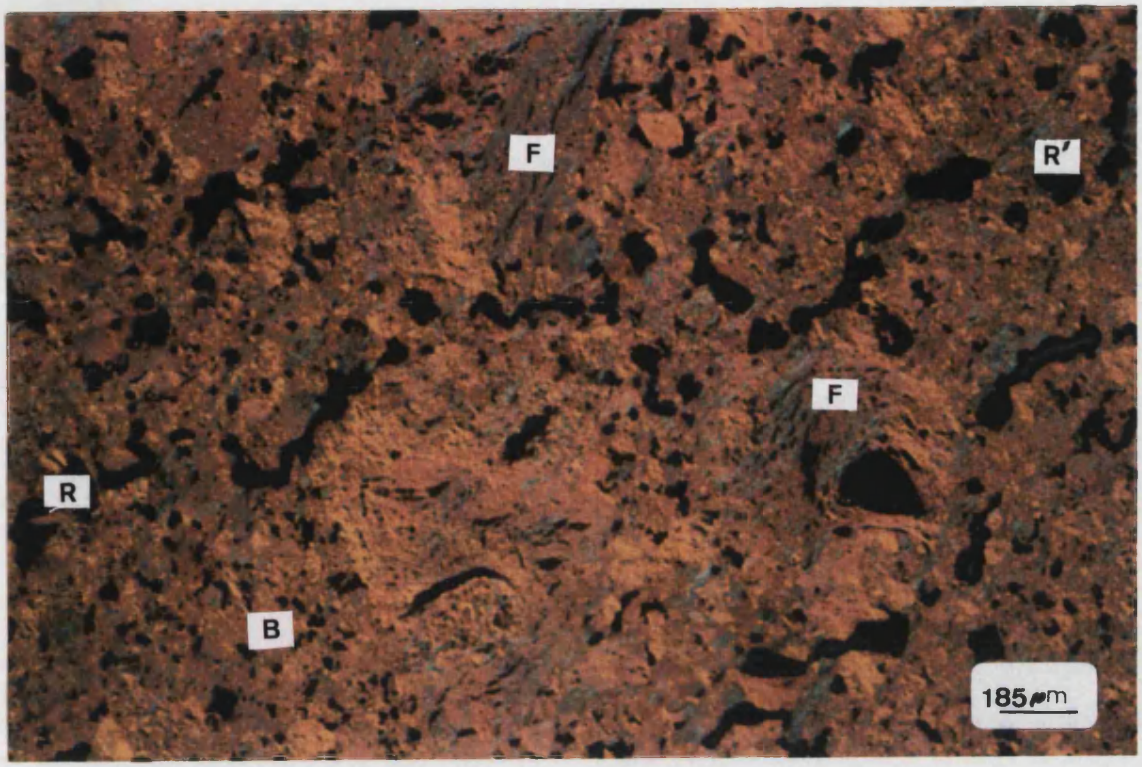

FIGURE 6.9 : A polarised light micrograph of VNEC cut perpendicular to the extrusion axis (F - filler particle, B - binder phase, RR'- volatile gas escape routes).

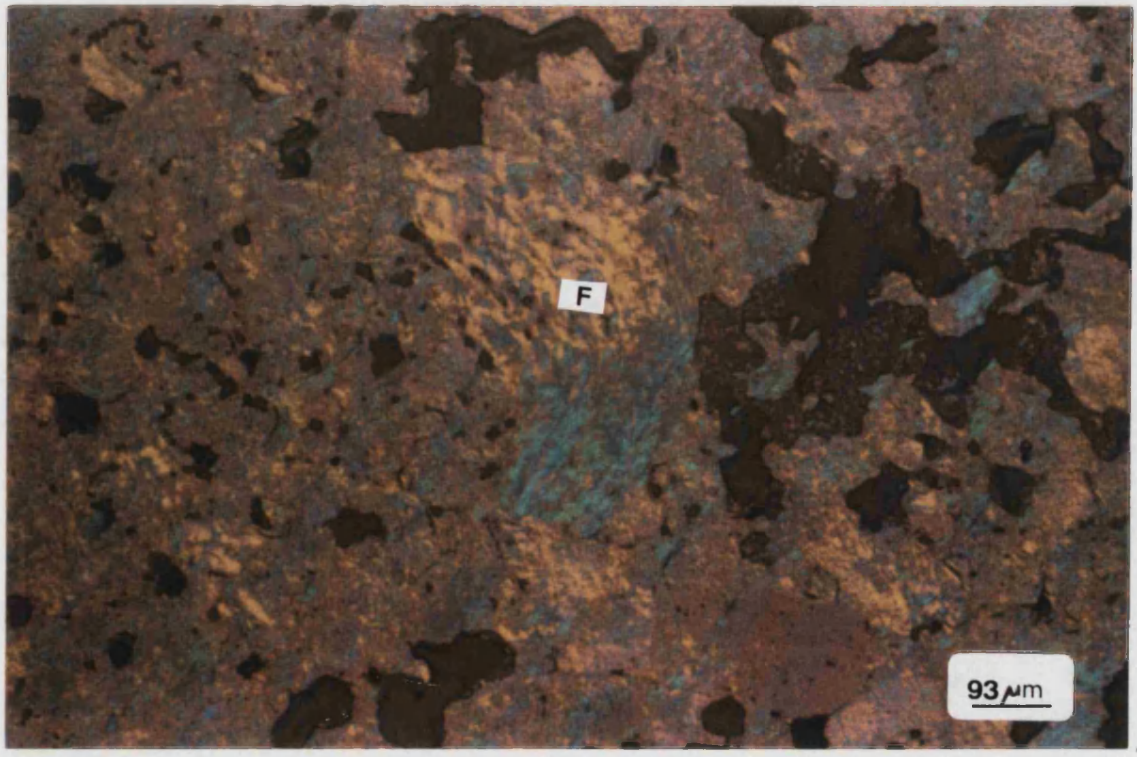

FIGURE 6.10 : A polarised light micrograph of VNEC showing a twin coloured filler particle (F) surrounded by mosaics and domains of the binder phase and pores.

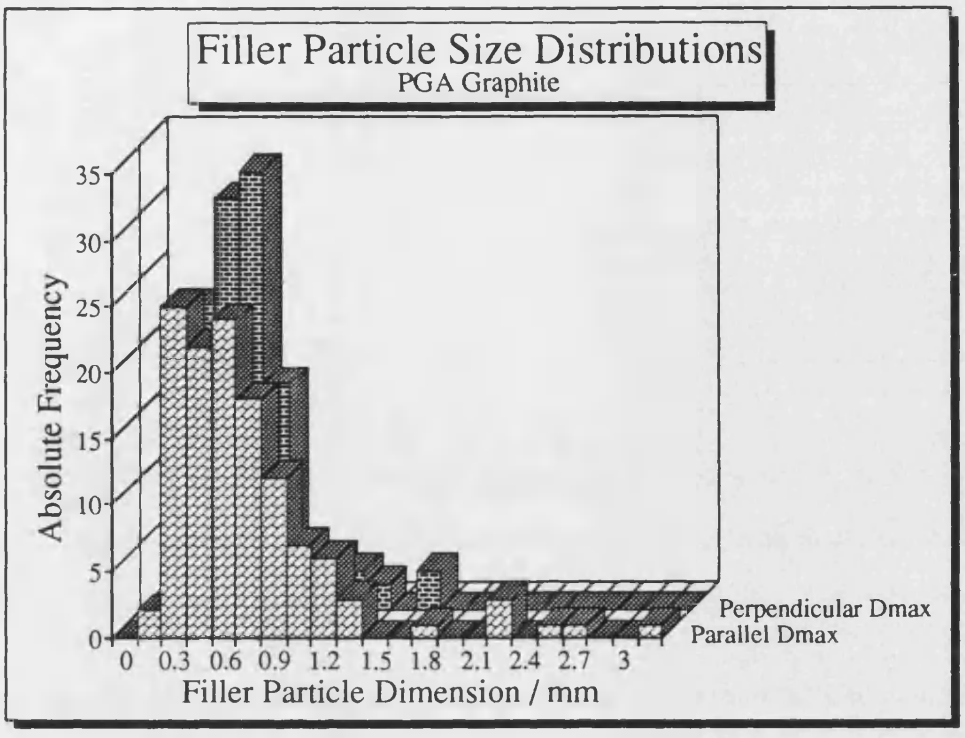

(a)

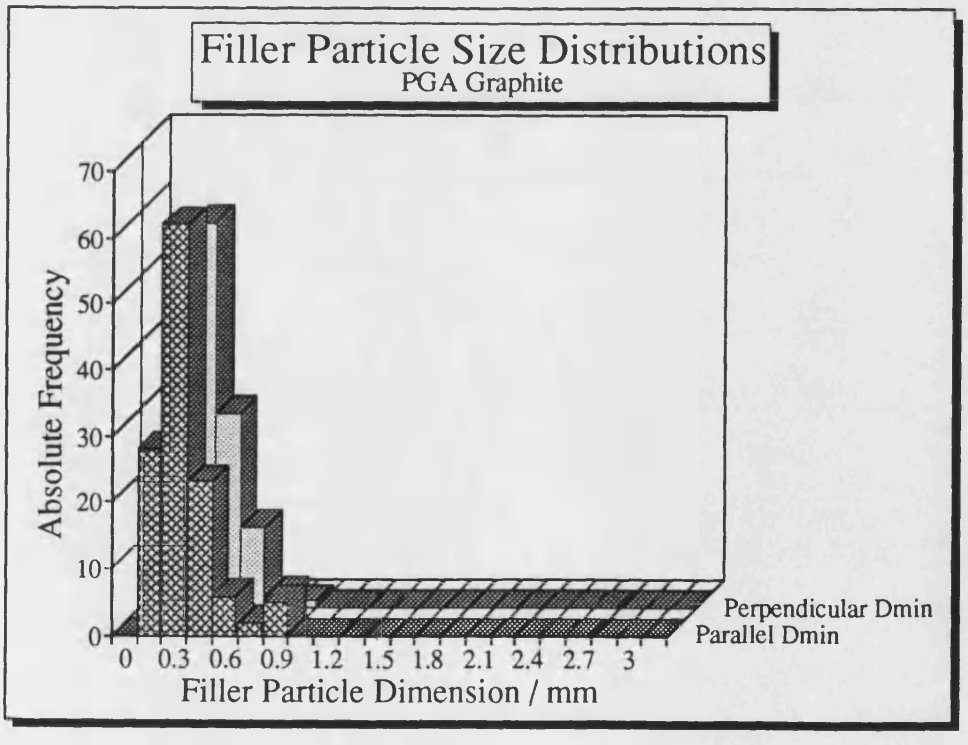

(b)

FIGURE 6.11 : Filler particle size distribution for PGA graphite cut parallel and perpendicular to the extrusion axis for (a) D_{max}, and (b) D_{min}.

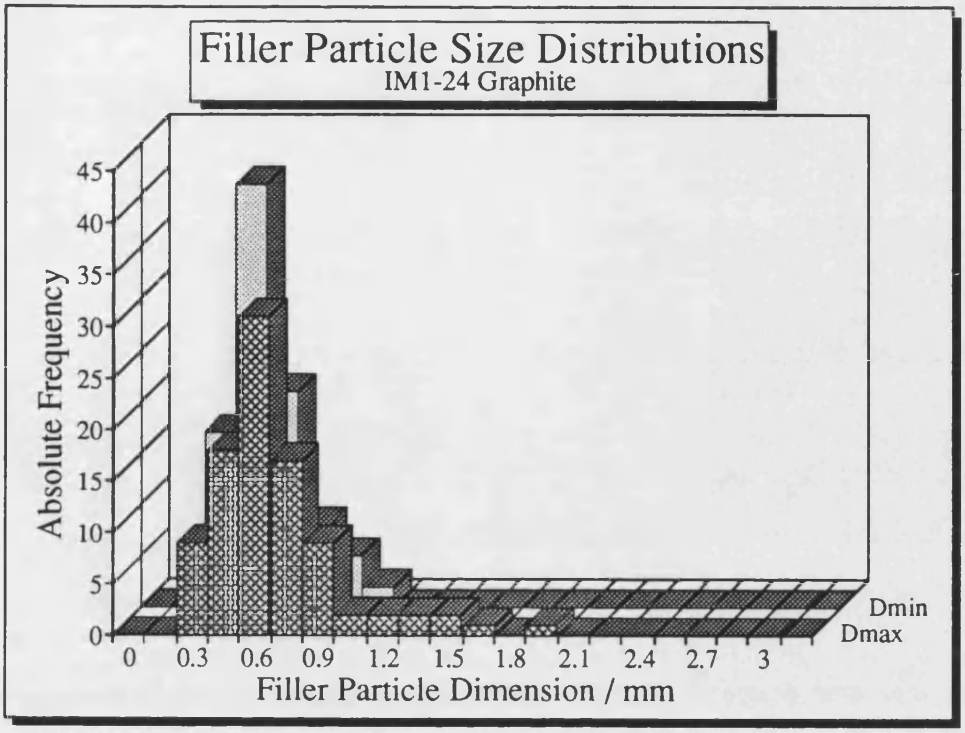

FIGURE 6.12 : Filler particle size distribution for IM1-24 graphite.

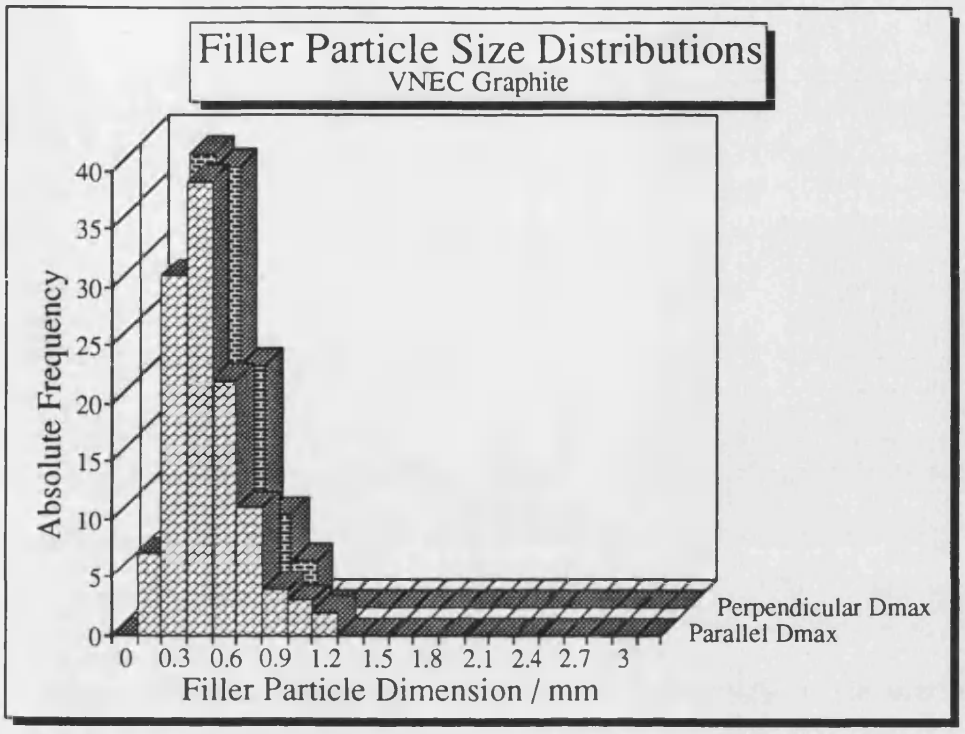

(a)

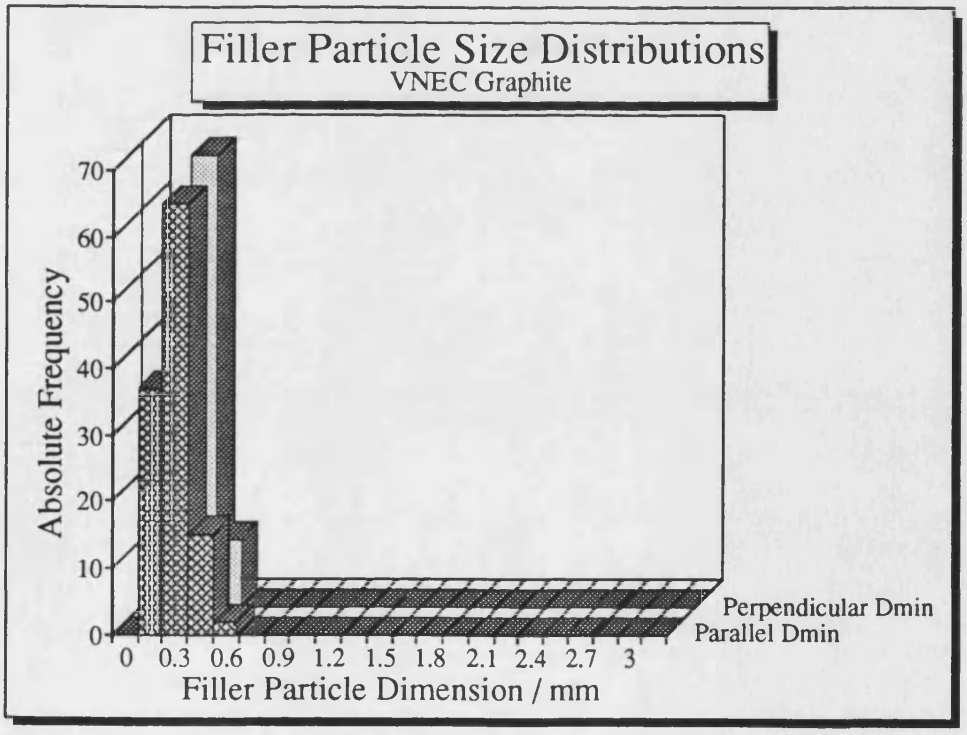

(b)

FIGURE 6.13 : Filler particle size distribution for VNEC graphite cut parallel and perpendicular to the extrusion axis for (a) D_{max}, and (b) D_{min}.

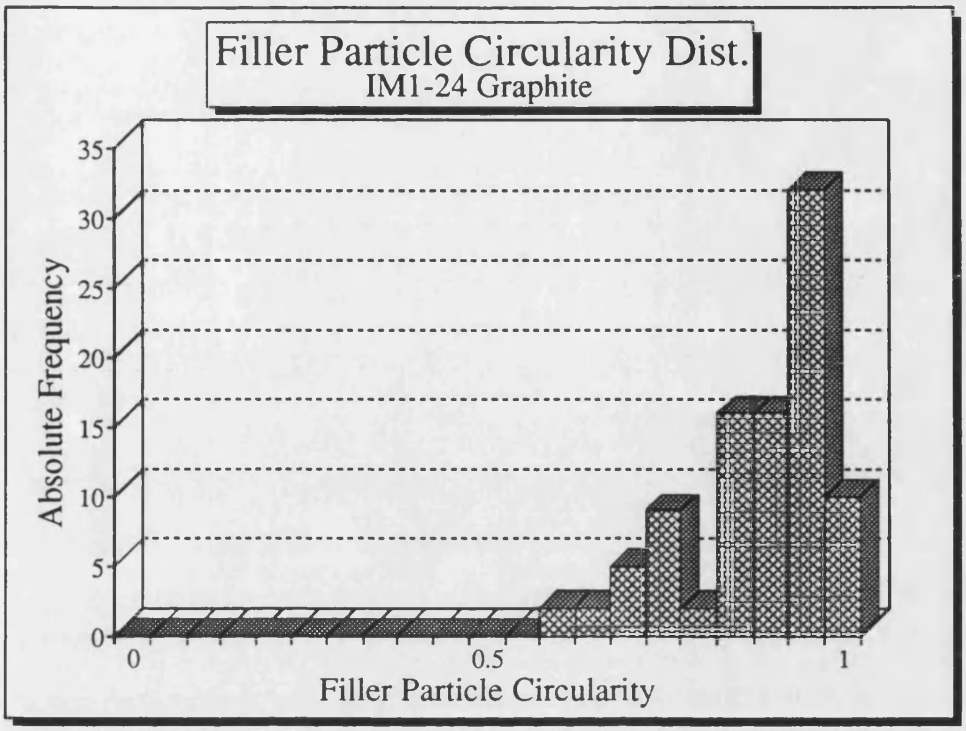

FIGURE 6.14 : Filler particle circularity distribution for IM1-24 graphite.

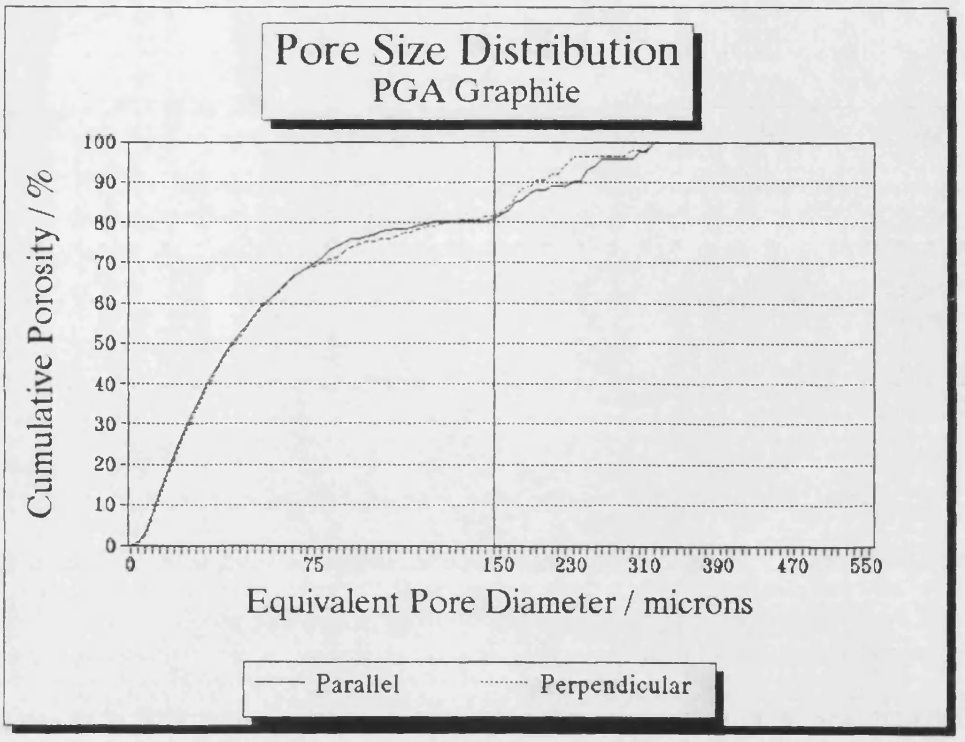

FIGURE 6.15 : The cumulative porosity (%) versus equivalent pore diameter for PGA graphite (change in scale at 150 μm).

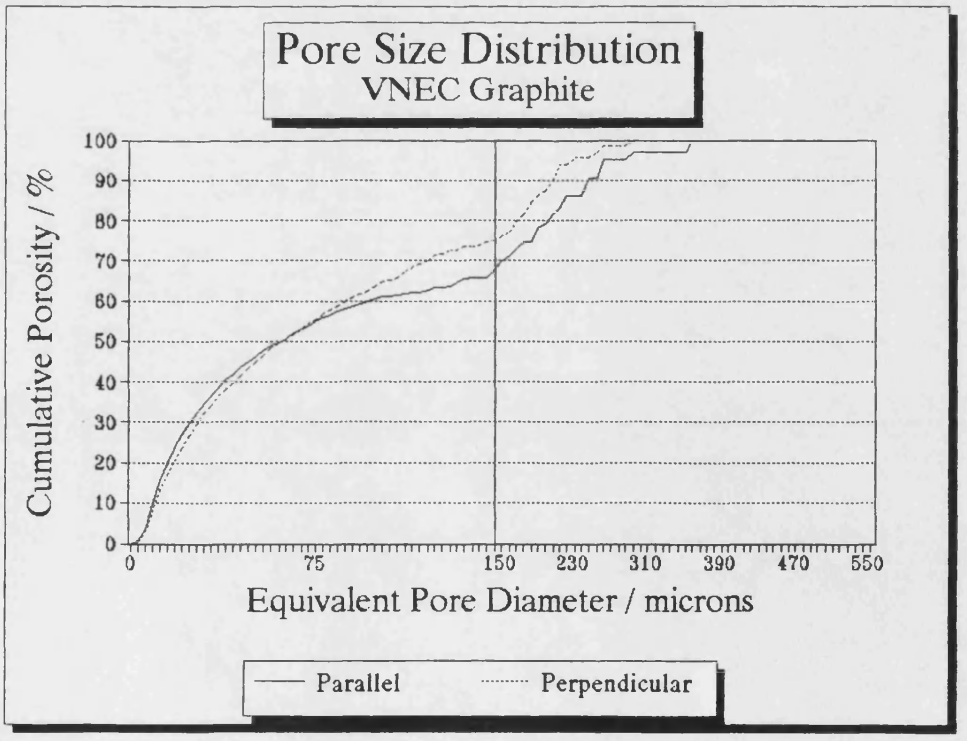

FIGURE 6.16 : The cumulative porosity (%) versus equivalent pore diameter for VNEC graphite (change in scale at 150 μm).

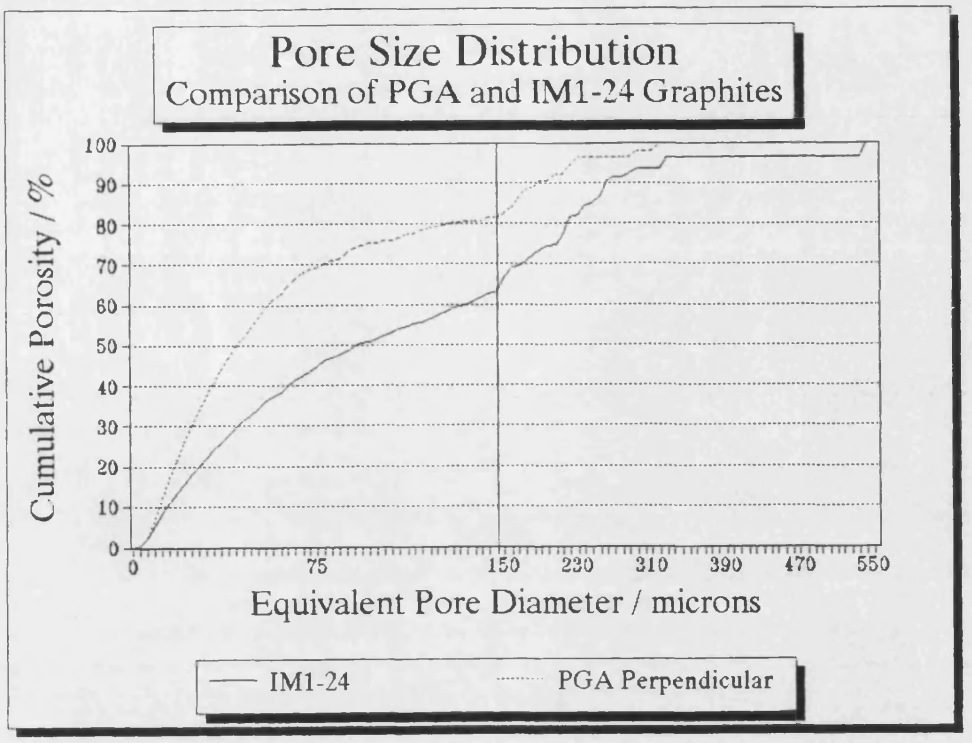

FIGURE 6.17 : Comparison of the cumulative porosity (%) versus equivalent pore diameter for IM1-24 and PGA (perpendicular) graphites (change in scale at 150 μm).

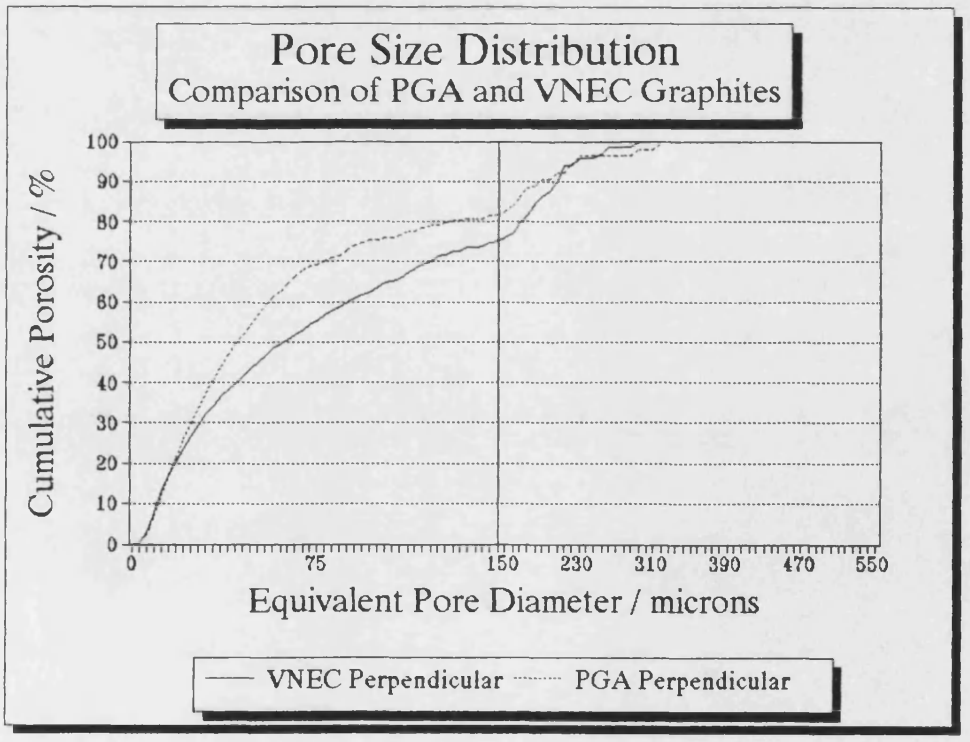

FIGURE 6.18 : Comparison of the cumulative porosity (%) versus equivalent pore diameter for PGA and VNEC graphites cut perpendicular to the extrusion axis (change in scale at 150 μm).

CHAPTER SEVEN : MECHANICAL PROPERTIES OF SELECTED NUCLEAR GRAPHITES

This chapter considers the mechanical characterisation of selected nuclear graphites described in Chapter Six. In addition to the physical parameters and information obtained in Chapter Six, this chapter provides mechanical data on the three selected graphites (PGA, IM1-24 and VNEC), such as the strength in tension, compression, and flexure. Many authors have reported values for the strength of PGA and IM1-24 (*e.g.* Brocklehurst, 1977) but no reference has been found which reports any mechanical data for VNEC. The general stress-strain behaviour of polygranular graphites is well known, and for PGA has been reported many times (*e.g.* Nightingale, 1962), but no reference has been found that presented the stress-strain behaviour for IM1-24 graphite in both tension and compression. This chapter also includes studies on post-fracture examination of fracture surfaces, and fracture toughness data. Together Chapters Six and Seven provide useful information for interpreting acoustic emission responses presented in Part C of this thesis and their relevance to fracture, for example, why a particular graphite may emit more acoustic emission than another.

7.1 Density and Porosity Determination

Density measurements were carried out in accordance with the ASTM standard for bulk density (ASTM C559-79). Each specimen was dried in an oven at 110 °C for at least two hours, cooled in a desiccator and then weighed. The volume was determined by taking the average of four measurements along each external dimension for each specimen, and at least ten specimens were used for each grade of graphite.

The difference between the bulk density, ρ_b, of the graphite specimen and the graphite single crystal density, ρ_c = 2.26 g cm^{-3}, is attributed to porosity. Therefore, the fractional porosity, P, is defined as

$$P = 1 - (\rho_b / \rho_c) \quad (7.1)$$

7.2 Dynamic Elastic Modulus Determination

The dynamic elastic modulus, E_d, was measured by the fundamental frequency method (ASTM C747-74, Re-approved 1979) (Figure 7.1) from ten specimens of each grade of graphite. The size of PGA, IM1-24 and VNEC graphite specimens was 20 x 20 x 150 mm^3 while Nittetsu EO4 and P2 and VFT-Pitchcoke graphites had a specimen size of 10 x 10 x 70 mm^3.

The resonant frequency is a natural vibration frequency which is determined by the elastic modulus, density and dimensions of the test specimen. A specimen in the fundamental transverse resonance mode contains two nodal points of zero displacement, located at 0.224L from each end, where L is the length of the specimen. The specimen is supported by knife edges at each nodal point. The specimen is mechanically vibrated by hitting it with a tapper at the outer most edge of the specimen. The resulting vibration is then detected by an audio pickup on the opposite edge, amplified, and stored in a transient recorder. The stored image may then be displayed on an oscilloscope, and recorded using a chart recorder. For a straight beam of rectangular cross section, the dynamic elastic modulus, E_d (Pa) is

$$E_d = A_R M f^2 / W \quad (7.2)$$

where A_R is a dimensional constant that depends upon the shape and size of specimen, and Poisson's ratio (tabulated in ASTM C747-74), M is the mass of the specimen (kg), f is the frequency of fundamental transverse or flexural mode of vibration (Hz) and W is the width dimension of the bar (m).

7.3 Strength Determination in Tension, Compression and Flexure

All specimens were tested using an Instron 1195, as described in Chapter Nine.

7.3.1 Specimen Geometry

The material used for mechanical characterisation of selected graphites was taken from the same source as that for acoustic emission testing, described in Chapter Nine, and the bulk graphite source is assumed to be uniform throughout (*i.e.* each specimen has not been marked with its original location). For the three selected graphites, PGA, IM1-24 and VNEC, the stressed volume in all cases was 20 x 20 x 150 mm^3. The geometry of the specimens was determined primarily by acoustic emission testing requirements; these are described in Chapter Nine together with details of requisition, machining and the design of a special tensile apparatus. In addition to strength determination, the AE response was monitored simultaneously; these AE results are reported in Chapter Ten.

7.3.2 Strength Calculations

The tensile strength of graphite is a measure of the ultimate load-carrying capacity of a specified beam in pure tensile loading. Graphite can usually support higher loads in compression than in any other mode of stress, and therefore a compression test provides a measure of the maximum load-bearing capacity of an article. The tensile or compressive strength (MPa) is given by the maximum load on the specimen at failure divided by that cross-sectional area of the specimen.

The flexural strength of graphite is a measure of the ultimate load-carrying capacity of a specified beam in bending. Flexural stress is calculated by a formula derived by simple beam bending relationships (ASTM D790-80) such that the stress experienced by the outer fibre of the material, σ (Pa) is given by

$$\sigma = 3\omega l / 2bd^2 \qquad (7.3)$$

where ω is the load (N), l is the load span (m), b is breadth (m) and d is depth (m) of the specimen. The load-span for all tests was 80 mm with a knife edge diameter of 4 mm.

7.4 Static Mechanical Properties of Selected Graphites

Table 7.1 presents mechanical property data measured in this work for the three selected graphites (PGA, IM1-24 and VNEC). PGA is the weakest graphite in all testing modes, due to its coarse texture and high porosity. The densities of IM1-24 and VNEC are not significantly different (95% confidence), and therefore, not surprisingly, their strengths in both tension and flexure are not significantly different (95% confidence). However, IM1-24 is 39% stronger than VNEC in compression. This is probably because the spherical Gilsocarbon filler particles in IM1-24 are inhibiting shear, whereas the pitchcoke filler particles in VNEC are facilitating shear. This is supported by the nature of the failure mode in compression for each graphite grade: compressive failure of PGA is characterised by a classic 45° shear deformation, but the extent of this type of shear mode is less in VNEC graphite and it is least in IM1-24 graphite. This is described in more detail later in this chapter.

Strengths reported in the literature (*e.g.* Brocklehurst, 1977) compare reasonably with those observed in this work. For PGA graphite, the strengths reported in Brocklehurst's review (1977) are within one standard deviation of the mean strength in Table 7.1, for all modes of loading. However, Brocklehurst (1977) also reports higher strengths in tension, flexure and compression for IM1-24; these are 22 MPa, 33 MPa and 85 MPa, respectively. Pickup *et al.* (1986) reported an even higher flexural strength of 43.56 ± 2.79 MPa for IM1-24. The dynamic moduli for these graphites are also broadly in line with literature values, although the value for PGA appears higher

than published. Pickup *et al.* (1986) report values for dynamic modulus of both PGA and IM1-24 as 12.1 ± 1.0 GPa and 12.4 ± 0.7 GPa, respectively, whereas Brocklehurst (1977) reports 11 GPa and 10 GPa, respectively. These differences in properties probably reflect variability in the structure of the graphite material. The structure and properties of graphites can vary with location within a given article and between different articles due to batch to batch variations. It is generally found for extruded polycrystalline graphites that the strength increases with elastic modulus (*i.e.* a graphite is stronger parallel to extrusion axis), therefore the mechanical properties determined in Table 7.1 represent the most favourable properties for PGA and VNEC.

	PGA			IM1-24			VNEC		
	Mean	**S.D.**	**n**	**Mean**	**S.D.**	**n**	**Mean**	**S.D.**	**n**
Density / g cm^{-3}	1.739	0.014	10	1.819	0.005	10	1.807	0.016	10
Fractional Porosity / %	23.05			19.51			20.05		
Dynamic Modulus / GPa	14.14	1.42	10	10.90	0.25	10	11.72	0.90	10
Tensile Strength / MPa	11.04	1.00	6	14.22	1.53	7	14.33	2.36	5
Compressive Strength/MPa	34.50	5.80	6	72.15	3.69	9	51.98	5.01	6
Flexural Strength / MPa	20.11	2.98	10	25.81	2.35	10	28.52	3.85	5

Table 7.1 : Static Mechanical Properties of Three Selected Nuclear Graphites.

Losty (1970) reports that the flexural strength, σ_f, of graphites normally falls between 1.3 and 1.5 of the tensile strength, σ_t. The failure stress of the selected graphites in flexure is greater than in tension on average by a factor of 1.82 for PGA and IM1-24, and 1.99 for VNEC. The higher values for the ratio, σ_f / σ_t, found in the present work can be attributed to a stressed-volume dependence of the ratio, σ_f / σ_t, as shown experimentally by Brocklehurst (1977). He demonstrated that the tensile and flexural strengths are a function of the specimen volume, and for approximately the same size specimen used in this work, the ratio of the tensile strength to flexural strength (four point) is ~1.7.

7.5 Stress-Strain Curves of PGA and IM1-24 Graphites

Cyclic tensile and compressive stress-strain curves (longitudinal) were obtained for PGA and IM1-24 graphites, using strain gauges which were attached to the graphite surface using a polyester adhesive. The voltage signal from each strain gauge was directed to the Marandy AE analyser (described in Chapter Nine) and amplified with a gain of 1000, before storage by the computer and conversion to %strain. The stress-strain curves for VNEC was not obtained due to insufficient material.

7.5.1 PGA

Cyclic tensile and compressive stress-strain responses for PGA are non-linear as shown in Figure 7.2 (a) and (b), respectively. This feature of the mechanical behaviour of polygranular graphites is generally attributed to basal plane shear and microcracking (Seldin, 1966). The tensile stress-strain curve shows increasing hysteresis with peak stress in the 5 MPa and 10 MPa cycles before failure at about 0.11 %strain. At low stress, the slopes of the curves obtained after stress cycling are nearly parallel. There is a permanent set on unloading which increases with peak stress.

The compressive stress-strain curves show for PGA, Figure 7.2 (b), increasing hysteresis after stress cycling in increments of 5 MPa up to 25 MPa (~70% σ_f). At this point, the strain gauge failed to respond correctly due to buckling of the gauge. The elastic modulus, as determined by the slope of the stress-strain curve, decreases with increasing stress. Although, the stress-strain behaviour in compression is superficially similar to that in tension, the strain to failure is much greater and the slopes of the curves at low stress are no longer parallel. The compressive stress-strain curve for PGA closely resembles that of the single crystal (Losty, 1970).

7.5.2 IM1-24

Figure 7.3 (a) and (b) show typical non-linear cyclic stress-strain curves for IM1-24 in tension and compression, respectively. The deviation from the Hookean behaviour is less than that for PGA in both tension and compression. The tensile stress-strain curve shows increasing hysteresis in the 5 MPa, 10 MPa and 15 MPa cycles before failure at about 0.16 %strain, and the elastic modulus decreases with increasing stress. There is a permanent set on unloading which increases with the increasing peak cyclic stress.

The compressive stress-strain curve for IM1-24, Figure 7.3 (b), shows increasing hysteresis after stress cycling in increments of 5 MPa up to 30 MPa (~42% σ_f), at which point the strain gauge buckled. As for PGA, the elastic modulus, as determined by the slope of the stress-strain curve, decreases with increasing stress, but to a lesser extent. Although the stress-strain behaviour of IM1-24 in compression is similar to that in tension, the compressive strain to fracture is much greater. The deviation from Hookean behaviour for IM1-24 in compression is much less than for PGA, indicating greater resistance to plastic deformation.

7.5.3 Comparison of the Stress-Strain Diagrams

A semi-quantitative comparison of the extent of "plastic" deformation may be obtained using Jenkins' model (1962b), described in Chapter Three. Jenkins' (1962b) described the stress-strain curves of a graphite subjected to stress cycling by

$$\varepsilon = A\sigma + B\sigma^2 \qquad \text{(Initial loading)} \qquad (7.4)$$

$$\varepsilon_m - \varepsilon = A(\sigma_m - \sigma) + B(\sigma_m - \sigma)^2/2 \qquad \text{(Unloading)} \qquad (7.5)$$

$$\varepsilon - \varepsilon_0 = A\sigma + B\sigma^2/2 \qquad \text{(Re-loading to the previous maximum)} \qquad (7.6)$$

where ε, ε_m, ε_0, σ and σ_m are strain, maximum strain, permanent set at zero load, applied stress and maximum applied stress, respectively. The coefficients A (=1/E, where E is Young's modulus) and B are material constants, and are related to the extent of elastic and plastic deformation, respectively. The coefficient A is calculated from the best fit slope of a plot of $(\varepsilon_m - 2\varepsilon_0)$ versus the maximum stress (σ_m) on each stress cycle (Figure 7.4). The coefficient B can be calculated by the best fit slope of the permanent set (ε_0) versus the square of the maximum stress (σ_m^2) on each stress cycle (Figure 7.5). Table 7.2 presents the calculated A and B coefficients for both PGA and IM1-24 in tension and compression.

	A / x 10^{-2} GPa^{-1}	B / GPa^{-2}
PGA		1.17
PGA in Compression	7.99	1.40
IM1-24 in Tension	6.38	1.14
IM1-24 in Compression	7.21	0.33

Table 7.2 : Coefficients A and B (Jenkins' Model, 1962b) for IM1-24 and PGA Graphites in Tension and Compression

For both PGA and IM1-24 graphites, the coefficient A is less in tension than in compression. Figure 7.4 shows that at higher compressive stresses (above the tensile strength), the slope of the line, *i.e.* the coefficient A, increases. This accounts for the higher values of the coefficients A observed in compression, since these values are derived from best-fit lines. It is at these high stresses that the Jenkins' model (1962b) proved unsatisfactory (Woolley, 1965) and therefore the values of A obtained from compressive stress cycling are probably an overestimate.

From Jenkins' model, the coefficient A is the reciprocal of the elastic modulus. Therefore the ratio of the coefficients A for PGA to IM1-24 should be approximately equal to the ratio of the dynamic moduli, E_d, (see Table 7.1) of IM1-24 and PGA, *i.e.*

$$A\,(PGA)/\,A\,(IM1\text{-}24) \approx E_d\,(IM1\text{-}24) / E_d\,(PGA) = 0.77 \qquad (7.7)$$

In tension, the ratio of the coefficients A is 0.65, which is in reasonable agreement with the ratio of dynamic moduli. However, in compression, the ratio of the coefficients A is 1.11, reflecting the greater limitation of the Jenkins' model applied to compressive stress cycling. The coefficients B in tension for both PGA and IM1-24 graphites are similar, but this is not so in compression (Table 7.2). In line with the trend seen for the coefficients A, the coefficient B for PGA in compression is greater than in tension. However, this is not the case for IM1-24, where the coefficient B in compression is only ~29% of the value in tension. This suggests that in compression, IM1-24 undergoes much less plastic deformation than is the case for PGA, as expected from a comparison of compressive stress-strain curves in section 7.5.2 (Figures 7.2(b) and 7.3(b)). Jenkins (1962b) gives values for the coefficients A and B for a reactor graphite (similar to PGA) in the direction parallel to the extrusion axis. He found the coefficient A to lie between 7.25-10.15 $x10^{-2}$ GPa^{-1} and the coefficient B to lie between 3.35-5.02 GPa^{-2}. The values for the coefficient A presented in this work (Table 7.2) are similar to that found by Jenkins (1962b), but for the coefficient B, Jenkins' values are greater, probably because he considered higher stresses.

7.6 Post Fracture Examination

It is well known that in all modes of loading, the deformation of polycrystalline graphite is mainly by microcracking and basal plane slip (Kelly, 1981). Microcracking is often preceded by shear along basal planes. This shear continues until obstructed, probably by the surrounding matrix, before microcracks are nucleated (Williamson, 1962 and Brocklehurst, 1977). The amount of shear preceding microcracking will vary depending on the texture of the graphite. Each microcrack grows by cleavage with increasing stress until obstructed by barriers, such as grain boundaries, or until it coalesces with another microcrack. Catastrophic failure will occur when a flaw has

reached a critical size by either accumulation of microcracks or by growth to satisfy the Griffith's criterion, as suggested by some models presented in Chapter Four.

Macro-examination of the failed graphite specimens, from all modes of loading, may provide valuable information regarding the specific fracture mechanism. For each grade of graphite, the mode of failure may indicate the extent of shear preceding microcracking and ultimate failure. This will provide supporting evidence for the interpretation of acoustic emission results. For example, it has been shown that crystallite shear generates significant amounts of acoustic emission (Ioka and Yoda, 1987). In addition to visual examination of specimens, the Scanning Electron Microscope (SEM) may be used to examine the fracture surfaces in finer detail. The SEM has the advantage over the optical microscope in that it does not polish away or erode features of the fracture surface such as crack-bridging grains. It also gives valuable information on the topography of the specimen, which can support inferences made from visual examination. The SEM used in the present work was a JEOL T330, and was most useful in the magnification range from x35 to x500. No specimen preparation was required except attaching the graphite specimen to the sample holder by a graphite putty (to aid the conduction of electrons). Goodhew and Humpherys (1988) describe in detail the workings and techniques of SEM.

7.6.1 Tension and Flexure Fracture Surfaces

Not surprisingly, tension and flexure fracture surfaces are similar. In both types of fracture, the path of the crack tends to be linked to a narrow volume of material running normal to the plane of the maximum tensile stress. In flexural failure, the crack path tends to be attracted to the upper knife edge by the strong stress concentration. Models of the fracture of graphite have suggested that in tension, the catastrophic crack path is initiated from a point of critical stress intensity and it expands by linking up with smaller cracks in its way (*e.g.* Buch, 1976). In flexure, the crack path is initiated by tensile failure on the outer fibre of the material, and it fails by

advance of the crack tip through the material. Although the inner fibre of the material experiences compressive stresses, this only amounts to a small fraction of the compressive failure stress, and consequently, compressive failure is not usually observed as part of flexural failure.

Figures 7.6 (a), (b) and (c) and Figure 7.7 (a), (b) and (c) show optical macrographs of typical tensile and flexural failure specimens of PGA, IM1-24 and VNEC graphites, respectively. The fracture surface of PGA shows a slight inclination to the normal of the tensile stress axis (up to 25°) rather than a flat surface perpendicular to the stress axis, and there are large scale irregularities on the surface. For VNEC, the fracture surface is similar to PGA, but has much smaller irregularities due to its much smaller mean filler particle size. These characteristics of the fracture surface for PGA are shown in Figures 7.8 and 7.9. Figure 7.8 shows a SEM micrograph of PGA from a tensile fracture surface. There are three filler particles, one marked C and two marked P, which are cleaved and protruding particles, respectively. The cleaved particle illustrates the ease with which the propagating crack path will travel through favourably oriented particles. However, the protruding particles, indicate the obstruction caused to the propagating crack from filler grains oriented normal to the propagating direction. Figure 7.9 clearly shows a protruding filler particle with a SEM micrograph taken normal to the fracture surface. Figure 7.10 shows an optical micrograph of the fracture surface of PGA cut parallel to the extrusion direction. It illustrates the pronounced effect unfavourably-oriented filler particles can have on the direction of the propagating crack, which in this case is deflected by 90° around the particle.

Therefore, for needle-coke graphites, filler particles that are preferentially oriented parallel to the tensile stress, a dominating feature is cleaved grains lying parallel to the fracture surface. For needle-coke particles which are normal to the crack plane, the

dominating feature is crack deflection around the filler particle. These fracture processes help to explain the large scale irregularities seen in Figures 7.6 and 7.7.

For IM1-24, the tensile fracture surface is granular and perpendicular to the applied stress (see Figures 7.6(b) and 7.7(b)). Previously, the flexural fracture surface of IM1-24 has been characterised as consisting of "cusps" and "domes" created by the spherical Gilsocarbon filler particles (Pickup, 1984). Pickup (1984) suggested that this dominant feature was caused by the outer "onion-skin" layers of the Gilsocarbon filler particles being cleaved, with the circumferential cleavage occurring in the direction parallel to the basal plane orientation within the filler particle. In his studies of dynamic crack propagation in IM1-24, Burchell (1986) observed cracks to propagate circumferentially through the outer part of the "onion-skinned" array of the calcination cracks, and parallel to the basal plane alignment, creating "cusps" and "domes" in the fracture surface. Figure 7.11 is a SEM micrograph of the tensile fracture surface of IM1-24 which illustrates such an effect. The tensile fracture surface also shows "split" Gilsocarbon filler particles, as in Figure 7.12. Only half of the Gilsocarbon particle is present, indicating that the crack path travelled through the middle of the particle. However, the right hand side of the particle has cleaved in a similar manner described by Pickup (1984). An interesting feature of this Gilsocarbon particle (Figure 7.12) is the central calcination pore/crack with minor cracks branching from it. A possible cause of the "split" Gilsocarbon particle in Figure 7.12 is crack initiation from the central calcination crack on application of tensile stress. Figure 7.13 shows a Gilsocarbon with such possible crack growth: fine cracks on both sides of an inherent pore are present within a Gilsocarbon just below the fracture surface.

7.6.2 Compression Fracture Surfaces

Generally, the compressive failure mechanisms differs from tensile failure in that instead of a rapid unstable propagation of a single crack, there is a slow extension of many cracks to form a process or "crushed" zone (Ashby and Jones, 1986). As

suggested by previous authors (*e.g.* Ioka and Yoda, 1987), slip initially occurs along the basal planes oriented 45° to the applied stress. At higher loads, slip occurs along basal planes oriented near to 45°. Failure models (Chapter Four) suggest slip continues along basal planes and favourably oriented domains until halted by obstacles, *e.g.* grain boundaries. At sufficiently high stresses, these regions will initiate cracking parallel to the applied stress axis. At very high loads, the density of cracks reaches a maximum and is so large that they link to provide shear zone of intense cracking enough to give way under load and separate the two fracture surfaces (Ashby and Jones, 1986).

Figure 7.14 (a), (b) and (c) show typical examples of failed compressive specimens for PGA, IM1-24 and VNEC graphites, respectively. The three selected graphites differ significantly in their failure mode. As explained above, fracture by shear failure may be expected, as in the case of PGA (Figure 7.14 (a)), to occur along the planes of principal shear stress which lie at an angle between 30° and 45° of the line of applied stress, due to the development of critical shearing stresses on planes inclined to the direction of compression. However, for IM1-24 (Figure 7.14 (b)), the failure mode is much more complex, and instead of two broken pieces as in PGA, IM1-24 shatters in to many pieces. Essentially, within a Gilsocarbon filler particle there is no easy slip mechanism provided by favourably oriented domains, and hence higher stresses are required to overcome the resistance to shear. This leads to a more complex mechanism as described below.

Typically, as in Figure 7.14(b), the failed specimens of IM1-24 consist of three types of fracture surface; tensile failure normal to the applied stress (R), tensile failure parallel to the applied stress (L) and shear failure inclined to the applied stress (S). Each of these three types of fracture surface are created at different stages of the failure mechanism. As the applied stress increases, the density of microcracks increases, but is not intense enough for the specimen to give way and fail. However, on increasingly

higher loads, the compressive strain increases until the lateral strain reaches the tensile failure strain and a longitudinal break results, which accounts for tensile failure parallel to the applied stress (L). As the crack grows, this process sufficiently weakens the structure to a state where shear failure (S) can be induced by the crushing action of the loading mechanism, which partly destroys the evidence of the original failure mode. At such high stresses, the sudden relaxation of the specimen by complete shear failure cause recoil stress waves to travel through the remainder of the specimen causing tensile failure surfaces normal to the applied stress (R). Some evidence to support this mechanism is provided by Figure 7.15 which presents the lateral strain versus applied stress curves for two opposite sides of a specimen of IM1-24. The lateral failure strain in this case, ~0.25% is much greater than that experienced in tensile tests, ~0.16% (see Figure 7.3 (a)). In this particular case, the two lateral strain curves deviate from each other at very high stresses, ~70 MPa, suggesting that direct axial compression is transformed into buckling.

SEM micrographs of PGA and IM1-24 failure surfaces in compression support the failure mechanism suggested. Figures 7.16 and 7.17, for PGA and IM1-24, respectively, show the crushed shear zone of intense cracking. These failure surfaces are completely different to the failure observed in tensile testing (Figures 7.8 and 7.11). The outer "onion-skin" layers of the Gilsocarbon are crushed and appear like "corn flakes" (Figure 7.17), but for PGA, the flakes are slab-like suggesting easier shear and cracking than for IM1-24.

For VNEC, the compressive failure mode is similar to PGA, but there is a double cone shear type of failure accompanied by recoil tensile failures (Figure 7.14 (c)) (John, 1992). In most cases, the main fracture surface is inclined at angles ~35-45° to the applied stress, indicative of the principal stress axis. Examination of the failed compressive specimens indicate that the ease of shear in each graphite is given by PGA>VNEC>>IM1-24.

7.7 Fracture Toughness of Selected Graphites

7.7.1 Specimen Geometry

Fracture mechanics tests were carried out on Single Edged Notched Beams (SENB) (see Figure 4.1), of two sizes, (a) 20 x 20 x 150 mm^3 and (b) 10 x 10 x 70 mm^3. In all tests, a notch to depth ratio (a/w) of 0.5 was adopted, and a notch root radius of <5 μm, assumed to be equivalent to a sharp crack (Pickup, 1984 and Burchell, 1986), was produced by tapping a razor blade across the tip of a machined 0.30 mm wide slot. For IM1-24, PGA and VNEC, a specimen size of 20 x 20 x 150 mm^3 was used (similar in size to and from the same source as that used in the AE cyclic testing programme), but for VFT-Pitchcoke, and Nittetsu EO4 and P2 graphites, a specimen size of 10 x 10 x 70 mm^3 was used. Accurate measurements of the notch depths and root radii were made using a Nikon Profile Projector (model 6CT2) at magnifications of x20 and x50. Each SENB specimen was loaded in flexure (3 point) on an Instron 1122 with a crosshead speed of 0.05 mm min^{-1} and in all cases the span to width ratio (s/w) was 4. The knife edge diameter in all cases was 4 mm.

7.7.2 Critical Stress Intensity Factor (K_{Ic})

Standard methods for measuring critical stress intensity factor, K_{Ic}, (ASTM E399) strictly only apply to metallic materials, typically in the form of SENBs, which require a sharp crack to be fatigued into the specimen beneath a machined defect. The stress intensity factor, K_I, is the magnitude of stress field around an ideal-crack tip (in mode I opening) in a homogeneous, linear-elastic body (ASTM E616-81); it characterises the crack extension resistance under conditions of crack-tip plane strain. Under these conditions, K_{Ic} is considered to be a characteristic property of the material which measures its resistance to crack propagation. For materials which are not linear elastic the K_{Ic} value will be dependent on the notch sensitivity and it is a function of the

plasticity of the crack tip. For a sharp crack of length, a, under tensile loading, the stress intensity factor ($Nm^{-3/2}$) for a linear elastic material may be written

$$K_I = Y \sigma a^{1/2} \qquad (7.8)$$

where Y is a geometrical factor and σ is the applied stress. Brown and Srawley (1969) for a SENB gave a polynomial expression for Y as a function of the aspect ratio a/w of the crack in the specimen of thickness w. Therefore in the critical case, K_{Ic} values may be obtained from the nominal strength and the crack depth. In this work, critical stress intensity factors (K_{Ic}) for various grades of graphite were determined by using an experimental method similar to those described by Davidge and Tappin (1968) and Rose (1985). The value of K_{Ic} ($MNm^{-3/2}$) may be determined using the following equation

$$K_{Ic}=[A_0+A_1(a/w)+A_2(a/w)^2+A_3(a/w)^3+A_4(a/w)^4] / [bw^2/6Ma^{1/2}] \qquad (7.9)$$

where a is the notch length (m), w the beam depth (m), b the beam breadth (m) and M the bending moment (Nm). For a loading span to beam width ratio (s/w) of 4:1 the values of the constants are; A_0=1.93, A_1=-3.07, A_2=14.53, A_3=-25.11, A_4=-25.80, whereas if the loading span to beam width ratio (s/w) is 8:1 the constants are A_0=1.96, A_1=-2.75, A_2=13.66, A_3=-23.98, A_4=-25.22 (Brown and Srawley, 1969).

The fracture toughness values calculated using this method described above do not take into account the presence of an inherent flaw (Brocklehurst, 1977 and Rose, 1985) which increases the notch length by adding an additional crack below the machined notch.

7.7.3 The Inherent Flaw Size (δa)

If the critical stress intensity factor is assumed to be a material constant, then a value for the inherent flaw size of the material may be calculated from the strength of an equivalent unnotched rectangular beam. Therefore the inherent flaw size should also be a material property.

The unnotched beams are assumed to contain an inherent flaw size, δa, whereas the notched beam has a machined notch of size, a_0, plus the inherent flaw size, δa, ahead of the crack tip, *i.e.* an effective notch depth $a = a_0 + \delta a$. Using equation 7.9, δa is calculated by plotting the stress intensity factor as a function of a range of assumed values of δa for both unnotched and notched beams. Figure 7.18 presents a typical example of such a plot for IM1-24 graphite. In Figure 7.18, the curved line represents the case of an unnotched beam, the K_{Ic} value rising rapidly as the assumed values of δa increase. The straight line represents the increase in K_{Ic} with additional crack length for the SENB specimen. The values of δa and K_{Ic} for IM1-24 are obtained from the intercept of the curves for notched and unnotched specimens (Rose, 1985).

7.7.4 Effective Surface Energy (γ_f)

An alternative fracture mechanical parameter, based on a thermodynamical energy balance approach, is the work of fracture (effective surface energy, γ_f). γ_f is the average energy expended during crack propagation per unit area of crack surface, A, in the formation of a new surface. The work of fracture is calculated from the load-deflection curve of a SENB specimen subjected to controlled crack growth (see Figure 4.2). Controlled crack growth is attained when the elastic energy stored in the specimen and the apparatus is not enough to complete the fracture process, and additional external work is required. In the present work, the mode of fracture is then said to be stable. The effective surface energy, γ_f, was calculated for a range of graphites using the method described by Davidge and Tappin (1968). γ_f is obtained by measuring the work done to fracture completely a specimen in a controlled manner, *i.e.*

the energy produced by external work was transformed completely into the effective surface energy of the specimen. The total work done in each test was measured by calculating the energy, U, under the curve. The effective surface energy is given by

$$\gamma_f = U / 2b(d-c) \qquad (7.10)$$

where b is the breadth of the specimen (m), c the notch depth (m) and d the depth of the specimen (m).

The value, γ_f, has two main limitations. Firstly, besides the thermodynamical surface energy associated with formation of the principal propagating crack, it also includes energy expended in regions remote from the propagating crack such as subcritical microcracking, plastic deformation around loading points, acoustic and kinetic energy of advancing cracks. Secondly, the geometric area of fracture (2b(d-c)) is used in the calculation rather than the fracture surface area which includes fine scale surface irregularities (*e.g.* see Figures 7.8 and 7.11). Taking these two points into consideration, the effective surface energy, γ_f, is always an over-estimate.

7.7.5 Non-Ideality Parameter

For linear elastic materials

$$G_{Ic} = 2\gamma_s = K_{Ic}^2/E \qquad (7.11)$$

where γ_s is the thermodynamical surface energy of the graphite, G_{Ic} is the critical strain energy release rate and E is the Elastic modulus. According to the principles of Linear Elastic Fracture Mechanics (LEFM), deformation can only occur by the elastic stretching and breaking of bonds, and the value of G_{Ic} calculated from K_{Ic} represents the energy required per unit of new crack surface resulting from purely elastic deformation. For graphites there is much evidence that fracture is accompanied by

basal plane shear and microcracking in the process zone remote from the principal propagating crack. Therefore, graphite does not behave as a LEFM material and the experimentally-measured value of surface energy, γ_f, is greater than the thermodynamical surface energy, γ_s. Pickup (1984) and Burchell (1986) defined a non-ideality parameter, P, which is a measure of the deviation of a graphite from LEFM behaviour

$$P = (2\gamma_f - K_{Ic}^2/E) / 2\gamma_f = 1 - G_{Ic}/2\gamma_f \qquad (7.12)$$

For a LEFM material, $\gamma_f = \gamma_s$ and P = 0, whereas for a non-LEFM material $\gamma_f > \gamma_s$ and $0<P<1$. Pickup (1984) and Burchell (1986) used the surface energy required to initiate cracking, γ_i, determined by the compliance calibration method (Davidge and Tappin, 1968), rather than γ_f in their work, but in both cases $1>P>0$ and higher values of P denote increasing deviation from LEFM behaviour.

7.7.6 Results

Table 7.3 presents brief mechanical data for Nittetsu-EO4, Nittetsu-P2 and VFT-Pitchcoke graphites. Mechanical Data for the PGA, IM1-24 and VNEC graphites have already been presented in Table 7.1. Although Nittetsu-E04 and Nittetsu-P2 graphites have different filler particle size distributions, the measured properties from the two graphites are very similar.

	VFT-Pitchcoke	Nittetsu-EO4	Nittetsu-P2
Density / g cm^{-3}	1.85 ± 0.01	1.84 ± 0.02	1.85 ± 0.01
Fractional Porosity / %	18.24	18.43	18.17
Dynamic Modulus / GPa	9.46 ± 0.33	11.97 ± 0.17	12.04 ± 0.10
Flexural Strength / MPa	29.45 ± 2.86	43.80 ± 2.70	46.44 ± 2.11

TABLE 7.3 : Mean Mechanical Data For VFT-Pitchcoke, Nittetsu EO4 and Nittetsu P2 Graphites (± 1 S. D.).

Table 7.4 presents fracture mechanics data for all six graphites, and Figure 7.19 illustrates the trends shown by this small selection of graphites. For all graphites, the fracture toughness, K_{Ic}, varies between 0.8-1.5 $MNm^{-3/2}$ (Brocklehurst, 1977). For all graphites presented in Table 7.4, the fracture toughness varies between 1.0 and 1.4. Pickup *et al.* (1986) presents fracture toughness values for PGA and IM1-24 as 1.34 ± 0.05 $MNm^{-3/2}$ and 0.84 ± 0.06 $MNm^{-3/2}$, respectively. These literature values are in reasonable agreement with the experimentally-determined values in Table 7.4. The Nittetsu graphites are replacing the VFT-Pitchcoke graphite as the standard fuel sleeve material, and the reason why is ably demonstrated in Tables 7.3 and 7.4: Nittetsu graphites are stronger and have a higher fracture toughness, K_{Ic}. This is important for refuelling purposes when the fuel sleeve can be subjected to severe impact loads. VNEC and IM1-24 graphites have similar fracture toughness, K_{Ic}, values. These two graphites also have similar tensile and flexural strengths (see Table 7.1). VFT-Pitchcoke and PGA have the lowest values of fracture toughness, K_{Ic}.

Table 7.4 also presents effective surface energy values, γ_f, from 160 to 200 Jm^{-2}. This is in line with those values presented by Brocklehurst (1977) which were 50-200 Jm^{-2}. The γ_f values are larger than the surface energy values at crack initiation, γ_i, presented by Pickup *et al.* (1986) as expected, which were 99.1 ± 15.2 Jm^{-2} and 62.8 ± 7.0 Jm^{-2} for IM1-24 and PGA, respectively. This supports the postulate by Brocklehurst (1977) that crack propagation is harder than crack initiation. The higher γ_f values can be attributed to subcritical cracking and crack branching. In comparison to the other two graphites (IM1-24 and VNEC), PGA has a standard deviation nearly three times as much. This may be the result of the higher degree coarseness in the structure of PGA graphite (*e.g.* Figure 6.1) than the other two graphites (*e.g.* Figure 6.6).

The inherent flaw size for nuclear graphites varies from 0.1-1.5 mm (Brocklehurst, 1977). Experimentally-determined values (Table 7.4) range between 0.3 and 1.5 mm, and therefore are consistent with inherent flaw sizes published by other workers.

These values can not easily be attributed to any single microstructural feature, indeed they are considerably larger, *e.g.* they are much larger than the equivalent pore and filler particle sizes presented in Chapter Six. However, they are representative of the texture of these graphites. Coarser-textured graphites are generally weaker than other graphites, but generally have higher values of inherent flaw size, δa, *i.e.* PGA>IM1-24>VNEC>VFT>Nittetsu.

The non-ideality parameter, P, attempts to combine stress and energy parameters and measure the degree of non-linear mechanical behaviour as previously described. Youfa Yin *et al.* (1991) presents values of P for IM1-24 and PGA as 0.28 ± 0.10 and 0.54 ± 0.08, respectively. However, these values were based upon the surface energy required to initiate fracture, γ_i, and not the effective surface energy, γ_f. The values of P presented in Table 7.4 for the graphites follow the order of PGA>VNEC>IM1-24. This trend supports earlier work (§7.5.3) in that IM1-24 resists plastic deformation to a greater degree than other graphites. PGA graphite has the highest value of P which illustrates the coarseness of its texture and the ease of shear deformation. VNEC has an intermediate value of P suggesting a finer texture but with easier shear mechanism than IM1-24.

	K_{Ic} / $MNm^{-3/2}$			γ_f / Jm^{-2}			δa / mm	P
	Mean	**S.D.**	**n**	**Mean**	**S.D.**	**n**		
PGA	1.073	0.120	10	187	22	10	1.51	0.782
IM1-24	1.245	0.031	9	163	8	8	0.97	0.564
VNEC	1.269	0.018	5	201	7	5	0.68	0.659
VFT	1.06	0.08	10				0.64	
Nittetsu P2	1.33	0.03	10				0.29	
Nittetsu EO4	1.37	0.03	10				0.36	

TABLE 7.4 : Fracture Mechanics Data For Six Selected Graphites

The more non-linear a graphite, the easier shear will occur. Generally, non-linear graphites are more porous, where the porosity provides space for the accommodation

of deformation. Therefore in the case of compression, it may be expected that the more non-linear a material the lower its strength, *i.e.* IM1-24 is the strongest graphite in compression compared to VNEC and PGA but has the lowest value of P. Figure 7.20 shows for PGA, IM1-24, and VNEC that the higher the compressive strength, the lower the non-ideality parameter, P.

7.8 Summary

This chapter has presented mechanical properties mainly for three graphites; PGA, IM1-24 and VNEC. IM1-24 and VNEC graphites have been shown to have slightly greater strength in tension and flexure than PGA, this is attributed to the coarser texture and higher porosity of PGA. The compressive strength of IM1-24 is greater than those of the other two graphites. This is attributed to the inhibition of shear deformation by the Gilsocarbon filler particles, whereas pitchcoke filler particles facilitate shear for the other two graphites. Evidence has been presented to support this suggestion in the form of stress-strain diagrams (Figures 7.3 and 7.4), the Jenkins' model (1962), post fracture examination (Figure 7.14(b)) and fracture toughness measurements (Table 7.4). Post fracture examination demonstrated for PGA and VNEC that irregularities in the fracture surface are caused by filler particles with crack deflecting properties, but if favourably aligned would provide an easy cleavage route. For IM1-24, the Gilsocarbon filler particle in tensile failure was shown to "split" in addition to the previously established circumferential cleavage. Compression failure for PGA and VNEC generally followed an shear mechanism with fracture planes inclined to the applied stress. However, the failure mode for IM1-24 was much more complex consisting of longitudinal cracking followed by shear failure and recoil tensile failure. Further mechanical data, *e.g.* non-ideality parameter, was provided to support the suggestion that IM1-24 resists plastic deformation to a greater extent than other graphites.

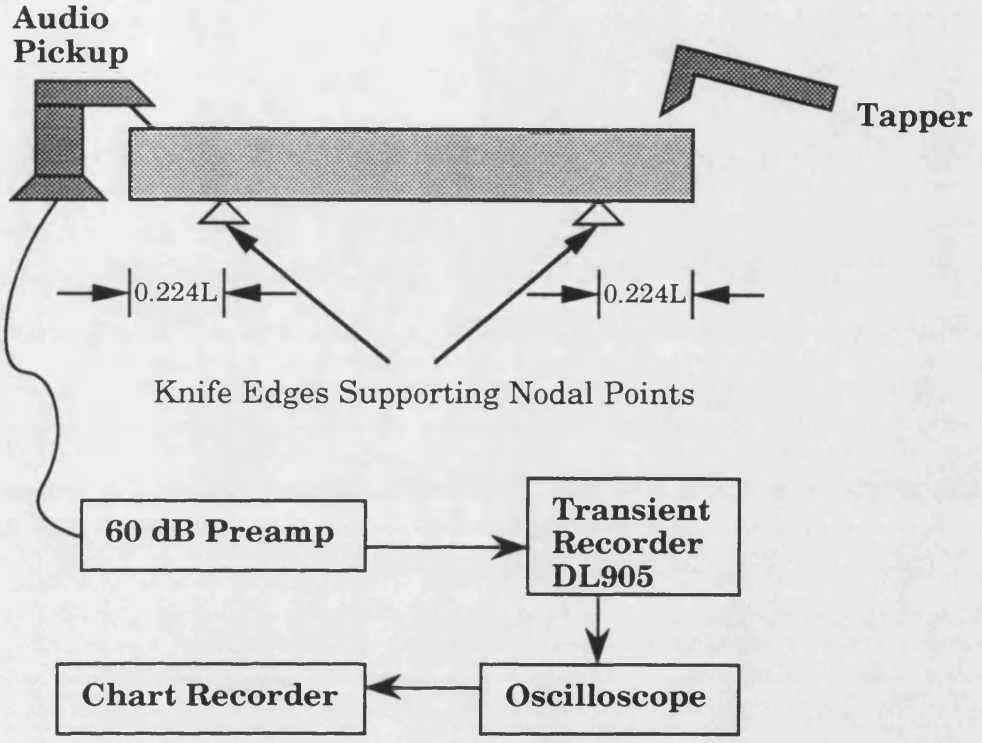

FIGURE 7.1 : The experimental determination of dynamic elastic modulus.

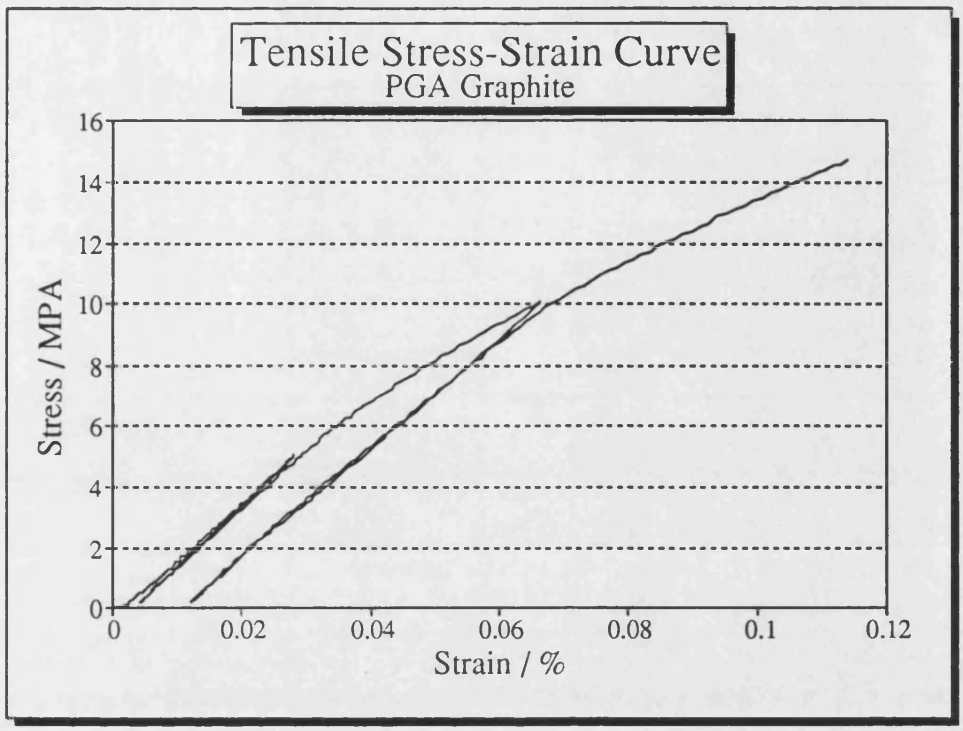

(a)

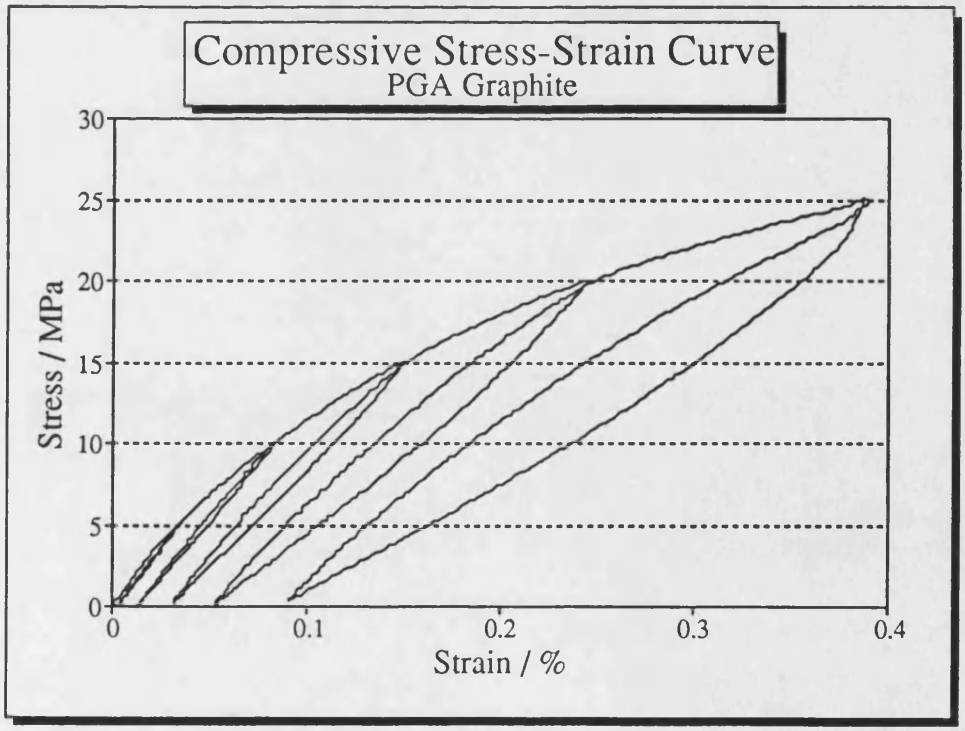

(b)

FIGURE 7.2 : Typical cyclic stress-strain responses for PGA graphite (longitudinal axis parallel to the extrusion axis) in (a) tension and (b) compression.

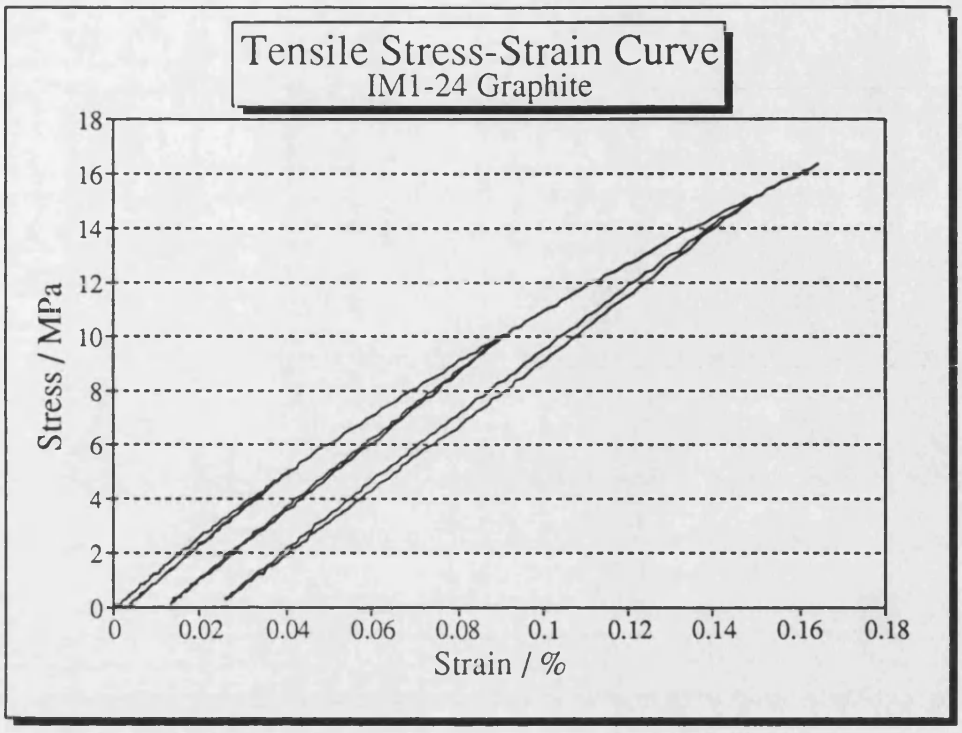

(a)

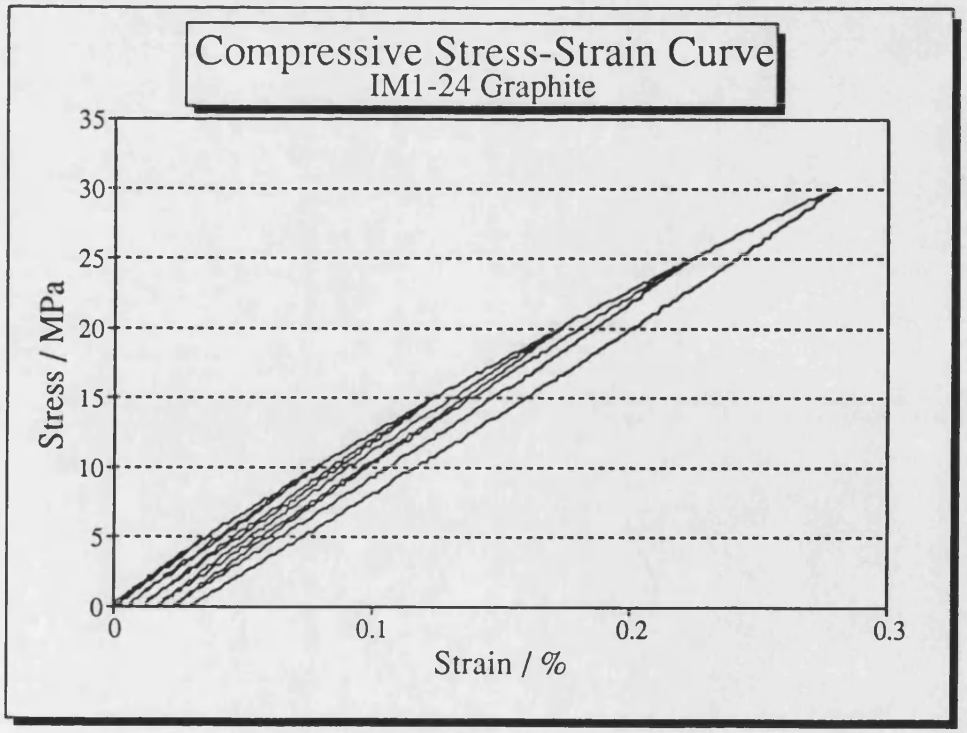

(b)

FIGURE 7.3 : Typical cyclic stress-strain responses for IM1-24 graphite in (a) tension and (b) compression.

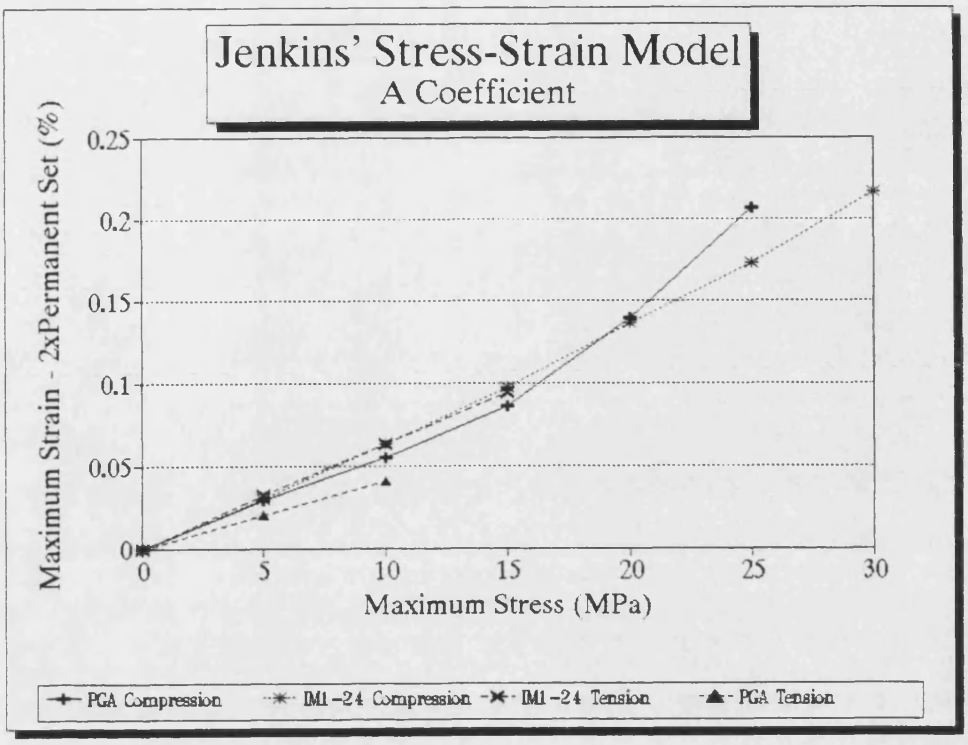

FIGURE 7.4 : The maximum strain minus twice the permanent set (ε_m-$2\varepsilon_0$) versus the maximum stress (σ_m) on each stress cycle for PGA and IM1-24 in tension and compression.

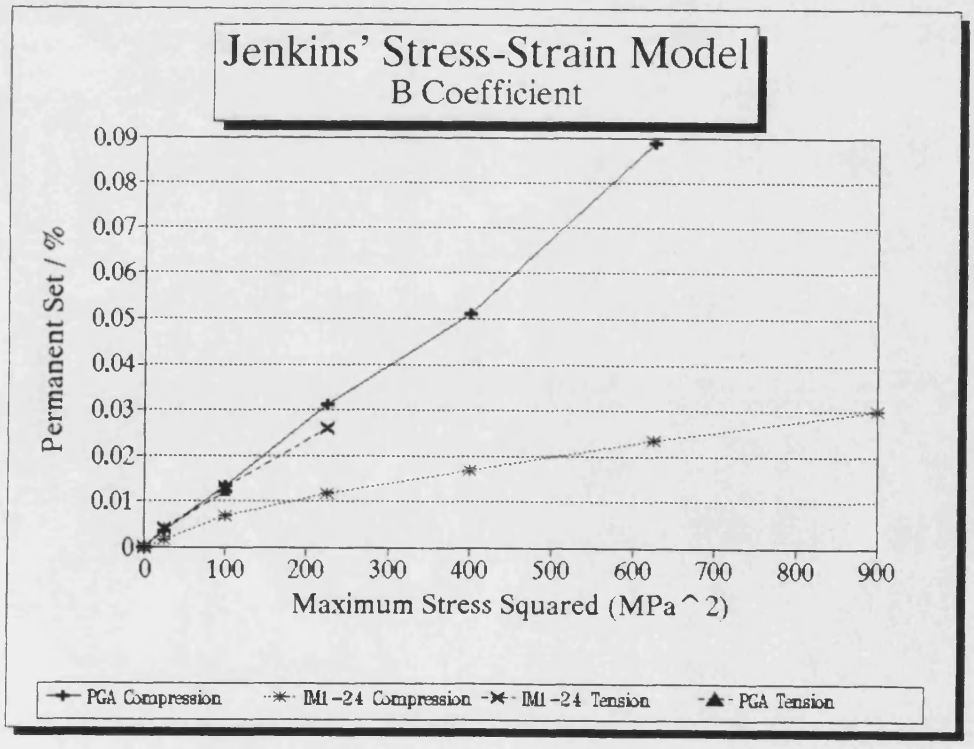

FIGURE 7.5 : The permanent set (ε_0) versus the square of the maximum stress (σ_m^2) on each stress cycle for PGA and IM1-24 in tension and compression.

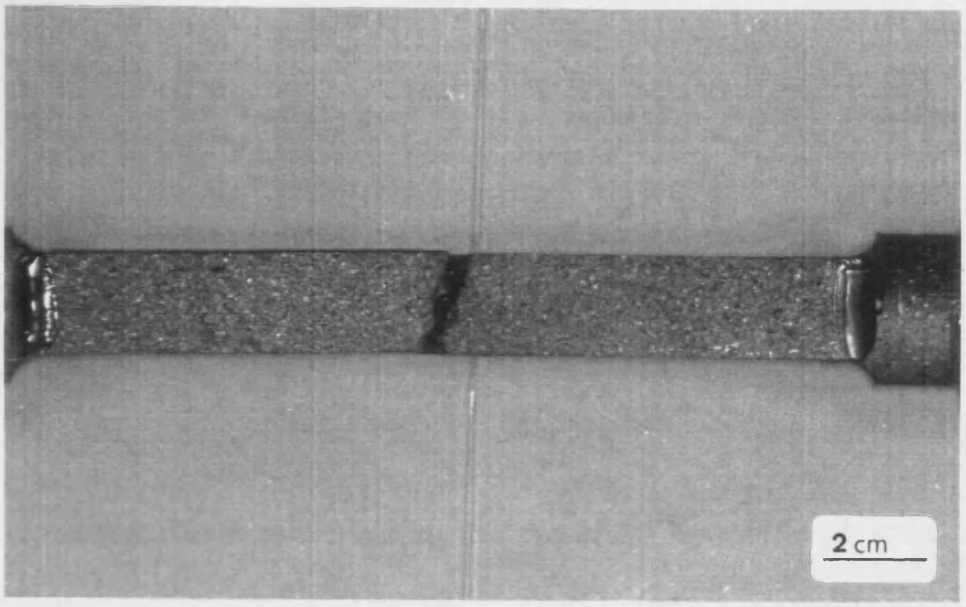

FIGURE 7.6 (a) : A typical tensile failure specimen of PGA graphites.

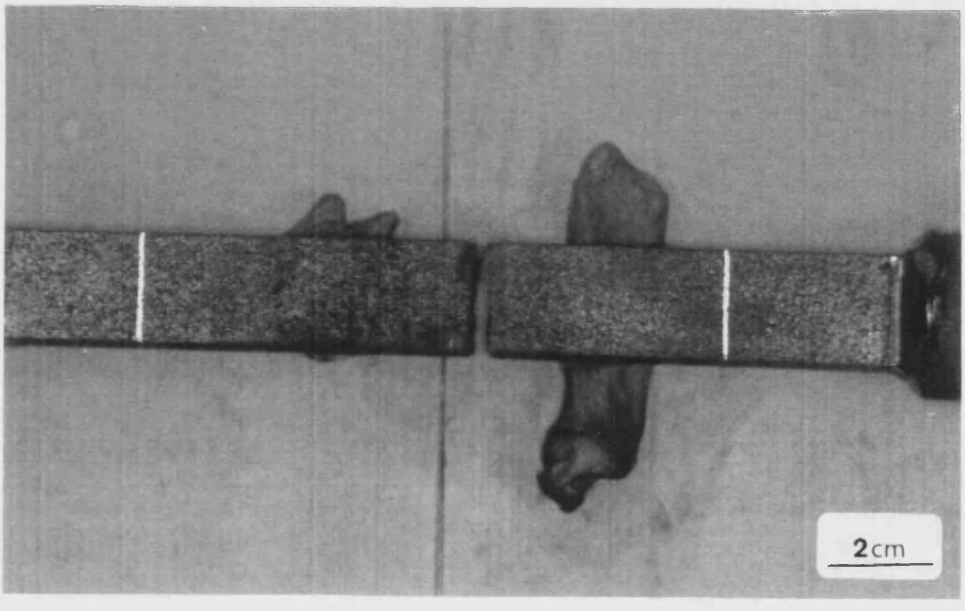

FIGURE 7.6 (b) : A typical tensile failure specimen of IM1-24 graphite.

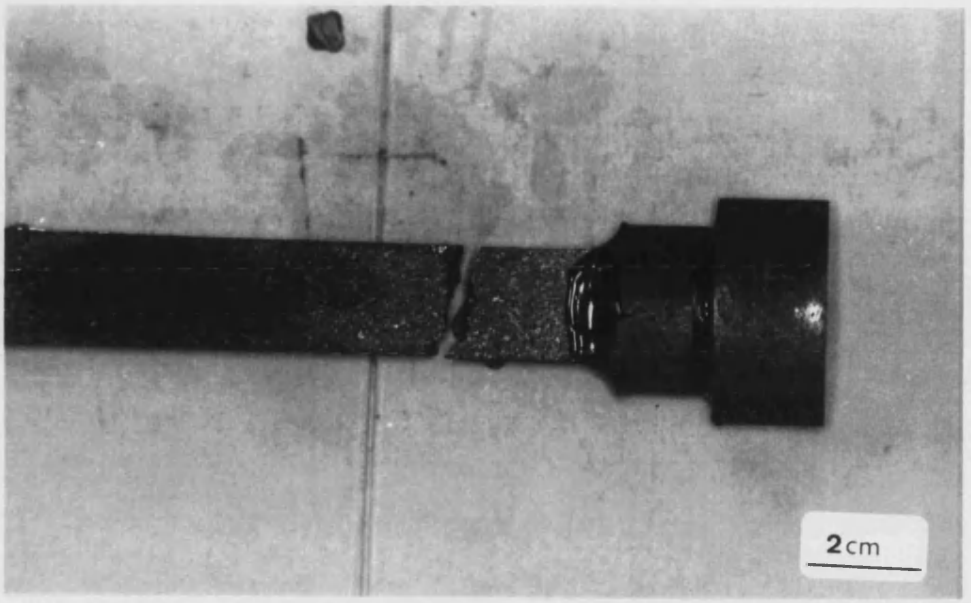

FIGURE 7.6 (c) : A typical tensile failure specimen of VNEC graphite.

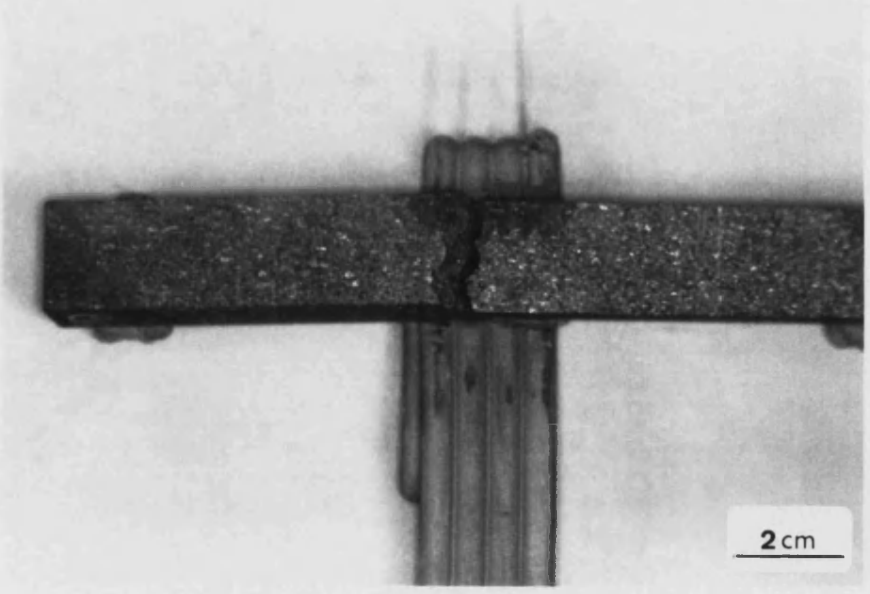

FIGURE 7.7 (a) : A typical flexural failure specimen of PGA graphite.

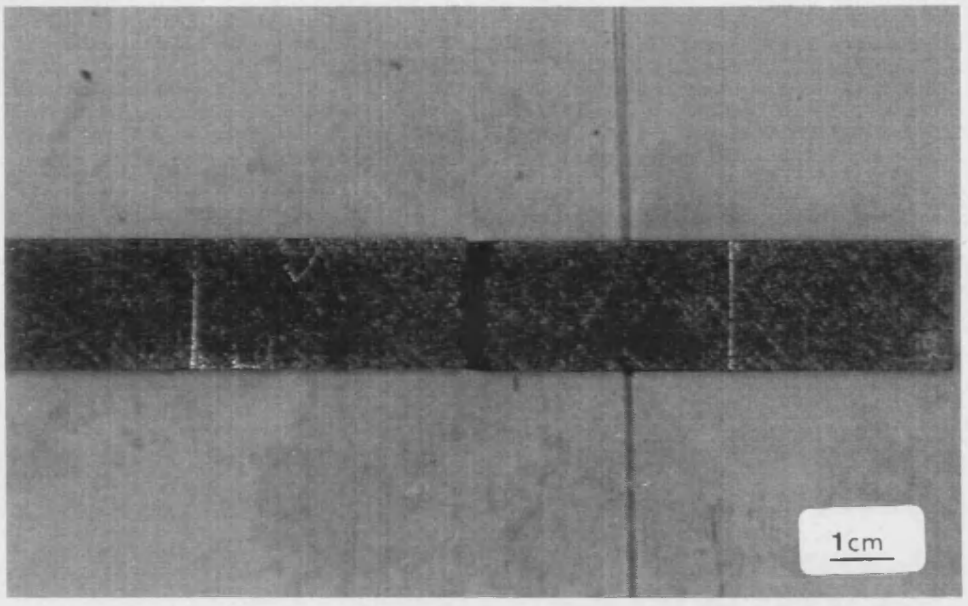

FIGURE 7.7 (b) : A typical flexural failure specimen of IM1-24 graphite.

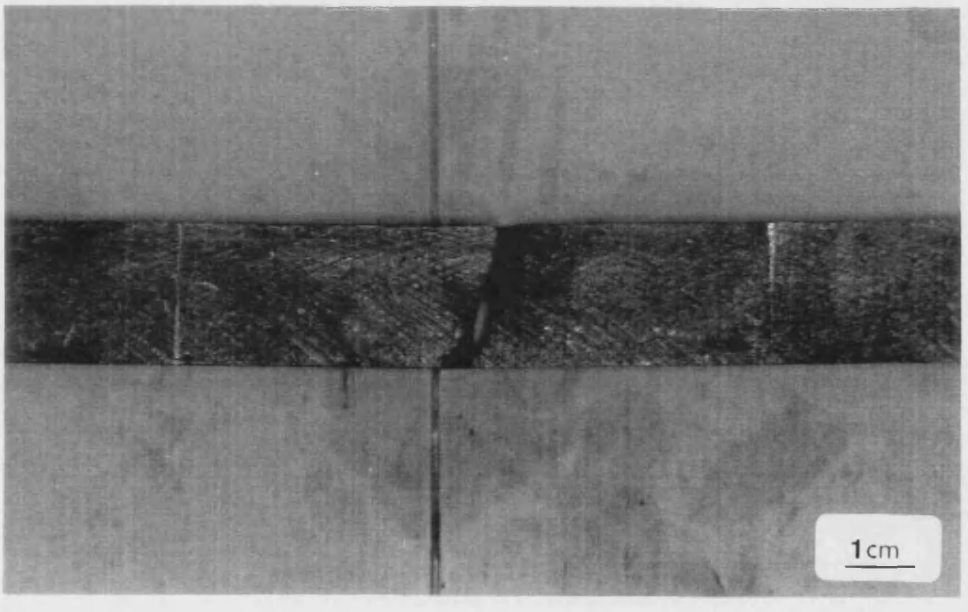

FIGURE 7.7 (c) : A typical flexural failure specimen of VNEC graphite.

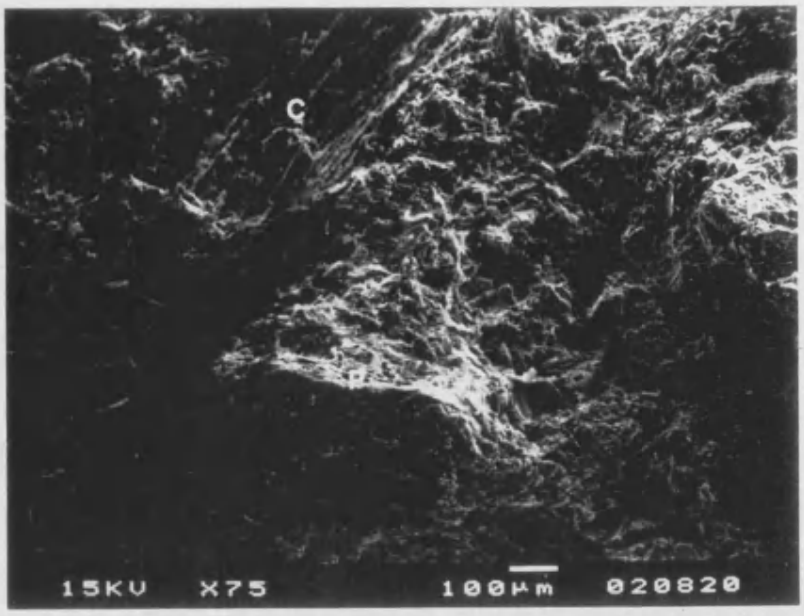

FIGURE 7.8 : A SEM micrograph of a typical PGA tensile fracture surface (C - cleaved filler particle, P - protruding filler particle)

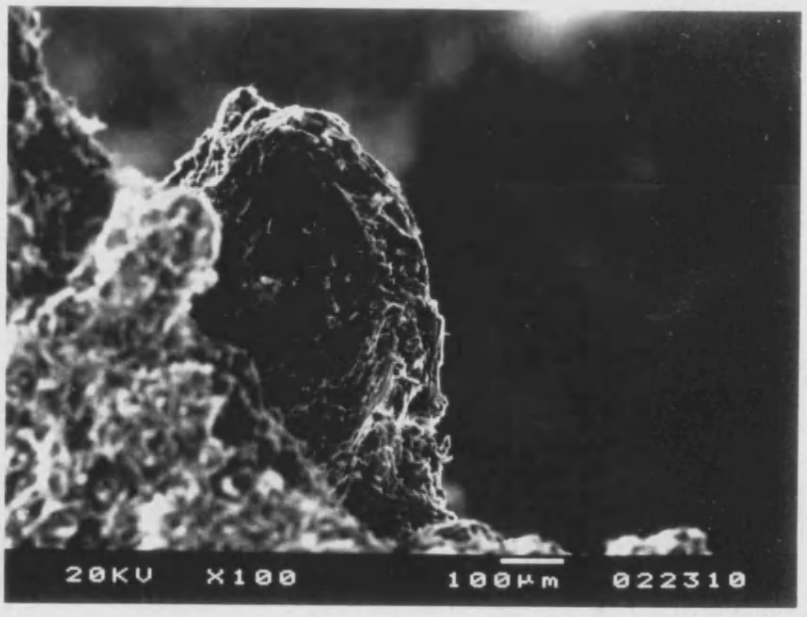

FIGURE 7.9 : A SEM micrograph of a typical PGA tensile fracture surface (taken normal to the fracture surface) of a protruding filler particle.

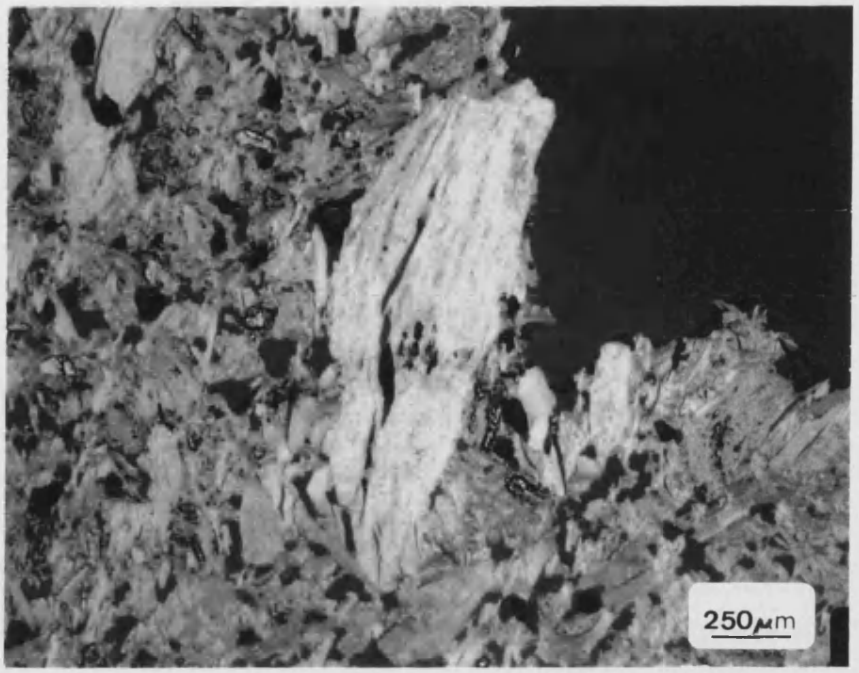

FIGURE 7.10 : An optical micrograph of a cross-section of a PGA tensile fracture surface cut parallel to the extrusion direction illustrating the effect a filler particle can have on the crack path.

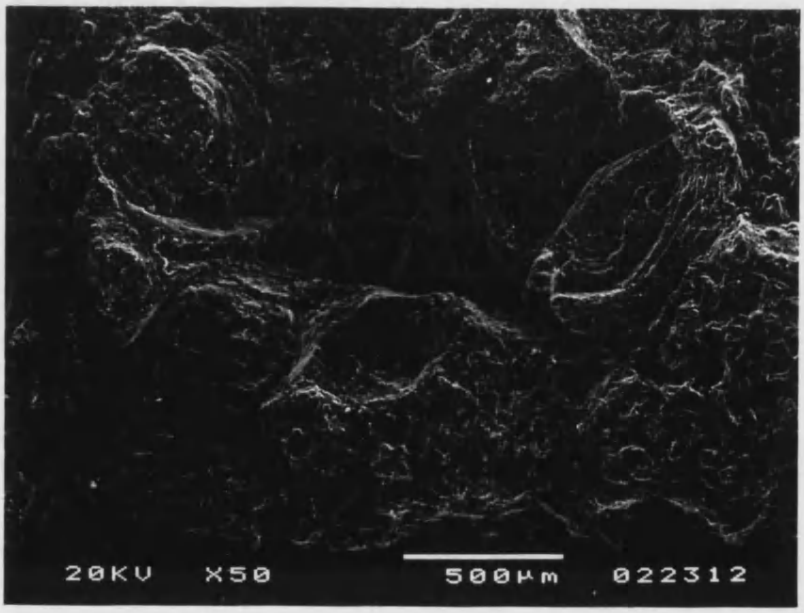

FIGURE 7.11 : A SEM micrograph of a typical tensile fracture surface for IM1-24 showing the apparent "cusps" and "domes" created by the Gilsocarbon filler particles.

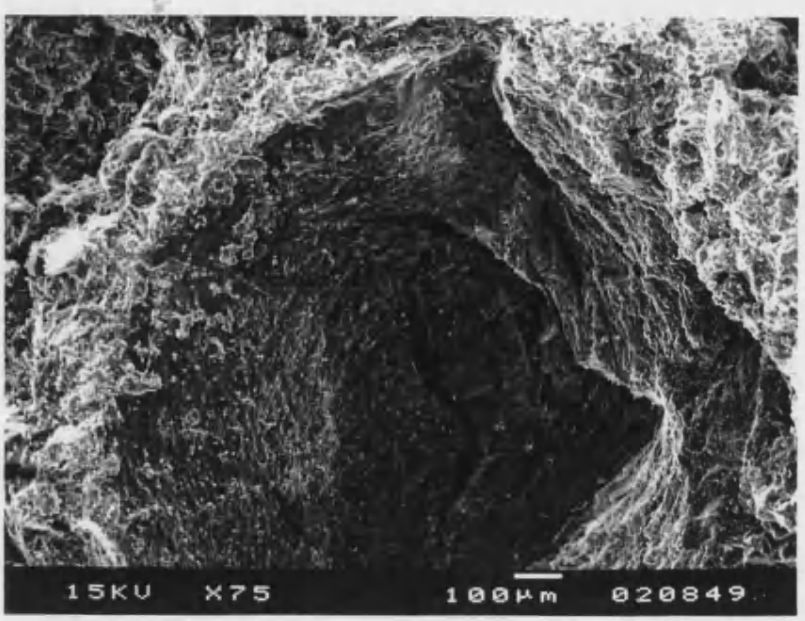

FIGURE 7.12 : A SEM micrograph of a tensile fracture surface for IM1-24 showing a split Gilsocarbon particle.

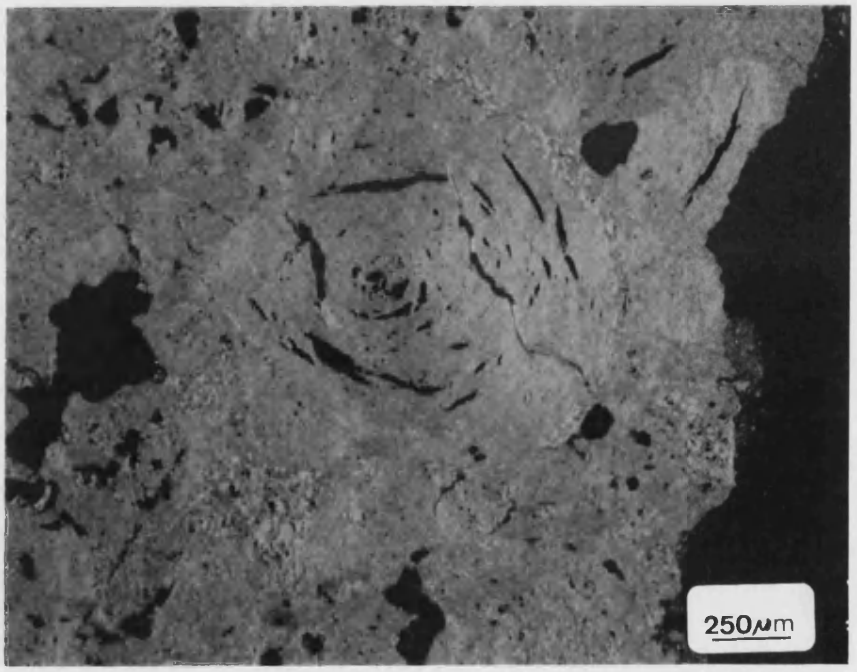

FIGURE 7.13 : An optical micrograph of a cross-section of a tensile fracture surface for IM1-24 showing fine cracks (F) on either side of an inherent calcination crack.

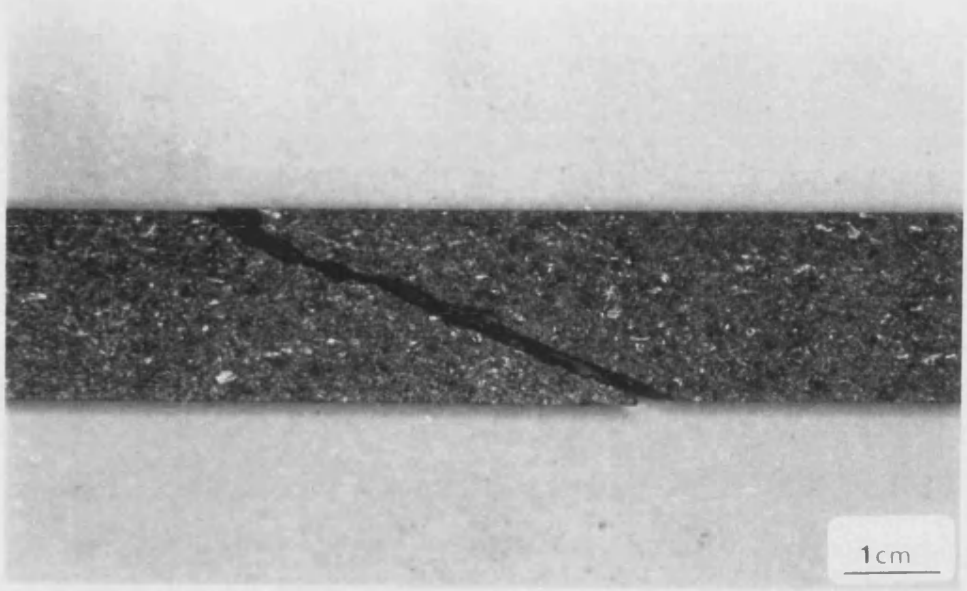

FIGURE 7.14 (a) : A typical compressive failure specimen of PGA graphite.

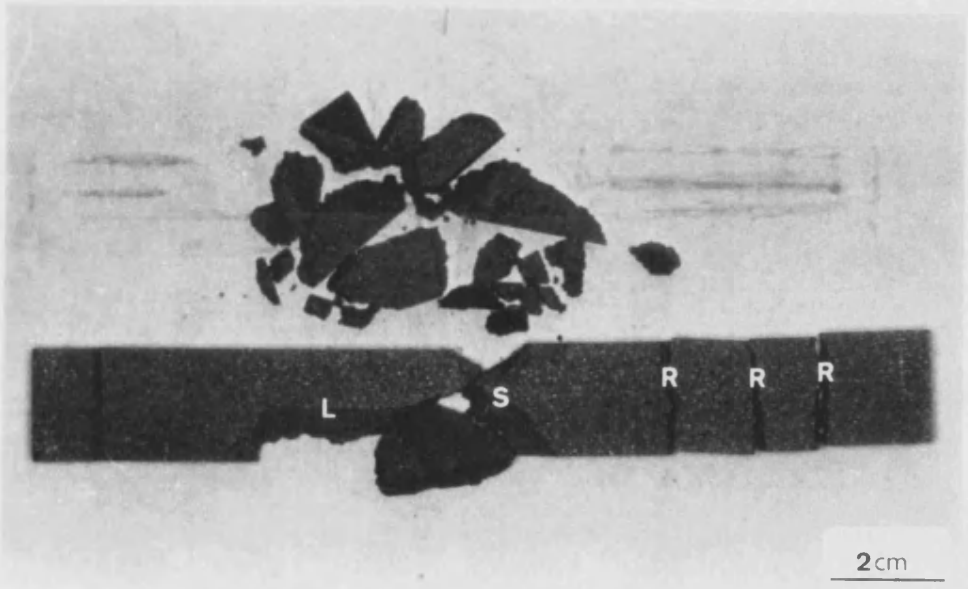

FIGURE 7.14 (b) : A typical compressive failure specimen of IM1-24 graphite (R - recoil tensile fracture; L - lateral tensile strain fracture; and S - shear fracture).

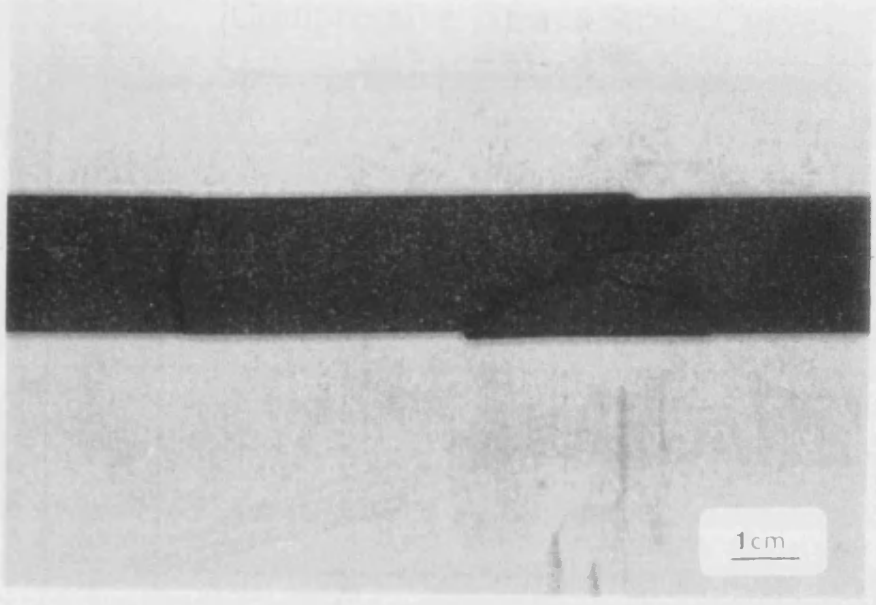

FIGURE 7.14 (c) : A typical compressive failure specimen of VNEC graphite.

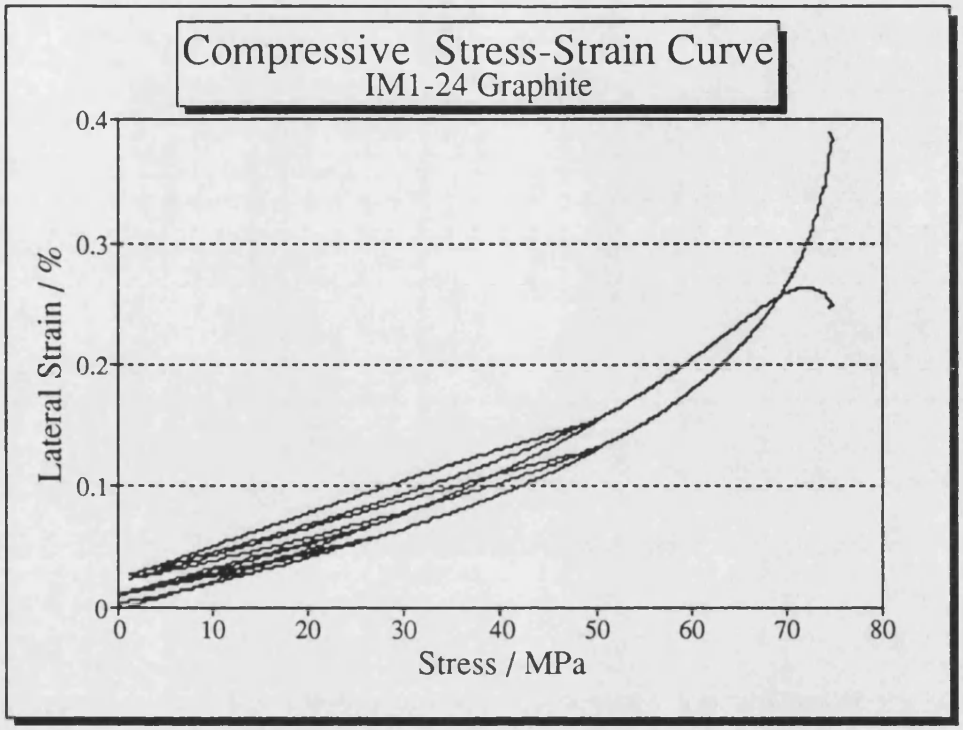

FIGURE 7.15 : A lateral strain versus applied stress curve for IM1-24 in compression.

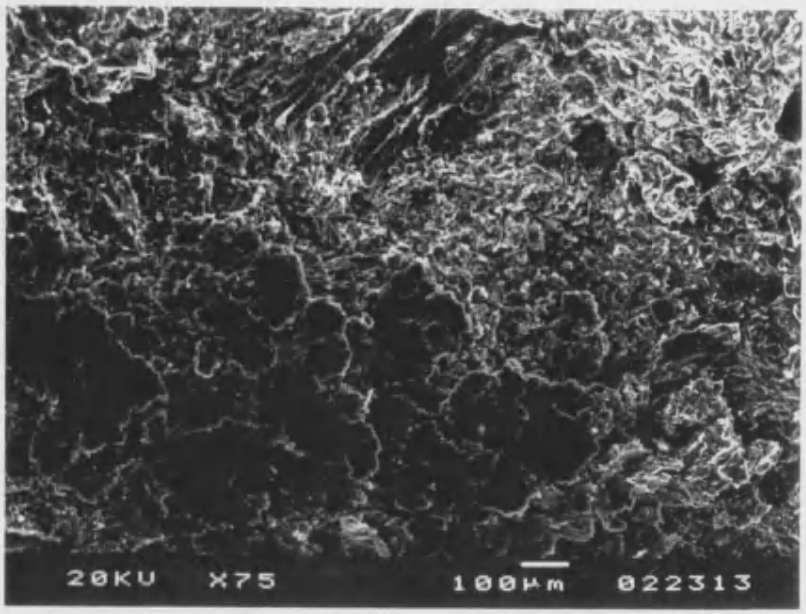

FIGURE 7.16 : A SEM micrograph of a compressive fracture surface of PGA showing the crushed shear zone of intense microcracking.

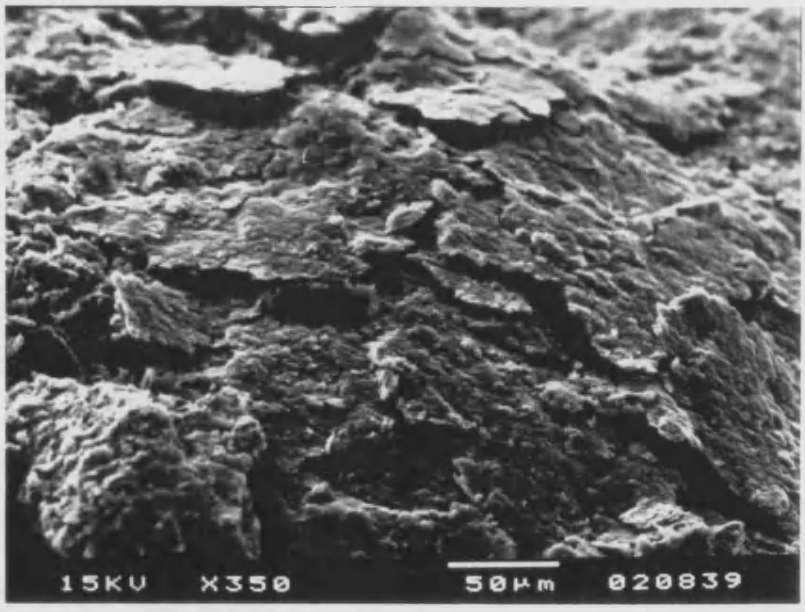

FIGURE 7.17 : A SEM micrograph of a compressive fracture surface of IM1-24 showing the appearance of "corn flakes" forming the crushed shear zone of intense microcracking.

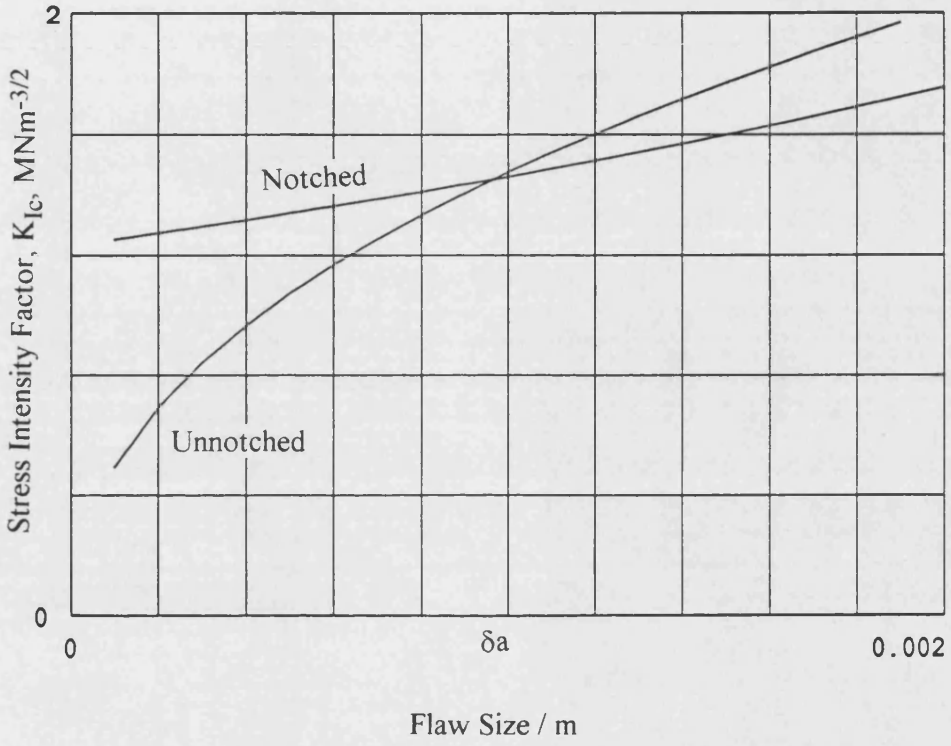

FIGURE 7.18 : A typical example of the stress intensity factor for notched and unnotched beams versus increasing notch size, a, for IM1-24 (δa is the inherent flaw size and the intercept of the two curves).

FIGURE 7.19 : A plot of the mean mechanical properties for six nuclear graphites.

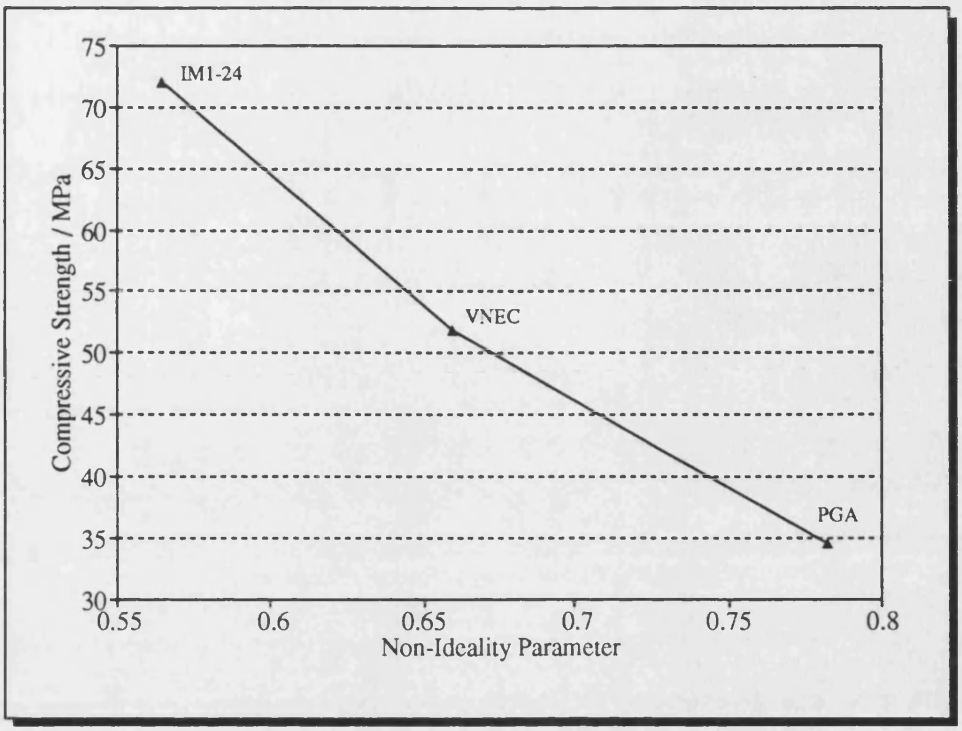

FIGURE 7.20 : A plot of compressive strength versus non-ideality parameter for PGA, IM1-24 and VNEC nuclear graphites.

Part C : Acoustic Emission From Nuclear Graphites

CHAPTER EIGHT : A REVIEW OF ACOUSTIC EMISSION

8.1 Acoustic Emission

This chapter presents a brief review of acoustic emission and a summary of published studies of acoustic emission from polycrystalline graphites. Acoustic Emission (AE) results from transient elastic waves which are generated by rapid bursts of energy from localised sources, such as rupture or dislocation movement of atomic planes, within a stressed material (Green, 1987 & ASTM E610-82). AE is created when a fraction of the kinetic energy of the propagating crack is transmitted into the bulk of the solid in the form of stress waves (Birchon, 1976 & Swindlehurst and Wilshaw, 1976). Nichols (1976) describes sources of AE as microdynamical deformation processes such as slip, shear, cleavage, microcracking, twinning, martensitic phase transformations, dislocation break-away from pinning points and vacancy coalescence. The material, deformation mode and AE instrument parameters determines the measured AE response. AE is non-directional and most AE generating processes act as point source emitters, radiating acoustic energy in spherical wavefronts.

Early observations of AE were made by tinsmiths who noted the "cry of tin", the sound emitted during twinning deformation (Drouillard, 1979). The earliest use of AE probably occurred in seismology, with the characterisation of earthquakes in terms of energy released, location and depth (ASTM STP 505, 1972 and Nichols, 1976). Joseph Kaiser (1950) conducted the first serious investigation of AE from stressed materials; he observed AE from polycrystalline specimens of zinc, steel, aluminium, copper and lead, and he concluded that grain boundary sliding was the source of the AE. Kaiser also observed that no further AE was produced upon reloading a specimen until the previous maximum load had been exceeded, and therefore suggested that AE was irreversible in those polycrystalline metals. This phenomenon is now called the Kaiser effect (ASTM E610-82).

Drouillard (1979) lists all AE publications up to 1978. Surveys of AE by Ying (1973), Stone and Dingwell (1977) and Scott (1991) describe AE for a wide range of materials and include suggested mechanisms of AE generation, experimental techniques and applications; all concluded that AE is a useful technique for evaluating materials and structures, and is of help in understanding the dynamics of deformation in solids. Ying (1973) suggested for ceramic materials that the sudden increase of AE counts might imply or relate to the creation or propagation of microcracks. In general, all these reviews concentrate on AE from metals and composites, ceramic and graphite materials receiving little attention.

Bartle (1974) at an early stage of the development of AE testing techniques emphasised the need to standardise experimental procedures and assessment techniques in order to ensure reproducibility of results. The areas of possible standardisation include transducer coupling and response, amplifier gains, trigger levels, signal processing and attenuation of AE. Birchon (1976) reviews the potential of AE in non-destructive testing and outlines the partition process leading to the creation, propagation and attenuation of stress waves in AE testing. He further describes the sensitivity of the technique and quotes a humorous law of AE: "Because it was not heard, it does not mean it did not happen!".

The AE signal consists of discrete wave packets, similar to damped sinusoidal waves, which are termed AE events. The AE technique provides various ways to characterise each AE event. An idealised AE event signal, Figure 8.1, shows the definitions of various terms. The start and finish of an AE event is determined by the electronic threshold of the AE instrument: the time between the start and finish of an event is the event duration. The start of a new event occurs only after a period of inactivity, *i.e.* a deadtime (further described in Chapter Nine). The rise-time of an event is the time from the first crossing of threshold to the peak amplitude. Each AE event consists of a

number of ringdown counts, each count corresponding to a crossing of the threshold. In general, the AE signal can manifest itself in two forms; continuous or burst emission associated with plastic and brittle materials, respectively (Nakasa, 1973). Continuous emission may be considered as low level burst emission at a high rate. Often the two types of AE are mixed, *i.e.* AE high level bursts within a continuous AE background. Figure 8.2 presents examples of burst and continuous wave emission captured from stressed graphite using the AE system described in Chapter Nine.

The waveform obtained by AE equipment has been shown to be substantially modified from that at the source of the AE. It is important to note that the analysed AE waveform is an electrical response resulting from the excitation of the piezoelectric crystal within the AE transducer by the stress wave, and therefore highly sensitive to experimental conditions. The AE response will depend mainly on four factors; (i) the material; (ii) the nature of the deformation process; (iii) local stresses at the defect; and (iv) the environment. Modifications occur during the propagation of the AE wave through the specimen and the transducer due to discontinuities or from reflections at free surfaces. For these reasons, AE testing of different specimens must be done under comparable conditions, and use of different AE systems to compare similar responses must be treated with extreme caution.

Pollock (1973) used a simple spring-mass model to represent the generation of a failure event by an instantaneous reduction in the stiffness of one of the springs. He examined the kinetic energy available in the vibrations of the remaining spring system, and, assuming that it was this energy that was available for conversion to acoustic energy, he concluded that the energy liberated as AE is not a fixed proportion of the released strain energy, but rises in proportion to the magnitude of the source event. Stone and Dingwell (1977) suggested that this model shows the stress wave generated by an event contains two different types of energy; (i) a high level short term energy packet due to the event itself, and (ii) a lower level, longer term supply of energy

emanating from the decaying oscillation of the nearby material.

Examination of the relative number of AE events at different amplitude levels can provide a useful method of distinguishing between individual failure mechanisms. Pollock (1973) formulated an empirical power law based on experimental data for the distribution of the AE peak amplitudes, a, of the form

$$n(a)=(a/a_0)^{-b} \qquad (8.1)$$

where n(a) defines the fraction of the emission population whose peak amplitude exceeds a, a_0 is the lowest detectable amplitude and the exponent b is used to characterise the amplitude distribution. He showed, using the exponent b, that the amplitude distributions depend on the material and deformation mechanisms. The exponent b was usually found to lie between 0.4 and 2 for most materials studied. If a deformation process proceeds by generating a large proportion of high amplitude events, then the value of b is small, but if there is a large proportion of small amplitude events then the exponent b is large.

AE responses of some materials subjected to cyclic loading exhibit the Felicity effect (ASTM E-7 Proposal P199), which is a deviation from the classic Kaiser effect, where, upon cyclic loading, some AE occurs before the previous peak stress is reached. The Felicity effect is used in the AE examination of reinforced thermosetting resin pipe (ASTM E1118-86) and fiberglass reinforced plastic resin tanks and vessels (ASTM E1067-85).

8.2 Acoustic Emission From Synthetic Graphites

The first report of AE from polycrystalline graphites came inadvertently from Andrews *et al.* (1960) while investigating the stress-strain relationship for cyclic loading of a

reactor graphite. They reported hearing a "cracking noise" during initial stressing, no noise during unloading and no noise during re-stressing until the previous stress was exceeded, *i.e.* a Kaiser effect was observed in the aural frequency range. Gilchrist and Wells (1969) monitored AE from compressive testing of two graphites. For an isotropic graphite, no AE was detected until near the failure stress, whereas for an anisotropic graphite, AE was detected long before failure. On stress cycling the anisotropic graphite to increasing stress levels, AE only re-occurred after the previous peak stress was exceeded, *i.e.* a Kaiser effect was found. The authors believed that this indicated that the noises are caused by non-conservative processes, either cracking or plastic deformation. They also observed two groups of noises of large and small amplitudes. They attributed large amplitude noises to the propagating crack and the small amplitude noises to either microcracking or closure of pores.

Kraus and Semmler (1978) observed AE from industrial polygranular carbons and graphites subjected to mechanical stresses (tensile and flexural) and thermal stresses. On stress cycling to increasing loads, AE was only detected when the previous peak stress was exceeded, *i.e.* a Kaiser effect was found. They noted that after considerable time or after heat treatment, a relaxation effect would cause AE during the first new load cycles below the previous peak stress. During heat treatment of the baked material up to 2500 °C, AE could be observed in the temperature range 1400-1700 °C due to the formation and evolution of sulphur compounds which create microporosity ("sulphur puffing"). On cooling a graphitised body, strong AE was observed in the temperature range 2200-1500 °C. Although Kraus and Semmler offered no explanation for this phenomenon, it may be due to the formation of Mrozowski cracks.

Burchell *et al.* (1985) and Burchell (1986) investigated the AE response from six industrial graphites subjected to monotonic flexural loading to failure. For each graphite, except PGA, at the onset of stress, the cumulative AE event count increased rapidly as the failure stress was approached. For PGA, from 50% of the failure stress,

the rate of cumulative AE event count with increasing stress gradually decreased; no explanation was given for this response. They showed the AE response was characteristic of graphite type and microstructure (i) by comparison of the filler particle size to the cumulative AE event count at failure, and (ii) by showing that the AE response curve is related to the deviation from linearity of the stress-deflection curve. Coarse-grained materials undergo a greater degree of subcritical cracking and generally emitted more AE, and had more marked curvature of the stress-deflection curve than fine-grained graphites. For the six graphites they attempted to fit the Pollock power law to their data, but in an incorrect form:-

$$m(a) = (a/a_0)^{-b'} \qquad (8.2)$$

where m(a) is the fraction of events in the emission population in each amplitude level. Interestingly, they found that their data fitted this equation quite well. They also found that the exponent b' increased with grain size, *i.e.*, the proportion of small amplitude events increased with grain size. They also found that b' value decreased with increasing load, indicating a greater proportion of high energy events at higher loads. They postulated that small amplitude AE events are mainly generated from cleavage of favourably oriented basal planes within domain structure, and the extension of cracks into the binder result increasing proportion of larger amplitude AE events with increasing stress.

This is supported by Youfa Yin *et al.* (1991) in AE studies on an electro-thermic graphite where a high cumulative AE event count in this coarse-textured graphite is attributed to basal plane cleavage and extensive micro-cracking in a large process zone. They also found that porosity, flexural strength and elastic modulus varied with radial position within the extruded graphite log, but there was no significant variation in the cumulative AE event count with radial position.

Burchell *et al.* (1986b) compared the AE response from unirradiated, fuel sleeve (pitchcoke) graphite to twelve specimens of a similar irradiated graphite when subjected to monotonic loading to failure in three point bend tests. They also examined three other unirradiated graphites. In all cases, the onset of AE was from zero stress. As-received, irradiated specimens showed a near-linear AE response with increasing stress, whereas annealed, irradiated specimens showed a rapidly increasing AE response. These results support earlier observations linking the AE response to non-linear stress-strain behaviour. For irradiated graphites, as with earlier findings for unirradiated graphites, the proportion of higher amplitude events and the cumulative number of AE events at failure both increase with mean particle size, whilst the mean flexural strength decreases with increasing particle size. Half of the irradiated specimens were annealed before testing. The as-received, irradiated specimens were much stronger than similar unirradiated specimens, but they did not show a significantly different AE event count at failure. Overall, the as-received, irradiated specimens showed a greater strength, but a smaller AE event count at failure when compared to the annealed specimens. These effects were attributed to defects acting as pinning points for dislocations caused by neutron irradiation. The annealed specimens had lower strength compared to the unirradiated specimens, due to increased porosity following radiolytic oxidation. For the annealed specimens there was an increase in the cumulative AE event count at failure compared to the as-received material; this highlights the effect of porosity on AE event counts.

Ioka *et al.* (1986) and Ioka and Yoda (1987) examined the AE from tension and compression stress cycling of IG-11 polycrystalline graphite. They found AE on unloading which was attributed to reverse plastic deformation as suggested by Jenkins' model of deformation (Jenkins, 1962, see Chapter Three). They monitored the AE as a RMS voltage signal after amplification, and did not consider other AE parameters, *e.g.* event counts. They observed both continuous and burst emissions, which were attributed to basal plane slip and sub-critical fracture, respectively. During re-loading

of IG-11 graphite specimens, they showed that the RMS voltage slowly increased, until the applied stress exceeded the maximum stress of the previous loading, when the RMS voltage then rapidly increased (Figure 8.3). However, they made no attempt to explain the change in slope. From this they concluded that there is no Kaiser effect in polycrystalline graphites.

Ioka and Yoda (1987) presented a bicrystal model of two adjacent filler particles adjoined by binder to explain their results. They consider the first particle to have its basal planes parallel to the uniaxial compressive load, and that the second particle's basal planes are oriented at an angle to the load axis (see Figure 8.4). They suggested that when a load is applied, the first particle will experience a purely elastic stress, but the second will experience an elasto-plastic stress. Therefore back-stresses will be generated in the filler particle with pure elastic strain, and which will lead to reversed plastic deformation upon unloading in the second particle. It is this second particle that will generate AE on re-loading. They concluded that in both tension and compression, polycrystalline graphite undergoes reversible plastic deformation, and therefore the Kaiser effect does not occur.

Ioka *et al.* (1990a) examined the compressive deformation of an unirradiated, isotropic, nuclear graphite, IG-11, by examining the acoustic emission RMS voltage. The RMS voltage of AE is usually used to study continuous-type AE which results mainly from the movement of dislocations. They observed that continuous-type AE under compressive loading gradually increased to a certain strain level (typically 40% of failure strain) and then decreased for further loading, with burst emissions over the whole range (Figure 8.5 (a)). They offered no explanation for this effect, except that it represented slip deformation, but it may be suggested that the decrease in RMS voltage is due to the pinning of shearing crystallites. On re-loading a specimen they hardly observed any burst emission. However, re-loading an annealed specimen gave a similar response but with a reduced burst emission count compared to an as-received

specimen (Figure 8.5 (b)). Ioka *et al.* also examined the RMS voltage signal for specimens with a 7% weight loss following thermal oxidation. At no point did the RMS voltage signal decrease with increasing strain. The monotonically increasing RMS signal indicates that slip of particles is no longer being restricted by the binder, which apparently preferentially oxidises. They concluded that burst emission did not affect the RMS signal and was due to microcracking in the graphite under external loading and may be detected using AE event counting techniques.

Ioka *et al.* (1990b) examined the AE caused by microfracture from annealed, unirradiated graphite specimens after pre-stress for four isotropic graphites loaded in tension and compression using event counting techniques. For an as-received sample in tension and compression, they first recorded AE activity at around 25% and 20% of the fracture stress, respectively, possibly indicating that the threshold for detecting AE was too high. They implied that their AE measurements did not detect slip deformation, but that it can be detected using an RMS voltage method (Ioka *et al.*, 1990a). The authors suggested that microfracture within graphite can be divided into cleavage between basal planes within grains and binder fracture. They assumed basal plane cleavage consumes less energy than binder fracture, due to the weak van der Waals interplanar bonding. Consequently, they attributed low and high energy events to basal plane cleavage within grains and binder fracture, respectively. They pre-stressed a specimen in tension and compression to 90% of the fracture stress and then reloaded it while monitoring the AE. After unloading, the same specimens were annealed and reloaded to the same stress. From a comparison of both AE relative energy distributions they observed little AE after pre-stressing, but significantly more AE after annealing. In addition to recovery of slip deformation from heat treatment they also attributed the reoccurrence of AE to recovery of cleavage between basal planes in grains in both tension and compression.

Ioka *et al.* (1990a & 1990b) proposed a deformation mechanism in tension for

polycrystalline graphite. The basal planes of filler grains oriented at 45° to the applied stress will deform plastically at a small stress and this plastic deformation may be detected by an increase in RMS voltage. The number of filler particles that deform plastically will increase with increasing stress, and at high loads, shearing of the binder region will occur. In the case of filler particles oriented perpendicular to the loading axis, cleavage between basal planes is expected to occur easily, but propagation will be opposed by the binder until high loads are applied. The combination of these cracks will eventually lead to ultimate failure. In compression, a similar mechanism is proposed, but the slip in the filler grains is opposed by the binder region at low stresses. They proposed that with increasing loads, cleavage within basal planes would occur most easily in the filler grains whose basal planes are parallel to the loading axis, due to resolved tensile stresses perpendicular to the basal plane.

Oakden and Cotton (1988) investigated the AE responses after performing two series of tests on a near-isotropic Gilsocarbon graphite, grade GCMB: (i) three point cyclic loading with increasing loads in steps of 2 MPa to failure, and (ii) reverse three point bend tests, following a similar pattern as the first series, except the specimen was turned over so that the loading direction was reversed in the next cycle. In addition, they also performed a number of cyclic tensile and compressive tests. All experiments showed the rate of AE to increase with applied stress. They stated that their results from the first series of tests exhibited the Kaiser effect, but there were AE events before the previous peak stress. It appears that they used a less rigid definition, *i.e.* the Kaiser effect occurred if there is a sudden large increase in the rate of AE. They estimated the previous peak stress by extrapolating back along the linear part of the AE curve to the stress axis. The second series of results from reverse bend tests did not clearly show the Kaiser effect at low stresses, but a Kaiser effect became more distinct at higher stresses. Their investigation revealed two types of AE event. A plot of log (ringdowns in each event) versus amplitude showed two groups, named type I and II events. Type I events were found to have short rise times, few ringdowns and

relatively high amplitude and were common to all tests. Type II events were more varied but were generally longer in duration, had longer rise times and more ringdowns and generally only found in reverse bend tests. Although the authors suggested type I events occurred before type II, no explanation was given for the origin of these different events, nor why reverse bend tests should have two types of AE event.

Previous AE studies of stressed polycrystalline graphites have been shown to be unsatisfactory, especially those using cyclic loading. Most authors have only considered evidence from a limited number of specimens and therefore it is not surprising that so much confusion and conflicting evidence has been presented regarding the Kaiser effect. No study has recognised the possibility of the Felicity effect in polycrystalline graphites. This review has clearly demonstrated the need for a sound, statistically-based study of AE from nuclear graphites in order to assess if AE monitoring of trepanned specimens may offer a potential method to determine residual stresses in the graphite moderator core. The work presented in this thesis attempts to provide a definitive study of AE responses from nuclear graphites subjected to cyclic stresses, and to characterise quantitatively the AE response.

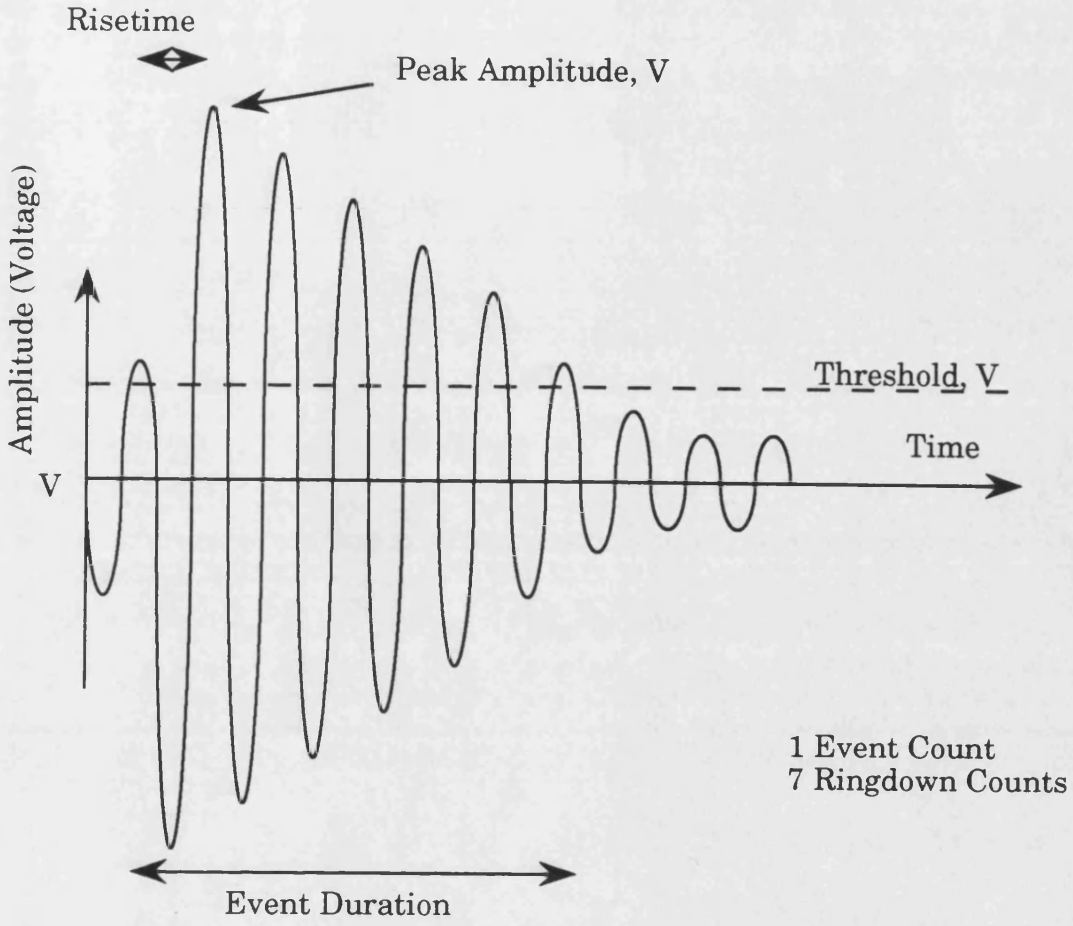

FIGURE 8.1 : An idealised AE event signal showing the definitions of various terms.

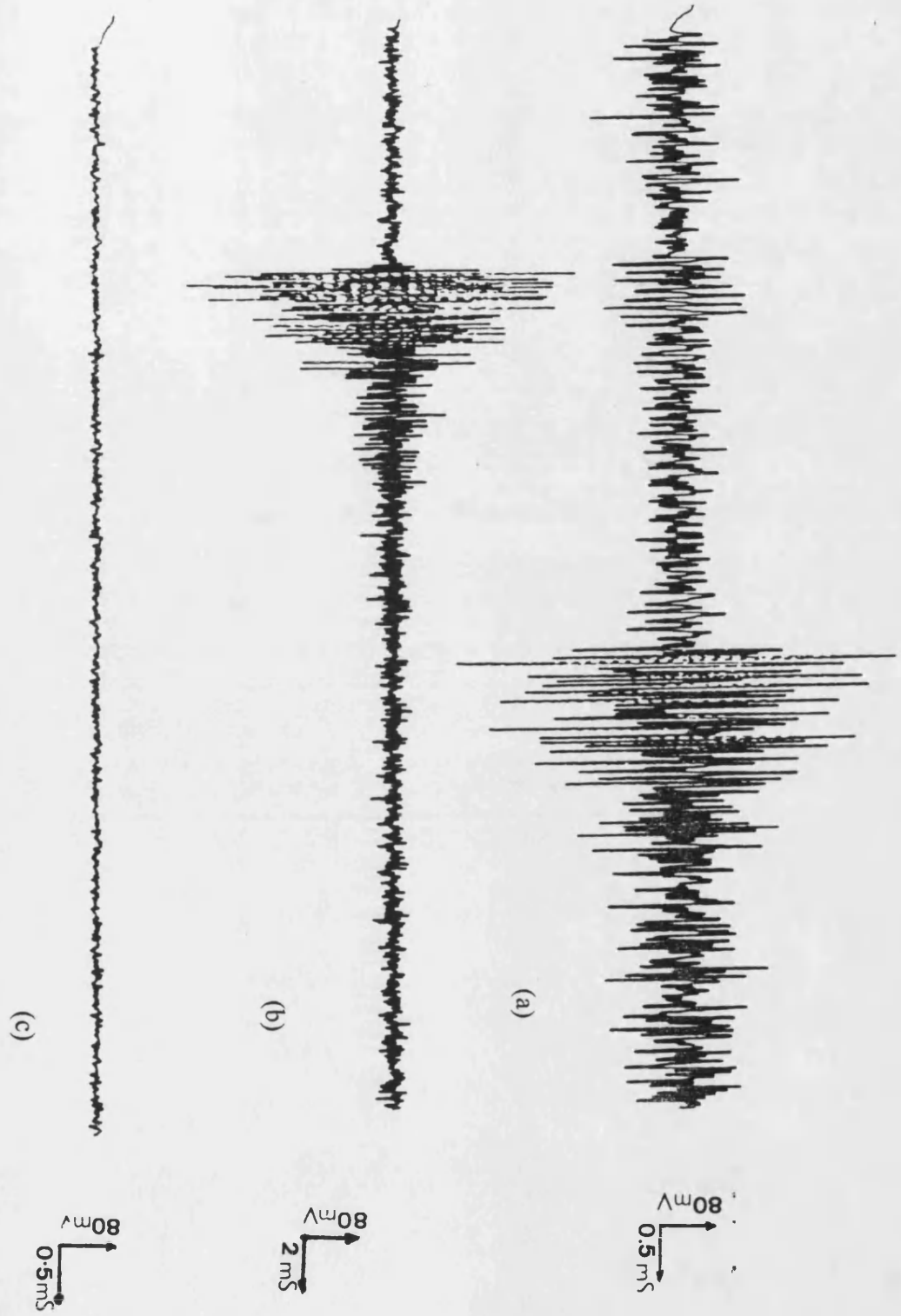

FIGURE 8.2 : Examples of burst and continuous wave emission captured from a stressed graphite sample: (a) continuous emission, (b) burst emission, and (c) background trace.

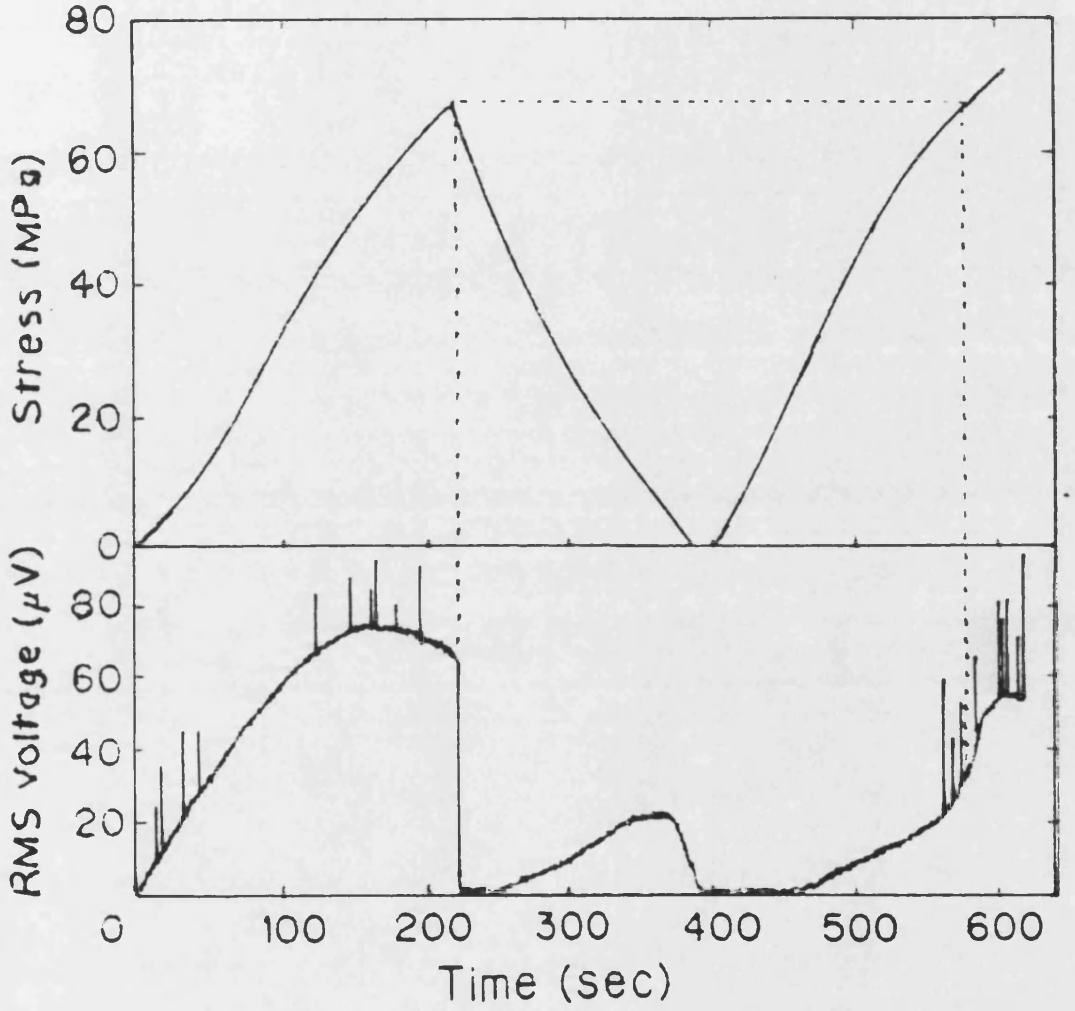

FIGURE 8.3 : A RMS voltage-time AE response for IG-11 graphite (Ioka and Yoda, 1987) showing the presence of continuous and burst emission on loading, continuous on unloading, and continuous only until the pre-stress value on re-loading.

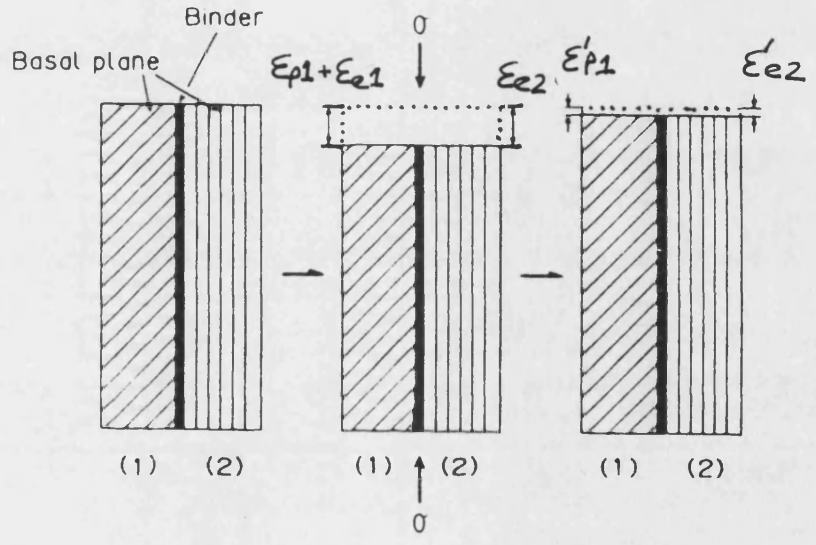

FIGURE 8.4 : Ioka and Yoda (1987) bicrystal model to describe the reversed plastic deformation behaviour of a polycrystalline graphite.

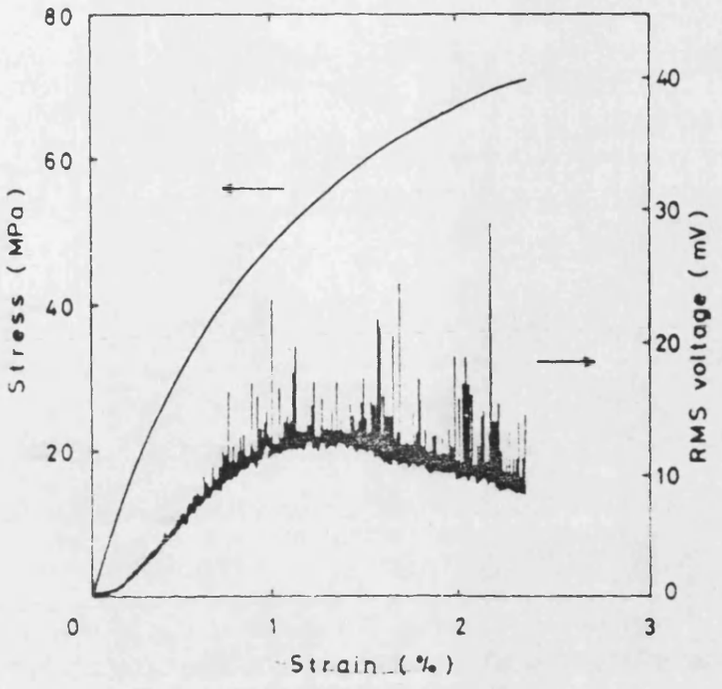

FIGURE 8.5 : Examples of stress-strain and AE RMS voltage-strain curves for IG-11 graphite under compressive loading for (a) as-received sample, and (b) for an annealed sample (at 1872 K) after a pre-stress of 90% of compressive strength (Ioka *et al.*, 1990a).

CHAPTER NINE : ACOUSTIC EMISSION EXPERIMENTAL SYSTEMS AND DETAILS

9.1 Introduction

This chapter describes the AE systems used in this work. All AE work at the University of Bath presented in this thesis was done using the Marandy MR1004 AE system. For the work carried out at Berkeley Nuclear Laboratories (including that done on the irradiated material), both the Marandy AE system and the AECL system were used simultaneously. All data obtained from both systems were analysed in the same way.

All specimens except those used to measure work of fracture and curved beam specimens were tested using an Instron 1195 screw driven universal testing machine with a variable crosshead speed from 0.5 to 100 mm min^{-1}. The majority of testing was done with a 100 kN loadcell and chart recorder calibrated at 10 kN full scale deflection, and a chart speed of 10 mm min^{-1}. For all AE testing the crosshead speed was set at 0.5 mm min^{-1}. In tension, two uniaxial universal joints were used to eliminate misalignment and provide a true uniaxial load. In compression, two compression platens were used as prescribed in ASTM C695-81. Work of fracture specimens were tested using an Instron 1122 testing machine which is similar to the Instron 1195, but with a slower crosshead speed of 0.05 mm min^{-1}.

9.2 Specimen Geometry

Various geometries are used for mechanical tests in this work, depending on material availability and experimental aims. For the majority of experimental work, the specimen geometries are described below, for smaller experiments, the specimen details are given where appropriate. Where material has been machined from blocks,

moderator bricks or fuel sleeves, the material is assumed to be uniform throughout, *i.e.* each specimen has not been marked with its location within the graphite article.

9.2.1 AE Cyclic Testing Programme

Previously, other workers have used a rectangular beam (10 x 10 x 70 mm^3) for mechanical and AE testing of nuclear graphites, similar to the size obtainable from trepanning the moderator brick or that which can be cut from a fuel sleeve (Pickup, 1984; Rose, 1985; Burchell, 1986). In this work a decision was made to increase the size of specimens, so as (i) to allow a larger amount of AE events to be recorded, and (ii) to facilitate of coupling of the AE transducer to the specimen. Therefore the standard sample size used in this work was 20 x 20 x 150 mm^3, for the entire AE cyclic loading programme and for all loading modes.

An AE cyclic testing program was followed for three nuclear graphites, PGA, IM1-24 and VNEC. For IM1-24, specimens were cut from an unirradiated moderator brick (No. 30B8819) of size ~900 x 450 x 450 mm^3, which is identical to that used in the AGR. PGA specimens were cut from a large rectangular block of size ~915 x 200 x 200 mm^3, which is similar to that used as the moderator brick in the Magnox reactor. VNEC specimens were cut from an unirradiated cylindrical AGR fuel sleeve of length ~650 mm and diameter 105 mm. For PGA and VNEC, all specimens were cut with their longitudinal axis parallel to the extrusion direction (*i.e.* parallel to the length of the brick). All the specimens requisitioned for the AE program are listed in Table 9.1. All graphite specimens requisitioned from Berkeley Nuclear Laboratories were machined under clean conditions and the specified surface finish was 0.8 μm or better where grain structure permits.

Material	Specification (mm^3)	No. Requested	No. Required For Full Programme	No. Received
IM1-24	20x20x150	80	50	80
	25x20x150	0	0	32
	25x20x240	10	10	19
	25x20x120	10	10	19
	25x32x150	10	10	16
	Tensile	50	30	56
PGA	20x20x150	80	50	60
	Tensile	50	30	32
VNEC	20x20x150	80	50	27
	Tensile	50	30	15
Total		**420**	**270**	**356**

TABLE 9.1 : Initial Specimen Requisition From Berkeley Nuclear Laboratories

In addition to AE monitoring, tensile and compressive stress-strain data were also collected on selected samples, using strain gauges (type FLA-6-11, manufactured by Tokyo Sokki Kenkyujo Co., Ltd.) which were attached to the graphite surface using a polyester adhesive (P-2, supplied also by Tokyo Sokki Kenkyujo Co., Ltd.). The voltage signal from each strain gauge was directed to the Marandy AE analyser and amplified with a gain of 1000, before storage by the computer and conversion to %strain.

9.2.1 (a) Tensile Specimens

The tensile specimen and apparatus designed for AE testing in this project are shown in Figure 9.1 and 9.2, respectively. A square cross section on the AE tensile specimen was chosen, rather than circular cross-section as specified in ASTM C565-83, because (i) it allows a constant AE "active" volume for all mechanical tests, including compression and flexural tests; (ii) it is based on an industrial "standard" specimen presently used by Berkeley Nuclear Laboratories; (iii) it provides a large plane surface to ensure effective coupling of the transducer, and (iv) it allows for ease of flexural testing after initial tensile stressing.

9.3 Acoustic Emission Apparatus

AE is detected at the surface of the graphite specimens by a Dunegan-PAC WD (piezo-electric ceramic lead zirconate-titanate crystal) transducer; chosen for its size (16 mm diameter), its sensitivity (-73 dB with reference to 1 V/μbar at the transducer) and its wideband, non-resonant frequency response between 0.1 and 1.1 MHz. It is known that smaller transducers would result in a lower output voltage and hence a lower sensitivity. Two transducers were purchased from the same batch so that if the first transducer was broken in the middle of the testing programme, then the AE responses using the second transducer should not be significantly different. For unirradiated specimens, the transducer was applied to the specimen using compression and bonding methods (ASTM E650-85) by petroleum jelly and a specially-designed transducer mounting fixture. The transducer is connected to a 60 dB pre-amplifier, which produces a output signal of high amplitude and low impedance which can be processed by conventional techniques by the main AE amplifier systems. As noted in §9.1, two AE systems were used in this work; (i) Marandy MR1004 AE Analyser, and (ii) AECL AE Acquisition System.

9.3.1 Marandy MR1004 AE Analyser

The Marandy AE Analyser which carries out amplitude sorting and ringdown counting, is designed as a research tool. It incorporates a highly accurate amplitude level and threshold (±0.1 dB) digital setting and has four analogue inputs for monitoring load and strain data. The Marandy AE system sorts the AE events with maximum amplitude above 10 mV into 26 amplitude levels (1 to 25), each 2.4 dB wide. Events with an amplitude larger than 10 volts will be registered in amplitude level 26 (over-range). The threshold voltage is adjustable in eight steps from 10 to 69.18 mV. The AE threshold used in this project was 62.4 dB (equivalent to 13.2 mV), with respect to

1μV at the transducer. The instrumentation used has a fixed deadtime of 100 μs, and the experimental arrangement is illustrated in Figure 9.3.

Before each test session, each analogue input is calibrated to ±10 V using the MR1004/P program from Marandy Ltd.. AE data is collected using their MR1004 program, while a real-time histogram of cumulative AE events versus amplitude level is displayed. All AE event data accumulated during an experiment are written to disk during the test by the creation of a AE binary datafile (*.AEB). By default, the Marandy system updates the *.AEB file every second, but it may be reset to update the *.AEB file up to every five minutes. In addition to the time, load, strain, and cumulative AE event count, the *.AEB data file also contains cumulative ringdown counts, event and ringdown rates and cumulative AE event counts for the 26 amplitude levels. The captured AE waveforms may be displayed using an HM208 memory oscilloscope and recorded by a X-Y plotter (examples of captured waveforms were presented in Chapter Eight). Data management and analysis of *.AEB is described in §9.3.4.

For monitoring the AE response of irradiated graphite at Berkeley Nuclear Laboratories, the same experimental procedure was used with the exception that a transducer was supplied by Berkeley Nuclear Laboratories for work within the shielded facility and load data were supplied by a ±2 V output voltage signal from the NENE test rig from within the shielded cell. The AE transducer was attached to the irradiated specimen by silicone rubber for open laboratory tests and silicone grease for in-cell measurements.

9.3.2 AECL AE Acquisition System

The AECL AE system used by Berkeley Nuclear Laboratories is designed to provide an inspection capability rather than as a research instrument. The AECL system was used simultaneously with the Marandy system at Berkeley Nuclear Laboratories to

compare AE responses from unirradiated and irradiated curved beam specimens from differing AE systems, as shown in Figure 9.4. These results are presented in Chapter Twelve.

The AECL system carries out amplitude sorting and ringdown counting, and it is capable of measuring cumulative AE events with corresponding load. The cumulative AE event count was recorded manually at each increment of load as well as the amplitude distribution at peak or failure load. The AECL system threshold is set using a 10 turn potentiometer ranging from 0.01 to 1 V. The threshold was set at 13.2 mV, which is approximately equivalent to that for the Marandy AE system, but the AECL system has a fixed deadtime of 200 μs.

The AECL AE system has of five components: (a) an analogue module with variable gain and a meter that indicates AE activity; (b) two adjoined LCD 3 decade display counter modules measuring either events or ringdowns; (c) an amplitude distribution unit (ADU) which measures cumulative or density amplitude distribution of the AE resolved in to twenty amplitude levels, each of which is 3 dB wide; (d) a parametric module displaying the corresponding load signal from NENE test rig; and (e) a computer interface module providing data output facilities to an IBM compatible computer.

Work carried out in the shielded cell environment presented certain problems. Due to protective barriers, the length of connecting cables between instruments is much longer than in the open laboratory, which causes a loss of electrical signal. For example, a loss of signal occurred between the loadcell within the shielded cell and the control box outside. This particular problem was overcome by calibrating the 5 kN loadcell using a circular steel hoop where the deflection is known for a given load. In addition, the BNL shielded facility has a poor electrical earth, which caused occasional spikes in electrical signals. This is severe problem for AE work and therefore each piece of

equipment was checked for electrical isolation, and each AE system was checked for extraneous noise. Eventually all these experimental problems were overcome, and it is evident from the AE responses described in Chapter Twelve that it is possible to eliminate unwanted side effects of in-cell testing.

9.3.3 NENE Test Rig

A NENE tension/compression test rig was used to load in three-point flexure, unirradiated and irradiated Stage I and II curved specimens (these are described in Chapter Twelve); load data were recorded by monitoring the output of the load-cell connected to the crosshead. The crosshead speed was controlled by means of a servo motor driving two ball-screws attached to the crosshead. This motor was controlled via an RS232 interface port using an IBM PC compatible computer, with the software programmed to operate the crosshead at variable speeds from 0.1 mm min^{-1} to 100 mm min^{-1}. For all tests, the crosshead speed was 0.1 mm min^{-1}. Load measurements were recorded by monitoring the output of the load-cell connected to the crosshead.

9.3.4 File and Data Handling

AE data handling proved to be a considerable problem in this work and so the system developed for data handling and filing is briefly described in this section. The *.AEB file (§9.3.1) may be converted to a comma separated file (CSV), which is an ASCII format file, using the RFPLOTS program. This program also displays brief file information on completion. A CSV file may be imported into some commercial spreadsheets. The Quattro Pro version 3.0 spreadsheet was adopted for file analysis in this project; this spreadsheet was unable to import the CSV file satisfactorily. A special utility program "CSV2QPRO" was written to adjust the CSV file for importation into Quattro Pro 3.0 and it created a *.PRN file. The *.PRN file was imported in to Quattro Pro 3.0 as a comma delimited file and the AE file saved as a *.WQ1 file. The *.WQ1 file consists of columns of; Time, Total Events, Total Ringdowns, Event Rate, Ringdown Rate, Amplitude Levels 1 to 26, for storing

cumulative AE events in each level, and channels AD1 to AD4 which refer to the four analogue channels. AD1 is usually used for load and AD2 for strain while the other two are generally unused. All intermediate files can be deleted to save space but the *.AEB and *.WQ1 are kept as well as backup files. Since in excess of 1000 AE files were saved, all data files were compacted using the special storage facility PKPAK program.

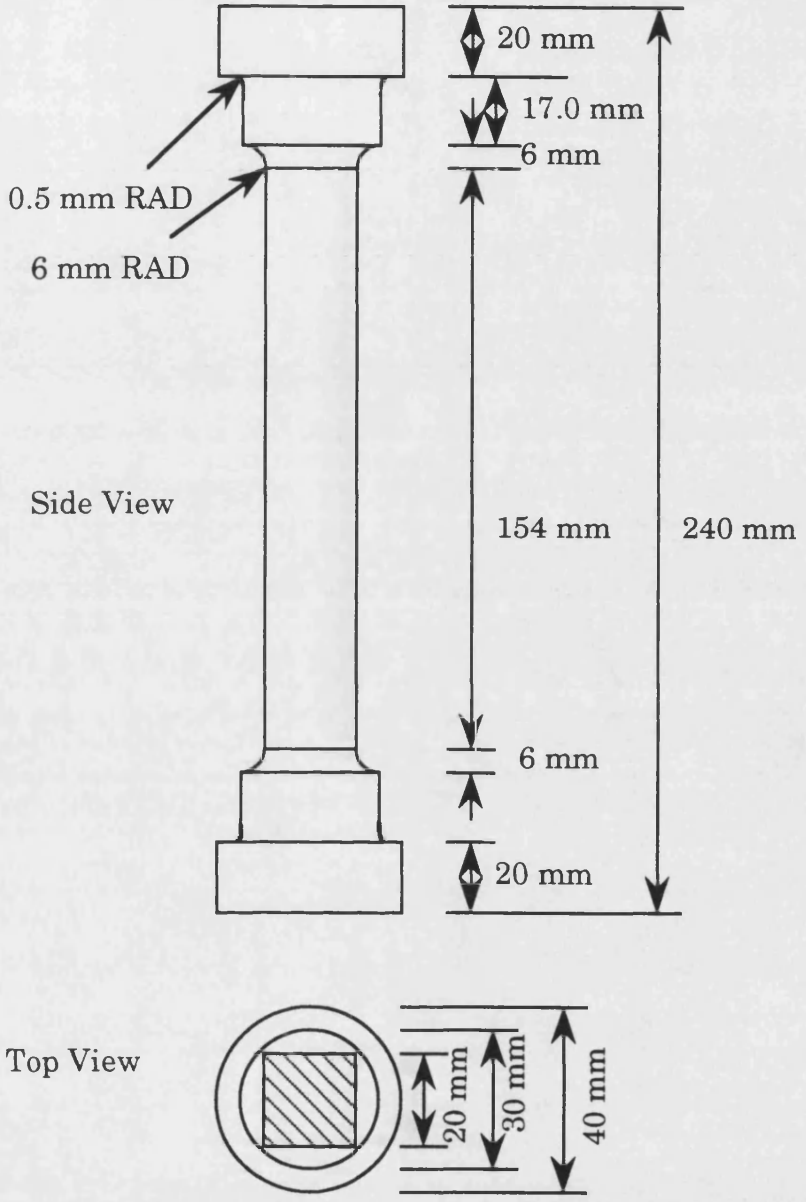

FIGURE 9.1 : The graphite tensile specimen designed for AE testing.

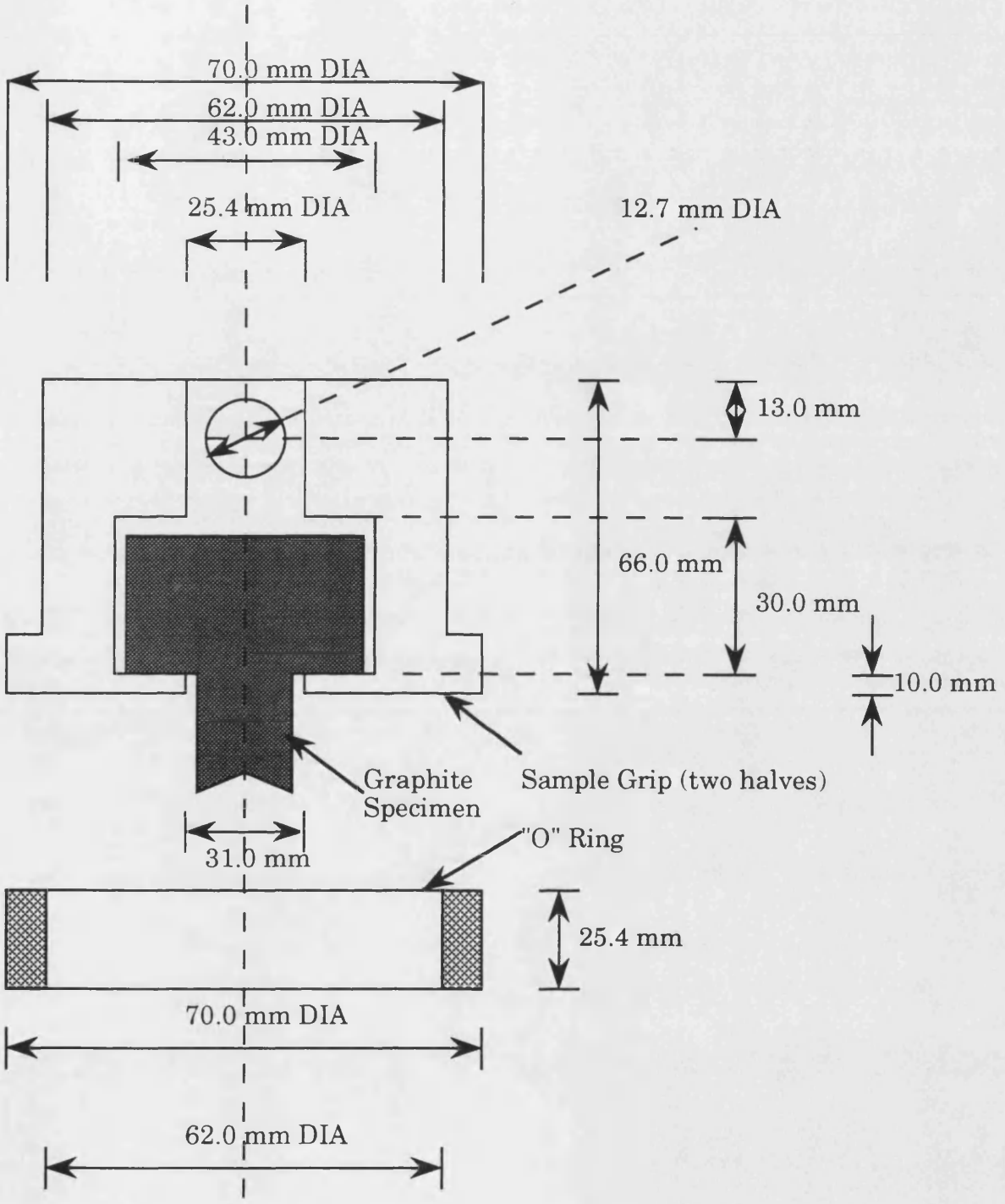

Material : Mild Steel
No. Reqd : 2

FIGURE 9.2 (a) : The tensile graphite specimen holder designed for AE testing.

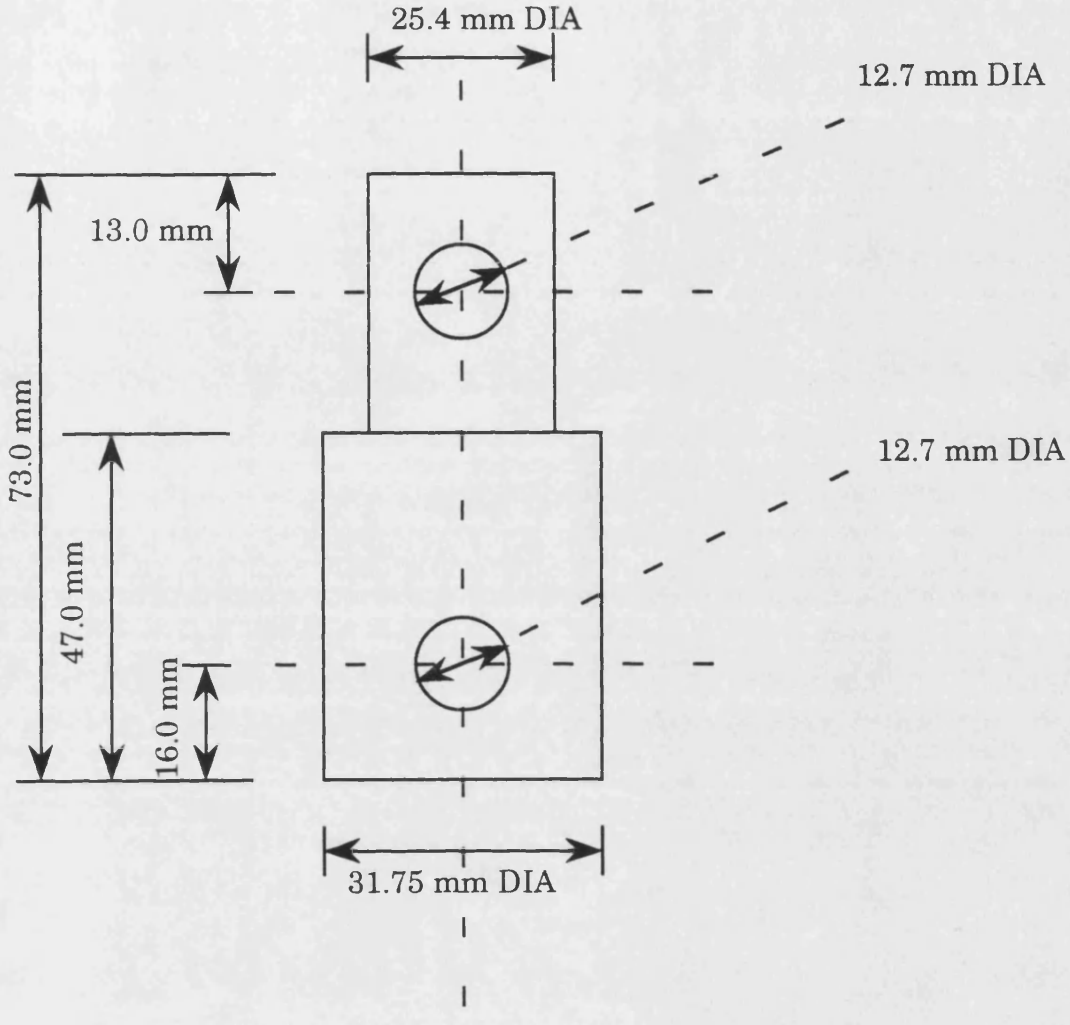

Material : Mild Steel
No. Reqd : 2

FIGURE 9.2 (b) : The linking joint between the graphite specimen holder and the Instron 1195 designed for AE testing.

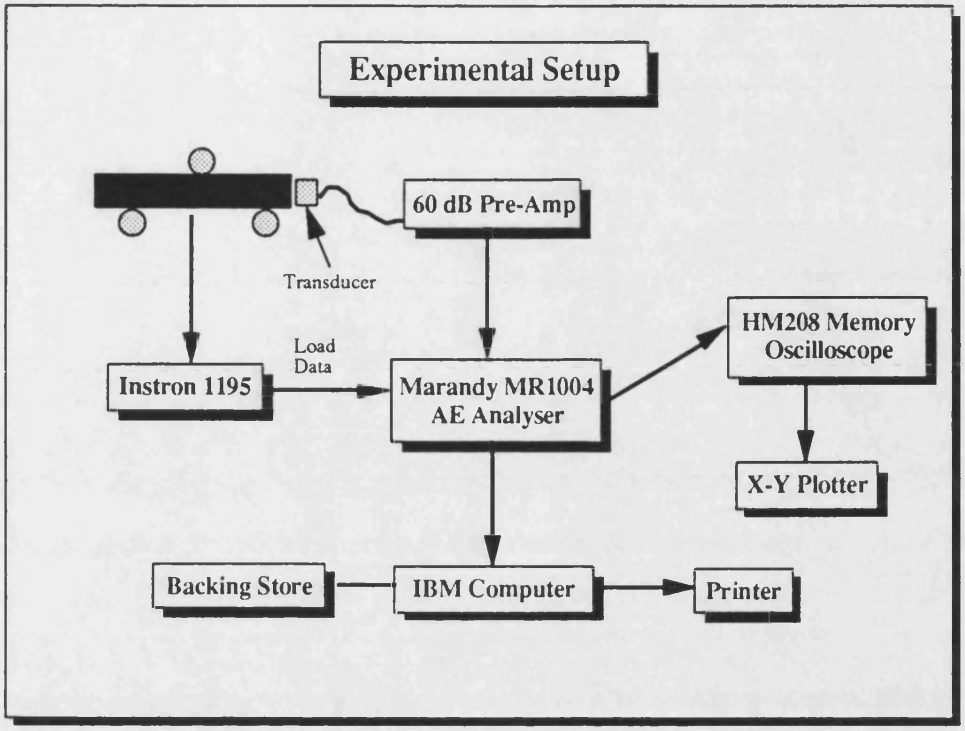

FIGURE 9.3 : The experimental arrangement for AE monitoring of unirradiated graphite at Bath University.

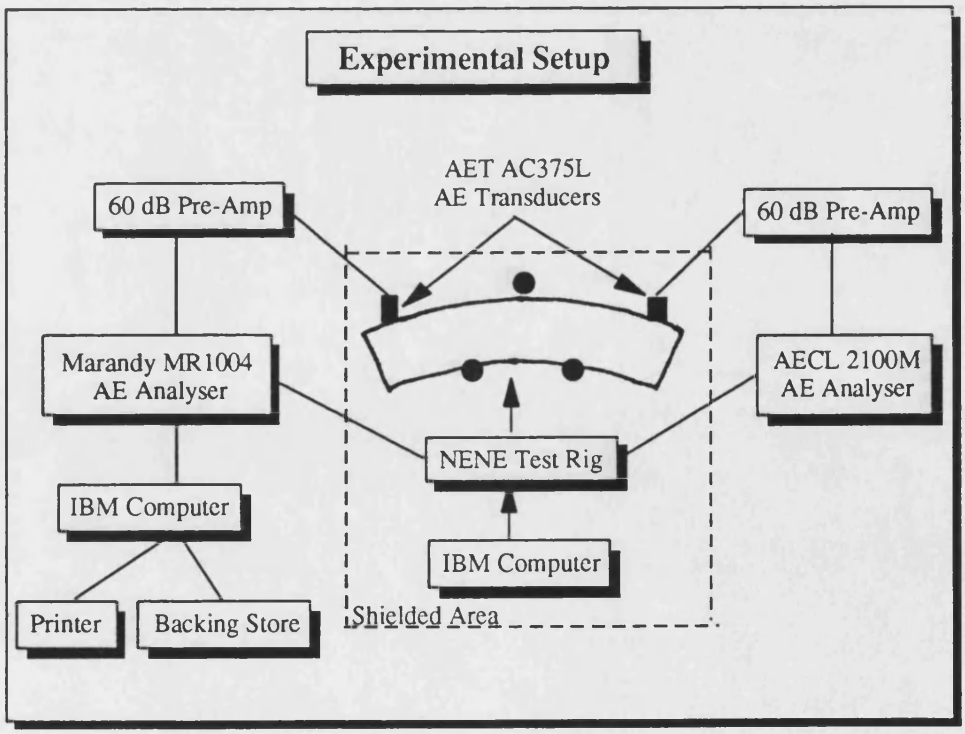

FIGURE 9.4 : The experimental arrangement for AE monitoring of irradiated graphite at Berkeley Nuclear Laboratories.

CHAPTER TEN : ACOUSTIC EMISSION RESPONSES FROM THREE UNIRRADIATED NUCLEAR GRAPHITES

10.1 Introduction

This chapter reports an investigation into the acoustic emission (AE) responses from three nuclear graphites (PGA, IM1-24 and VNEC) subjected to monotonic and cyclic loading in tension, compression and flexure. This is the first systematic study of AE generated from nuclear graphites, which considers the effect of pre-stress, and relates the AE responses to mechanical and fracture behaviour in tension, compression and flexure. The AE response from monotonic loading to failure is first considered before cyclic loading in tension, compression or flexure. The effect on the AE response from either tensile or compressive pre-stress before flexural loading is also considered. The last series of experiments are of particular importance, since Nuclear Electric plc currently uses the flexural test on trepanned specimens to determine the structural integrity of moderator blocks (the trepanned specimens have been subjected to either a tensile or compressive pre-stress in the reactor (see Chapter Five)).

10.2 Acoustic Emission Responses From Monotonic Loading

10.2.1 Experimental Programme

AE responses were obtained for three unirradiated nuclear graphites (PGA, IM1-24 and VNEC) monotonically loaded to failure in tension and flexure. AE responses from compression loading to failure were not obtained because the "explosive" failure mode in compression (see Chapter Seven) would expose the AE transducer to an unacceptable risk. Measurements of strength were carried out simultaneously for each testing mode and these were reported in Chapter Seven.

10.2.2 Results

AE sources from most industrial graphites can be termed critically active, *i.e.* the rate of change of the cumulative AE event count, ΣN, increases with increasing stress, σ (ASTM E569-85). Figure 10.1 (a)&(b) shows the AE response from the three graphites (PGA, VNEC and IM1-24) subjected to monotonic loading to failure in tension and flexure, respectively. The relationships between ΣN and σ at high stresses can be described approximately by the empirical relationship $\Sigma N = A\sigma^B$, where A and B are constants, as illustrated in Figure 2.

For all graphites, in tension and flexure, the AE response (Figure 10.1 (a) & (b)) shows that ΣN increases rapidly as the fracture stress is approached. Similar behaviour was found by Burchell (1986) for the majority of graphites studied in flexure. The comparison of AE responses from monotonic loading of various graphites are indicative of the texture of the graphite, and the amount of deformation before failure. For all graphites, AE starts at the lowest applied stress. This is in contrast to some previous work (Kraus and Semmler, 1978, and Pickup *et al.*, 1982), were an onset stress was observed. The absence of an onset stress is not surprising, since the stress-strain behaviour of the graphite single crystal at room temperature shows marked basal plane slip which is activated at a low critical shear stress ~0.03 MPa (Kelly, 1981). The detection of AE at low stress in this work is attributed to the improved technology and sensitivity of the AE detection system compared with earlier work.

The trend of ΣN versus σ in flexure is similar to the AE response in tension, but they differ in two ways; (i) the failure stress in flexure is greater than in tension on average by a factor of 1.82 for PGA and IM1-24, and 1.99 in VNEC (see Table 10.1 and Chapter Seven), and (ii) the ΣN in tension is greater than that in flexure by a factor of 2.1 for IM1-24, 3.2 for PGA and 3.5 for VNEC. The stressed volume in flexure is much smaller than in tension, and consequently the ΣN is less for flexural loading, because the process zone, in which AE generating processes occur, is generally

confined to a localised region of high tensile stress, although a small number of AE events are probably generated in the inner region of the test specimen from a compressive stress.

Table 10.1 shows the AE data for monotonic loading of three nuclear graphites. In both tension and flexure, the ratio of ΣN at failure, for PGA, VNEC and IM1-24 is approximately 10:5:1. As discussed by other workers (Pickup, 1984 and Burchell, 1986) the high value of ΣN for PGA can be related to its coarser texture compared to the other two graphites. Although the mean strength for VNEC is slightly higher than for IM1-24, but not significantly different (95% confidence), VNEC emits twice as much AE in tension, suggesting that VNEC undergoes a greater degree of subcritical cracking.

	PGA	**IM1-24**	**VNEC**
σ_f (tension) / MPa	11.04 ± 1.00 (6)	14.22 ± 1.53 (7)	14.33 ± 2.36 (5)
σ_f (compression) / MPa	34.5 ± 5.8 (6)	72.15 ± 3.69 (9)	51.98 ± 5.01 (6)
σ_f (flexure) / MPa	20.11 ± 2.98 (10)	25.81 ± 2.35 (10)	28.52 ± 3.85 (5)
ΣN at σ_f (tension)	66752 ± 9263 (5)	6018 ± 1861 (6)	33368 ± 8947 (5)
ΣN at σ_f (compression)	No Data	No Data	No Data
ΣN at σ_f (flexure)	20779 ± 6296 (10)	2827 ± 1057 (10)	9508 ± 3049 (5)

TABLE 10.1 : Mean Strengths, σ_f, and ΣN (± 1 S.D.) at Failure For Monotonic Loading of Three Nuclear Graphites in Tension, Compression and Flexure (the number of specimens used are in parenthesis).

10.3 Investigation of the Effect of Specimen Geometry Upon Cumulative AE Event Counts

No study has ever examined the effect of specimen size and geometry of nuclear graphites upon the AE response. Therefore, an investigation of the effect of specimen geometry upon the AE response, *i.e.* cumulative AE event count, at constant stress for IM1-24 graphite was performed. Four specimen sizes were chosen to study the effects of length, cross-sectional area and volume: 20 x 20 x 150 mm^3 (Size A); 20 x 25 x 240

mm^3 (Size B); 20 x 25x 120 mm^3 (Size C); and 32 x 25 x 150 mm^3 (Size D) (see Table 10.2). Specimen sizes B and D have twice the volume of specimen sizes A and C; specimen size B has twice the length of specimen size C; and specimen size D has twice the cross-sectional area of specimen size A. The specimens were obtained from the same source as in the AE cyclic testing programme described in Chapter Nine. Ten specimens of each specimen size were stressed to 15 MPa in compression while AE was monitored. Analysis of ΣN at a particular stress for area, length and volume may indicate the possible effect of specimen geometry on the AE response and thereby enabling correlation between all AE results from different test pieces.

10.3.1 Results

Each specimen size was stressed in compression to 15 MPa, and the cumulative AE event count, ΣN extracted at ~5, ~10 and ~15 MPa from each AE data file. Table 10.2 presents the results of the investigation of specimen size upon the AE response at a particular stress. Table 10.2 also shows in units of volume (v), length (l) and cross-sectional area (a) how each specimen size varies, *e.g.* size D has twice the volume and twice the cross-sectional area of size A. The mean ΣN was calculated from the best eight samples from a group of ten, *i.e.* the highest and lowest values were eliminated to counter any effect of exceptionally good or bad coupling of the transducer to the specimen.

The mean ΣN at each stress for all specimen sizes are similar, with on average the standard deviation representing 24% of the mean. No obvious association can be identified from Table 10.2 which links specimen geometry with the mean ΣN, apparently indicating that the mean ΣN is independent of specimen volume. It is possibly that the specimen size range considered is too small, or the scatter in the ΣN is too large to reveal any effect. These tests were also conducted at compressive stresses up to 15 MPa, which is only ~$0.21\sigma_f$. Therefore, the differences in ΣN between sizes A, B, C and D in Table 10.2 may be much smaller than they are at failure. In addition,

a further complication is that IM1-24 gives low AE event counts compared to PGA and VNEC, as demonstrated for flexural and tensile loading in Figure 10.1. A comparison plot of typical AE responses under compressive loading from each specimen size, Figure 10.3, shows that each size has a similar response, and only at 15 MPa are the curves beginning to separate. It is important to mention here that the experiment was confined to low stresses, since the residual stresses in a moderator graphite in a nuclear reactor are ~5 MPa.

Sample	Volume	Length	Area	Size	Stress / MPa			ΣN		
					Mean	S.D.	n	Mean	S.D.	n
A	v		a	20x20x150	5.04	0.11	10	104	31	8
B	2v	2l		20x25x240	5.07	0.07	10	53	11	8
C	v	l		20x25x120	4.97	0.09	10	67	22	8
D	2v		2a	32x25x150	5.04	0.05	10	81	21	8
A	v		a	20x20x150	10.03	0.10	10	332	71	8
B	2v	2l		20x25x240	10.00	0.06	10	236	68	8
C	v	l		20x25x120	10.02	0.05	10	233	62	8
D	2v		2a	32x25x150	10.01	0.06	10	275	43	8
A	v		a	20x20x150	15.10	0.06	10	827	123	8
B	2v	2l		20x25x240	14.98	0.08	10	710	197	8
C	v	l		20x25x120	15.07	0.09	10	627	172	8
D	2v		2a	32x25x150	15.01	0.06	10	751	95	8

TABLE 10.2 : ΣN at Different Stresses For IM1-24 In Compression For Four Different Specimen Sizes.

In summary, although it may be expected that a higher mean ΣN is found when the specimen volume is doubled, over the specimen size considered in this work, no relationship was found. Any effects due to specimen volume that might be present in these experiments are not seen due to the scatter of ΣN from IM1-24. The scatter is in part attributed to IM1-24 being a poor source of AE, compared to the other two graphites, and the low stresses used in these experiments. In order for a relationship between the cumulative AE event count and specimen geometry to be estimated a much larger specimen size range would need to be considered, and also a higher stress range.

10.4 Acoustic Emission Responses From Single-Mode Cyclic Loading

10.4.1 AE Cyclic Experimental Programme

An experimental programme was devised to determine whether or not the Kaiser effect occurs in nuclear graphites. A Kaiser effect occurs when AE is only generated if the stress applied on the sample equals or exceeds that of the previous peak stress. At present, Nuclear Electric plc trepans cylindrical specimens from moderator brick bore walls, and among other things, determines their flexural strength. The bore of a moderator brick in early life generates internal tensile stresses of the order of 5 MPa up to ~18 EFPY (see Chapter Five). It is these internal stresses that Nuclear Electric plc have to determine in order to validate their safety models. If the AE response is recorded simultaneously when trepanned specimens are subjected to mechanical tests, and if the Kaiser effect is present, then the internal stress may be calculated at the bore.

In the present work, each test specimen was loaded in either tension, compression or flexure to 5 MPa, unloaded, re-loaded to 10 MPa, unloaded and re-loaded to 15 MPa. The first cycle is intended to simulate the internal stress generated within the reactor core, and the subsequent cycles simulate mechanical testing of the trepanned irradiated specimen. The AE response is recorded for all the three cycles, and the effect of pre-stress upon the AE response can then be studied. AE responses from cyclic loading were obtained for three unirradiated nuclear graphites (PGA, IM1-24 and VNEC).

10.4.2 Results

Table 10.3 presents for PGA, IM1-24 and VNEC graphites, the mean cumulative AE event count at peak load, ΣN, for each test cycle in tension, compression and flexure. Since the mean failure strength of the three graphites in tension is less than 15 MPa, the mean ΣN at 15 MPa include some at failure. There is a large standard deviation in most modes which illustrates both the microstructural heterogeneity in graphite, and the inherent "noise" associated with acoustic emission and its signal processing

techniques. As expected ΣN at peak load increases with increasing applied stress in all testing modes; this trend is illustrated for flexural testing in Figure 10.4. Figure 10.5 compares the ΣN at 15 MPa for each graphite in each testing mode. In all three cyclic testing modes, ΣN (PGA) > ΣN (VNEC) > ΣN (IM1-24) (95% confidence), *i.e.* AE increases with increasing coarseness of texture of the graphite, in agreement with the trend previously reported for AE from monotonic stressing to failure (§10.2).

		PGA			IM1-24			VNEC		
Stress / MPa		**5**	**10**	**15**	**5**	**10**	**15**	**5**	**10**	**15**
Tension	**Mean**	3606	33109	36558	88	892	4488	900	8736	14832
	S.D.	974	8950	9018	51	362	1536	364	6885	2904
	n	6	6	6	10	10	10	5	5	5
Compression	**Mean**	10600	23733	12161	169	230	484	244	2031	3782
	S.D.	5723	9642	2916	136	81	116	211	1725	2946
	n	10	10	10	9	9	8	5	5	5
Flexure	**Mean**	460	1581	3697	23	69	184	41	159	401
	S.D.	320	967	2217	19	48	133	29	92	204
	n	10	10	10	10	10	10	5	5	5

TABLE 10.3 : Cumulative AE Event Count at Peak Load, ΣN, (± 1 S.D.) for Cyclic Loading of Three Nuclear Graphites in Tension, Compression and Flexure (where n is the number of samples).

In all but two cases, ΣN (tension) > ΣN (compression) > ΣN (flexure) (95% confidence) at 5, 10 and 15 MPa. The mean ΣN for tensile loading are higher than for compressive loading, probably because the maximum stress in tension is close to the failure stress, whereas in compression it is less than 50% of the failure stress. Fewest AE events are observed in flexure due to the process zone being confined to a localised region of high tensile stress in the outer fibres of the specimen.

All AE responses with increasing stress for each graphite and each loading mode show a very similar trend, except for PGA in compression. Figure 10.6 gives an example of an AE response for IM1-24 from cyclic loading; similar AE responses were found for PGA and VNEC graphites. On the first cycle, ΣN increases progressively from zero stress, and in subsequent cycles, AE resumes at stresses which approach, but are less

than the previous peak stress, *i.e.* a Kaiser effect is not observed. In each cycle, the ΣN rise near-exponentially. These responses are examples of the Felicity effect (see Figure 10.9).

The AE response from PGA with increasing compressive stress differs from the other eight cases, as shown in Figure 10.7. On the first cycle ΣN increases progressively from zero stress, and the second and third cycles show a Felicity effect which is similar to the example shown in Figure 10.6. However, in the second and third cycles, ΣN does not continue to rise near-exponentially. On the second cycle, at stresses between 8 and 10 MPa, the rate of change of ΣN with stress decreases, and in the third cycle, almost immediately after the previous peak stress (~10 MPa) has been exceeded, ΣN remains almost constant with increasing stress.

This response prompted the recording of the AE response from PGA when loaded monotonically in compression to failure, Figure 10.8. The ΣN rises near-exponentially until half the failure strength, and then the rate of AE generation decreases, but with a small increase in the rate immediately prior to failure, thus forming an unusual S shaped curve. PGA also produces substantially more AE in compression than the other two graphites (Table 10.3). The failure mode of PGA in compression is dominated by shear processes (see Figure 7.14 (a)). Therefore, it is reasonable to suggest that the majority of AE events in PGA are generated by shear processes. The reduction in the rate of generation of AE in the range σ = 10-20 MPa, Figure 10.8, may indicate that the shearing mechanism within filler particles is being inhibited or "pinned". In PGA, because of the coarse texture of the filler particles, the crystallites can shear unhindered into large voids before being pinned or inhibited, probably by the binder phase. The small sharp rise in AE immediately prior to failure, Figure 10.8, may indicate that enough energy has been supplied by the loading system to overcome the "pinning", causing the nucleation of microcracks. These rapidly grow and link up leading to catastrophic failure.

Other workers (*e.g.* Burchell *et al.*, 1985) occasionally found AE responses for PGA graphite tested in flexure which are similar to that shown in Figure 10.8, *i.e.* an S-shaped curve. This was not found for flexural testing of PGA in this work. Their AE responses may be the result of unwanted shear effects, *i.e.* the span to width ratio (4:1) of their three-point bend specimens was too small to eliminate shear effects. It is also possible that the ratio of the filler particle size to the volume of their specimens was too small. Allard *et al.*, (1991) have argued that shear effects can occur if the specimen size for flexural loading is too small in relation to the filler particle size.

Table 10.4 compares for the three graphites, mean ΣN at 5, 10 and 15 MPa extracted from data files from monotonic loading to failure, and the additive ΣN, including those of prior cycles, at the end of each cyclic load for tension and flexure. Since the mean failure strength of the three graphites in tension is less than 15 MPa, the mean ΣN at 15 MPa include some at failure. There is no significant difference (95% confidence) between the additive ΣN from cyclic loading and the corresponding values of ΣN obtained from monotonic loading, due to the large scatter in AE results. This suggests that for cyclic loading there is an insignificant amount of AE on unloading between cycles. In harmony with this view, very little or no AE was detected upon unloading during cyclic loading of the three graphites. On unloading, the reduction in strain energy is relatively slow, being controlled by the cross-head speed of the Instron. Thus possible recovery processes which may occur on unloading, such as microcrack closure, do not give rise to detectable AE.

		PGA			IM1-24			VNEC		
Monotonic Loading										
Stress / MPa		**5**	**10**	**15**	**5**	**10**	**15**	**5**	**10**	**15**
Tension	**Mean**	5238	43488	56746	81	1396	5734	1203	11891	21314
	S.D.	4252	24798	21290	36	633	2334	422	7038	6360
	n	6	6	5	6	6	4	5	5	3
Flexure	**Mean**	774	3248	8930	40	102	268	59	386	1206
	S.D.	284	1197	3597	31	74	201	34	271	862
	n	10	10	10	10	10	10	5	5	5
Cyclic Loading (Additive)										
Tension	**Mean**	3606	36715	73273	88	980	5468	900	9636	24471
	S.D.	974	9924	18942	51	413	1949	364	7249	10153
	n	6	6	6	10	10	10	5	5	5
Flexure	**Mean**	460	2041	5738	23	92	276	41	200	601
	S.D.	320	1287	3504	19	67	200	29	121	325
	n	10	10	10	10	10	10	5	5	5

TABLE 10.4 : Comparison of Additive ΣN (± 1 S.D.) For Monotonic and Cyclic Loading of Three Nuclear Graphites in Tension and Flexure (where n is the number of samples).

In summary, for the three nuclear graphites subjected to cyclic loading in tension, compression and flexure, a Felicity effect is observed, *i.e.* AE is detected at lower stresses than previously applied. In all the AE responses recorded there was no evidence for the Kaiser effect in nuclear graphites. The Felicity effect that is observed may be attributed to recovery processes that occur on unloading and at zero load. Recovery in graphites has been previously demonstrated by Andrew *et al.* (1960) in creep studies at ambient temperatures; the permanent set at zero load was seen to decrease with time. The Felicity effect may be due to a number of factors associated with recovery. These include (i) the relaxation of residual strain at zero stress, *e.g.*, the reversal of shear mechanisms as a result of back-stresses arising from elastic restraint; and (ii) the re-adhesion of cracked surfaces leading to, *e.g.*, the rubbing and crushing of cracked surfaces and debris on both unloading and reloading. Further experiments which provide AE evidence for recovery processes in these graphites are provided in Chapter Eleven.

10.5 Quantitative Methods For Characterisation of AE Responses From Cyclic Loading

10.5.1 The Felicity Ratio

The Felicity effect may be characterised by the Felicity ratio, F, (ASTM E-7 Proposal P199) which is the ratio of the onset stress of AE, σ_0, to the previous maximum stress experienced by the specimen, σ_p, *i.e.*

$$F = \sigma_0 / \sigma_p \qquad (10.1)$$

(Figure 10.9). Therefore, the Felicity effect occurs when F is less than unity and a Kaiser effect occurs if F=1.

The Felicity ratio has two main disadvantages as a tool to characterise AE on cyclic loading: (i) it does not take account of the amount of AE prior to the previous maximum stress level, and (ii) the onset stress is difficult to determine and may require an arbitrary threshold to be set. There are many alternative arbitrary thresholds that may be considered to determine the onset stress, σ_0, including the following: (i) the first or the first n events; (ii) a crude percentage of the total number of event counts for each cycle, usually between 5-10% (ASTM E-7 Proposal P199); (iii) a critical value of ringdown count or event rate; (iv) extrapolation of the AE curve to the stress axis; (v) the point of maximum rate of change of ΣN with stress on the AE curve. In all the methods but the last, the threshold must be set by experience of the operator based on previous results and knowledge of the material. The last method depends on whether enough events are present at the part of slope at maximum rate of change, *i.e.* a low AE event count would lead to an indeterminate value or a value which would have a large error. In all cases, low number of AE events would lead to spurious results

10.5.2 The Recovery Ratio

A new and alternative parameter to the Felicity ratio, which may be used to characterise AE responses on cyclic loading and which attempts to quantify recovery between load cycles is proposed in this work. It is called the Recovery ratio, B, which is defined as the ratio of the cumulative AE event count (N_2) on cycle (n+1) at the previous peak stress and the cumulative AE event count (N_1) at the peak stress on cycle n, shown in Figure 10.9, *i.e.*

$$B = N_2 / N_1 \qquad (10.2)$$

If a Kaiser effect occurs in the AE response then B=0, but, if a Felicity effect occurs, then 0<B<1. The Recovery ratio is a precise measurement, and it does not depend on arbitrary or calculated thresholds set by the operator, as is the case for the Felicity ratio. A disadvantage of the Recovery ratio, B, is that it does not take account of the case where σ_o exceeds σ_p, although, in all the AE responses recorded in this work, this phenomenon was never observed.

Recovery Ratio, B							
		PGA		**IM1-24**		**VNEC**	
		5 MPa	**10 MPa**	**5 MPa**	**10 MPa**	**5 MPa**	**10 MPa**
Tension	**Mean**	0.097	0.072	0.066	0.088	0.111	0.076
	S.D.	0.026	0.009	0.035	0.016	0.045	0.013
	n	6	6	10	10	5	5
Compression	**Mean**	0.041	0.138	0.058	0.122	0.083	0.086
	S.D.	0.021	0.104	0.023	0.032	0.024	0.025
	n	10	10	9	8	4	5
Flexure	**Mean**	0.092	0.090	0.124	0.153	0.161	0.091
	S.D.	0.064	0.032	0.133	0.081	0.152	0.063
	n	10	10	10	10	5	5

TABLE 10.5 : Recovery Ratios, B (± 1 S.D.) at 5 and 10 MPa For Three Nuclear Graphite in Tension, Compression and Flexure (where n is the number of samples)

The Recovery ratio, B, was calculated for 5 and 10 MPa for the three selected graphites after three consecutive load cycles as described above. Mean values of B for

all graphites in all testing modes, Table 10.5, range from 0.04 to 0.16. Thus, the number of AE events generated on the (n+1) cycle before the previous peak stress is a significant fraction of the ΣN at the previous peak stress. In all but one case, B>0 (95% confidence) confirming that the Kaiser effect is not observed in these cases.

Table 10.3 shows that mean values of ΣN for flexural cyclic loading are much less than those for tensile and compressive cyclic loading. This translates to a large scatter in the B values for flexural loading compared to the other two modes, Table 10.5. Bearing this limitation in mind, the mean B values for flexural loading are not significantly different from those for tensile cyclic loading, as might be expected from the similar response of graphites to those deformation modes described in Chapter Seven. Flexural loading will therefore not be considered further in this discussion.

In cyclic compressive loading, the mean B value at 10 MPa for all three graphites is greater than at 5 MPa (although only slightly greater for VNEC) suggesting that the increased pre-stress causes an increasing extent of recovery on unloading. This result is consistent with the postulate that basal plane shear (which is the dominant initial response of graphites to compressive loading) is reversible to some extent upon unloading as a result of back-stresses (Ioka and Yoda, 1987). This trend is not found for cyclic tensile loading where the mean values of B at 5 and 10 MPa are not significantly different from each other. This may indicate that on cyclic tensile loading to 5 and 10 MPa, there is a greater proportion of microcracking, which is non-recoverable, than there is in compressive loading. This explanation is plausible when the difference in compressive and tensile failure modes for these graphites are considered (Chapter Seven) and the fact that 10 MPa is a higher fraction of the tensile failure stress than it is of the compressive failure stress. Thus, although B values are subject to large scatter, these results are in broad agreement with the postulate that microcracking is a non-recoverable process that basal plane is reversible on unloading,

as suggested by Ioka and Yoda (1987) and in a theoretical model by McLachlan *et al.* (1989).

10.6 Acoustic Emission Responses From Mixed-Mode Cyclic Loading

When a specimen is trepanned from the reactor core, the geometry of specimen and the difficulty of remote handling require Nuclear Electric plc to test in flexure. In the reactor, the moderator brick experiences tensile and compressive stresses, and therefore, it is useful to study the effect upon the AE response in flexure of either a tensile or compressive pre-stress. Specimens were stressed in either tension or compression to 5 MPa, unloaded and then re-stressed to 10 MPa in flexure. The special design of the tensile specimen allowed secondary testing in flexure for this purpose.

		PGA		IM1-24		VNEC	
Stress / MPa		**5**	**10**	**5**	**10**	**5**	**10**
Load Pattern		**T**	**F**	**T**	**F**	**T**	**F**
Tension	**Mean**	5303	414	94	12	631	28
/ Flexure	**S.D.**	2008	118	27	10	163	15
	n	6	6	10	10	5	5
		C	**F**	**C**	**F**	**C**	**F**
Compression	**Mean**	11921	2162	73	91	234	253
/Flexure	**S.D.**	3401	993	31	31	133	281
	n	10	10	10	10	5	5

TABLE 10.6 : Cumulative AE Event Counts for Three Nuclear Graphites in Mixed Mode Cyclic Stressing (T - tension, C- compression and F - flexure).

In mixed mode cyclic loading, fewer AE events are seen in the secondary flexural cycle after a tensile pre-stress than after a compressive pre-stress. Indeed, the values of ΣN after compressive / flexural cyclic loading to 10 MPa , Table 10.6, are very close to the additive values of ΣN for the single mode cyclic flexural loading to 10 MPa shown in Table 10.4. This is consistent with the view that the dominant processes in flexural loading are similar to those which occur in tension, whereas in compression,

particularly at low loads, the dominant processes is shear deformation. Thus the small increase in ΣN for flexural loading after tensile pre-stress is because the specimen has already experienced significant tensile stresses. This is not the case for flexural loading following a compressive pre-stress, and consequently a large ΣN is found on flexural loading to 10 MPa.

		PGA		IM1-24		VNEC	
Monotonic Loading		**5 MPa**	**10 MPa**	**5 MPa**	**10 MPa**	**5 MPa**	**10 MPa**
		T/C	**F**	**T/C**	**F**	**T/C**	**F**
Tension	**Mean**	5238	3248	81	102	1203	386
Flexure	**S.D.**	4252	1197	36	74	422	271
	n	6	10	6	10	5	5
Compression	**Mean**	10600*	3248	169*	102	244*	386
Flexure	**S.D.**	5723	1197	136	74	211	271
	n	10	10	9	10	5	5
Mixed Mode Loading		**5 MPa**	**10 MPa**	**5 MPa**	**10 MPa**	**5 MPa**	**10 MPa**
Tension	**Mean**	5303	414	94	12	631	28
Flexure	**S.D.**	2008	118	27	10	163	15
	n	6	6	10	10	5	5
Compression	**Mean**	11921	2162	73	91	234	253
Flexure	**S.D.**	3401	993	31	31	133	281
	n	10	10	10	10	5	5

TABLE 10.7 : Comparison of Cumulative AE Events From Each Individual Cycle Between Monotonic and Mixed Mode Loading (T/C - monotonic loading to 5 MPa in tension or compression, data from Table 10.4, (* indicates the data originates from the first cycle to 5 MPa in compressive cyclic loading, Table 10.3) and F - monotonic flexural loading to 10 MPa, Table 10.4)

Table 10.7 compares the ΣN from mixed mode loading with monotonic loading at equivalent stresses. Again, it is clearly demonstrated that the ΣN from the secondary flexural cycle after tensile pre-stress is much less than that experienced in monotonic loading, but the ΣN from flexure after compressive pre-stress is similar to that experienced in monotonic loading to 10 MPa, *i.e.* a compressive pre-stress of 5 MPa has no effect upon the ΣN obtained on subsequent flexural loading to 10 MPa. This is in agreement with earlier observations, Table 10.6.

		PGA	IM1-24	VNEC
Stress / MPa		**5 MPa**	**5 MPa**	**5 MPa**
Tension / Flexure	**Mean**	0.011	0.032	0.006
Load Cycles	**S.D.**	0.009	0.040	0.006
	n	6	10	5
Compression / Flexure	**Mean**	0.050	0.345	0.117
Load Cycles	**S.D.**	0.041	0.419	0.102
	n	10	10	5

TABLE 10.8 : Recovery Ratio, B, (± 1 S. D.) for Three Nuclear Graphites in Mixed Mode Cyclic Stressing

Table 10.8 presents the Recovery ratio, B, for the three graphites at 5 MPa, for mixed-mode cyclic loading. For each graphite, the Recovery ratio in the tension-flexure loading pattern is less than in compression-flexure test pattern, highlighting the effect observed for mean ΣN values, *i.e.* the tension-flexure loading cycle produces less AE on the second cycle than the compression-flexure cycle.

The sharply contrasting AE responses after tension-flexure and compression-flexure mixed mode cyclic testing is illustrated for VNEC graphite in Figure 10.10 (a) and (b); results from the other two graphites are similar. In tension-flexure the AE response in the secondary flexural cycle is flat, whereas the AE response in the flexural cycle following a compressive pre-stress, Figure 10.10 (b), is similar to other AE responses found in this work, with a near exponential rise in ΣN with increasing stress. In the case of the tension-flexure load cycles, Figure 10.10 (a), although the stress at the outer fibre is in excess of 5 MPa, the flat AE response in the flexural cycle is probably because other regions, due to the nature of the flexural test, are not experiencing stresses in excess of 5 MPa and therefore not emitting much AE. No such effect is seen in the compression-flexure AE response, Figure 10.10 (b).

Thus, an important observation from this section is that tensile and compressive pre-stresses act in different ways in relation to the generation of AE upon subsequent

flexural testing. Specifically, tensile pre-stress results in a low value of ΣN on subsequent flexural stressing, indicating that the tensile pre-stress has a strong influence upon AE which accompany subsequent flexural testing. By contrast, there is a large increase in ΣN on flexural stressing after a compressive pre-stress, which suggests that there is a weak relationship (if any at all) between AE on flexural stressing and a compressive pre-stress.

10.7 AE Amplitude Distributions

An examination of AE amplitude distributions may provide insights into the energetics of the AE generation. Most AE amplitude distributions reported in the literature conform to the Pollock distribution, but this work presents for the first time the amplitude distribution of PGA in compression that does not conform to the Pollock distribution and evidence is provided for the failure mechanism. However, the Pollock distribution is often mis-understood and results wrongly analysed. The Pollock distribution of the AE peak amplitudes is of the form

$$n(a) = (a/a_0)^{-b} \qquad (10.3)$$

where n(a) defines the fraction of the emission population whose peak amplitude exceeds a, a_0 is the lowest detectable amplitude and the exponent b is used to characterise the amplitude distribution (Pollock, 1979). Appendix I provides a brief mathematical treatment of the distribution in relation to the Marandy AE system, which shows that to obtain a Pollock distribution from results of the Marandy AE system, a plot of the logarithm of total number of AE events above amplitude level x (inclusive of those AE events in x), log N(x), versus the amplitude level number, x, gives a straight line of gradient -0.12b and the intercept on the log N(x) axis will equal log $N(a_0)$.

10.7.1 Amplitude Distributions From Nuclear Graphites

All amplitude distributions except that from PGA in compression obey the Pollock law. A typical example of a Pollock distribution is presented in Figure 10.11, and it shows the change in the distribution with increasing stress to failure. Figure 10.11 shows a slight decrease in the slope with increasing stress. This is due to the higher proportion of higher energy AE events emitted at higher stress levels. These results are agreement with Burchell (1986), who suggested for graphites in flexural loading, from plots of M(a) versus x, where M(a) is the number of AE events in amplitude level x, that there is a greater proportion of higher amplitude events at higher stresses shown by the slope of the line decreasing with increasing stress. Typically, the Pollock b value for the three graphites ranges between 1.4 and 2. Stone and Dingwall (1977) reported that most materials gave a Pollock b value ~1 which should be regarded as the standard distribution. This suggests that graphites in relation to other materials generate a higher proportion of low energy events which presumably correspond to the easy shear and slip of crystallites.

Figure 10.12 presents an example of an amplitude distribution from PGA in compression. Above about 20 MPa, the distribution deviates from the Pollock law and this deviation clearly corresponds to the reduction in the rate of emitted AE events shown in Figure 10.8. From Figure 10.12, it can be seen that above 20 MPa there is no increase in low amplitude events, but a "bowing" of the distribution at high amplitude levels, representing a significant increase in the proportion of higher energy AE events. The lack of additional low energy events at high stresses probably corresponds to the pinning of shearing crystallites, as discussed in §10.4.2. In the mid-range of amplitude levels (~3 - ~13) and at low stresses (up to ~15-20 MPa), AE conforms to the Pollock law with values of b in excess of 2. This shows that under compressive loading to ~15-20 MPa, PGA emits a high proportion of low energy events than VNEC and IM1-24 in any testing mode examined in this work. This is

consistent with the other evidence presented in this work that shear deformation in compression occurs to a greater extent in PGA than in the other two graphites.

The amplitude distributions from cyclic loading do not vary much from those seen in monotonic loading to failure. At each peak stress, the Pollock distribution is linear and is nearly parallel to that for the previous load cycle, but with a slightly lower slope showing that the proportion of high energy events is increasing. The amplitude distributions from mixed-mode cyclic loading support the observations reported earlier in §10.6. In tension-flexure mode, the AE amplitude distribution for the flexural cycle is similar to that for the tensile cycle, as shown for PGA in Figure 10.13 (a); the slopes of the Pollock distributions are similar, but as expected that for the flexural cycle is displaced to lower log N(x) values. For the compressive-flexure cycle, the compressive pre-stress amplitude distribution shows no resemblance to that of the flexural cycle (Figure 10.13 (b)). This supports the evidence presented earlier that the tensile and compressive pre-stresses act in different ways in relation to the generation of AE upon subsequent flexural testing.

10.8 Summary

Typical AE responses from PGA, IM1-24 and VNEC in tension and flexure from monotonic loading of nuclear graphites show that the ΣN rapidly increase with increasing stress. These AE responses are indicative of texture and the amount of deformation before failure.

For IM1-24, no simple relationships was found between ΣN and specimen size at constant stress over the range of stresses and specimen sizes considered. This was mainly due to the low number of AE and their scatter.

For cyclic loading of the three graphites studied, the cumulative number of AE events, ΣN, were in the order: ΣN(PGA) > ΣN(VNEC) > ΣN(IM1-24) in tension, compression and flexure. For a particular graphite and a particular stress, it was found that ΣN(tension) > ΣN(compression) > ΣN(flexure). This behaviour was attributed to the different fractions of the failure stress the specimen experienced in each testing mode. For all graphites and test modes, except for PGA in compression, the AE response in monotonic loading was similar to that shown in static loading, *i.e.* the ΣN increased rapidly with increasing stress. However, PGA in compression deviates from this behaviour at approximately half the failure stress when the rate of generation of AE decreases with increasing stress. This is attributed to the pinning of shear deformation, which is overcome just prior to failure.

For the three nuclear graphites subjected to single mode cyclic loading in tension, compression and flexure, a Felicity effect is observed, *i.e.* AE is detected at lower stresses than the previously-applied peak stress. In all the AE responses recorded there was no evidence for the Kaiser effect in nuclear graphites. The Felicity effect may be attributed to recovery processes that occur on unloading and at zero load. A new parameter, called the Recovery ratio, B, was proposed to attempt to quantify the amount of recovery. Mixed-mode compressive-flexural and tensile-flexural cyclic loading suggested that tensile and compressive pre-stresses act in different ways in relation to the generation of AE upon subsequent flexural testing. A tensile pre-stress caused the subsequent flexural load to produce much less AE then a compressive pre-stress.

All AE amplitude distributions obeyed the Pollock law, except for PGA in compression. Typically, the amplitude distribution is linear over the range of amplitudes for all stresses up to failure. However, for PGA in compression, the amplitude distribution deviates from the Pollock law at high stresses where there is a

much higher proportion of high amplitude events causing a "bowing" effect in the Pollock distribution.

The next chapter extends the investigation into recovery in nuclear graphites and examines the effect of recovery mechanisms on the AE response, and the dependency on time.

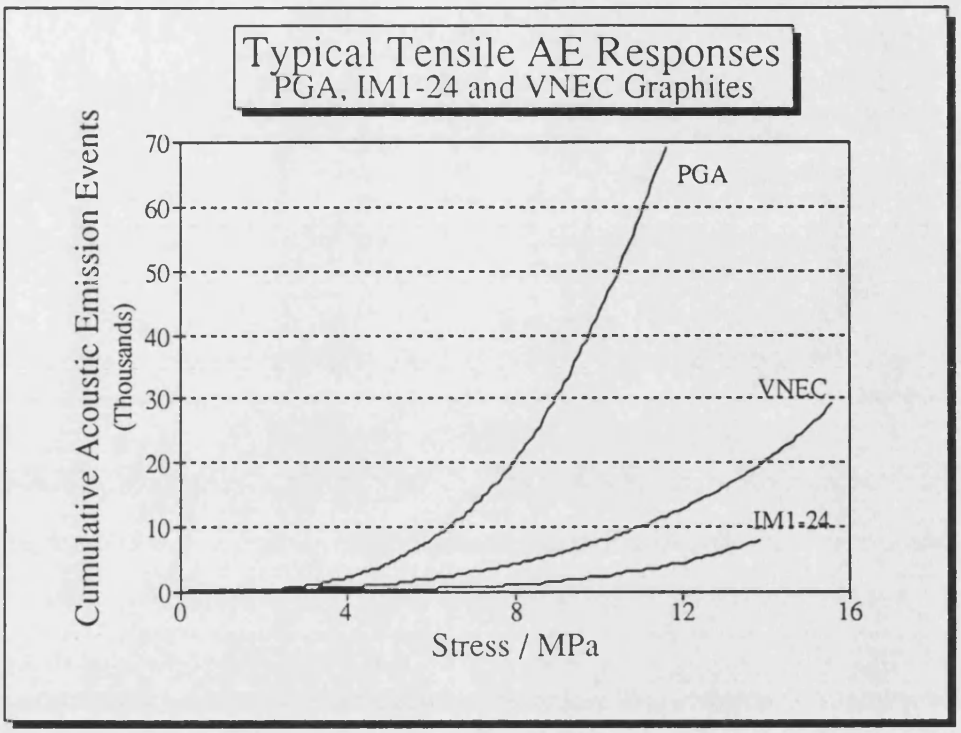

(a)

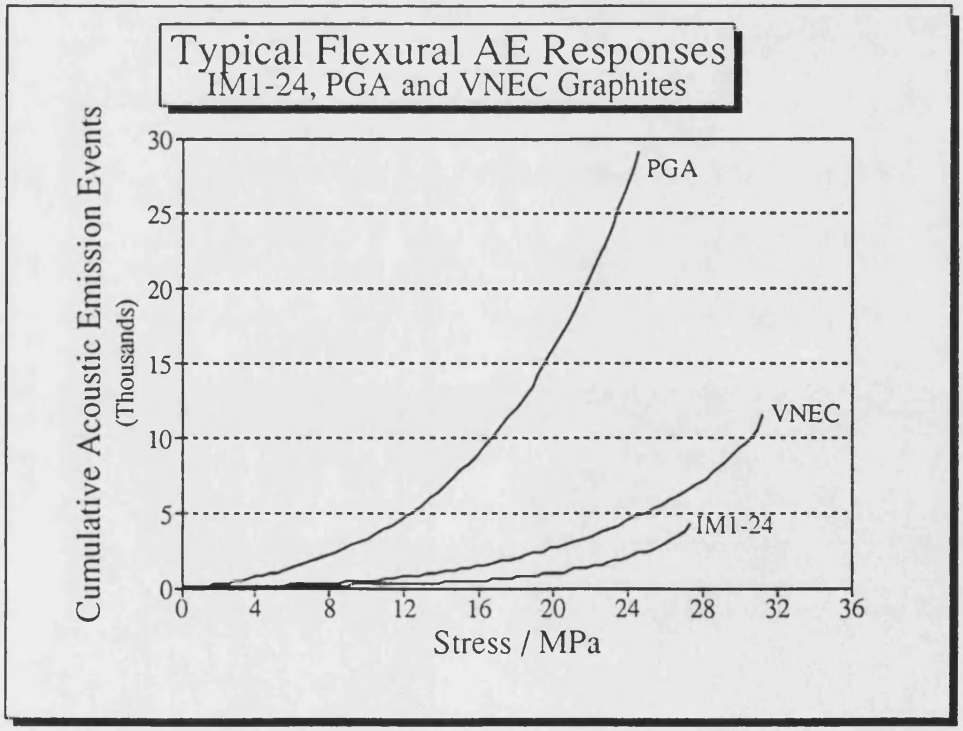

(b)

FIGURE 10.1 : Typical AE responses from three nuclear graphites (PGA, IM1-24 and VNEC) subject to monotonic loading to failure in (a) tension and (b) flexure.

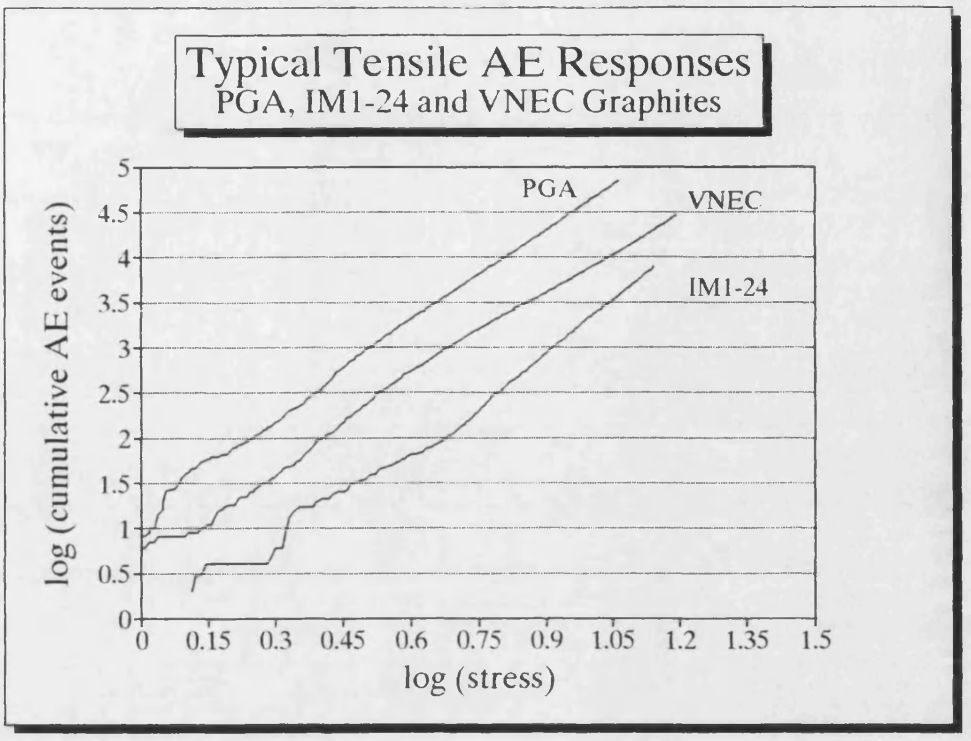

FIGURE 10.2 : A plot of the logarithm of cumulative AE event count versus the logarithm of applied stress for PGA, IM1-24 and VNEC graphites loaded monotonically to failure in tension illustrating the relationship $\Sigma N = A\sigma^B$.

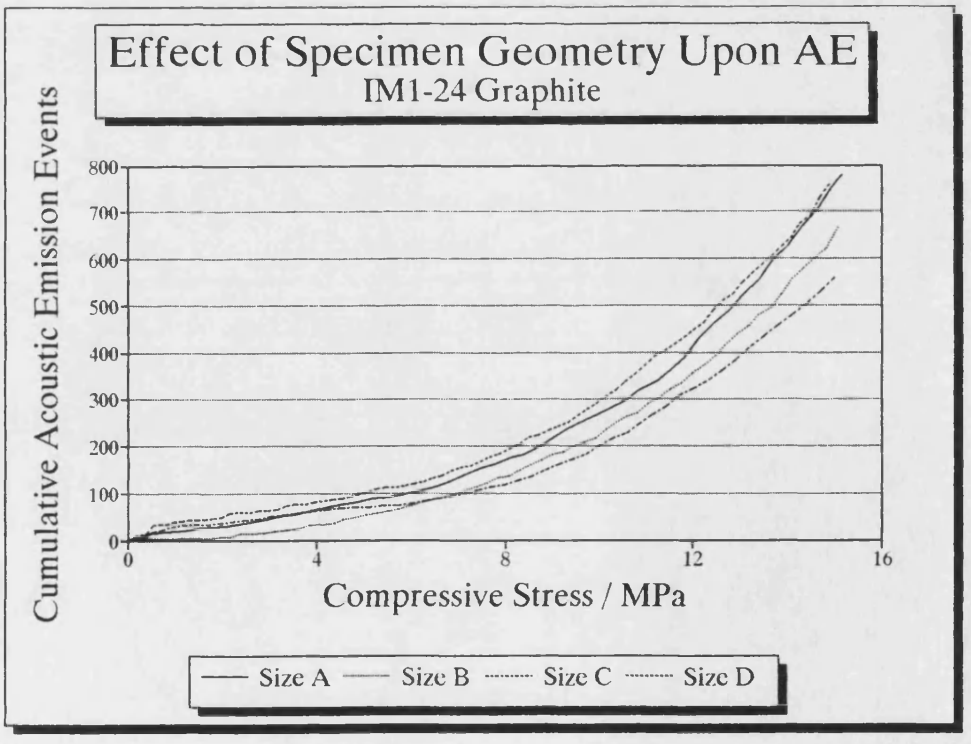

FIGURE 10.3 : A plot of typical AE responses for four different specimen sizes of IM1-24 graphite under compressive loading.

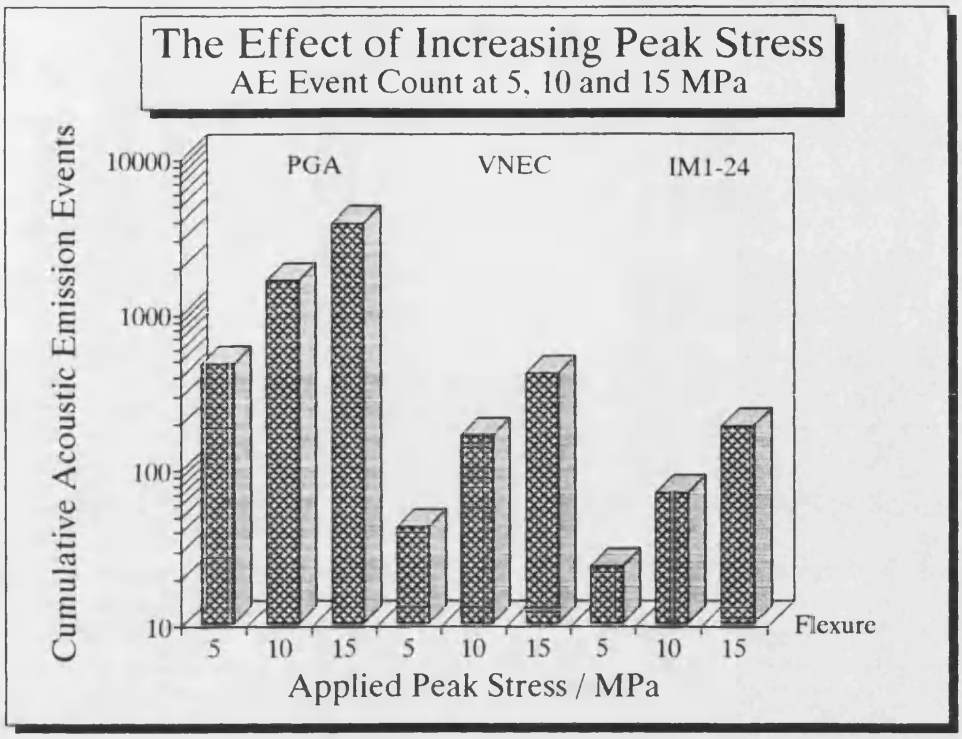

FIGURE 10.4 : A chart for PGA, IM1-24 and VNEC graphites showing the rise in cumulative AE events with increasing peak applied stress in cyclic loading.

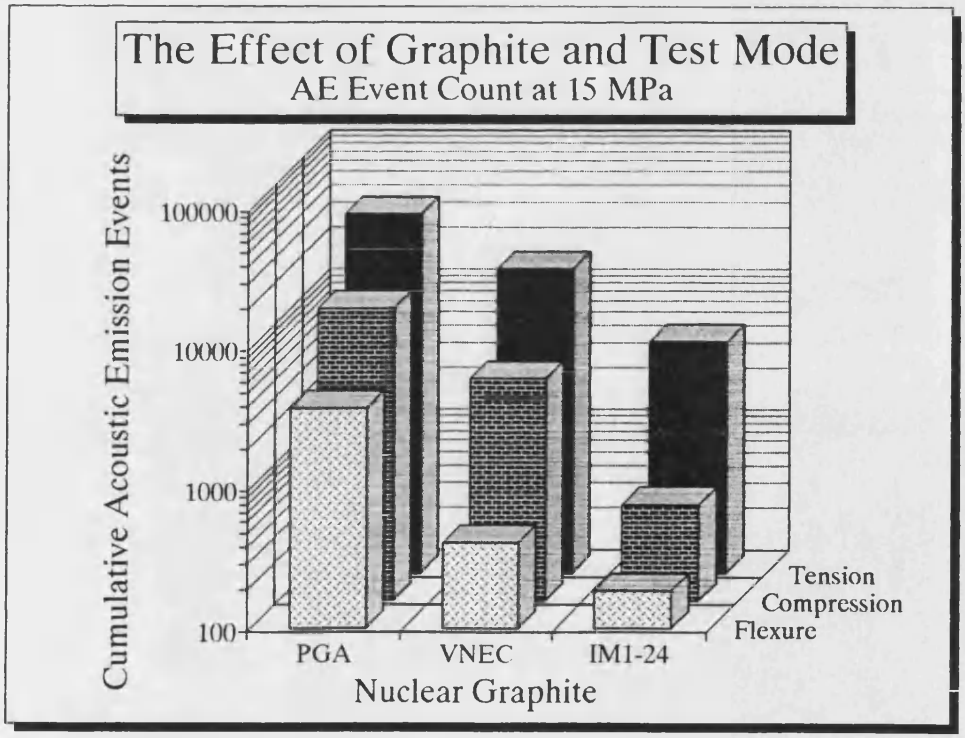

FIGURE 10.5 : An illustration showing the effect of the graphite and test mode upon the magnitude of cumulative AE event count (for a third load cycle to 15 MPa).

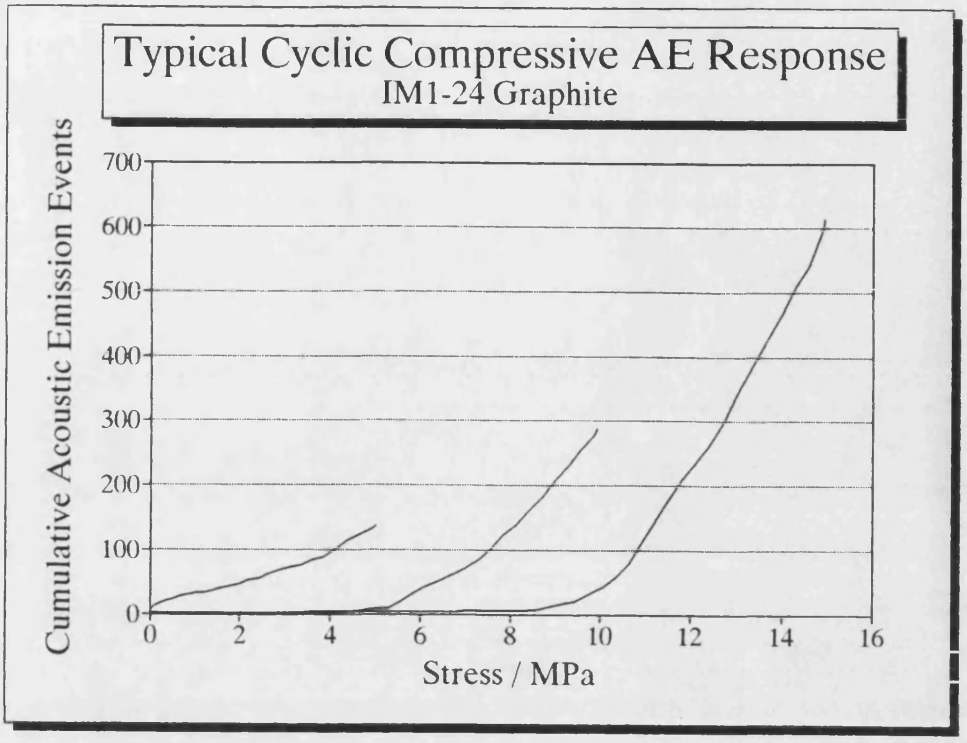

FIGURE 10.6 : A typical AE response from a nuclear graphite subjected to cyclic loading.

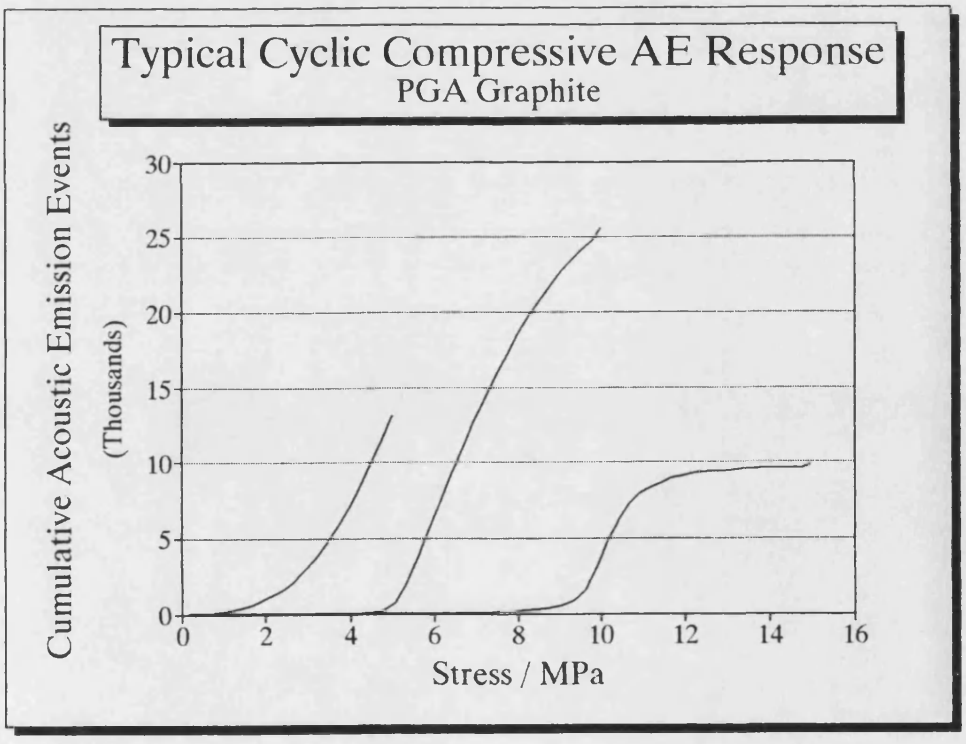

FIGURE 10.7 : An example of an AE response from PGA graphite subjected to compressive cyclic loading showing the rate of change of ΣN decreasing with applied stress on the second and third load cycles.

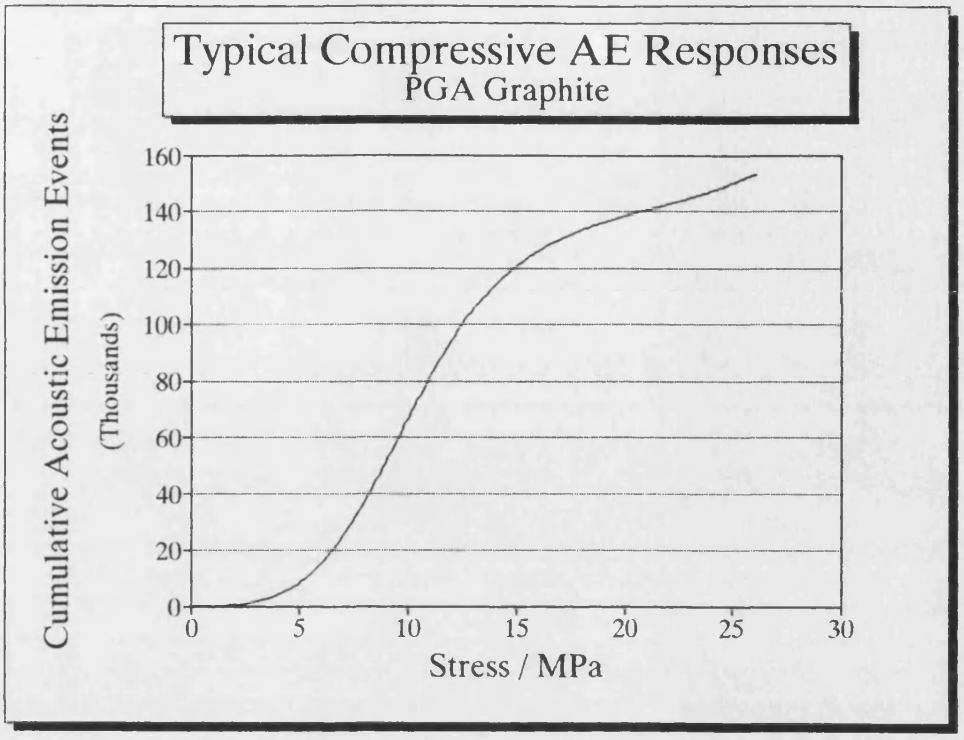

FIGURE 10.8 : An example of a S-shaped AE response from PGA graphite monotonically loaded to failure in compression.

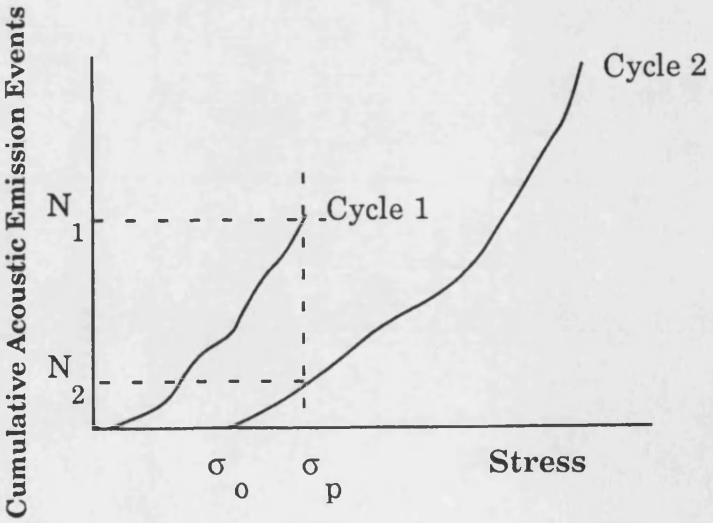

FIGURE 10.9 : An illustration of an AE response showing the definitions of the Recovery ratio, B ($=N_2/N_1$), and the Felicity effect, F ($=\sigma_0/\sigma_p$).

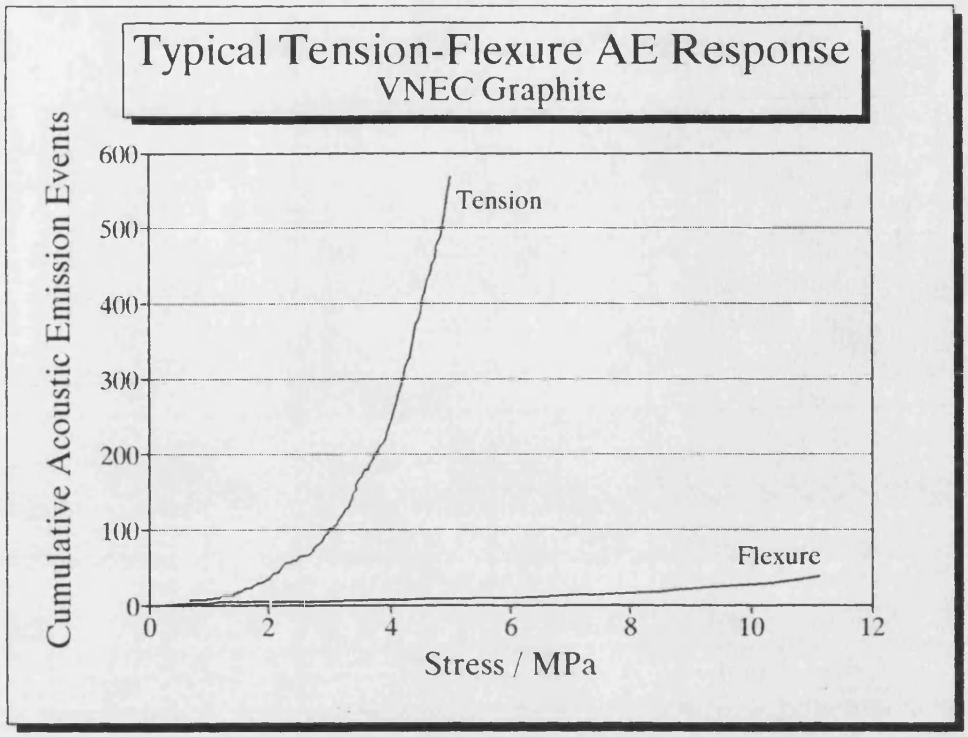

FIGURE 10.10 (a) : A typical AE response from VNEC graphite subjected to two load cycles to 5 MPa (tension) and 10 MPa (flexure), respectively.

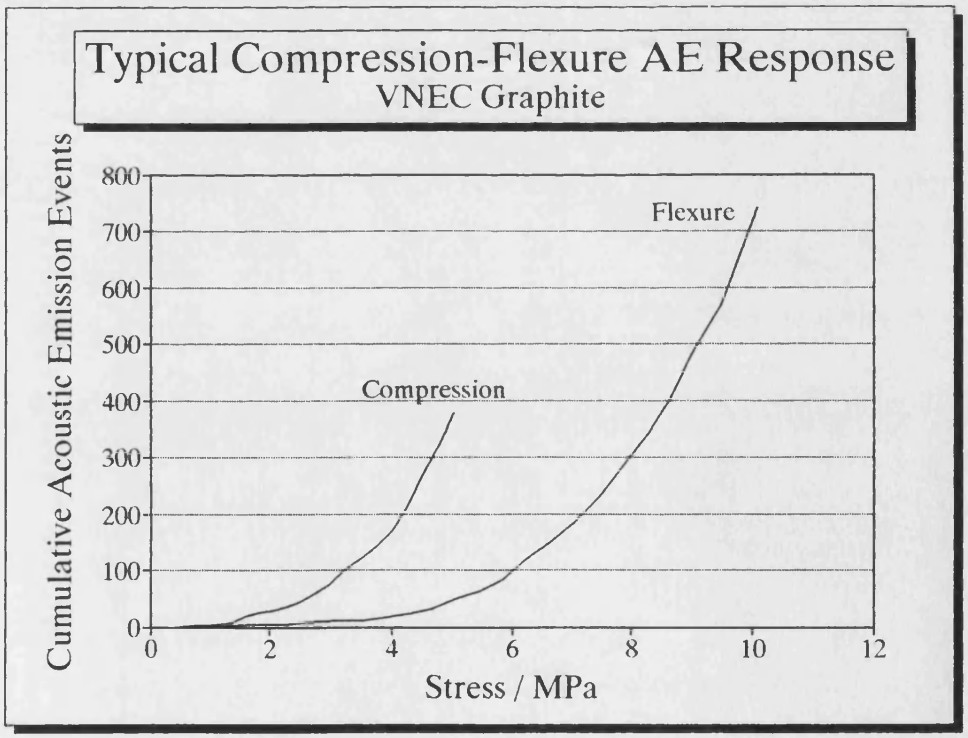

FIGURE 10.10 (b) : A typical AE response from VNEC graphite subjected to two load cycles to 5 MPa (compression) and 10 MPa (flexure), respectively.

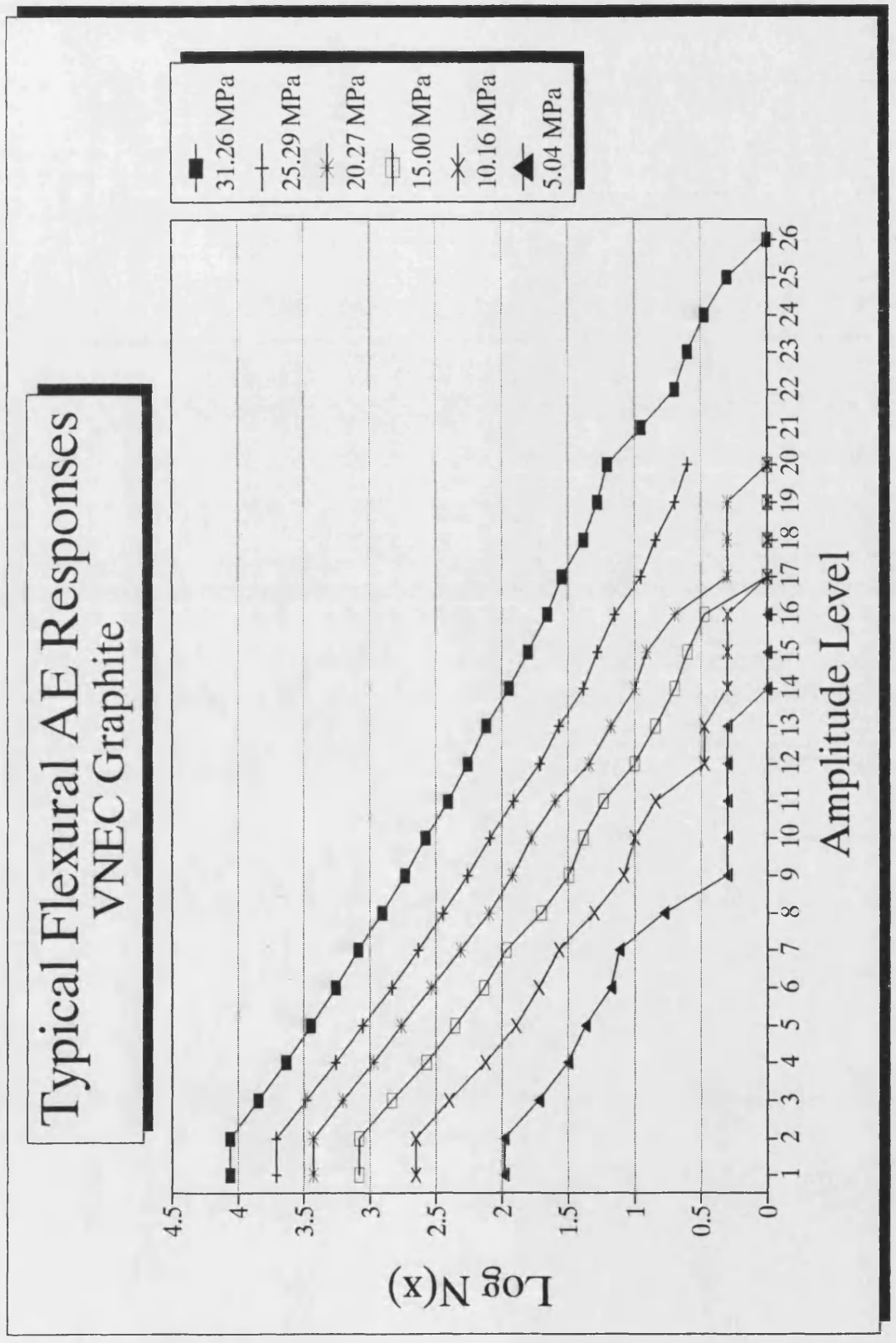

FIGURE 10.11 : A typical AE amplitude distribution illustrating the Pollock distribution (for VNEC graphite monotonically loaded to failure).

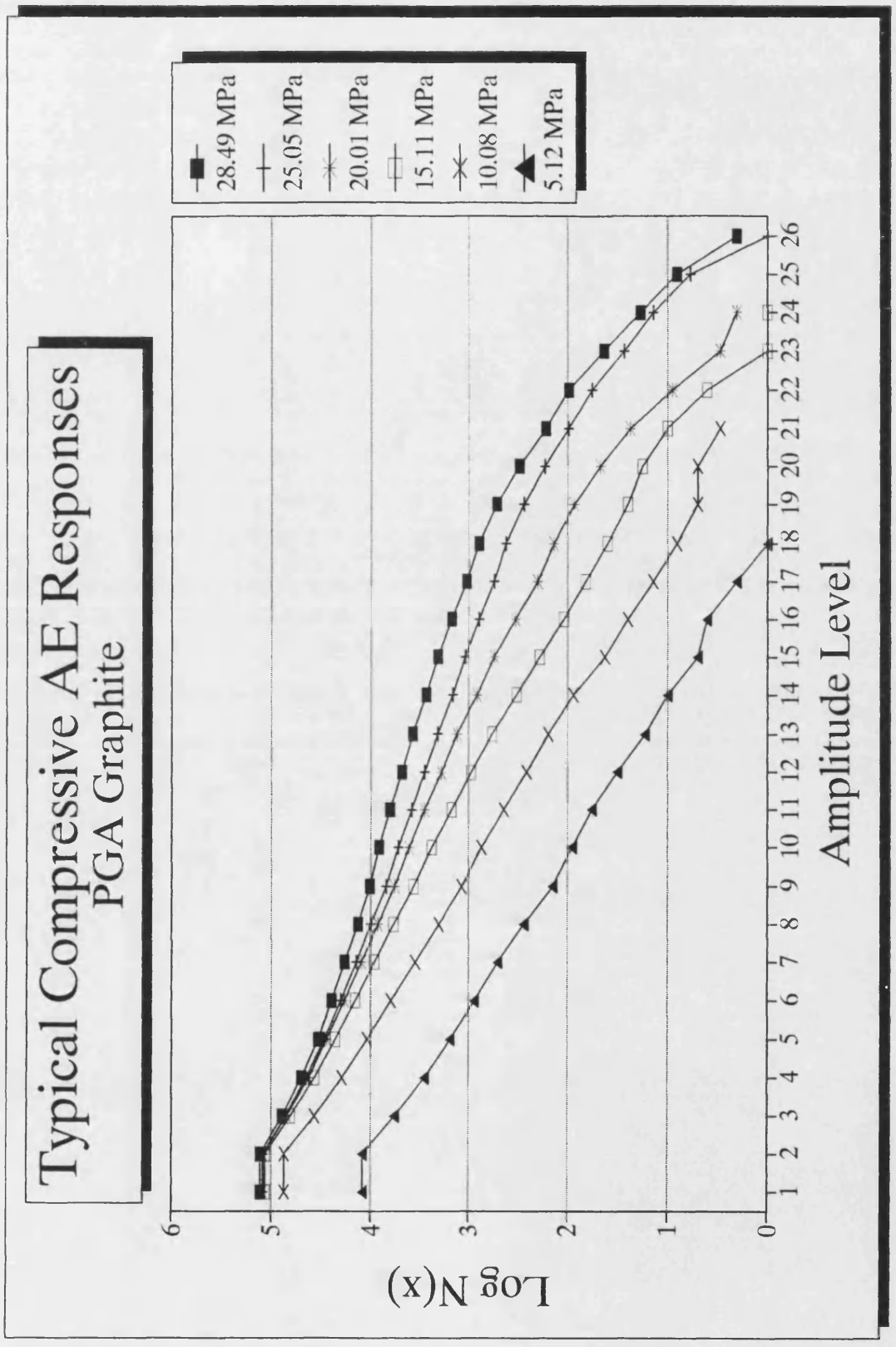

FIGURE 10.12 : An amplitude distribution for PGA graphite loaded monotonically to failure in compression showing the "bowing" effect and the deviation from the Pollock distribution.

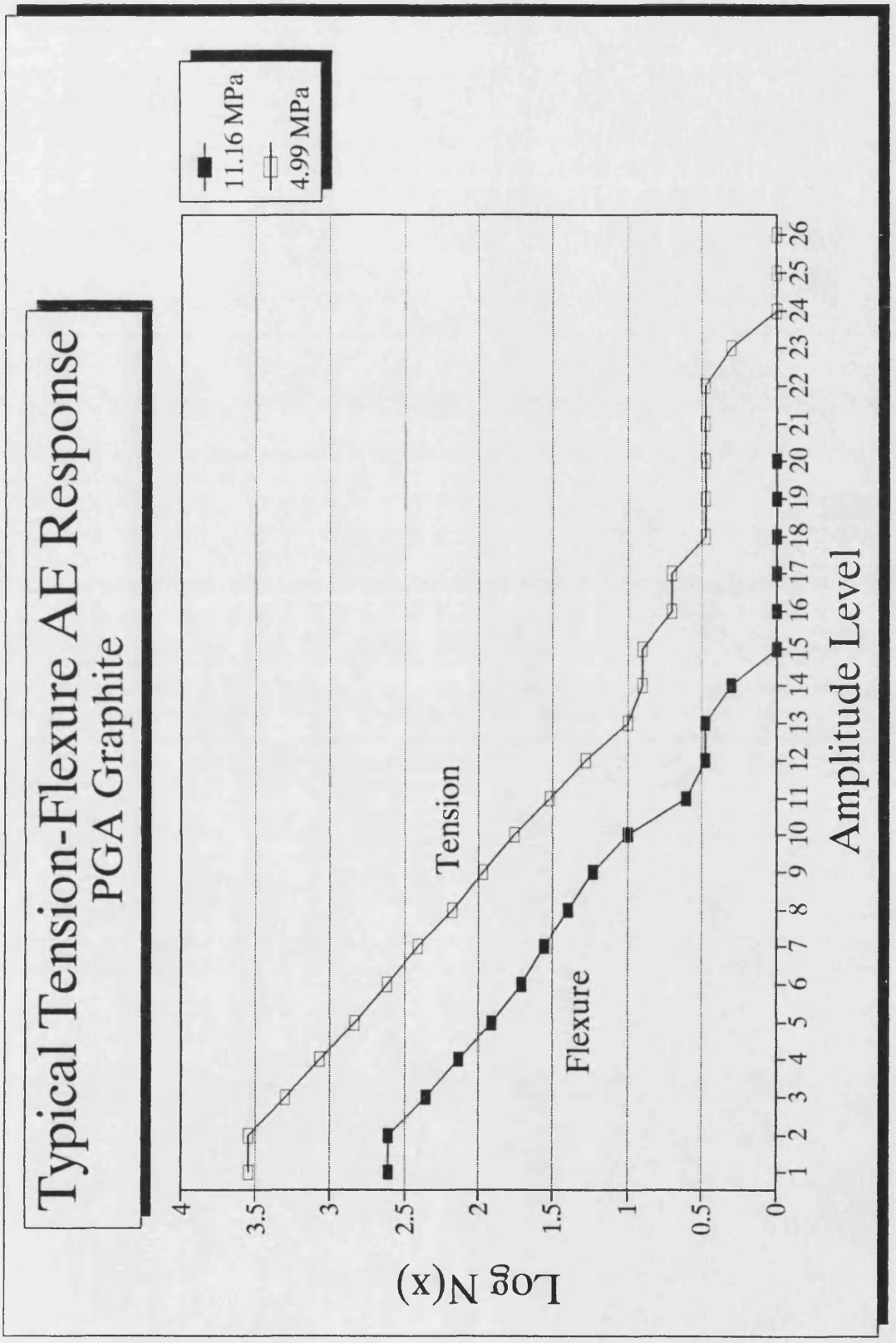

FIGURE 10.13 (a) : An example of an amplitude distribution for PGA graphite subjected to two load cycles to 5 MPa (tension) and 10 MPa (flexure), respectively.

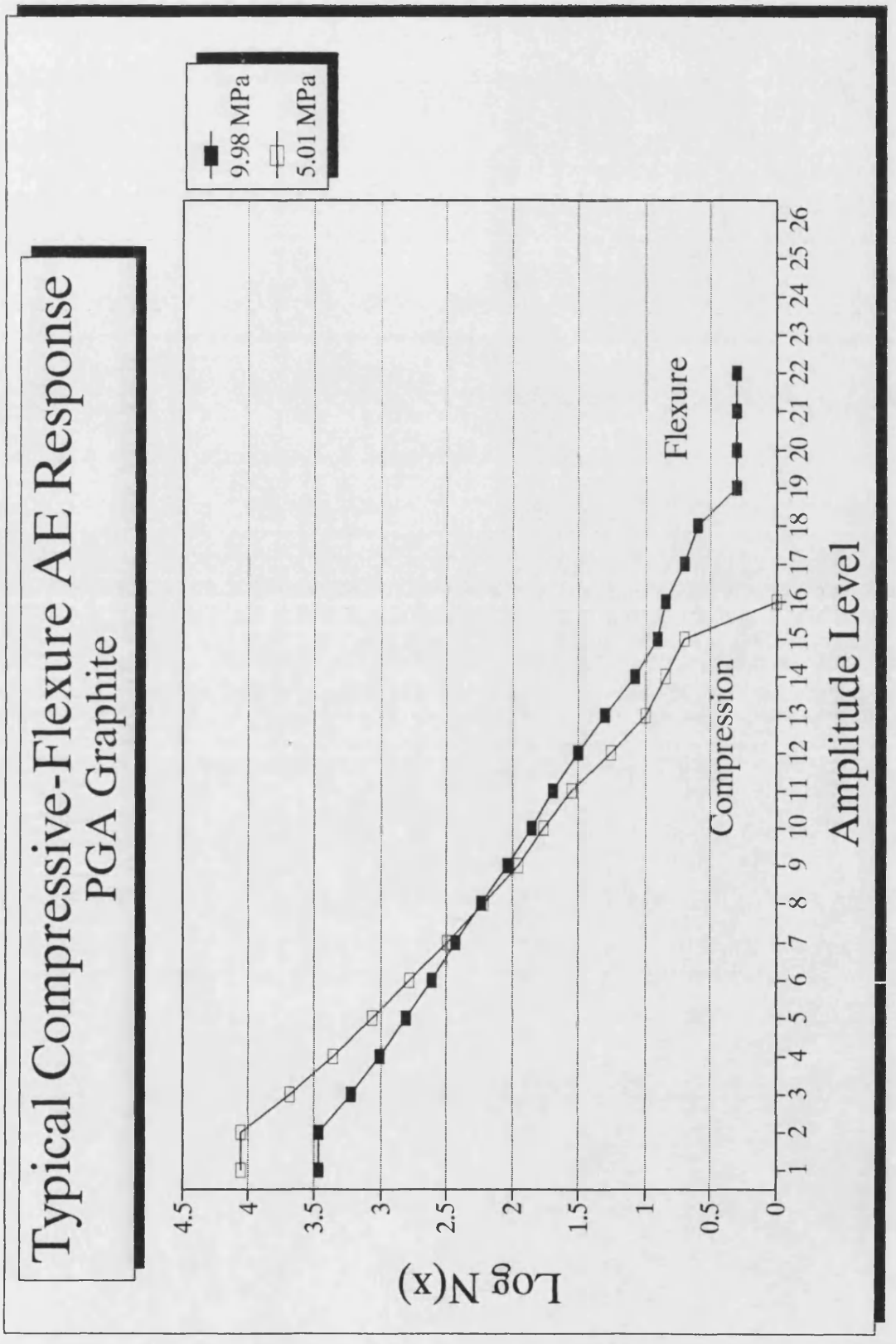

FIGURE 10.13 (b) : An example of an amplitude distribution for PGA graphite subjected to two load cycles to 5 MPa (compression) and 10 MPa (flexure), respectively.

CHAPTER ELEVEN : INVESTIGATION OF RECOVERY IN THE ACOUSTIC EMISSION RESPONSE WITH TIME

11.1 Introduction

The presence of the Felicity effect in nuclear graphites was demonstrated in Chapter Ten, and it was suggested that such behaviour was due to recovery mechanisms. In this chapter, an investigation of the time-dependent behaviour and recovery processes of graphite revealed by acoustic emission (AE) is presented. Two types of experiments are considered. In the first type, the amount of recovery between successive load cycles, indicated by the Recovery ratio, with time at zero stress between load cycles (§11.2) is investigated. The second type of experiment considers the amount of AE emitted at constant applied strain, and at zero stress after a load cycle, for a period of time (~16 hours) (§11.3).

11.2 The Relationship Between the Recovery Ratio and Time

11.2.1 Preliminary Experiment

A preliminary experiment was performed to demonstrate: (i) the effect of time between successive load cycles upon the AE response, *i.e.* whether there is an increasing Recovery ratio, B; and, (ii) the reproducibility of the Recovery ratio, B.

Specimens of IM1-24 graphite (20 x 20 x 150 mm^3) previously unstressed, and from the same source and similar to that used in the AE cyclic testing programme, were subjected to one of two test patterns: (i) ten specimens of IM1-24 were subjected to three consecutive, compressive load cycles to 5 MPa, 10 MPa and 15 MPa, as previously described in Chapter Ten (Set I); and, (ii) another six samples of IM1-24 graphite (20 x 20 x 150 mm^3) were loaded in compression to 5 MPa, unloaded, and immediately re-loaded to 10 MPa, unloaded and then only after one month re-loaded

to 15 MPa (Set II). For both sets of specimens, the Recovery ratio was calculated at both 5 MPa and 10 MPa.

Table 11.1 presents the B value at 5 MPa and 10 MPa for both sets of specimens. As previously demonstrated in Chapter Ten, for both sets of specimens, the B value increases from 5 MPa to 10 MPa and the two values of B are significantly different (95% confidence). As expected, B values at 5 MPa for both Set I and II specimens are not significantly different (95% confidence), since the time between unloading and re-loading of the first and second load cycles in both test patterns is zero. This demonstrates the reproducibility of the Recovery ratio, B. However, B values at 10 MPa for both Set I and II specimens are significantly different (95% confidence), even though the standard deviation of B at 10 MPa has increased from 25% to 75% of the mean for Set I and Set II specimens, respectively. For Set II specimens, the one month time span before reloading to 15 MPa has the effect of increasing B to three and half times the B value for Set I specimens at 10 MPa. Therefore, this experiment has shown that for a group of nominally identical specimens, that the B value remains constant after loading to 5 MPa followed by immediate reloading. It has further demonstrated a possible time-dependence of "recovery" in nuclear graphites by an increase in the B value after one month. This preliminary study has prompted the need to investigate this phenomenon further (reported in §11.2.2).

Recovery Ratio, B				
	IM1-24 Graphite			
	5 MPa	**10 MPa**	**5 MPa**	**10 MPa**
	Set I		**Set II**	
Mean	0.058	0.122	0.092	0.426
S.D.	0.023	0.032	0.087	0.345
n	9	8	6	6

TABLE 11.1 : The Recovery Ratio, B, For IM1-24 Graphite at 5 MPa and 10 MPa For The Two Test Patterns.

11.2.2 Quantitative Recovery-Time Experiment

This experiment extends the work described in the previous section by attempting to quantify the relationship between the "recovery" in nuclear graphites, shown by the Recovery ratio, and the time at zero stress between successive load cycles.

The standard experimental specimen size of 20 x 20 x 150 mm^3 was not available for this experiment due to the large number of specimens required, and therefore smaller specimens (10 x 10 x 70 mm^3) of IM1-24 were provided by Berkeley Nuclear Laboratories. These specimens were from a different source than that previously used in the AE testing programme. IM1-24 suffers from the disadvantage that in relation to other graphites it gives fewer AE events. However, it does have the advantage that this study becomes more relevant to the industrial aims of this project since IM1-24 is the moderator in the AGR.

Batches of six IM1-24 specimens (42 specimens in all) were subjected to two compressive load cycles: (i) loaded to 30 MPa and unloaded; and, (ii) after time, t, reloaded to 40 MPa and then unloaded, where t was 0, 10^0, 10^1, 10^2, 10^3, 10^4 and 10^5 minutes. For each time, t, the mean Recovery ratio, B, was calculated for each batch of six specimens at 30 MPa. These specimens were loaded to a higher stress than in §11.2.1 to increase the number of AE events generated from the smaller specimen.

11.2.2.1 Results

Figure 11.1 (a) and (b) give two typical examples of AE responses for zero time and 10^5 minutes between two successive load cycles, respectively. Figure 11.1 (a) is similar to that found for compressive cyclic loading discussed in Chapter Ten. However, as in Figure 11.1 (b), the AE response for a second load cycle after time t (>0) at zero load differs from that for immediate reloading. On subsequent load cycles, although the onset of AE was at zero stress, and after a short rise in ΣN at low stress, ΣN remained constant until the previous peak stress was approached. For

example, Figure 11.1 (b) differs from the first AE response (Figure 11.1 (a)) in that there is an initial rise in the ΣN at the onset of stress until ~8 MPa; on increasing stress there is little AE generation until just prior to the previous peak stress, at ~25 MPa, when ΣN begins to rise sharply. The initial release of AE at the low stress presumably relates to low energetic and easy deformation processes, and the initial AE increases with time at zero load between load cycles. Since these events do not occur if a specimen is immediately re-loaded, then they must be related to the recovery of the specimen.

Figure 11.2 presents a plot of the Recovery ratio, B (± 1 S.D.) versus time at zero stress between the two successive load cycles. Overall, there is a gradual increase of ~35% in the Recovery ratio, B, with logarithmic time over the three month period. The increase in mean values of B with t may be fitted to a linear relationship of the form

$$B = 7.2 \times 10^{-3} \log_{10} t + 0.083 \qquad (11.1)$$

with a Pearson's r coefficient of 0.68. The linear approximation of increasing B with log t (eqn. 11.1) is accounted for by the initial rise in ΣN in the AE response (see Figure 11.1(b)), *i.e.*, as time at zero stress between load cycles increases, the initial rise in ΣN also increases. The standard deviation in B values generally increases with time, and therefore the true trend is probably masked by the very large standard deviation at large times, *e.g.* at $t=10^5$ minutes, the standard deviation is ~57% of the mean B value. This is illustrated by none of the mean B values being significantly different (95% confidence) from the B at zero time, except that at 100 minutes. There are three possible causes for the large increase in the standard deviation: (i) variability in the quality of re-coupling of the transducer after time t; (ii) the recovery shown in each individual specimen is subject material variability, *i.e.*, some specimens are more prone or have a greater probability to recover or relax than others; or, (iii) the measurement

of recovery (*i.e.*, at 30 MPa) is remote from the initial increase in ΣN (*i.e.*, at ~0-8 MPa). Since the increase in ΣN which accounted for the increase in the B value occurred below 10 MPa, a modification was made to the Recovery ratio (in this special case only) to take account of this, so that a closer examination of recovery at low stresses can be made. Instead of calculating the ratio of ΣN values on the n^{th} and $(n+1)^{th}$ cycles at the peak stress on the n^{th} cycle, for the "special" case only, the ΣN values were also determined at 10 MPa giving the value B'.

Figure 11.3 presents the Recovery ratio at 10 MPa, B', versus time, t, at zero stress between load cycles. The plot is similar to Figure 11.2 in that there is a gradual increase in B' with logarithmic time over the three month period, but the increase in B' is more marked than for B. The increase in mean B' values with t may be fitted to a linear relationship of the form

$$B' = 56.7 \times 10^{-3} \log_{10} t + 0.034 \qquad (11.2)$$

with a Pearson's r coefficient of 0.91, which is much higher than for a similar relationship for B, demonstrating that the increase in ΣN at low stresses is much more time dependent than any increase in ΣN at higher stresses.

11.3 Semi-Quantitative Stress Relaxation Experiment

It has now been demonstrated using AE that recovery processes occur in nuclear graphites on unloading to zero stress between successive load cycles and the extent of recovery is time dependent. The work presented in this section aims to demonstrate that the acoustic emission technique can be used to study relaxation and recovery processes at constant strain and also at zero stress for long periods of time.

11.3.1 Experimental Details

AE was recorded from both PGA and IM1-24 graphite specimens (20 x 20 x 150 mm^3) subjected to two types of tensile and compressive load patterns: (i) monotonically loaded to stress, σ_1, unloaded and the AE monitored for a time, t, at zero stress; and, (ii) monotonically loaded to stress, σ_1, and AE monitored for time, t, at constant strain before unloading to zero stress; t was approximately 16 hours in all cases. For PGA and IM1-24 graphite, σ_1 was 70% and 80% of the failure strength, respectively. A lower value of σ_1 was used for PGA since the probability of failure was greater, as indicated from the standard deviation of the mean strength (see Table 7.1). The eight specimens used were from the same source and similar to that used for the AE cyclic testing programme described in Chapter Nine.

11.3.2 Results

For both types of test, curves of cumulative acoustic emission event count, ΣN, versus time were similar. Figure 11.4 (a) and (b) present examples of ΣN versus time curves for both (i) constant strain, and (ii) at zero stress after a load cycle (for PGA in compression). Both curves show that initially there is a rapid rise in ΣN after which the rate of AE generation gradually decreases with time, although AE is still being generated even after ~16 hours. The shapes of the curves of ΣN versus time suggest that the AE is generated by microstructural events, and not from background noise since in the latter case the rate of AE generation would be approximately constant. The curve shape also suggests that eventually ΣN will reach a limiting value, *i.e.*, there is a maximum amount of "recovery" that can occur.

For those specimens monitored at constant strain, ΣN after 10^3 minutes increased by between 0.8 and 3.4% of ΣN at the start of monitoring (see Table 11.2). The AE generated in graphite specimens monitored at zero stress after a load cycle varies between <0.1% to 1.4% of the ΣN immediately after unloading (see Table 11.3). It was shown in the stress cycling experiments presented in Chapter Ten that the number

of AE events generated on reloading was ~10% of the AE events generated at the previous peak stress, and these were considered to be the result of recovery mechanisms. These experiments have shown that the number of AE events generated at zero stress after a previous load are less than 2% of AE events generated at the previous peak stress. This suggests that the relaxation processes which occur at zero stress are sufficient to cause "new" AE events on reloading polycrystalline graphites.

Creep in graphites at ambient temperatures was first demonstrated by Andrew *et al.* (1960) who measured creep strain directly using cantilever beams. Since that time there has been very little additional published work on creep of graphites at ambient temperatures. By contrast, creep and creep strain recovery for graphites at high temperatures have been well documented (*e.g.* Zukas and Green, 1968). Thermally activated creep of a reactor graphite is just detectable at ~1200 °C and only becomes rapid at ~2500 °C. At temperatures below 2000 °C, the creep strain consists of a primary (or transient) creep with a barely detectable secondary component (Losty, 1970). Very few studies consider creep below 1500 °C, probably because primary creep is assumed to be insignificant at these temperatures.

When graphite is held at constant strain in the temperature range 2100 to 2700 °C, the material relaxes and a reduction in stress may be expected (Smith, 1968). In the present work at ambient temperatures, for both PGA and IM1-24 graphites, no significant stress relaxation (<0.2% σ_1) is recorded at constant compressive strain, but in tension the applied stress decreases by ~5% over 16 hours, as shown in Figure 11.5 (for IM1-24). Possibly, this may be attributed, in part, to the relaxation of the tensile apparatus and uniaxial joints. Smith (1968) studied the tensile stress relaxation at temperatures between 2100 °C and 2700 °C and recorded a reduction of ~45% at 2300 °C after 2.5 hours. Smith (1968) assumed the relaxation mechanisms to be closely related to those responsible for creep.

Davidson and Losty (1958) first demonstrated for a range of carbon and graphite materials, including reactor graphite, that significant transient creep and creep strain recovery occurred at temperatures between 1000 °C to 2000 °C, using spring and cantilever specimens. They found that the strain after time t (in minutes) fitted the relationship

$$\varepsilon_t = \sigma [1/E_T + (C/E_0) \exp(-E_1/RT) \log t/1 + Dt \exp(-E_2/RT)] \quad (11.3)$$

where σ is the applied stress, E_0 and E_T are the Young's moduli at ambient temperature and at temperature T (K), respectively, C is a constant (~13), D is a constant, E_1 and E_2 are activation energies of primary and secondary creep, and R is the gas constant. At a particular stress and temperature, equation 11.3 simplifies to

$$\varepsilon_t = A + k \log t + Bt \quad (11.4)$$

where A ($=\sigma/E_T$), k and B are constants. If

$$k_1 = \exp(-E_1/RT) \quad (11.5)$$

and

$$k_2 = \exp(-E_2/RT) \quad (11.6)$$

then

$$k = Ck_1\sigma / E_0 \quad (11.7)$$

and

$$B = Dk_2\sigma \quad (11.8)$$

Losty (1970) quotes the activation energies for primary and secondary creep for a reactor graphites above ~2000 °C as ~85 kJ mol^{-1} and ~170 kJ mol^{-1}, respectively. The activation energy for secondary creep, E_2, is sufficiently high that the contribution to the creep strain from secondary creep is negligible below 1500 °C. Similarly,

Davidson and Losty (1958) also suggested that the creep recovery above 1500 °C on removing the load conformed to the function

$$\varepsilon_t' = A' + k' \log t \qquad (11.9)$$

where ε_t' is the strain after time t at zero stress, and A' and k' are constants. However, they did not discuss the meaning of the constants A' and k', nor did they present any results.

Andrew *et al.* (1960) detected creep in a reactor graphite at ambient temperatures by measuring small increases in deflection of end-loaded cantilevers and showed that creep strain increased logarithmically with time. The amount of creep was small compared with the overall deflection of the rod, *e.g.* after eight hours, the total creep amounted to 2% of the total deflection. As the creep strain increased with time of loading, the permanent set on unloading also increased, but was subject to some recovery after a few hours. They attributed this behaviour to the formation, opening and closing of microcracks in the binder phase, which are similar to Mrozowski cracks.

Jenkins (1963) investigated primary creep in graphites between 20 °C and 1500 °C and proposed a model of primary creep which considered it as a thermally-activated process which gave the approximate relationship

$$\varepsilon(t) - \varepsilon(t^*) = K \ln (t/t^*) \qquad (11.10)$$

where $\varepsilon(t)$ is the strain after time t, $\varepsilon(t^*)$ is the strain after one minute and K is a constant. Thus, this relationship is of the same form as that found experimentally by Davidson and Losty (1958) (eqn. 11.4). Recovery of the creep strain on removal of the stress was predicted to obey a similar logarithmic law.

The phenomenon shown in Figure 11.4 (a) resembles, in shape, a high temperature primary creep curve for a polycrystalline graphite (*e.g.* see Pugh, 1971 or Dergunov *et al.*, 1972). Acoustic emission occurs as a result of abrupt relaxation mechanisms. Thus, a possible explanation for the AE emitted at constant strain may be stress relaxation caused by localised creep within the material which is activated by the applied strain energy. If each localised creep mechanism consists of abrupt increments of local creep strain, $\Delta\varepsilon$, and each increment acts as an AE source, then the sum of AE events at time, t, ΣN_t, is directly related to the accumulation of creep strain increments, *i.e.*, $\Sigma N_t = f(\Sigma\Delta\varepsilon) = f(\varepsilon_t)$. Therefore, the ΣN - time curves for constant strain can be related to the creep equation (eqn. 11.4) presented by Davidson and Losty (1958), such that

$$\Sigma N_t = A_{ae} + k_{ae} \log t + B_{ae}t \qquad (11.11)$$

where A_{ae}, k_{ae} and B_{ae} are constants similar in nature to A, k and B in equation 11.4. Strictly equation 11.4 assumes an instantaneous Hookean response ($\varepsilon = \sigma/E$), whereas graphites are non-Hookean due to the occurrence of basal plane shear and microcracking which give rise to AE. However, in the context of the present experiment, the AE in response to the initial loading can be regarded as instantaneous in comparison with the additional AE which occurs over 16 hours. Thus, A_{ae} should represent the cumulative AE event count due to the instantaneous load at time t=0, ΣN_0. Therefore

$$\Sigma N_t = \Sigma N_0 + k_{ae} \log t + B_{ae}t \qquad (11.12)$$

As with the relationship found by Davidson and Losty (1958) (equation 11.4), the third term in equation 11.12 represents the contribution of secondary creep to the creep strain. To illustrate that at ambient temperatures $B_{ae} \approx 0$, equation 11.12 can be rearranged to give

$$(\Sigma N_t - \Sigma N_0) /t = (k_{ae} \log t) /t + B_{ae} \quad (11.13)$$

Thus a plot of $(\Sigma N_t - \Sigma N_0) /t$ versus log(t)/t will give a straight line through the origin if $B_{ae} \approx 0$, as is shown in Figure 11.6. This is the case for all the specimens tested. Therefore secondary creep is negligible and equation 11.12 now simplifies to

$$\Sigma N_t = \Sigma N_0 + k_{ae} \log t \quad (11.14)$$

Figure 11.7 presents ΣN_t versus log t for the ΣN-time curve presented in Figure 11.4(a). For both PGA and IM1-24 in tension and compression, similar trends were found. From Figure 11.7, a straight line can be extrapolated from the linear region of data points to the ΣN_t axis. This intercept represents the cumulative AE event count at t=0, ΣN_0, from the instantaneous deformation arising from the applied load. As can be seen from equation 11.14, the gradient of the plot is k_{ae}. Table 11.2 presents these results for specimens held at constant strain. The ΔΣN value presented in Table 11.2 represents the change in the ΣN over the first 1000 minutes of AE monitoring.

In line with the results presented in Chapter Ten, PGA is seen to emit more AE events than IM1-24 in tension and compression at peak load, and, in addition, this is also the case for those AE events emitted after reaching peak load over the test period. For both graphites, the value of ΔΣN in compression is greater than in tension which suggests that shear deformation is an important component of the creep mechanism. The values of k_{ae} follow similar trends to ΔΣN values, *i.e.* both are measures of the rate of rise of ΣN_t. The low values of ΔΣN and k_{ae} for IM1-24 in tension are in line with earlier findings (Chapters Seven and Ten) which suggest that the microstructure of IM1-24 prevents easy shear deformation from occurring.

Graphite	**IM1-24**	**IM1-24**	**PGA**	**PGA**
Test Mode	Tension	Compression	Tension	Compression
σ_1	80% σ_f	80% σ_f	70% σ_f	70% σ_f
ΣN_0	1767	48143	33500	137811
$\Delta\Sigma N$ (1000 mins)	60	805	530	1091
k_{ae}	16	261	176	371
B_{ae}	0	0	0	0
Stress Relaxation	~5%	<0.2%	~5%	<0.2%
$\Delta\Sigma N/\Sigma N_0$ (%)	3.4	1.7	1.6	0.8

Table 11.2 : AE Data For The Constant Strain Experiment

Using the data derived from the experimental results in eqn. 11.14, a model creep curve can be plotted as in Figure 11.8 which closely fits the experimental AE data.

For those specimens which were subjected to a load cycle and the AE monitored at zero stress, the AE generated may be attributed to "creep" recovery mechanisms, and therefore in a similar manner to AE generated at constant strain, the cumulative AE event count after unloading at time t, $\Sigma N_t'$ may be expected to fit a function similar to that suggested by Davidson and Losty (1958) (equation 11.9), such that

$$\Sigma N_t' = \Sigma N_0' + k_{ae}' \log t \qquad (11.15)$$

where $\Sigma N_0'$ is the cumulative AE event count immediately after unloading, k_{ae}' is a constant similar to k_{ae} in equation 11.14. Figure 11.9 presents a typical plot of $\Sigma N_t'$ versus log t (for the result presented in Figure 11.4 (b)) for specimens monitored at zero stress. In a similar manner to the data obtained for constant strain specimens, Table 11.3 presents the AE data obtained for those specimens monitored at zero stress after a load cycle. The values of $\Sigma N_0'$, except for PGA in tension, are similar to those values of ΣN_0 presented in Table 11.2, as expected. However, the values of $\Delta\Sigma N'$ are much smaller than the equivalent values of $\Delta\Sigma N$ in Table 11.2 showing that the extent of "creep recovery" at zero stress, for both graphites in both testing modes, is less than

under constant strain conditions. For both graphites k_{ae}'(tension) < k_{ae}'(compression) showing that the extent of creep recovery is less in tension. These results suggest that an important component of creep recovery is reversal of shear deformation as a result of back stresses due to boundary constraint as suggested by Ioka and Yoda (1987).

Graphite	**IM1-24**	**IM1-24**	**PGA**	**PGA**
Test Mode	Tension	Compression	Tension	Compression
σ_1	80% σ_f	80% σ_f	70% σ_f	70% σ_f
$\Sigma N_0'$	3207	52470	15887	155127
$\Delta\Sigma N'$	46	113	41	89
k_{ae}'	18	31	18	29
$\Delta\Sigma N'/\Sigma N_0'$ (%)	1.43	0.23	0.26	<0.1

Table 11.3 : AE Data For The Zero Stress Experiments

As in the case for constant strain experiments, using the data derived from the experimental results in equation 11.15, a model creep recovery curve can be plotted as in Figure 11.10 which fits that of the experimental curve reasonably well.

11.4 Summary

These semi-quantitative experiments have demonstrated the use of AE as a tool to investigate relaxation and recovery mechanisms. They have also provided substantial evidence to support the view that the Felicity effect observed on stress cycling graphites is due to recovery processes which occur upon unloading. They have also demonstrated that the extent of recovery shown in the AE response for a graphite is time and stress dependent, *i.e.* as time at zero stress between load cycles increases, the more a specimen tends to recover its original state. However, there is scope for further work which would explore the dependency of recovery processes on temperature and on the stress applied either at constant strain or prior to unloading. The temperature dependence of recovery processes would possibly allow the calculation of activation energies.

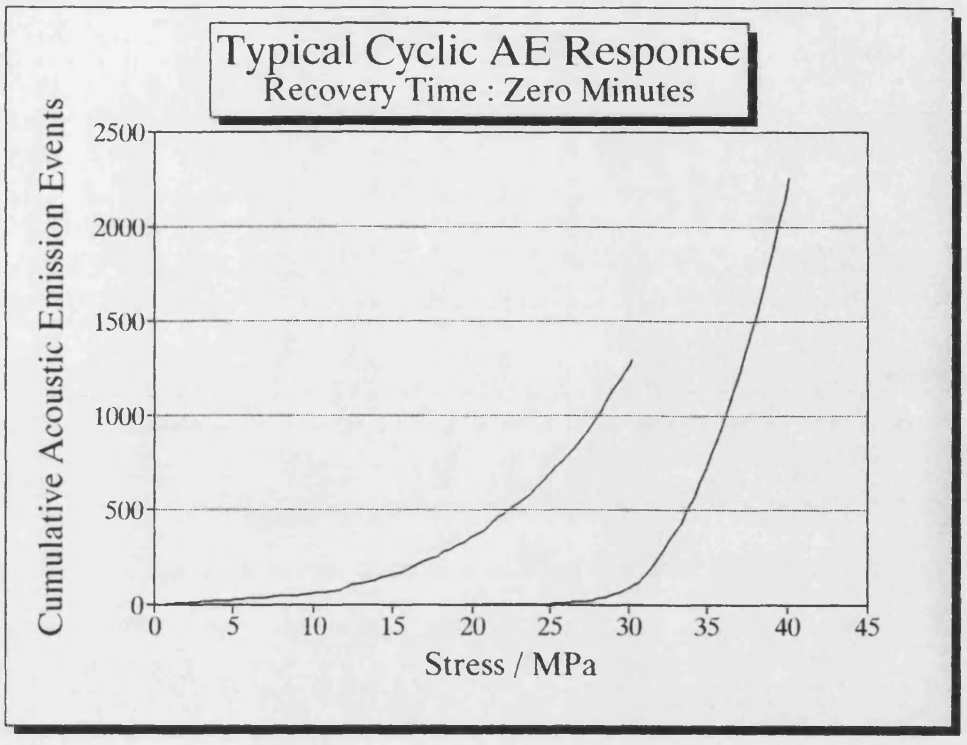

FIGURE 11.1 (a) : A typical AE response from IM1-24 graphite subjected to t compressive load cycles, where the time between each load cycle is zero.

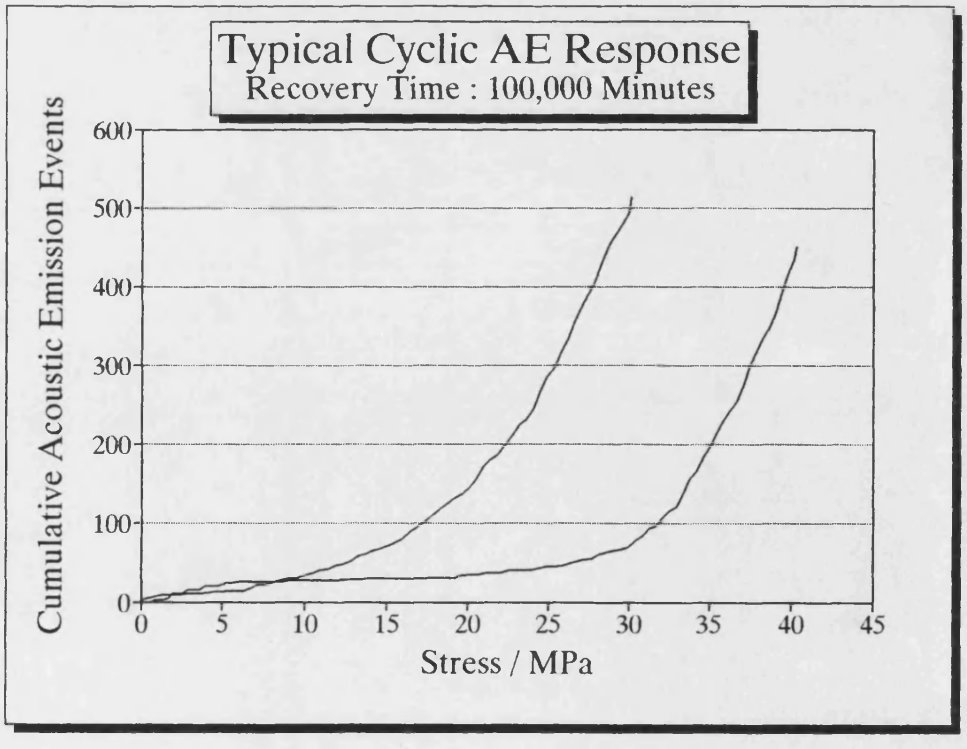

FIGURE 11.1 (b) : A typical AE response from IM1-24 graphite subjected to two compressive load cycles, where the time between each load cycle is 10^5 minutes

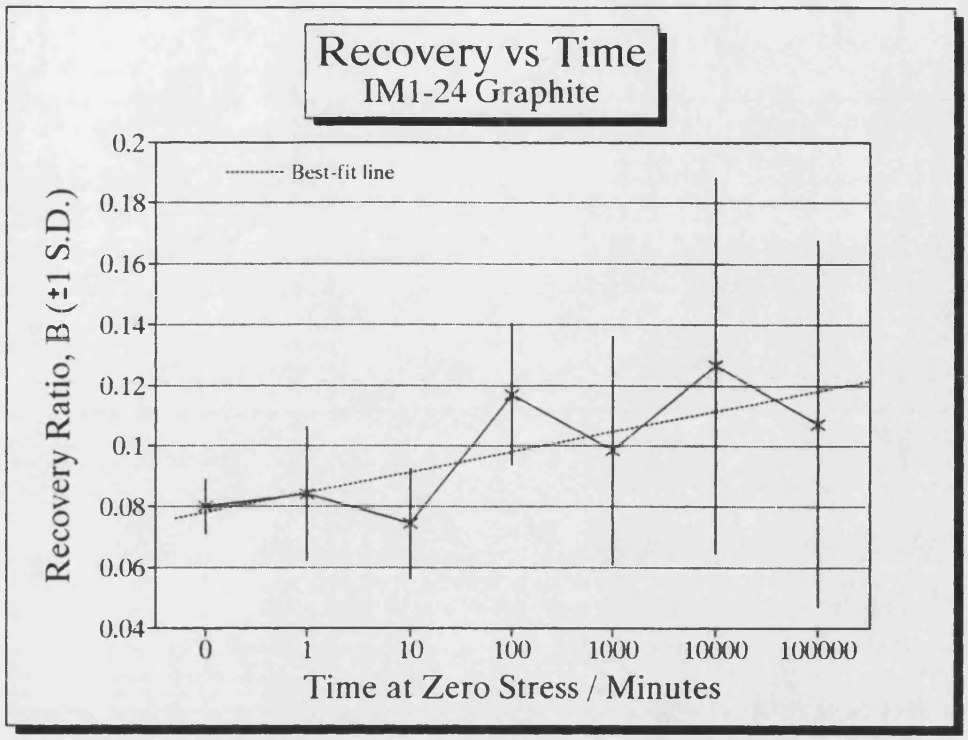

FIGURE 11.2 : A plot of the Recovery ratio, B (± 1 S.D.), versus time at zero stress between two successive load cycles.

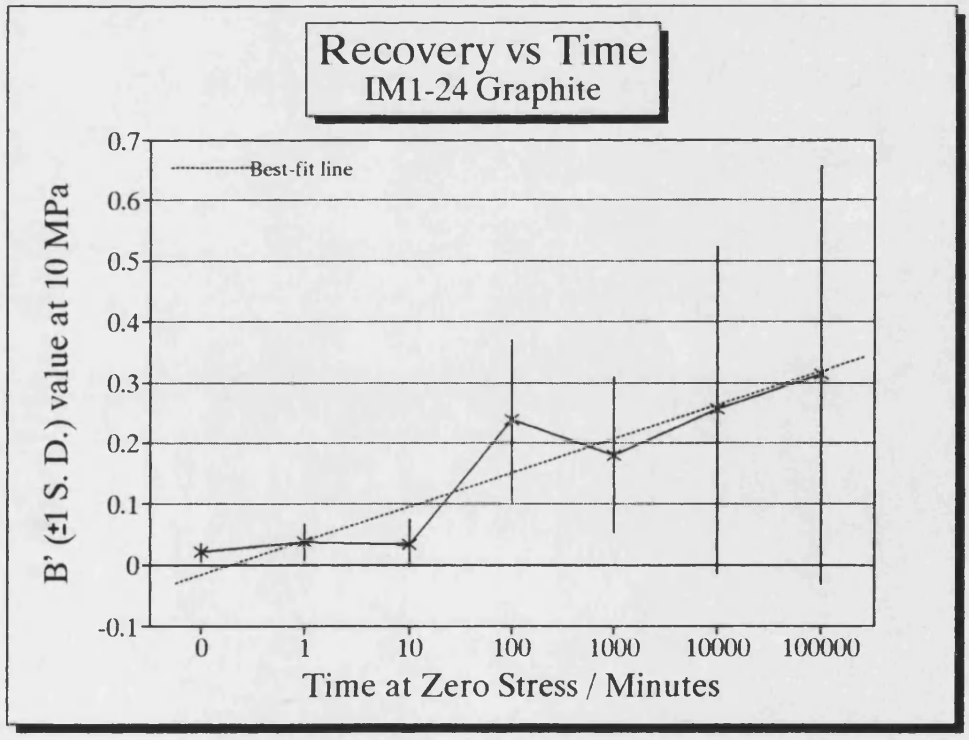

FIGURE 11.3 : A plot of the Recovery ratio at 10 MPa, B' (± 1 S.D.), versus time at zero stress between two successive load cycles.

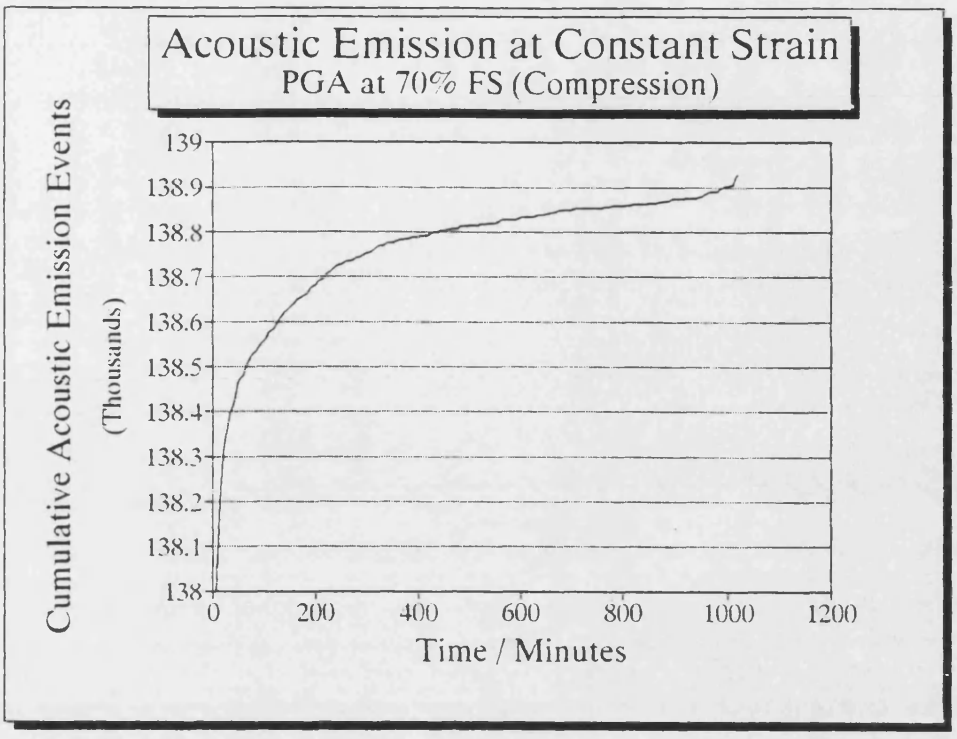

FIGURE 11.4 (a) : An example of ΣN versus time curve recorded for a specimen held in constant strain (PGA in compression at 70% failure strength).

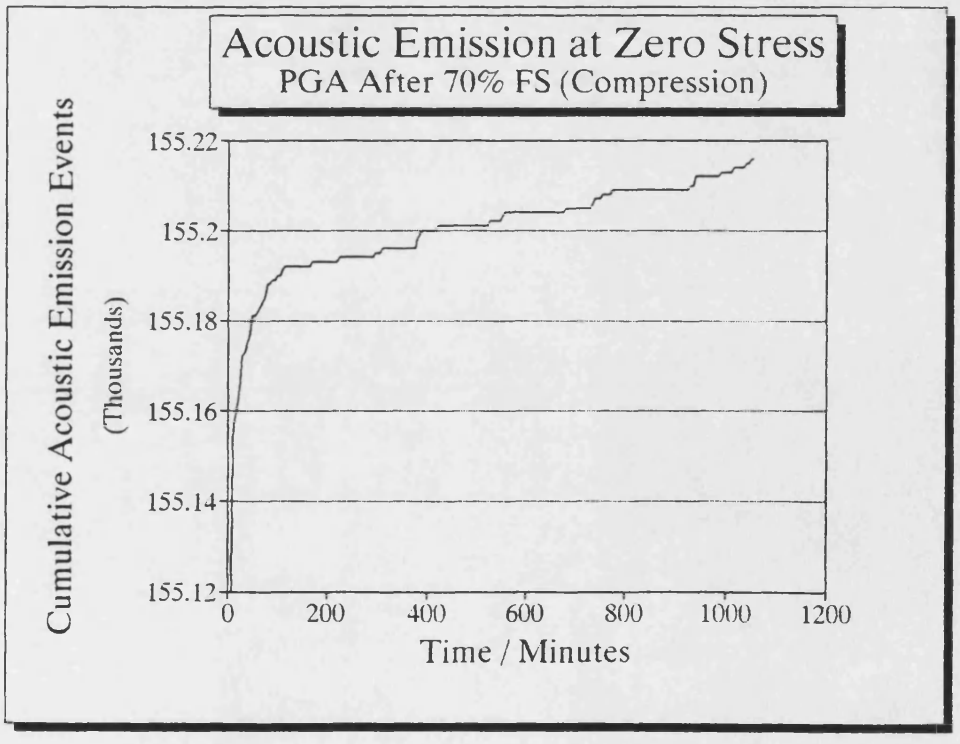

FIGURE 11.4 (b) : An example of ΣN versus time curve recorded for a specimen at zero load after a load cycle (for PGA after a load of 70% failure compressive strength).

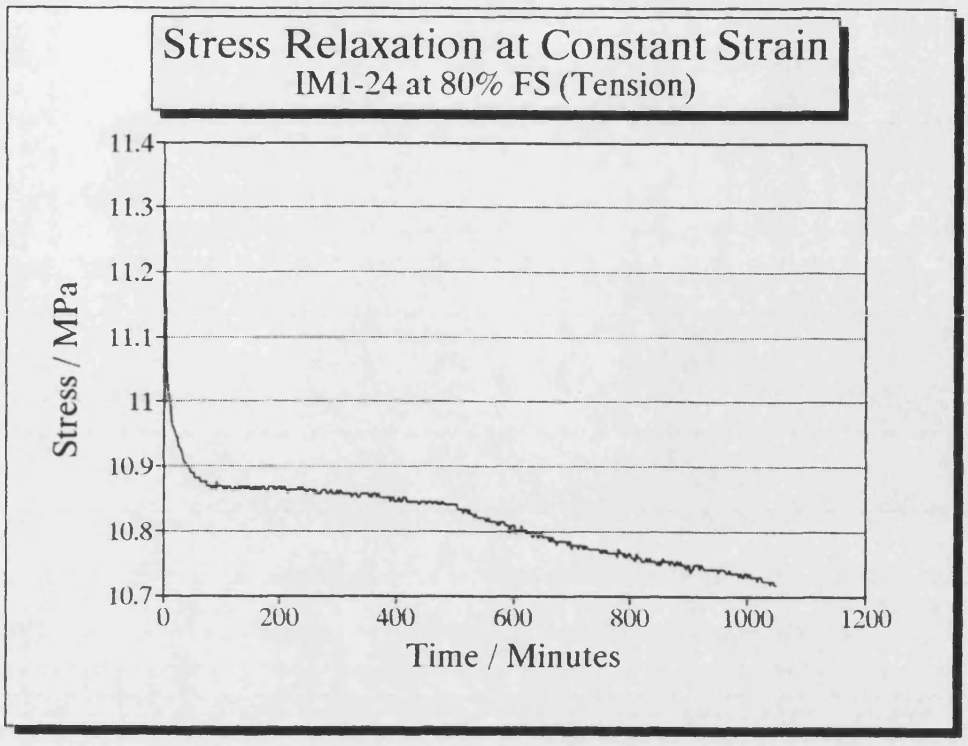

FIGURE 11.5 : A example of tensile stress relaxation for a graphite specimen at room temperature held at constant strain (IM1-24 at initially 80% failure strength).

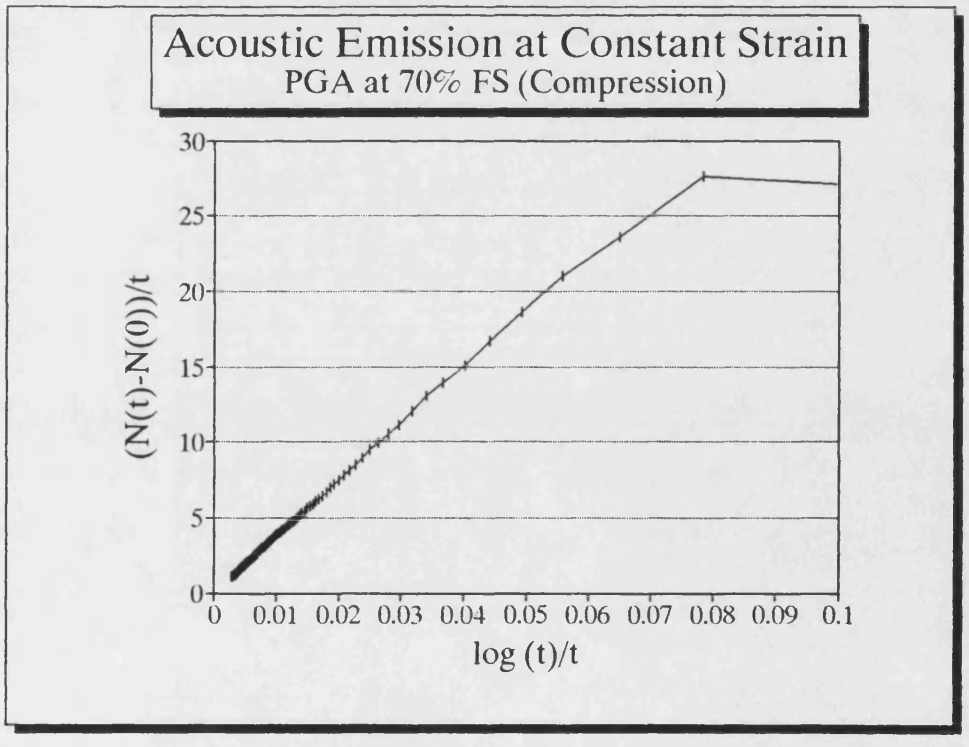

FIGURE 11.6 : A plot of $(\Sigma N_t - \Sigma N_0)/t$ versus log(t)/t illustrating the contribution to the ΣN-time curve from the secondary component of eqn. 11.4 is zero (*i.e.* $B_{ae} \approx 0$)

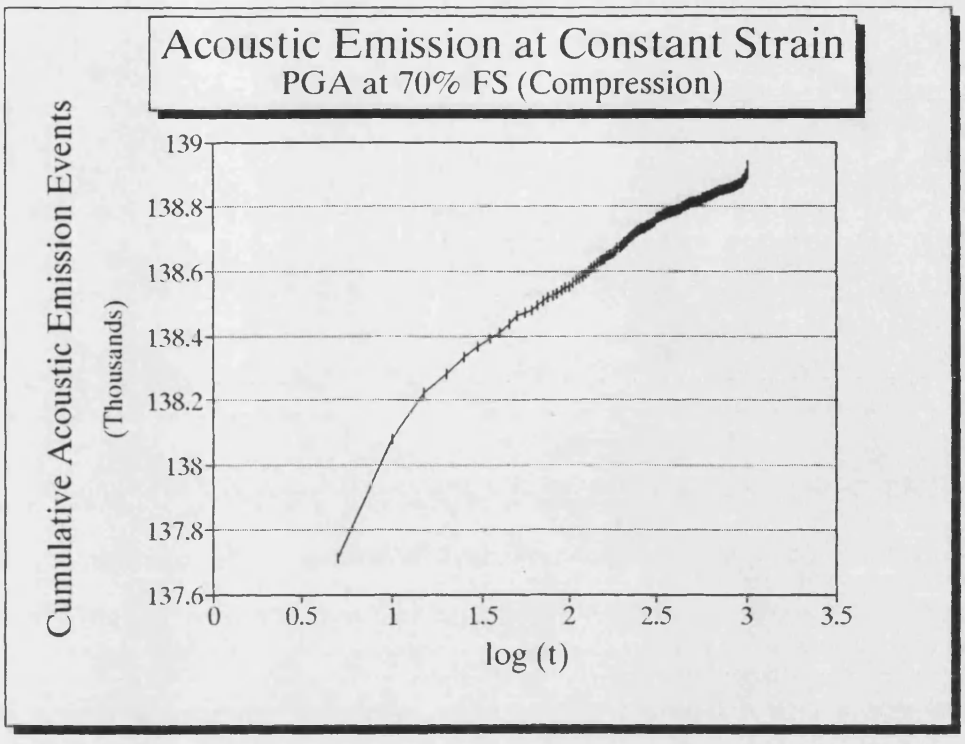

FIGURE 11.7 : A plot of ΣN_t versus log (t) for a specimen held in constant strain (PGA in compression, see Figure 11.4(a)).

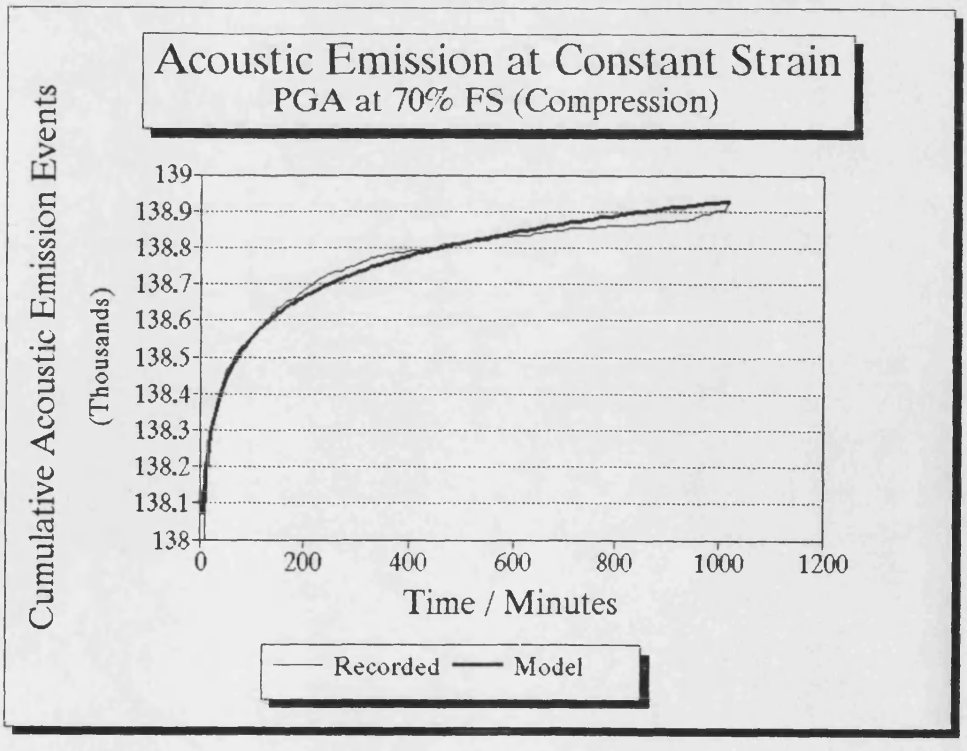

FIGURE 11.8 : A comparison plot of the recorded ΣN_t-time curve and the theoretical equation using experimental derived constants.

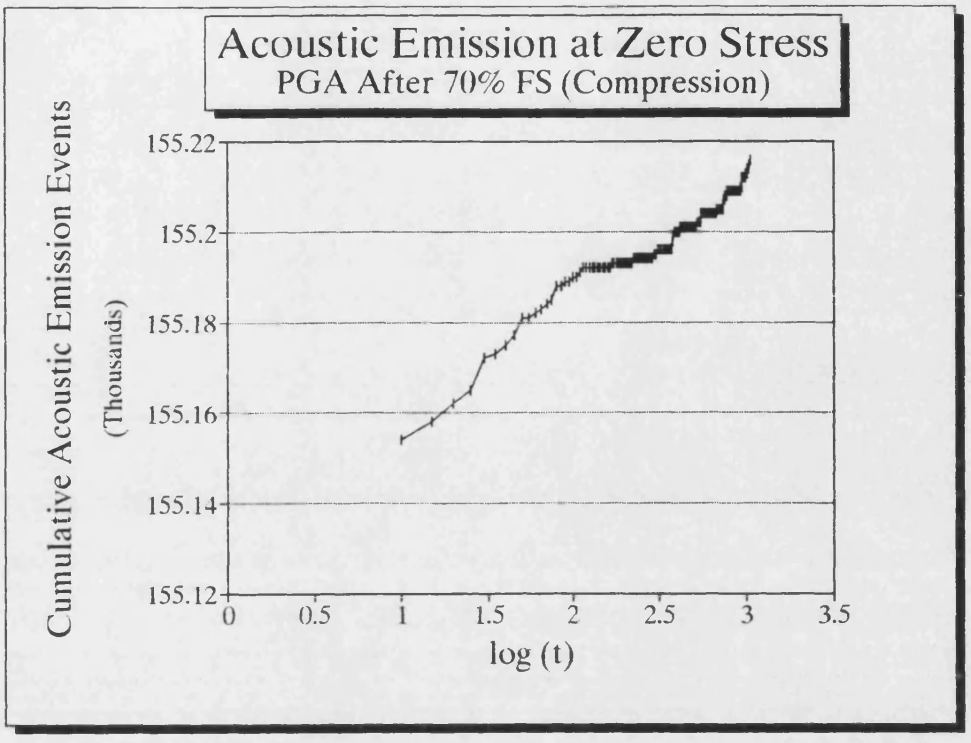

FIGURE 11.9 : A typical plot of $\Sigma N_t'$ versus log (t) for a specimen monitored at zero stress after a load cycle.

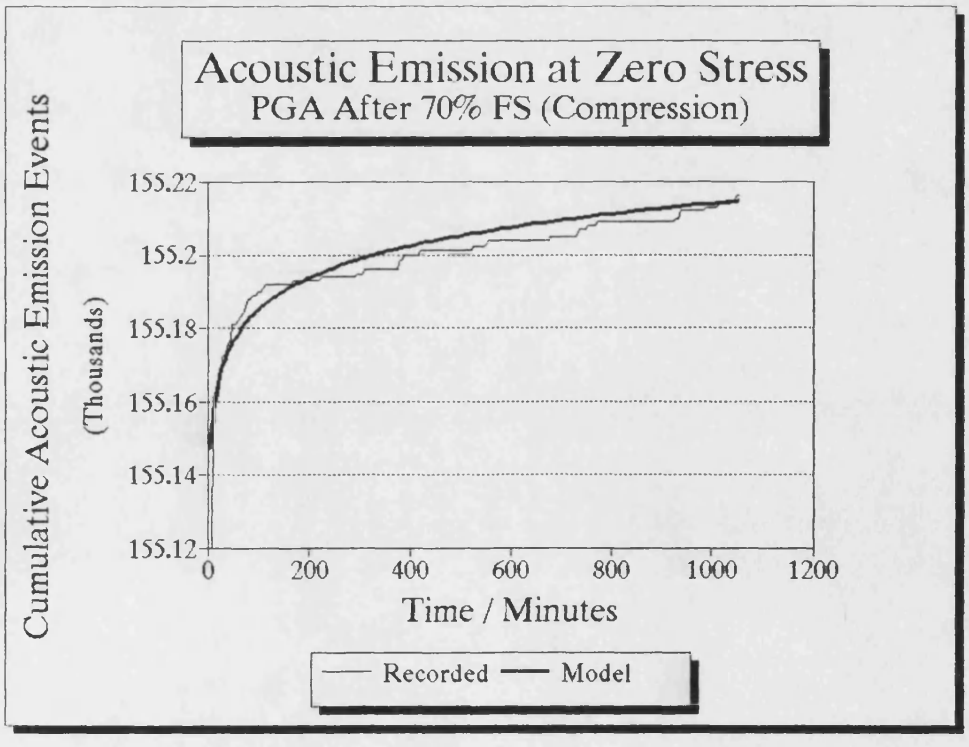

FIGURE 11.10 : A comparison plot of the recorded $\Sigma N_t'$-time curve and the theoretical equation using experimental derived constants.

CHAPTER TWELVE : ACOUSTIC EMISSION FROM IRRADIATED NUCLEAR GRAPHITE

12.1 Introduction

This chapter considers AE from irradiated graphite from a fuel sleeve discharged after a full lifetime (~5 years) in an Advanced Gas-Cooled Reactor (AGR). Since the mechanical and physical properties of irradiated graphite differ from unirradiated graphite due to the effects of reactor environment (see Chapter Five), differences in the AE response between irradiated and unirradiated graphite are to be expected. A comparative study of the AE responses of irradiated sleeve graphite compared to the that of similar unirradiated graphite is reported in this chapter.

It has been suggested by many authors (*e.g.* Scott, 1991) that various AE instruments produce different AE responses, and that absolute AE event counts are sensitive to the experimental system. For example, the AE signal may be conditioned by the resonant system comprising the transducer, specimen, amplifiers, *etc.* and therefore the resulting analogue output will differ from instrument to instrument. Any conclusion derived from AE studies must be able to stand up to scrutiny, and therefore to show confidence in the AE technique, a second and contemporary study was undertaken to compare the AE responses from two different experimental AE systems, used simultaneously (see Chapter Nine). The investigation reported in this chapter was carried out at Berkeley Nuclear Laboratories (BNL).

12.2 Experimental Details

12.2.1 Material

An experimental AGR Gilsocarbon sleeve graphite was chosen (rather than a standard needle-coke sleeve graphite) for this work because it is a similar type of graphite to

that used as the moderator (IM1-24), and also because the mean internal stresses of the specimens, generated in-reactor, were previously measured by a slot closure technique (Reed *et al.*, 1989). Nine graphite specimens were taken from two elements of a pilot loading Stage II fuel stringer (eight from element 4 and one from element 7). A Stage I fuel stringer typically consists of eight similar elements (plus other components). Each element is composed of 36 fuel pins held by steel braces within two graphite sleeves. A Stage II fuel stringer is an improved design from Stage I that enables higher doses (from 18 to 24 GWd/t_eU) and has a reduced probability of failure during life. A Stage II fuel element mainly differs from a Stage I fuel element in that it consists of a single, and consequently, thicker graphite sleeve (see Figure 12.1).

Gilsocarbon sleeve graphite is a near-isotropic graphite, similar to IM1-24, except that it has been extruded rather than moulded. There are two sources of manufacture, Union Carbide (BAEL) and Pechiney (SERS), which use the same spherical Gilsocarbon filler particles and an American pitch binder. Both the BAEL and SERS graphites have a static unirradiated elastic modulus of 9.63 GPa (Tucker, 1992) and a density of 1.83 g cm^{-3} (~19% porosity), but have different open pore volumes of 9.1% and 7.4%, respectively.

12.2.1.1 Unirradiated Stage I and Stage II Specimens

In addition to the irradiated graphite, unirradiated sleeve specimens were obtained so a that comparison could be undertaken to highlight the effect of reactor conditions upon the AE response. The unirradiated Gilsocarbon graphite originated from the end of a Stage I fuel sleeve. Curved beam specimens were machined from three hollow slices of the sleeve. One of the three slices was the butt of the Stage I sleeve with dimensions similar to a Stage II sleeve, thereby allowing some simulation of Stage II specimens to be made. Each specimen dimension was recorded for use in stress calculations.

12.2.1.2 Irradiated Stage II Specimens

Irradiated Gilsocarbon graphite specimens were obtained from a pilot loading stringer C3612 discharged in November 1989 from channel 3468 in the inner zone of Hunterston reactor 3. During life, the stringer experienced a stringer mean irradiation of 19.995 GWd/t_eU over 1437 equivalent power days. Hollow slices (~10 mm thick) of two Gilsocarbon graphite Stage II sleeve elements (elements 4 and 7) were obtained and cut (segmented in to eight pieces) into curved beams, as in Figure 12.1. Each irradiated curved beam specimen had an inner radius of 192.0 mm and a thickness of 22.8 mm (inclusive of outer ribs). Unlike the Stage I sleeve, the Stage II sleeve has a external surface with a ribbed profile (to reduce vibration during refuelling). Due to the difficulty of cutting ring specimens in a shielded area using manipulators, each specimen has a slight variation in thickness, therefore the average width, w, of each curved beam specimen was determined from 6 measurements along its length (Table 12.1) for use in stress calculations. Table 12.1 shows that the variation in thickness was between 3 and 7%.

Specimen Identification	Mean Thickness /mm
612/4/5/4	9.7 ± 0.4
612/4/5/7	10.2 ± 0.3
612/4/5/2	10.0 ± 0.4
612/4/5/3	9.8 ± 0.4
612/4/5/1	10.0 ± 0.7
612/4/3/4	9.3 ± 0.3
612/4/3/5	9.6 ± 0.4
612/7/4/1	8.6 ± 0.7
612/4/5/6	9.8 ± 0.3

TABLE 12.1 : The Designation Numbers and Mean Width, w, of Irradiated Gilsocarbon Sleeve Specimens.

Each specimen was marked with a serial number which identifies the location of the sample within the reactor, and thus the expected internal stress. The serial number consults of four parts separated by a slash (/), *e.g.* 612/4/2/3, which identify (i) the

stringer, *e.g.* 612; (ii) the fuel sleeve element *e.g.* 4; (iii) the ring within the sleeve, *e.g.* 2, and (iv) the sample number from the ring, *e.g.* 3. This experiment was limited to a small number of specimens due to the limited availability of irradiated material, the prolonged testing times and the availability of shielded facilities.

12.2.2 Flexural Strength of Curved Beams

The flexural stress in the outer fibre of a curved beam, σ (Pa) is given by (Timoshenko and Goodier, 1951)

$$\sigma = [12M\{2b^2 \ln(b/a)-b^2+a^2\}] / [3h^3\{(b+a)^2 - 4a^2b^2 \ln^2(b/a) / (b-a)^2\}] \qquad (12.1)$$

where h is beam thickness (m), a is inner radius (m), b is outer radius (m) and M is bending moment (Nm). For three-point flexural loading of Stage I and Stage II specimens, eqn. 12.1 simplifies to

$$\sigma = 1.05 \times 3\omega l / 2bd^2 \qquad \text{(Stage I)} \qquad (12.2)$$

$$\sigma = 1.08 \times 3\omega l / 2bd^2 \qquad \text{(Stage II)} \qquad (12.3)$$

where ω (N) is load at σ, l is the load span (m), b is breadth (m) and d is depth (m) of the specimen. These equations may be compared to the equivalent expression for loading of a rectangular beam given by equation 7.3 derived by simple beam bending relationships where the stress experienced by the outer fibre of the material, σ (Pa) is given by

$$\sigma = 3\omega l / 2bd^2 \qquad (12.4)$$

12.2.3 AE Experimental Details

The two AE experimental systems (Marandy and AECL, see Chapter Nine, Figure 9.4) were used simultaneously to record AE responses from curved beam specimens. Two AET AC375L transducers were used to capture the emitted AE and were coupled to the specimen surface using silicone rubber for in-laboratory tests and silicone grease for in-cell tests. Each transducer was placed at opposite ends of a curved beam specimen and connected to different 60 dB pre-amplifiers and AE systems, *i.e.* both AE systems were totally independent from one another. A load signal from the NENE test rig supplied load data to each AE system. The load-span for curved beam specimens using the NENE test rig was; (i) 60 mm for Stage I specimens; and (ii) 40 mm for Stage II specimens. The knife edge diameter in all cases was 4 mm.

AE responses (cumulative AE events, ΣN versus applied load, σ) were obtained for both unirradiated (in-laboratory and in-cell) and irradiated Gilsocarbon sleeve graphite subjected to two loading patterns: (i) three consecutive load-unload cycles to 5 MPa, 10 MPa and to failure in flexure (3 pt bend), and (ii) monotonically increasing flexural load to failure. The first loading pattern was designed to simulate the experiment on unirradiated graphite described in Chapter Ten and to test for the Felicity effect in the irradiated graphite specimen by applying a known pre-stress. The second loading pattern was designed to examine the extent of the Felicity effect (if any) arising from the internal stress induced from reactor conditions.

12.3 Experimental Results

12.3.1 Unirradiated Graphites

Figure 12.2 (a) & (b) present typical examples of AE responses from both AE systems for a Stage I curved beam specimen monotonically loaded to failure in flexure in the open laboratory. The trend in both cases is similar, although the ΣN values recorded by the Marandy system are greater. The AE response from the Marandy system is

noisier, although it is evident from Figure 12.2 (b) that the noise originated from the load-cell signal. This is because the output voltage from the NENE load cell is ± 2 V, *i.e.* a fifth of the optimum value for the Marandy instrument (± 10 V), and therefore there is a reduction in resolution.

Figures 12.3 (a) & (b) show examples of AE responses in the open laboratory using both systems for a Stage I curved beam specimen cyclically loaded to 5 MPa, 10 MPa and then to failure. Again, the two AE systems produce similar AE responses, but with the Marandy AE system recording higher ΣN values. Table 12.2 compares the ΣN for each of the three cycles from both AE systems. As expected, ΣN at failure is very much greater than at 5 MPa and 10 MPa peak loads; the ΣN values after the first and second cycles are ~0.4 and 1.5%, respectively, of the ΣN value at failure. For all load cycles, the difference between the ΣN from both systems are shown not to be significantly different (95% confidence). In both cases, a Felicity effect is observed, as found previously for other unirradiated graphites (Chapter Ten).

Figures 12.4 (a) & (b) show AE responses from both AE systems for an unirradiated Stage II specimen tested in the open laboratory. As might be expected, the AE responses for Stage II curved beams are similar to those found for Stage I beams and the results from the experimental systems are similar. Thus, the ΣN values after the first and second cycles are 0.6% and 2.2%, respectively, of the ΣN value at failure and a Felicity effect is observed.

12.3.2 Irradiated Graphites

All the tests on irradiated graphite were conducted within the shielded facility. At the same time as tests on irradiated specimens were conducted, unirradiated Stage II specimens, similar to those used in the open laboratory, were placed within the shielded cell and were loaded monotonically to failure in order to explore the effect of the cell environment on the AE response. Results from unirradiated specimens tested

in-cell were similar to those obtained in the open laboratory with values of ΣN falling within the range of those shown, *e.g.* in Figures 12.2 to 12.4.

In principle, the application of load to the irradiated graphite specimens by the NENE system within the cells should have increased smoothly. In the initial stages of work using the shielded facility an early decrease in load was observed, although this was accompanied by continual AE. This unusual response was attributed to the presence of the ribbed profile on the outer surface of sleeve samples which failed by crushing action of the knife edges at a fraction of the failure load of the sample. Therefore, the external ribbed profiles on the sleeve outer surface was removed in-cell by abrasion using SiC paper.

AE responses, Figures 12.5 (a) & (b), captured from both AE systems for an irradiated graphite subjected to consecutive load cycles to 5 MPa, 10 MPa and then failure, are very similar and they show that the onset of AE is at the start of loading, *i.e.* a Felicity effect is observed. The second load cycle is similar to that which may be expected from unirradiated graphite, *e.g.* Figure 10.6, but the AE clearly starts at zero stress. However, for most samples, the third load cycle, differs from the usual response from unirradiated graphites because more AE is generated than in the second cycle until just prior to the previous maximum stress; this leads to high values of the Recovery ratio, B $\approx$ 0.5-1.0. However, for each load cycle the AE response shows a change in gradient at stresses approximately equal to that of the previous stress level.

Table 12.2 presents the mean ΣN values for both AE systems for consecutive load cycles for both unirradiated and irradiated specimens. The Table shows that the strength of the irradiated material is much less than that of the unirradiated material, indicating that the effects of radiolytic oxidation greatly outweigh those of neutron hardening (Best *et al.*, 1985).

	Unirradiated								
	Stress / MPa			**AECL / AE Events**			**Marandy / AE Events**		
	Mean	**S.D.**	**n**	**Mean**	**S.D.**	**n**	**Mean**	**S.D.**	**n**
First Cycle	4.75	0.57	7	4	4	6	13	14	7
Second Cycle	9.85	1.35	7	15	8	7	34	19	8
Third Cycle (σ_f)	39.24	3.24	9	967	284	7	1022	385	8
	Irradiated								
	Stress / MPa			**AECL / AE Events**			**Marandy / AE Events**		
	Mean	**S.D.**	**n**	**Mean**	**S.D.**	**n**	**Mean**	**S.D.**	**n**
First Cycle	5.30	0.57	6	969	868	5	799	364	5
Second Cycle	11.12	0.67	6	1532	1061	5	2156	1920	5
Third Cycle (σ_f)	27.91	1.72	9	5480	2947	5	3691	3441	5

TABLE 12.2 : Cumulative AE Event Counts at Peak Stresses For Unirradiated and Irradiated Curved Beam Gilsocarbon Graphite.

Table 12.2 also shows, for all load cycles, that the ΣN values for irradiated graphites are significantly greater than for unirradiated graphite (95% significance). Higher AE for irradiated graphites is probably due to the development of porosity following radiolytic oxidation, as shown previously for unirradiated graphites (Pickup *et al.*, 1984). This may be illustrated by optical and UV light micrographs of a Gilsocarbon graphite subjected to different doses of irradiation, Figure 12.6 and Figure 12.7. At the lower dose, Figure 12.6, comparison of the optical and UV light micrographs shows that the cracks in the Gilsocarbon particle at G are closed. At the higher dose, Figure 12.7, these cracks are opened as a result of radiolytic oxidation of the graphite and neutron irradiation effects, as explained in Chapter Five. The increase in porosity with increasing irradiation dose will lead, in addition, to a higher number of stress concentrators, a coarser structure and a higher ΣN.

AE responses from both AE systems for irradiated graphite samples monotonically loaded to failure, Figure 12.8 (a) & (b), are very similar, with each showing an initial sharp rise and then a gradual rate increase in ΣN to failure. Both AE responses show the onset of AE from zero stress, and at no point does the ΣN increase abruptly with increasing stresses (as was found for unirradiated monotonically loaded graphites, *e.g.*

Figure 10.1 (a) and (b)). Therefore, AE responses from irradiated graphite do not show any evidence of a Felicity effect caused by internal stresses induced by the reactor environment.

Figure 12.9 presents an AE amplitude distribution at fracture for an irradiated graphite specimen loaded monotonically to failure in flexure. The figure illustrates that the AE amplitude distribution is not altered significantly from those presented in Chapter Ten, *e.g.* Figures 10.11, by exposure to reactor conditions, although the number of AE events has increased dramatically.

12.4 A Mathematical Method For the Calculation of the Internal Stress

Since no evidence for a Felicity effect is revealed from plots as in Figure 12.8, an alternative analysis of the AE data was considered. Figure 12.10 shows the event density versus stress for an irradiated graphite sample (612/4/5/6) loaded monotonically to failure, where the event density is the change in ΣN for each stress increment; in this case, 0.63 MPa. Inspection of Figure 12.10 shows that the event density begins to increase significantly beyond a stress of ~4 MPa. It is possible that the change in slope of the event density-stress plot is associated with the effect of a pre-stress. Some evidence for this view is presented in Figure 12.11 which shows the event density-stress plot for cyclically stressed irradiated graphite subjected to pre-stresses of 5 MPa and 12 MPa before final loading to failure. Inspection of Figure 12.11 shows a change in the slope of the event density-stress plot which is close to the previous peak stress (12 MPa). Therefore, in the case of the irradiated nuclear graphites, it is postulated that the change in slope of the $\Delta(\Sigma N)/\Delta\sigma$ plot marks the position of the internal stress experienced in the reactor. In order to identify the point at which the change in slope of the event density-stress curve occurred, a simple empirical analysis was used. It is assumed that the AE event density response is composed of two parts. For stresses, σ, below the pre-stress, σ_p, the AE event

density, $d(\Sigma N)/d\sigma$, is assumed to be constant with stress, while at stresses greater than σ_p, $\Delta\Sigma N/\Delta\sigma$, is assumed to increase linearly, *i.e.*

$$d(\Sigma N)/d\sigma = a \qquad \sigma<\sigma_p \qquad (12.5)$$

Actually, finite differences are plotted where $\Delta\sigma = 0.63$ MPa,

$$\Delta(\Sigma N)/\Delta\sigma = a$$

$$\Delta(\Sigma N)/\Delta\sigma = a + b(\sigma-\sigma_p) \qquad \sigma>\sigma_p \qquad (12.6)$$

where a and b are constants. The results in Figures 12.10 and 12.11 were fitted to the above equations using a least squares best fit method as shown in the figures. The same procedure was applied to AE data from two other graphite specimens loaded monotonically to failure (612/4/3/5 and 612/7/4/1). The values of a, b and σ_p are presented in Table 12.3.

Sample	a ± 1 S.D.	b ± 1 S.D.	σ_p ± 1 S.D.
612/4/5/6	27.4 ± 2.0	4.0 ± 0.5	4.4 ± 1.9
612/4/3/5	47.9 ± 2.0	10.0 ± 1.2	9.0 ± 1.0
612/7/4/1	37.3 ± 5.5	11.1 ± 2.7	17.0 ± 1.5
Unirradiated	~25	~12.5	~12.00

TABLE 12.3 : Constant in Equation 12.9 Fitted to the AE Density Curves for the Irradiated Samples

Table 12.3 shows that there is a wide variation in the parameters a and b for the three irradiated graphites. The values of σ_p for the three graphites lie in the range 4 - 17 MPa and each is significantly different from the others (95% confidence). It is useful to compare these values of internal stress with those observed from the slot-closure method (Reed *et al.*, 1992). In this method a slot of known width is cut in an irradiated graphite sleeve, and the internal stresses alter the shape of the sleeve and

reduce the slot width. The extent of the slot closure can be related to the internal stress. Measurements of the internal stresses by slot closure on sleeve C3612 discharged from Hunterston have been reported (Tucker, 1992) and are summarised in Table 12.4.

Designation	Static Unirradiated Young's Modulus/GPa	Mean Element Burn-up (GWd/t_eU)	Unirradiated Flexural Strength (4pt) / MPa	Internal (Hoop) Stress / MPa
Element 4	9.63	24.24	41.1	2.89 ± 0.38
Element 7	9.63	19.05	41.1	5.16 ± 0.32

TABLE 12.4 : Calculated Hoop Stress and Associated Data For Elements 4 and 7 Using the Slot Closure Technique (Tucker, 1992).

Although element 4 has a higher burn-up than element 7, the higher internal stress within element 7 is probably due to thermal stresses caused by the higher operating temperatures at the top of the fuel stringer (Table 12.4). Comparison of σ_p values in Table 12.3 and the internal hoop stresses in Table 12.4 shows that two of these values σ_p derived from the AE technique, are considerably larger than the hoop stresses obtained from the slot closure method. Considering the empirical nature of the method of identifying σ_p using the AE technique, it seems likely that the internal stress values obtained from the AE method are not associated with irradiation induced internal stresses. Certainly, more work is required before the AE method can be regarded as a reliable one.

12.5 Summary

In summary, for pre-stresses induced by an applied load, a Felicity effect is found for irradiated graphites which is similar to that found previously for unirradiated graphites. However, irradiated graphites monotonically loaded to failure also behaved in a similar way to unirradiated graphites, *i.e.* AE commenced as soon as the load was applied and

increased progressively with load. Thus, in this case, no evidence for a Felicity effect due to internal stresses was found. It is therefore unlikely that the AE technique is a viable technique to monitor internal stresses. After a full life time, the irradiated sleeve graphite has suffered significant weight loss which outweighed any beneficial effect from neutron irradiation and resulted in a significant loss in strength. These effects contributed to many more AE events being emitted than for unirradiated graphites. This is especially true at low stresses (see Table 12.2). AE from both unirradiated and irradiated graphites was recorded using two independent experimental systems (Marandy and AECL). The two AE systems compared well with each other producing very similar AE responses.

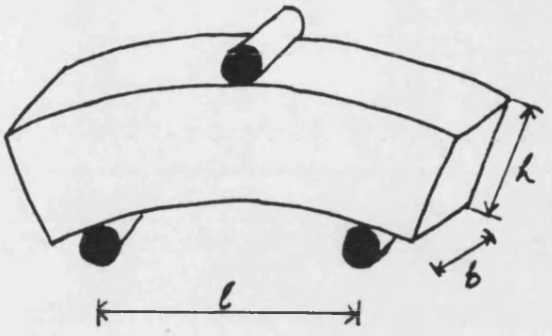

		Stage I	Stage II
h	Height / mm	16	22
b	Breadth / mm	12	10
l	Load span / mm	60	40

FIGURE 12.1 : Schematic illustration of a curved beam specimen between knife edges and the dimensions of Stage I and II specimens.

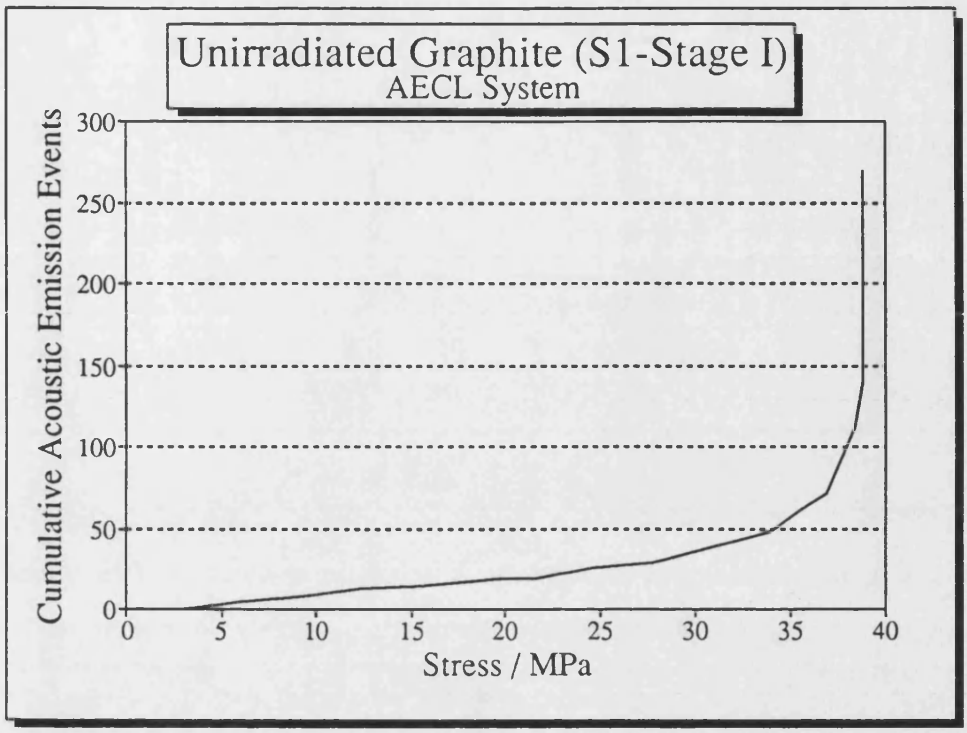

FIGURE 12.2 (a) : An example of an AE response recorded by the AECL system from an unirradiated Stage I curved beam specimen monotonically loaded to failure in the open laboratory.

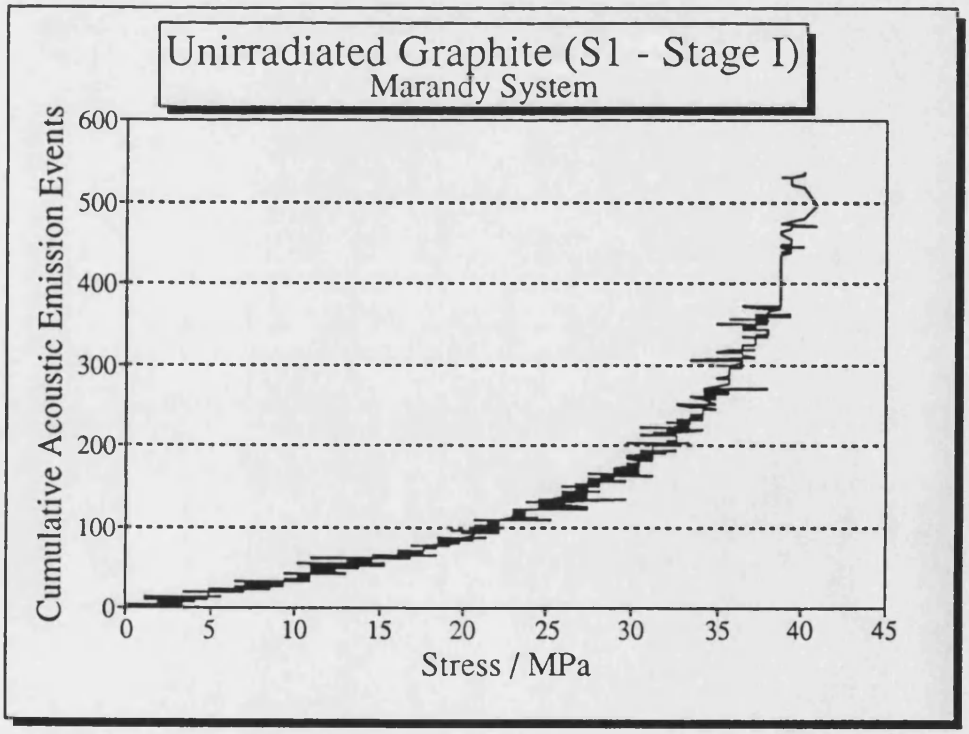

FIGURE 12.2 (b) : An example of an AE response recorded by the Marandy system from an unirradiated Stage I curved beam specimen monotonically loaded to failure in the open laboratory.

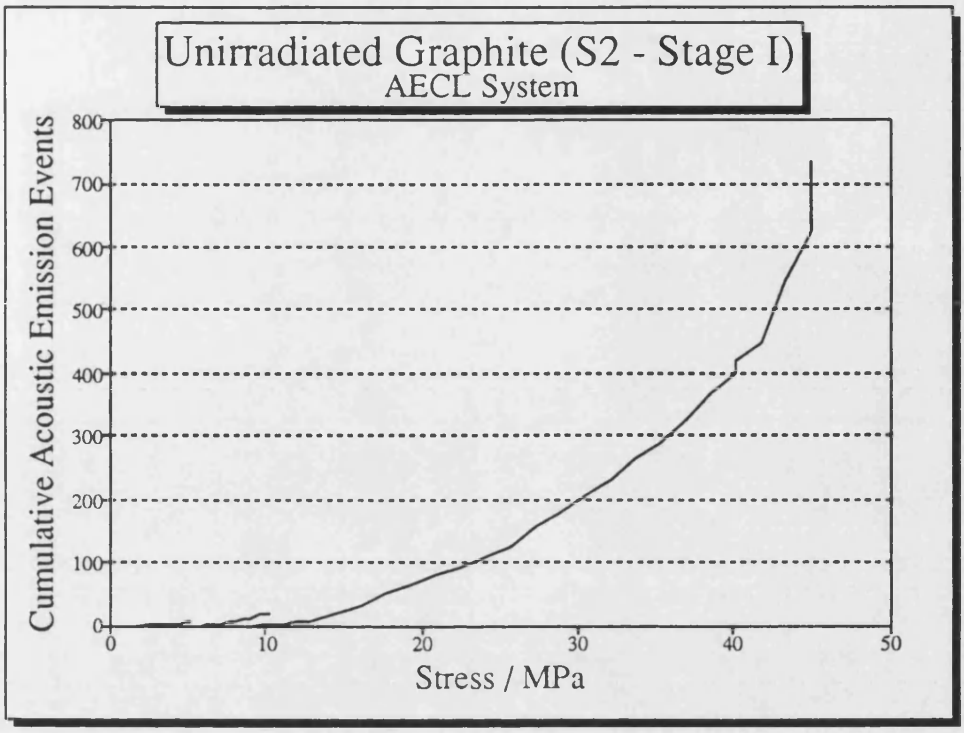

FIGURE 12.3 (a) : An example of an AE response recorded by the AECL system from an unirradiated Stage I curved beam specimen cyclically loaded to failure in the open laboratory.

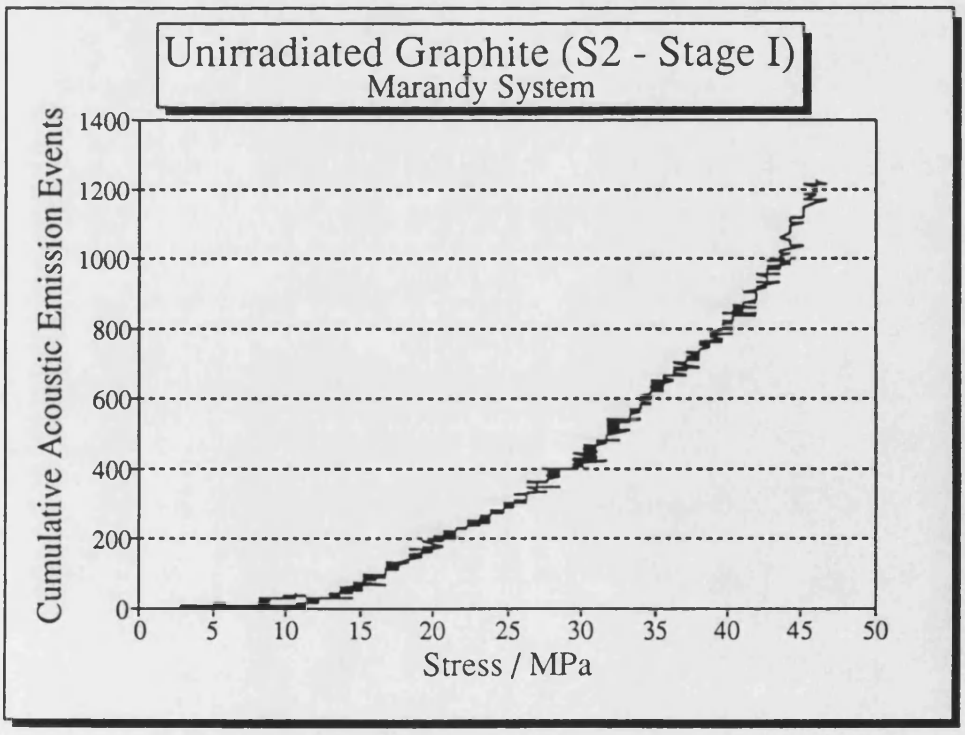

FIGURE 12.3 (b) : An example of an AE response recorded by the Marandy system from an unirradiated Stage I curved beam specimen cyclically loaded to failure in the open laboratory.

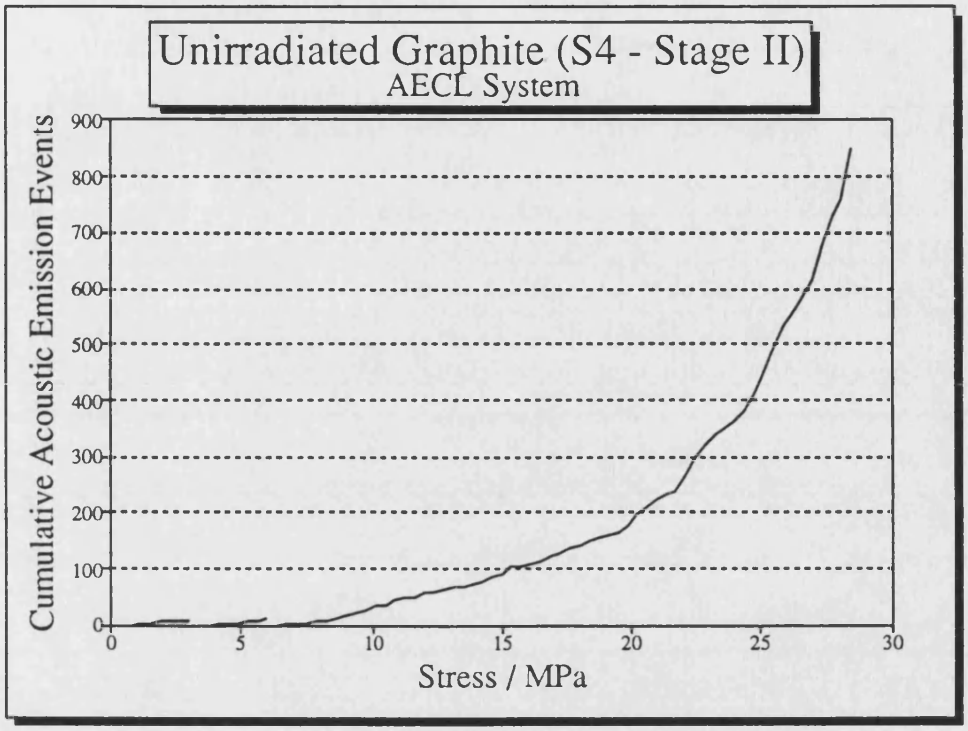

FIGURE 12.4 (a) : An example of an AE response recorded by the AECL system from an unirradiated Stage II curved beam specimen cyclically loaded to failure in the open laboratory.

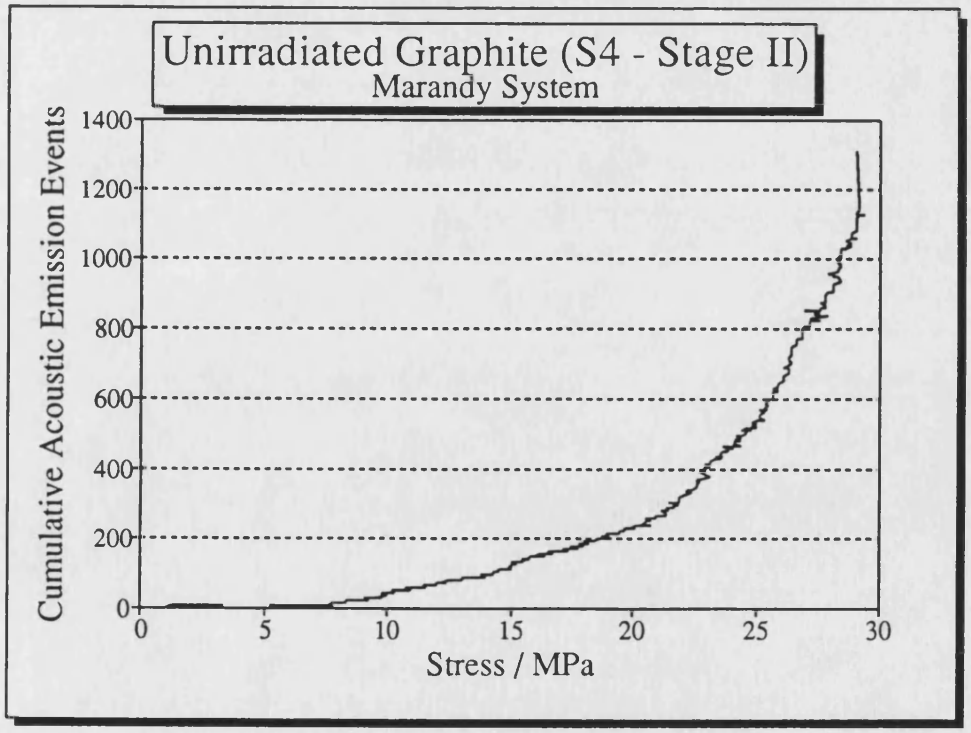

FIGURE 12.4 (b) : An example of an AE response recorded by the Marandy system from an unirradiated Stage II curved beam specimen cyclically loaded to failure in the open laboratory.

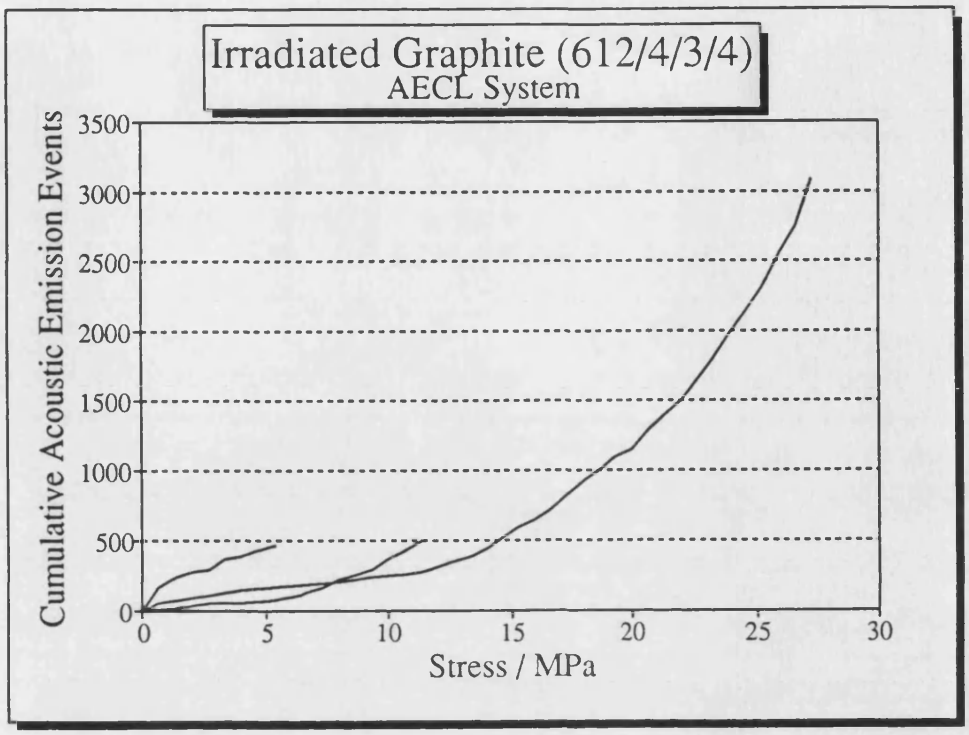

FIGURE 12.5 (a) : An example of an AE response recorded by the AECL system from an irradiated Stage II specimen subjected to three consecutive load cycles.

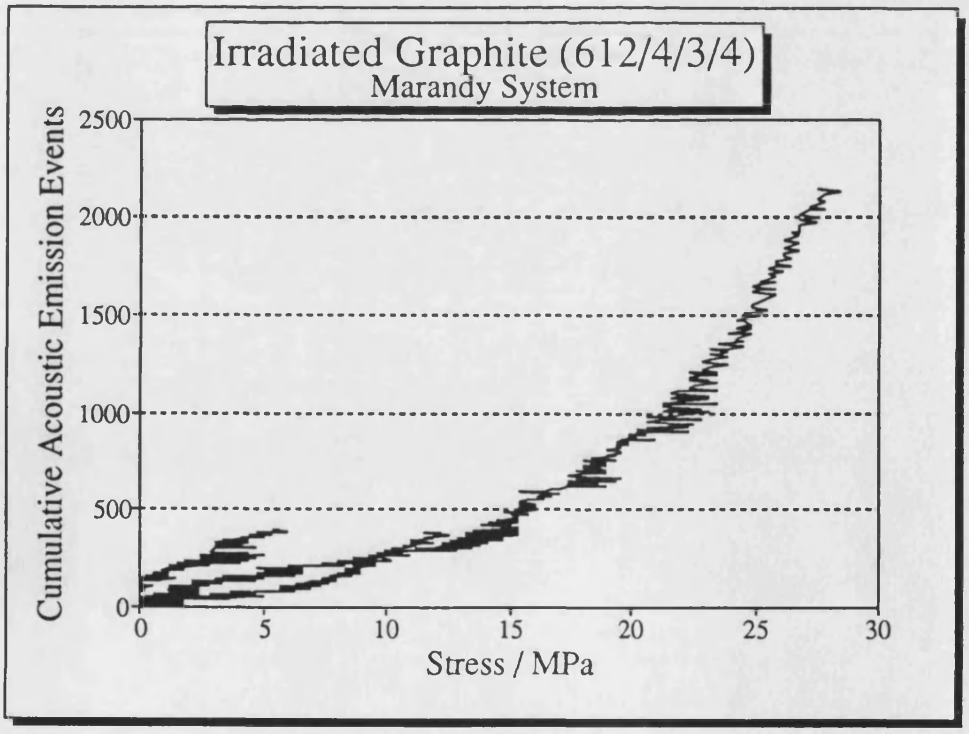

FIGURE 12.5 (b) : An example of an AE response recorded by the Marandy system from an irradiated Stage II specimen subjected to three consecutive load cycles.

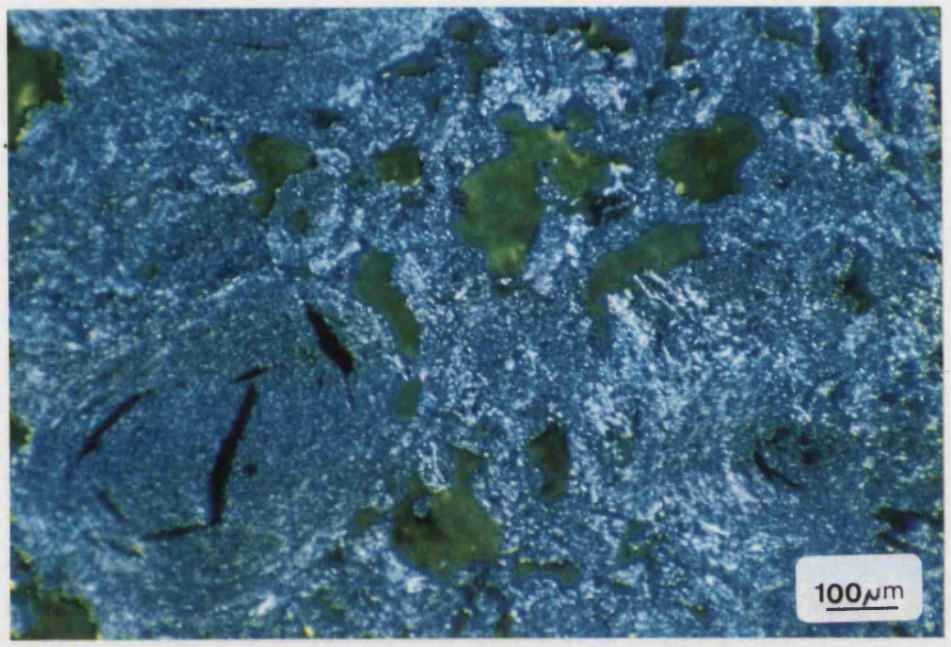

FIGURE 12.6 (a) : An optical micrograph of a fluorescent resin-impregnated irradiated Gilsocarbon graphite subjected to a dose of 553 GWd/g (courtesy of Nuclear Electric plc).

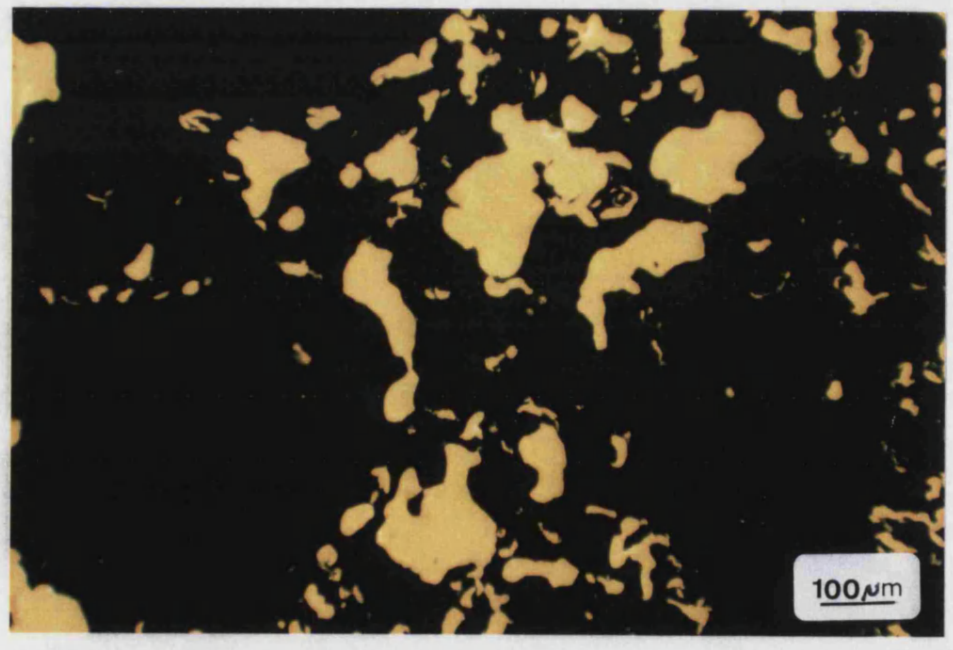

FIGURE 12.6 (b) : An UV micrograph of a fluorescent resin-impregnated irradiated Gilsocarbon graphite subjected to a dose of 553 GWd/g (courtesy of Nuclear Electric plc).

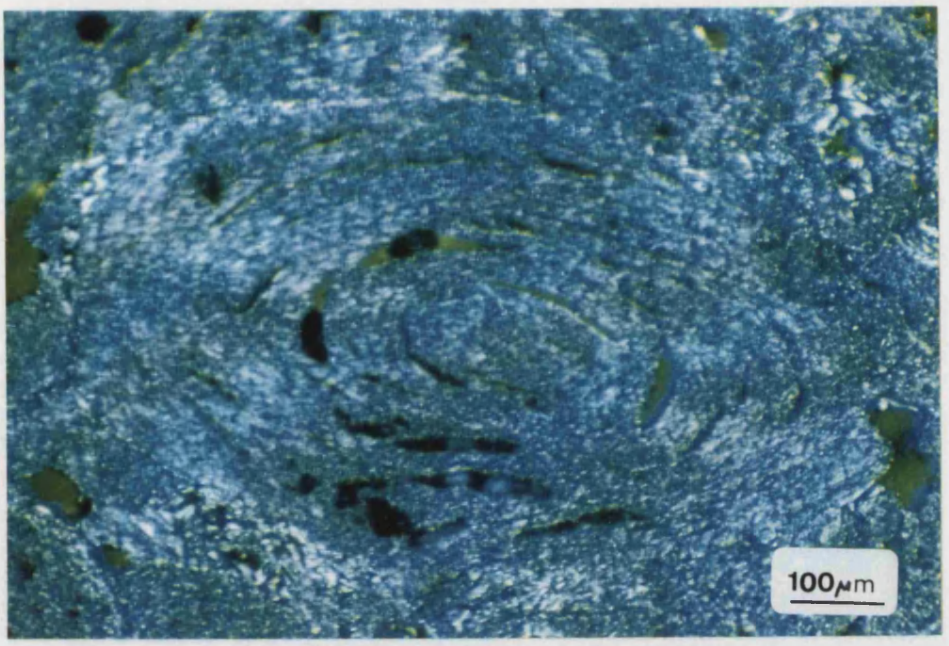

FIGURE 12.7 (a) : An optical micrograph of a fluorescent resin-impregnated irradiated Gilsocarbon graphite subjected to a dose of 1129 GWd/g revealing the open-pore structure caused by radiolytic oxidation (courtesy of Nuclear Electric plc).

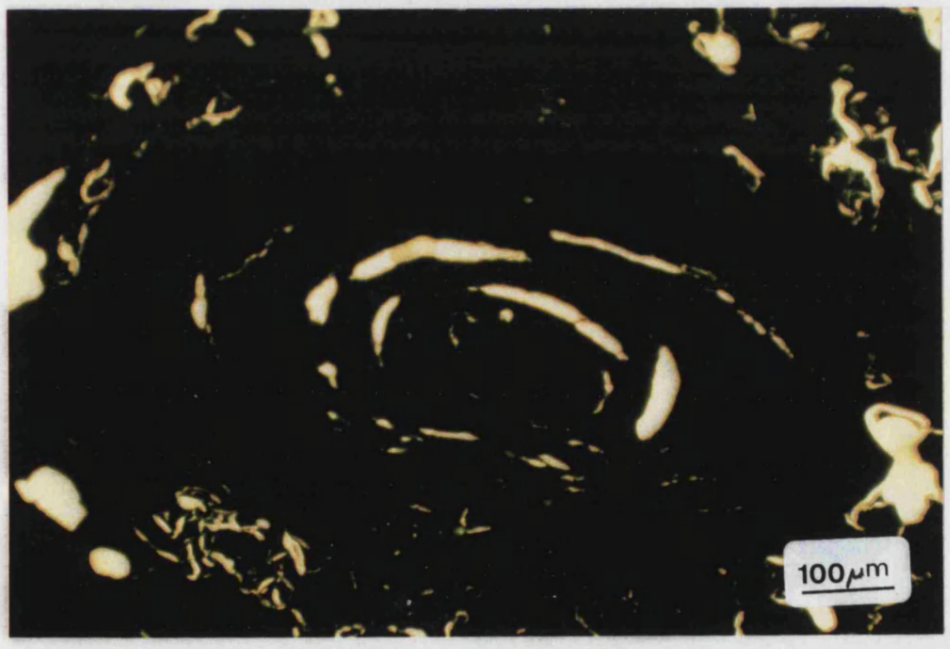

FIGURE 12.7 (b) : An UV micrograph of a fluorescent resin-impregnated irradiated Gilsocarbon graphite subjected to a dose of 1129 GWd/g revealing the open-pore structure caused by radiolytic oxidation (courtesy of Nuclear Electric plc).

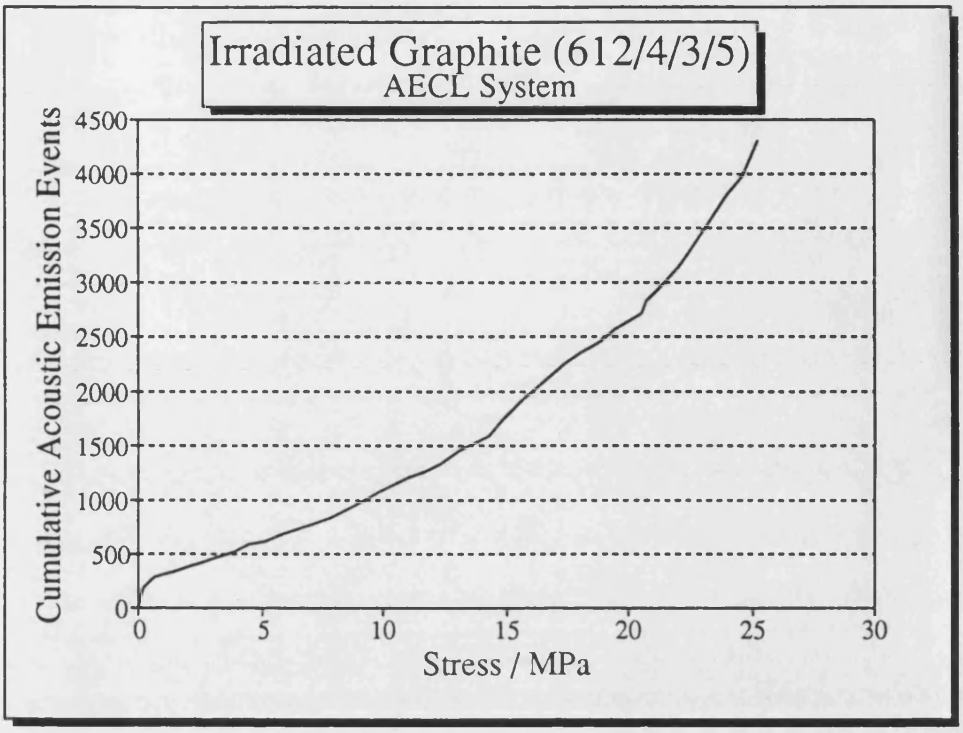

FIGURE 12.8 (a) : An example AE response recorded by the AECL system for an irradiated Stage II specimen monotonically loaded to failure.

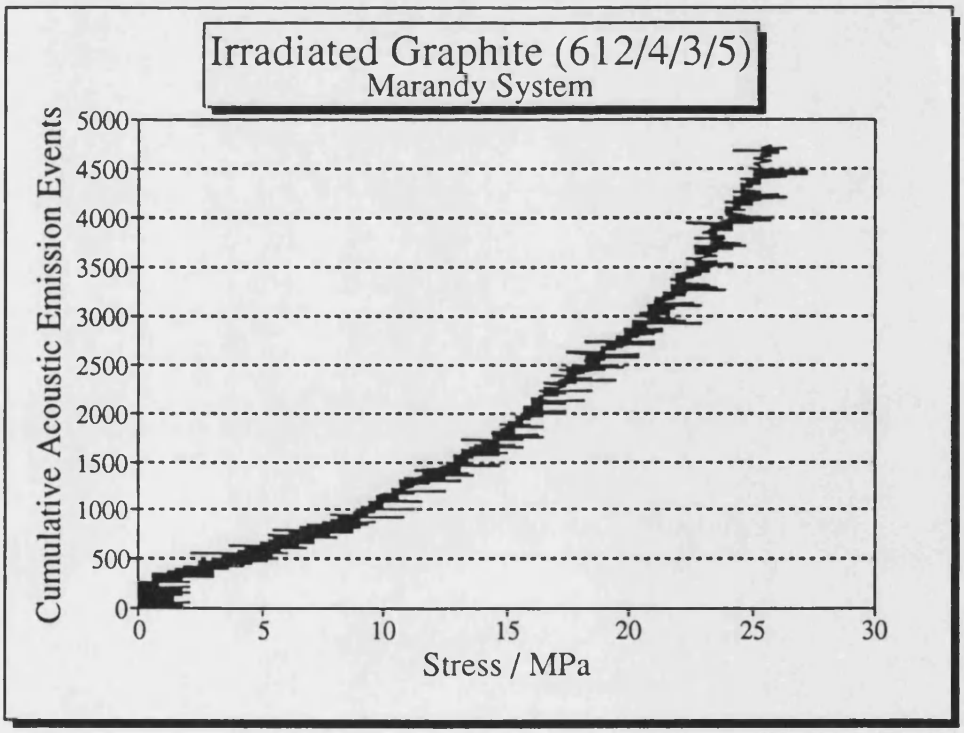

FIGURE 12.8 (b) : An example AE response recorded by the Marandy system for an irradiated Stage II specimen monotonically loaded to failure.

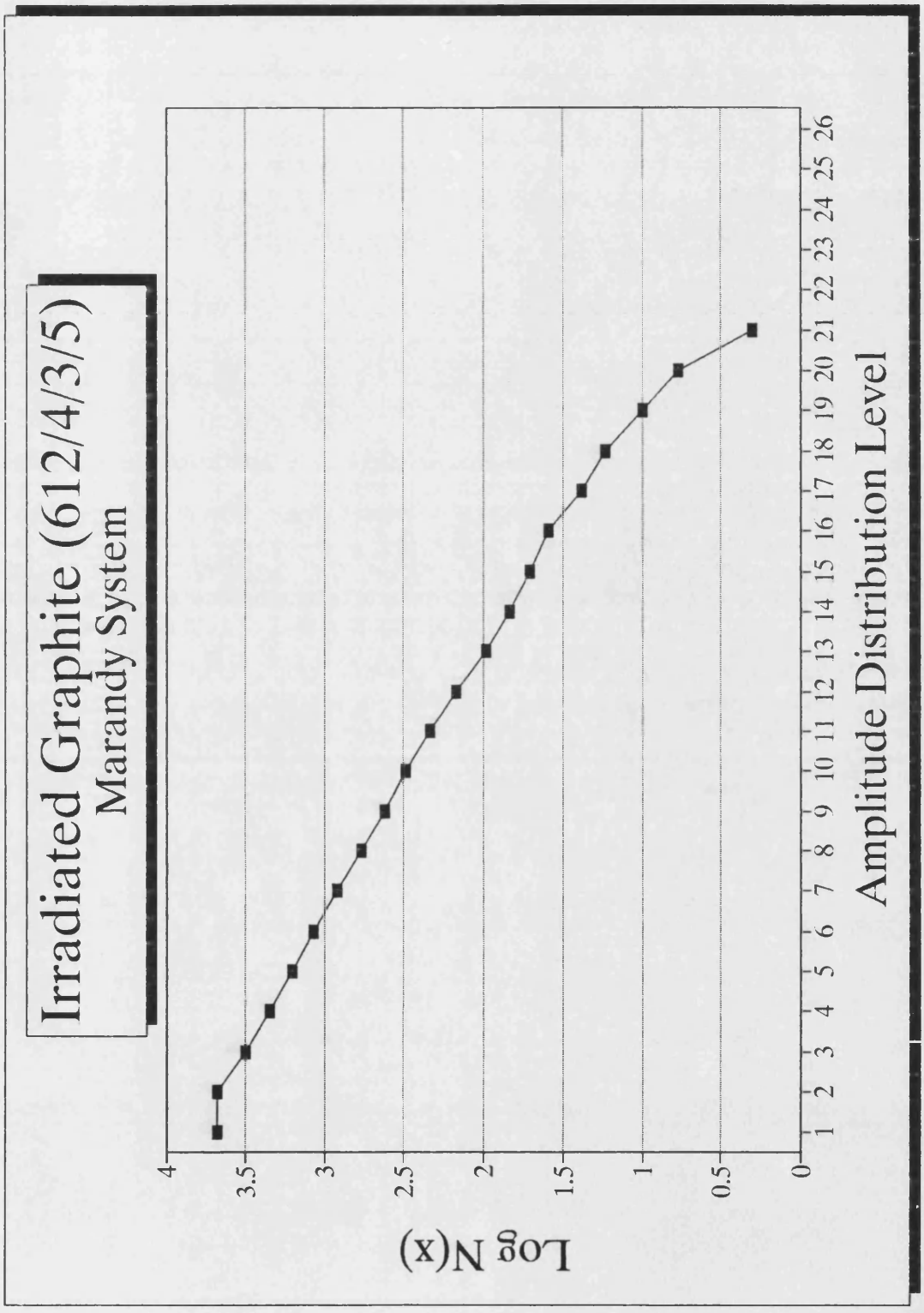

FIGURE 12.9 : An example of an amplitude distribution from an irradiated graphite specimen monotonically loaded to failure.

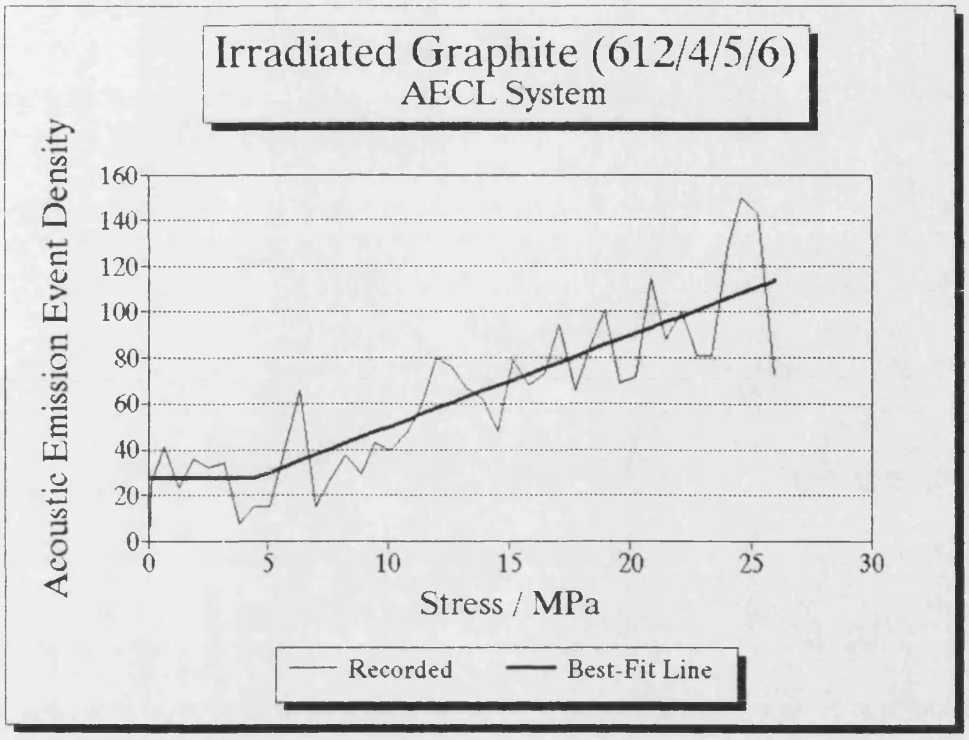

FIGURE 12.10 : An example of AE event density versus stress plot for an irradiated graphite monotonically loaded to failure.

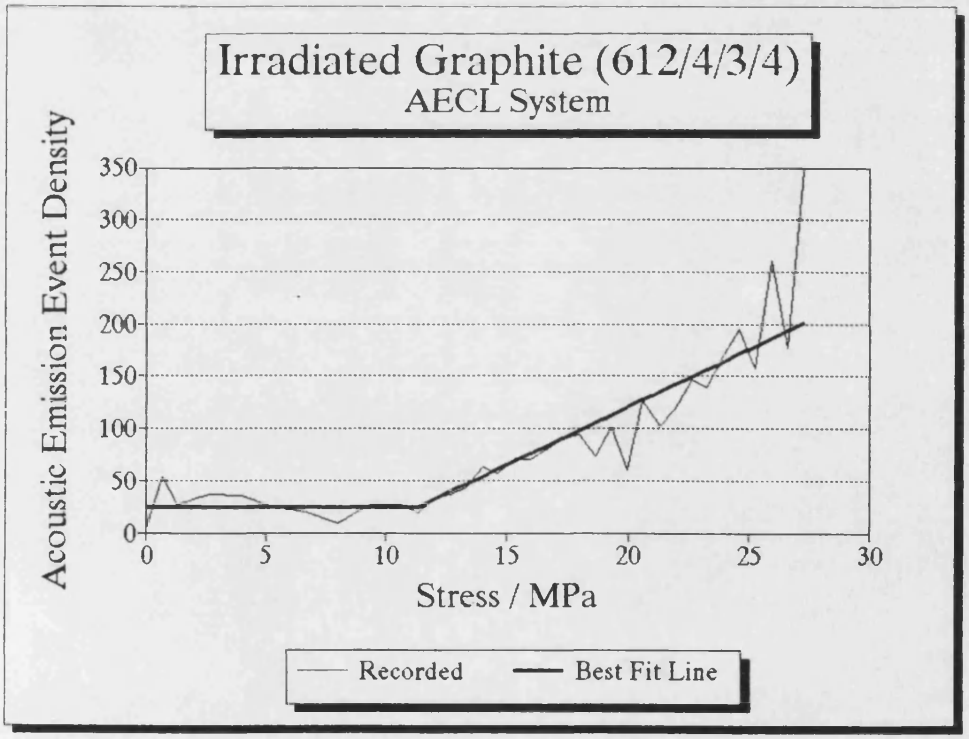

FIGURE 12.11 : An example of AE event density versus stress plot for a third load cycle for an irradiated graphite loaded to failure (pre-stress ≈ 12 MPa).

Part D : Discussion and Conclusions

CHAPTER THIRTEEN : DISCUSSION AND CONCLUSIONS

13.1 Introduction

The structural integrity of the moderator graphite within a thermal nuclear reactor is a limiting factor of its life. The moderator graphite experiences conditions within the core (*e.g.* fast neutron irradiation and radiolytic oxidation) that cause deformation processes to occur, which in turn cause internal stresses. If these stresses are allowed to increase sufficiently, in ways which augment external loads, then fracture of a moderator brick is possible. Therefore, effective monitoring of the structural integrity, *i.e.* the internal stresses, is required. Acoustic emission (AE) has been identified as a potential technique for determining the internal stress within the moderator core by use of the Kaiser effect, and this thesis has presented a study which has examined its feasibility. In addition, this thesis has also presented work where the AE technique has been used as a tool to investigate microstructural and relaxation processes within nuclear graphites. This chapter concludes this thesis by (i) summarising, in relevant sections, the main points noted in the previous chapters, (ii) by stating the main conclusions from this work, and (iii) by suggesting some future work.

13.2 Materials and Mechanical Properties

Most of the work presented in this thesis has considered three nuclear graphites; PGA, IM1-24 and VNEC. Both PGA and IM1-24 are moderator graphites in the Magnox reactor and the AGR, respectively, while VNEC was a candidate sleeve graphite for the AGR. Using polarised light microscopy, it was shown (Chapter Six) that these graphites had very different microstructures. PGA has the highest porosity and coarsest texture of the three graphites, and consequently it was the weakest in all mechanical testing modes. The microstructure of PGA consists of a variety of isochromatic regions with porosity dispersed throughout the microstructure. Filler

particles have elongated isochromatic regions, indicating long range order of crystallites which accounts for its anisotropic properties. The microstructure of VNEC was similar to, although finer, than that of PGA, and, consequently, these two graphites have some similarities in their mechanical behaviour. IM1-24 differs from these two graphites having spherical Gilsocarbon filler particles within a very fine binder phase, which accounts for its isotropic properties. Coarseness of microstructural texture of these three graphites decreased from PGA to VNEC to IM1-24.

Quantitative distributions of pore size and shape and filler particle size and shape were obtained by Image Analysis (IA). These results supported the qualitative observations made by optical microscopy. For PGA and VNEC graphites, there were differences in the filler particle and pore size distributions in the parallel and perpendicular directions, reflecting the alignment of particles on extrusion. IM1-24 was near-isotropic, but with a skewed filler particle shape distribution caused by fragmented particles. For IM1-24, image analysis also supported the qualitative observation that much larger pores are present in the binder phase than was found for the other graphites.

The non-linear stress-strain behaviour of polycrystalline graphites suggests that deformation includes sub-critical cracking and basal plane shear within a small process zone (*e.g.*, see reviews by Brocklehurst, 1977 and Kelly, 1981). However, for the three selected nuclear graphites, there were distinct differences in mechanical behaviour (Chapter Seven). In tension, PGA fracture surfaces were irregular and influenced by the presence of larger, crack-deflecting, filler particles, but for IM1-24 the fracture surface was normal to the applied stress, and consisted of cusps and domes created by cleavage of the outer skin layers of the Gilsocarbon filler particles. In addition, split Gilsocarbon particles were also observed on the fracture surface, due to the inherent calcination cracks.

In compression, PGA failed by shear to form two similar fracture surfaces along a 30-45° angle to the applied load, but IM1-24 underwent a more complex failure mechanism consisting of three stages (Chapter Seven). VNEC, in tension and compression, underwent similar fracture mechanisms to PGA. It was suggested that the ease and extent of shear deformation of these graphites follows the order PGA>VNEC>>IM1-24. This is supported by values of a non-ideality parameter of these graphites obtained from fracture mechanics (§7.7.6) which suggests that IM1-24 resists shear deformation to a much greater degree than other graphites. Quantitative analysis of the stress-strain diagrams (§7.5.3), using the Jenkins' model (1962), confirmed that IM1-24 underwent much less shear deformation than other graphites. These results emphasise that the mechanical behaviour of polycrystalline graphites depends sensitively upon their microstructure.

Due to its resistance to shear deformation, IM1-24 is very much stronger than PGA in compression. It is suggested that this is a consequence of the ability of the spherical Gilsocarbon filler particles within IM1-24 to resist easy shear mechanisms. Both PGA and VNEC graphites undergo easy shear mechanisms under compressive loading (*e.g.*, see Figures 7.14 and 7.17), which are facilitated by needlecoke filler particles. Essentially, needlecoke graphites provide long arrays of aligned crystallites, each supplying glissile dislocations within the basal plane, which provide a mechanism for slip. Such shear mechanisms are accommodated by the surrounding porosity, but are eventually constrained by the elastic constraint of the binder (Brocklehurst, 1977).

13.3 Acoustic Emission

Evidence has been presented which has confirmed that acoustic emission (AE) can provide valuable information relating to the microstructure and fracture of nuclear graphites. For example, the amount of AE generated from a graphite increases with

the coarseness of its texture (Burchell *et al.*, 1986); for the three graphites studied the AE event count at a given stress, ΣN, is in the order PGA > VNEC > IM1-24.

Generally, the shape of the AE response for a nuclear graphite subjected to monotonic loading is a near-exponentially increasing curve. The generation of AE starts at the onset of stress, and at low stresses may be attributed mainly to slip of basal planes. At increasingly higher stresses, it is postulated that there is a progressively increasing contribution from microcracking due to crack initiation, propagation and branching. Therefore, AE from polygranular graphites can be attributed to two main sources, microcracking and basal plane shear.

This thesis has presented new work on AE from three nuclear graphites in tension, compression and flexure in both monotonic and cyclic loading to failure. As is common for polycrystalline graphites, failure strengths for the three graphites were in the order compressive > flexural > tensile. For monotonic loading to any stress (less than the tensile strength), it was found that ΣN (tension) > ΣN (compression) >> ΣN (flexure). The high value of ΣN (tension) compared to ΣN (compression) is expected since the ratio of applied tensile stress to tensile strength is greater than the equivalent ratio for compressive stresses. However, compressive loading generates more AE at failure than does tensile loading due to the large component of AE generated from shear. Flexural loading generates the least AE since the AE sources are confined to a localised region of high tensile stress. This suggests that of the three testing modes, flexural loading is likely to be the least suitable for AE monitoring.

A relationship between graphite texture and a non-ideality parameter, P, was proposed by Pickup *et al.* (1985). Values of P for the three graphites were in the order IM1-24 < VNEC < PGA, and were shown to correlate with compressive strength in Figure 7.20 (Chapter Seven). Figure 13.1 also shows that there is a correlation between P and the amount of AE generated in tension, flexure and compression for these three

graphites. The more ideal a graphite is in mechanical behaviour the less AE is generated.

Prior to this project, there was considerable confusion over whether the Kaiser effect occurred in polycrystalline graphites. This confusion was caused by a small number of published studies with limited results from a few specimens. There was also confusion over the definition of the Kaiser effect in the literature, *e.g.* Ioka *et al.* (1987). Chapter Ten presented AE responses recorded from three nuclear graphites cyclically loaded to failure. In all cases, the AE responses did not exhibit a Kaiser effect, but instead a Felicity effect was observed. Previously, no study on AE from polycrystalline graphites has recognised a Felicity effect.

All AE responses from cyclic loading were similar, except for PGA loaded in compression. Usually, on the first load cycle, the rate of ΣN gradually increased with stress until the peak load. On subsequent load cycles, the onset of AE occurred prior to the previous peak stress, and then AE gradually increased with stress. However, for PGA loaded in compression, on the second and third load cycles, the rate of AE generation decreased with increasing stress after an initial period forming an unusual S-shaped curve. A similar AE response was observed from PGA monotonically loaded to failure in compression. This effect was attributed to the pinning of basal plane shear prior to microcracking. Further evidence for this suggestion was provided by AE amplitude distributions.

Most graphites produce an amplitude distribution which conforms to the Pollock law. However, for PGA loaded in compression, on increasing stress, the amplitude distribution deviates from the Pollock law (Figure 10.11) and bows (Figure 10.12) suggesting a reduction in the proportion of low energy events, *i.e.* shear, but continues to generate higher energy AE events corresponding to microcracking. It was demonstrated in mixed mode cyclic loading, that different AE sources operate in

tension and compression and they were independent of each other. In tension, it is proposed that the majority of AE sources are flaws within the material acting as stress raisers, but in compression, the majority of sources are probably shear planes.

13.4 Acoustic Emission and Recovery

Chapter Four reviewed previous published models for deformation which suggested that back-stresses operate within a stressed polycrystalline graphite. On unloading, these stresses cause reverse plastic deformation via shear (Jenkins, 1962; Ioka and Yoda, 1987, and McLachlan, 1992). A recent theoretical microstructural model (McLachlan *et al.*, 1989 and McLachlan, 1992) for deformation and fracture of graphite ascribed AE predominantly to microcracking and "inter-crystalline" shear. Microcracking was assumed to be an irreversible process, and therefore AE from this source was not regenerated on cyclic loading. However, "inter-crystalline" shear was assumed to be reversible, and AE from this source could be re-generated on reloading. The reversible behaviour was attributed to reverse slip of inter-crystalline shear ahead of the crack tip under the influence of back-stresses. These models are consistent with the conclusion that the Kaiser effect does not occur in polycrystalline graphites.

Previously, a Felicity effect in other materials has been characterised by the Felicity ratio, defined as the ratio of the stress at the onset of AE to the maximum stress on the previous cycle. In this work, the Felicity ratio was found to be unsatisfactory for characterising the AE responses, because it was subjective, and also it did not take account of the amount of AE emitted before the previous maximum stress. An alternative parameter was introduced in this thesis to characterise the Felicity effect, which took account of the amount of AE occurring on each load cycle prior to the previous peak stress. The parameter is called the Recovery ratio, B, defined as the ratio of ΣN on the $(n+1)^{th}$ cycle to ΣN on the n^{th} cycle at the previous maximum

stress. Values of B indicate that the number of AE events prior to the previous peak stress on the $(n+1)^{th}$ cycle was between 5-15% of ΣN on the n^{th} cycle.

Nuclear graphites do not show any significant AE on unloading, or at zero stress (if the graphite is immediately re-loaded). The mechanisms that give rise to AE on loading (*e.g.*, the propagation of microcracks and basal plane shear) are fast processes which generate rapid releases of energy. On unloading, there is a slow reduction in strain energy controlled by the speed of the crosshead speed of the Instron, *i.e.*, there is a gradual relaxation of the stressed graphite specimen. Thus, recovery processes which may occur on unloading, such as microcrack closure, do not give rise to detectable AE. Therefore, the relaxation processes that occur on unloading or at zero stress must account for the "recovery", and they sufficiently modify the microstructure and residual stress-fields within the graphite so that, on reloading, new AE events are generated at stresses below previously-applied maximum stress.

Clear evidence was reported in Chapter Eleven for the time-dependence at room temperature of relaxation mechanisms which generate AE, and which may contribute to the Felicity effect. Two types of experiment were undertaken. The first experiment investigated the effect of increasing the time at zero load between successive load cycles. In all cases, the start of AE generation occurred at the onset of stress, and there was a progressive increase in ΣN at low stresses with increasing time at zero stress. This resulted in a Recovery ratio which increased with time at zero stress. These results show that there are both time-dependent and time-independent processes which contribute to recovery in polycrystalline graphites.

The second experiment investigated the time dependence of the AE response from graphite by monitoring AE as a function of time at zero load (after applying a load cycle) or at constant strain (after an application of an initial load). The AE responses obtained strongly resembled creep strain-time curves. These AE curves fitted

equations similar to those proposed by Davidson and Losty (1958) for experimental creep and creep recovery curves above 1500 °C, and those theoretically derived, considering thermally-activated processes, by Jenkins (1963). The equations were obtained by replacing the creep strain with ΣN on the assumption that every increment in micro-creep strain will generate an AE event. Therefore, these experiments strongly suggest that the time-dependent component of the Felicity effect is due to thermally-activated creep processes.

Below 1500 °C, thermal creep in graphites is assumed to be negligible and unmeasurable (*e.g.*, Losty, 1970), but there are a few examples of recovery at ambient temperatures, *i.e.* thermal creep, in graphites such as that shown by Andrews *et al.* (1960). Therefore, AE is a sensitive technique and can reveal aspects of the mechanical behaviour of graphites which are either very difficult or impossible to study by other means.

At constant strain, thermally-activated creep driven by the strain energy may cause further slip of basal planes, and extension of existing stress-concentrating cracks and flaws, thus giving rise to AE. At zero stress after a load cycle, residual strain energy triggers AE events by reverse plastic deformation, leading to recovery. Presumably, the residual strain energy is concentrated as localised tensile and compressive micro-stresses (which average zero over the whole specimen). The extent of creep recovery was shown to be less in tension than in compression, suggesting an important component of creep recovery is reversal of shear deformation as a result of back-stresses due to boundary restraint.

There are many possible microstructural processes which can give rise to AE within a polycrystalline graphite, and which could contribute to a Felicity effect. The ease at which basal plane glide occurs suggests that some recovery must be a result of reversible plastic deformation, *i.e.* reversed slip along basal planes caused by back-

stresses, as suggested by Ioka and Yoda. (1987). This type of process will have an instantaneous effect on unloading plus a time-dependent effect due to thermal micro-creep within the material. Andrew *et al.* (1960) attributed their observed recovery of permanent set to the formation, opening and closing of microcracks in the binder phase, which are similar to Mrozowski cracks. Slagle (1967) also noted that on unloading, small cracks tended to close up, while larger crack tended to remain partially open which he assumed resulted in the permanent set. Other possible sources of AE may be due to frictional effects at grain boundaries or at crack surfaces. These may include sliding of crack surfaces over each other, crack bridging and the crushing of grains into debris which prevent the closure of a crack. Therefore, the Felicity effect may be due to a number of factors associated with recovery. These include:- (i) the reversal of shear mechanisms as a result of back stresses arising from elastic restraint (which is a function of time); and (ii) the re-adhesion of cracked surfaces leading to *e.g.* the rubbing and crushing of cracked surface and debris on both unloading and reloading.

13.5 Feasibility of an AE Technique to Monitor Internal Stresses

Chapter Twelve demonstrated that two independent experimental systems produced very similar results. Therefore, any AE technique developed could of been easily applied to any industrial application with the use of any system. However, the Kaiser effect in the AE response for unirradiated graphite has been shown not to occur (Chapter Ten) due to thermally-activated recovery processes (Chapter Eleven).

The AE responses from irradiated fuel sleeve graphites after a full life time subjected to cyclic loading showed a Felicity effect similar to that shown by unirradiated graphites, except that ΣN values were much greater due to increased porosity from radiolytic oxidation. In addition, irradiated graphites emitted a greater proportion of AE on subsequent load cycles. This was probably due to a higher density of stress

concentrators in the graphite caused by irradiation effects. The AE results from irradiated graphite monotonically loaded to failure revealed no evidence for residual stresses, *i.e.* there was no Felicity effect. Residual stresses estimated from the change in the rate of AE with applied stress did not agree with values of internal stress determined by a slot closure method (Chapter Twelve).

The irradiated graphite specimens used in this work came from an AGR sleeve discharged from one of the Hunterston reactors in November 1989 after a full life time. They were then too radioactive to test, and were kept for at least 100 days before transportation to and examination at Berkeley Nuclear Laboratories. This is typical of most irradiated components selected for post-irradiation examination (PIE). It appears that the minimum period of time from removal of a sleeve from the reactor to mechanical testing is six months. In this work, two years elapsed between the removal of the irradiated graphite from the reactor and PIE at Berkeley Nuclear Laboratories. Therefore, based on results obtained for unirradiated graphite (Chapters Ten and Eleven), it is expected that the irradiated graphites will have undergone a significant amount of recovery between removal from the reactor and PIE. This will have the effect of reducing residual stresses in the graphite. Therefore, it is possible that the residual stress measured by the slot closure method is an under-estimate of the stress in the reactor. Thus, in conclusion, the AE experiments on irradiated graphites reported in this work suggest that the AE technique will not provide a feasible method to determine internal stresses in the moderator core or in the fuel sleeves, due to relaxation processes which occur between removal of the graphite from the reactor and PIE.

13.6 Conclusions

This thesis has reported the first systematic study of acoustic emission from nuclear graphites. The main conclusions drawn from this work are as follows:-

(i) It has been demonstrated that AE is a viable tool to study microstructural processes which occur in polycrystalline graphites in response to complex stress-states. Specifically, AE can provide information relating to microstructure, mechanical behaviour and fracture of graphites. For example, the number of AE events, ΣN, increased with the coarseness of the microstructural texture of three graphites studied, *i.e.*, $\Sigma N(PGA) > \Sigma N(VNEC) > \Sigma N(IM1\text{-}24)$. In addition, new insights into the failure mechanisms have been gained, *e.g.*, it was suggested that IM1-24 graphite is less able to accommodate plastic deformation than PGA because its microstructure does not allow easy shear mechanisms.

(ii) Three nuclear graphites were stressed in tension, compression and flexure in both monotonic and cyclic loading to failure. It was found for all graphites, that at any particular stress, $\Sigma N(tension) > \Sigma N(compression) >> \Sigma N(flexure)$.

(iii) The work reported in this thesis has resolved the confusion in the literature over the Kaiser effect by showing that it does not occur in nuclear graphites. Instead, this study has demonstrated for the first time that AE responses from nuclear graphites subjected to cyclic loading exhibit a Felicity effect. All AE responses were similar, except for PGA loaded in compression. Typically, on the first load cycle, the rate of AE generation gradually increased until the peak load. On subsequent load cycles, the onset of AE generation occurred prior to reaching the previous peak stress, and then it gradually increased. However, for PGA loaded in compression, on subsequent load cycles, the rate of AE generation decreased after an initial load forming an unusual S-shaped curve. This effect was attributed to the pinning of the basal plane shear prior to microcracking. Amplitude distributions from PGA and other graphites support this interpretation.

(iv) The Felicity effect was attributed to relaxation and recovery processes that occur in polycrystalline graphites. A new parameter, called the Recovery ratio, B, was introduced to characterise the Felicity effect, which took account of the number of AE events occurring on each load cycle prior to the previous peak stress.

(v) AE has been shown to be a sensitive technique in some situations and may be used to reveal aspects of the mechanical behaviour of polycrystalline graphites which are difficult to study by other means. An investigation of changes in Recovery ratio with time at zero stress revealed that B increased logarithmically with time, suggesting that recovery mechanisms operate at zero load. Examination of the AE responses showed a progressive increase at low stresses in ΣN due to low energy events. It is also suggested that the amount of recovery will also depend on the applied stress and temperature.

(vi) An investigation into the generation of AE as a function of time at zero load after a load cycle, or at constant strain after an initial load, indicated that recovery was due to thermally-activated creep processes. These mechanisms occur at ambient temperatures which are commonly considered to be far below the temperature threshold recognised for the detection of thermal creep.

(vii) AE responses from irradiated specimens subject to cyclic loading showed a Felicity effect. However, monotonic loading of irradiated graphites showed no evidence of a Felicity effect due to residual stresses. Therefore, it is concluded that AE is not a feasible technique to monitor internal stresses in irradiated graphites. A Felicity effect was not found on monotonic loading of irradiated graphite because of recovery processes which occur in the time between removing the graphite from the reactor and PIE. It was also suggested that relaxation and recovery processes may have serious implications for other measurement methods, leading to an under-estimation of the internal stress in the reactor core.

13.7 Suggestions for Further Work

(i) The relaxation mechanisms indicated by the AE responses were shown to be time-dependent. Measurement of AE at various temperatures and stresses will yield further information on thermally-activated creep processes responsible for the Felicity effect. Such measurements will help improve the understanding of recovery mechanisms in polycrystalline graphites under different conditions.

(ii) It is possible that a Felicity effect may be detected at higher internal stresses in nuclear graphites such as those expected near the end of reactor life. The peak tensile stresses at the bore of AGR graphite bricks are ~5 MPa at 6 EFPY. The internal stresses change to compressive stresses >10 MPa beyond 20 EFPY (Reed *et al.*, 1991). Although, it has been concluded that it is not possible to determine by AE the residual tensile stresses early in reactor life, at the end of the life, the internal stresses are far larger in magnitude, and a Felicity effect may be detected by AE. Further tests on irradiated graphite at a range of fast neutron doses and radiolytic weight losses are required to understand fully the effect of irradiation dose upon the AE response. Such tests may also reveal the influence of recovery mechanisms on internal stress measurement techniques.

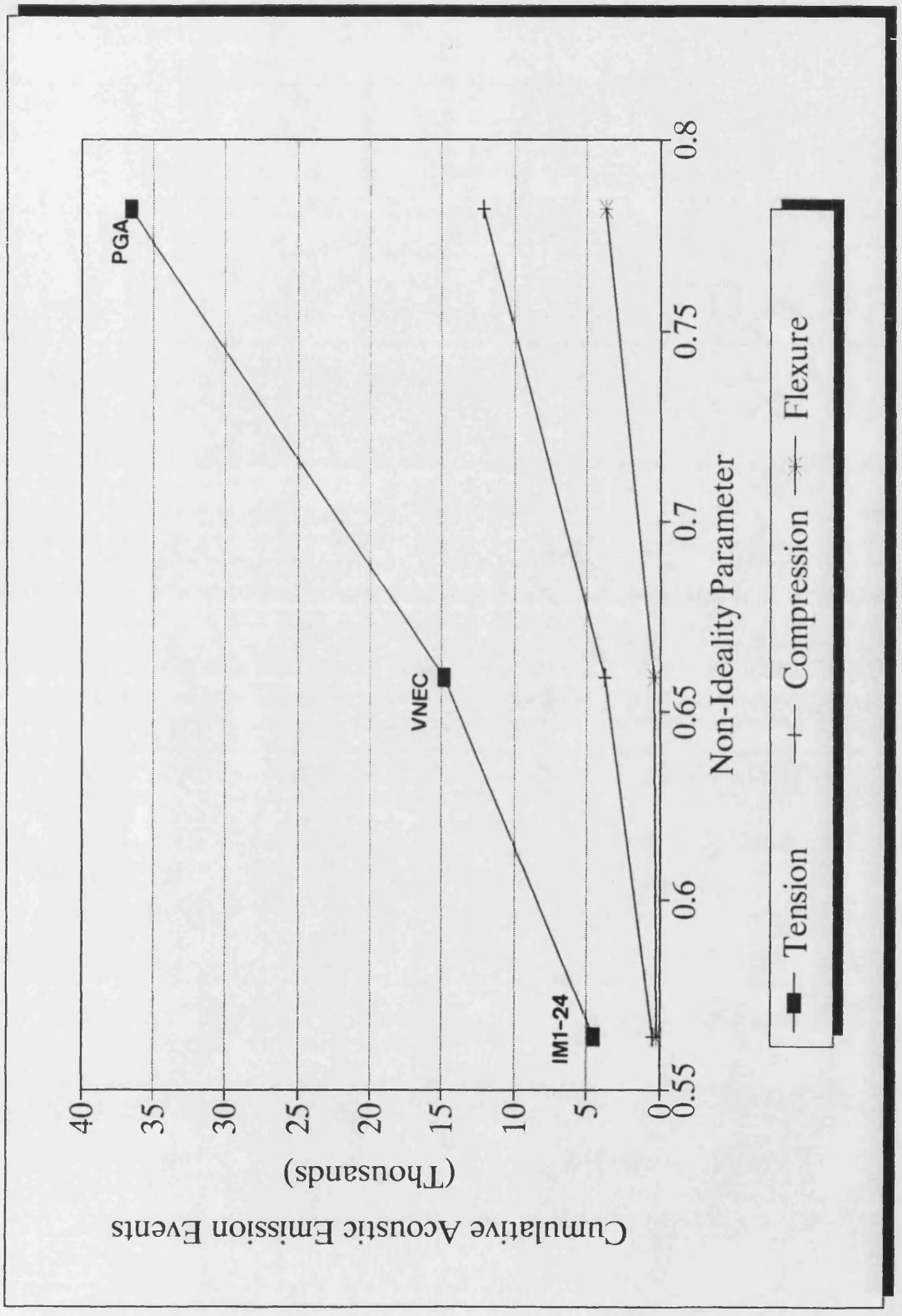

FIGURE 13.1 : A plot of the cumulative AE event count versus the non-ideality parameter in tension, compression and flexure for three nuclear graphites.

Appendix I : Pollock Distributions

The Pollock distribution of AE peak amplitudes (Pollock, 1979) is of the form

$$n(a) = (a/a_0)^{-b} \qquad (A.1)$$

where n(a) defines the fraction of the emission population whose peak amplitude exceeds a, a_0 is the lowest detectable amplitude and the exponent b is used to characterise the amplitude distribution. The minimum detectable threshold (a_0) on the Marandy MR1004 AE Analyser is 10 mV and each amplitude distribution level is 2.4 dB wide. The Marandy Analyser has 25 amplitude distribution levels and therefore the threshold of amplitude level, x, is given by 2.4x dB, thus the relationship between the amplitude of an AE event, a mV, and the threshold of the amplitude level is

$$2.4x = 20 \log (a/a_0). \qquad (A.2)$$

Equating equations A.1 and A.2 gives

$$\log n(x) \; (= \log n(a)) = -0.12bx \qquad (A.3)$$

where n(x) is the fraction of the emission population whose peak amplitude exceeds the minimum threshold of amplitude level x. The fraction of all AE events with amplitudes exceeding the minimum threshold in x, n(x) is

$$n(x) = N(x) / N(x_0), \qquad (A.4)$$

where N(x) is the number of events with amplitudes exceeding the minimum threshold in x, and $N(x_0)$ is the total number of AE events above the minimum detectable threshold a_0. Taking logs on both sides of equation A.4 gives

$$\log n(x) = \log N(x) - \log N(x_0). \quad (A.5)$$

Substituting equation A.3 in equation A.5 gives

$$\log N(x) = -0.12bx + \log N(x_0). \quad (A.6)$$

Therefore, to obtain a Pollock distribution from AE amplitudes from the Marandy system, we must plot the logarithm of the total number of AE events above amplitude level x (inclusive of those AE events in x), log N(x), versus the amplitude level number, x. The gradient of line will be equal to -0.12b and the intercept on the log N(x) axis will be equal to log $N(x_0)$. The value of b can than be compared to results from other systems.

BIBLIOGRAPHY

Allard, B., Rouby, D., Fantozzi, G., Dumas, D. and Lacroix, P. (1991). Fracture Behaviour of Carbon Materials, *Carbon*, 29, [3], 457-468.

Amelinckx, S., Delavignette, P. and Heerschap, M. (1965). Dislocations and Stacking Faults in Graphite, *Chemistry and Physics of Carbon* (Ed. P. L. Walker), 1, 1-71.

Anderson, J. C., Leaver, K. D., Rawlings, R. D. and Alexander, J. M. (1990). Materials Science, 4th Ed., Chapman and Hall.

Andrew, J. F., Okada, J. W. and Wobshall, D. C. (1960). Elastic Constants and Permanent Set in Carbons and Graphite at Room Temperature, Proc. 4th Biennial Carbon Conf., Pergamon Press, NY, 559-575.

Arragon, P. and Berthier, R. M. (1958). Caracterisation Mechanique Du Graphite Artificiel, *Industrial Carbon and Graphite*, Society of the Chemical Industry, 565-578.

Ashby, M. F. and Jones, D. R. H. (1986). Engineering Materials 2 (International Series on Materials Science and Technology; 39), Pergamon Press, Oxford.

ASTM C559-79 (1981). Standard Test Method for Bulk Density by Physical Measurement of Manufactured Carbon and Graphite Articles.

ASTM C565-83 (1987). Standard Methods of Tension Testing of Carbon and Graphite Mechanical Materials.

ASTM C695-81 (1987). Standard Test Method for Compressive Strength of Carbon and Graphite.

ASTM C747-74 (Reapproved 1979) (1981). Standard Test Method for Moduli of Elasticity and Fundamental Frequencies of Carbon and Graphite Materials by Sonic Resonance.

ASTM D790-80 (1981). Standard Test Methods for Flexural Properties of Plastics and Electrical Insulating Material.

ASTM E-7 Proposal P199 (1989). Proposed Terminology Relating to Non-Destructive Testing, Section B: Acoustic Emission.

ASTM E399 (1981). Standard Test Method for Plane Strain Fracture Toughness of Metallic Materials.

ASTM E569-85 (1989). Standard Practise for Acoustic Emission Monitoring of Structures During Controlled Stimulation.

ASTM E610-82 (1989). Standard Definitions of Terms Relating to Acoustic Emission.

ASTM E616-81 (1981). Standard Terminology Relating to Fracture Testing.

ASTM E650-85 (1989). Standard Guide for Mounting Piezoelectric Acoustic Emission Sensors.

ASTM E1067-85 (1989). Standard Practise for Acoustic Emission Examination of Fiberglass Plastic Resin (FRP) Tanks / Vessels.

ASTM E1118-86 (1989). Standard Practise for Acoustic Emission Examination of Reinforced Thermosetting Resin Pipe (RTRP).

ASTM STP 505 (1972). Acoustic Emission, A Symposium Presented at the December Committee Week ASTM, Bal Harbour, Florida, 7-8 Dec 1971.

Barinov, S. M. and Shevchenko, V. (1992). Invariance of the Work of Fracture Determination of Graphite Using Straight Edge-Notched Beam Samples, *Journal of Material Science Letters*, 11, 336-338.

Bartle, P. M. (1974). Stress Wave Emission Monitoring: Assessment, Correlation and Calibration, Inst. of Mech. Engs. Conf. Pub. 8.

Battey, M. H. (1981). Mineralogy for Students, 2nd Ed., Longman (London).

Bernal, J. D. (1924). *Proc. Roy. Soy. A.*, 106, 749.

Best, J. V., Stephen, W. J. and Wickham, A. J. (1985). Radiolytic Graphite Oxidation, *Progress in Nuclear Energy*, 16, [2], 127-178.

Birch, M. and Bacon, D. J. (1983). The Effect of Fast Neutron Irradiation on the Compressive Stress-Strain Relationships of Graphite, *Carbon*, 21, [5], 491-496.

Birch, M. and Brocklehurst, J. E. (1983). The Impact Endurance of Polycrystalline Graphite, *Carbon*, 21, [5], 497-510.

Birchon, D. (May 1976). The Potential of Acoustic Emission, *Brit. J. of NDT*, 18, 66-71.

Blackman, L. C. F. (Ed) (1970). Modern Aspects of Graphite Technology, Academic Press Inc. (London) Ltd..

Boehm, H. P. and Coughlin, R. W. (1964). Enthalpy Difference of Hexagonal and Rhombohedral Graphite, *Carbon*, 2, 1-6.

Boey, S. Y. and Bacon, D. J. (1986). Bend Strength of Graphite Under Pressure, *Carbon*, 24, [5], 571-574.

Bousfield, B. (December 1988). A Systematic Approach to Sample Preparation, *Metals and Materials*, 4, [12], 758-761.

Bousfield, B. (February 1989). High Resolution Photomicrography, *Metals and Materials*, 5, [2], 88-89.

Bousfield, B. and Bousfield T. (March 1990). Progress Towards a Metallography Standard, *Metals and Materials*, 6, [3], 146-148.

Brocklehurst, J. E. (1977). Fracture in Polycrystalline Graphite, *Chemistry and Physics of Carbon*, 13, 145-279.

Brown, W. F. and Strawley, J. E. (1969). Plane Strain Crack Toughness Testing of High Strength Metallic Materials, ASTM STP No. 410.

Buch, J. D. (1976). Mechanical Behaviour Model for Graphites, Properties Related to Fracture Toughness, ASTM STP 605, 124-44, A Symposium Presented at the 78th Annual Meeting American Society for Testing and Materials, Montreal, Canada, 22-27 June.

Burchell, T. D. (1986). Studies of Fracture in Nuclear Graphite, PhD Thesis, University of Bath.

Burchell, T. D., Cooke, R. G., McEnaney, B. and Pickup, I. M. (1985). Acoustic Emission From Polygranular Graphites, *Carbon*, 23, [6], 739-747.

Burchell, T. D., Pickup, I. M., McEnaney, B. and Cooke, R. G. (1986a). The Relationship Between Microstructure and the Reduction of Elastic Modulus in Thermally and Radiolytically Corroded Nuclear Graphites, *Carbon*, 24, [5], 545-49.

Burchell, T. D., Rose, A. P. G. and McEnaney, B. (1986b). Acoustic Emission From Irradiated Nuclear Graphite, *J. of Nuclear Materials*, 140, 11-18.

Burchell, T. D., Tucker, M. O. and McEnaney, B. (1987). Quantitative and Qualitative Studies of Fracture in Nuclear Graphites, Proc. BNES Conf. Materials for Nuclear Reactor Core Applications, Bristol UK.

Carpenter, E. W. and Norfolk, D. J. (1984). Lattice of Powder : Graphite Core Life, *Nucl. Energy*, 23, [2], 83-96.

CEGB (1984/5). Gas-Cooled Reactors, Achievements in Technology Planning and Research 84/5, 5-9.

Critchell, J. W., Judge, L. and Flewitt, P. E. J. (1988). AGR Moderator Graphite X-ray Stress Measurement, CEGB Report.

Cullity, B. D. (1978). Elements of X-ray Diffraction, 2nd Ed., Addison Wesley Publishing Company, Inc., USA.

Davidge, R. W. and Tappin, G. (1968). The Effective Surface Energy of Brittle Materials, *J. Mat. Sci.*, 3, 165-173.

Davidson, H. W. and Losty, H. H. W. (1958). Plasticity of Graphite, *Nature*, 181, 1057-1059.

Davidson, H. W. and Losty, H. H. W. (1960). An Interpretation of the Mechanical Behaviour of Carbons, Proc. 4th Conf. on Carbon, Buffalo, New York, 1959, Pergamon Press Ltd.

Dergunov, N. N., Krotov, A. I., Barabanov, V. N. and Anufriev, U. P. (1972). Tensile and Creep Behaviour of Polycrystalline Graphites, *Carbon*, 10, 19-27.

Drouillard, T. F. (1979). Acoustic Emission, A Bibliography with Abstracts, IFI/Plenum Press, USA, New York.

Fenn, R. H., Jones, A. M. and Wells, G. H. (1987). Measurement of Triaxial Residual Stresses in Composite Materials Using X-ray Diffraction, UKAEA, Harwell Publication AERE R 12901.

Gilchrist, K. E. and Wells, D. (1969). Acoustic Emission From Graphite Under Stress, *Carbon*, 7, 627-631.

Goodhew, P. J. and Humpheys, F. J. (1988). Electron Microscopy and Analysis (2nd Ed.), Taylor and Francis Ltd., London.

Green, R. Jr (1987). Encyclopaedia of Science and Technology, 6th Ed, 1, 63-65, McGraw Hill, NY.

Greenstreet, W. L., Smith, J. E. and Yahr, G. T. (1969). Mechanical Properties of EGCR-Type AGOT Graphite, *Carbon*, 7, 15-45.

Greenwood, N. N. and Earnshaw, A. (1986). Chemistry of the Elements, Pergamon Press Ltd, Oxford.

Griffith, A. A. (1920). The Phenomena of Rupture and Flow in Solids, *Phil. Tran. Roy. Soc.*, 221, 163.

Ioka, I. and Yoda, S. (1987). Acoustic Emission Caused By Reversed Plastic Deformation in Polycrystalline Graphite, *J. Nucl. Matl.*, 148, 344-350.

Ioka, I. and Yoda, S. (1990). Changes in Mechanical Properties of Graphites Parallel and Perpendicular to Compressive Prestress, *Carbon*, 28, [1], 159-164.

Ioka, I., Yoda, S. and Konishi, T. (1990a). Acoustic Emission For Polycrystalline Graphite Under Compressive Loading, *Carbon*, 28, [4], 489-495.

Ioka, I., Yoda, S. and Konishi, T. (1990b). Behaviour of Acoustic Emission Caused By Microfracture in Polycrystalline Graphites, *Carbon*, 28, [6], 879-885.

Ioka, I., Yoda, S., Oku, T. and Miyamoto, Y. (1986). Acoustic Emission From Polycrystalline Graphites, IAEA Spec. Meet. Graphite Compon. Struct. Des., 227-32, NIPPON Gensuiryowu Rep JAERI M86192.

Irwin, G. R. (1958). Fracture, *Handbuch der Physik*, Springer-Verlag, Berlin, 6, 551.

Jenkins, G. M. (1962a). Fracture in Reactor Graphite, *Journal of Nuclear Materials*, 5, [3], 280-286.

Jenkins, G. M. (1962b). Analysis of the Stress-Strain Relationships in Reactor Grade Graphite, *British Journal of Applied Physics*, 13, 30-32.

Jenkins, G. M. (1963). Transient Creep and Recovery in Graphite, *Phil. Mag.*, 8, 903-910.

Jenkins, G. M. (1965). The Stress-Strain Relationships of Polycrystalline Graphite Under Compression Up To Fracture, *Carbon*, 3, 93-94.

Jenkins, G. M. (1973). Deformation Mechanisms in Carbons, *Chemistry and Physics of Carbon*, 11, 189-242.

John, V. (1992). Testing of Materials, Macmillan Publishers Ltd., London.

Jones, D. D. and Reed, J. (1991). The Effect of Reactor Environment on the Fracture Strength of IM1-24, VFT, Nittetsu Graphite, Nuclear Electric Report TD/FCB/REP/0086/A.

Kaiser, J. (1950). PhD Thesis, Technische Hochshule, Munich, Germany.

Kelly, B. T. (1981). Physics of Graphite, Applied Science Publishers, London.

Kelly, B. T. (1982). Graphite - The Most Fascinating Nuclear Material, *Carbon*, 20, 3-11.

Kelly, B. T. (1992). Irradiation Creep in Graphite - Some New Considerations and Observations, *Carbon*, 30, [3], 379-383.

Knott, J. F. (1973, Reprinted 1981). Fundamentals of Fracture Mechanics, Butterworths, London.

Kraus, G. and Semmler, J. (1978). Die Charakerisierung Des Mechanischen-ver Haltens Von Kohlenstoff -Und Graphitmaterialien Mit Hilfe Der Schallemissionsanalyse, *Carbon*, 16, 185-190.

Lipson, H. and Stokes, A. R. (1943). The Structure of Graphite, *Proc. Roy. Soc. A*, 181, 101.

Logsdail, D. H. (1968). The Effect of Gaseous Environment on Flexural Strength of Graphite, *Carbon*, 6, pg 212.

Losty, H. H. W. (1970). Mechanical Properties, In:- Modern Aspects of Graphite Technology, Academic Press Inc. (London) Ltd. (Ed. Blackman, L. C. F.).

Losty, H. H. W. and Orchard, J. S. (1962). The Strength of Graphite, Proc. 5th Carbon Conf., University Park, PA, 1961, Pergamon Press, London, 1, 519-532.

Mantell, C. L. (1968). Carbon and Graphite Handbook, Interscience, New York.

Marsh, H. (Ed) (1989). Introduction to Carbon Science, Butterworths and Co. (Publishers) Ltd.

Mays, T. J. and McEnaney, B. (1992). A Review of Methods of Quantitative Optical Microscopy For Characterising Macropores in Carbon Materials, *Proc. Carbon '92*, Essen, 22-26 June 1992, 169-171.

McEnaney, B. and Mays, T. J. (1989). Porosity in Carbons and Graphites. In: Introduction to Carbon Science (H. Marsh, ed.), 153-196, London: Butterworths.

McLachlan, N. (1992). The Modelling of Polycrystalline Graphite Fracture and Deformation Properties, PhD Thesis, University of Exeter.

McLachlan, N. and Tucker, M. O. (1990). A Model to Describe the Fracture and Deformation Behaviour of Polycrystalline Graphite, Nuclear Electric Report TD/FCB/REP/0034/b.

McLachlan, N., Tucker, M. O. and Parry, M. J. (1989). Stress and the Microstructure of Graphite, 19th Biennial Conf. on Carbon, Penn. State University, 460-461.

Moore, R. V. (1971). Nuclear Power, Cambridge University Press.

Mrozowski, S. (1954). Mechanical Strength, Thermal Expansion and Structure of Cokes and Carbons, Proc. 1st and 2nd Conf. on Carbon, Waverley Press, USA.

Murdie, N., Edwards, I. and Marsh, H. (1986). Changes in Porosity of Graphite Caused by Radiolytic Gasification by Carbon Dioxide, *Carbon*, 24, [3], 267-275.

Nakasa, H. (1973). Application of Acoustic Emission to Material Diagnostics, Nuclear Power Plant Controlled and Instrumentation, Proc. of a Symposium Prague 22-26 Jan, IAEA, 461-478.

Nakayama, J. (1965). Direct Measurement of Fracture Energies of Brittle Heterogeneous Materials, *J. Am. Ceram. Soc.*, 48, [11], 583-587.

Newth, G. S. (1897). A Textbook of Inorganic Chemistry, 5th Ed

Nichols, R. W. (Ed) (1976). Acoustic Emission, Applied Science Publishers Ltd, London.

Nightingale, R. E. (1962). Nuclear Graphite, Academic Press Inc. Ltd. London.

Norfolk, D. J., Johnston, G. O. and Tucker, M. O. (1986). Achieving Optimum Graphite Performance in AGR Core and Fuel, Presented at the IAEA Specialists Meeting on Graphite Component Structural Design, Tokai Mura, Japan, 9-11 September, 176-181, JAERA Summary Report, NASA Conference Paper.

Oakden, M. M. and Cotton, R. (1988). Acoustic Emission Studies on a Nuclear Graphite, Proceedings of Carbon '88, University of Newcastle Upon Tyne, UK, 18-23 September (Eds McEnaney, B. and Mays, T. J.) 440-442, Institute of Physics.

Oku, T. and Eto, M. (1973). The Effect of Compressive Prestressing on the Mechanical Properties of Some Nuclear Graphites, *Carbon*, 11, 639-647.

Oku, T., Ishiyama, S., Eto, M., Manaka, M. and Aizawa, J. (1986). Fracture Mechanical Properties of Nuclear Graphite, Carbon '86: 4th International Carbon Conf., Baden-Baden, Germany.

Orowan, E. (1949). Fracture and Strength of Solids, *Rep. Prog. Phys.*, 12, 185.

Orowan, E. (1955). Energy Criteria of Fracture, *Weld. Res. Supp.*, 34, 157.

Patterson, W. C. (1976, Reprinted 1980). Nuclear Power, Harmondsworth, Penguin Books Ltd.

Pickup, I. M. (1984). The Influence of Thermal Corrosion Upon The Mechanical Properties of Nuclear Graphites, PhD Thesis, University of Bath.

Pickup, I. M., Cooke, R. G. and McEnaney, B. (1983). Acoustic Emission, Sub-Critical Events and Fracture of Heterogeneous Ceramics and Nuclear Graphites, *Science of Ceramics 12*, Proc. 12th Int. Conf. on Science of Ceramics Sponsored by the Assoication Europeanne de Ceramique, Saint-Vincent, Italy, July 27-30.

Pickup, I. M., McEnaney, B. and Cooke, R. G. (1986). Fracture Processes in Graphite and the Effects of Oxidation, *Carbon*, 24, [5], 535-543.

Pollock, A. A. (Oct 1973). Acoustic Emission-2, Acoustic Emission Amplitudes, *NDT Testing*, 264-269.

Poulter, D. R. (Ed) (1963). The Design of Gas-Cooled Graphite Moderated Reactors, Oxford University Press, London.

Prince N. and Brocklehurst, J. E. (1986). The Integrity of CAGR Moderator Bricks, Presented at the IAEA Specialists Meeting on Graphite Component Structural Design, Tokai Mura, Japan 9-11 September, 20-28, JAERA Summary Report.

Pugh, C. E. (1971). A Viscoelastic Representation of the Mechanical Behaviour of RVD Graphite at Elevated Temperatures, *Carbon*, 9, 327-340.

Reed, J., Swallow, K. and Neighbour, G. (1991). Acoustic Emission in Irradiated Graphite as a Method for Determining Internal Stress for In-Reactor Components, Nuclear Electric Report TD/FCB/MEM/1111.

Reynolds, W. N. (1968). Physical Properties of Graphite, Elseiver Co. Ltd.

Rose, A. P. G. (1985). Calculation of Critical Stress Intensity Factors of Nuclear Graphite From Small Specimen Tests, *Carbon*, 23, [4], 387-393.

Rose, A. P. G. and Tucker, M. O. (1982). A Failure Criterion for Nuclear Graphite, *J. Nuclear Materials*, 110, 186-195, North Holland Publishing Company.

Sakai, M., Urashima, K. and Inagaki, M. (1983). Energy Principle of Elastic-Plastic Fracture and Its Application to the Fracture Mechanics of a Polycrystalline Graphite, *J. Am Ceramic. Soc.* , 66, [12]868-874.

Sakai, M., Yoshimura, J., Goto, Y. and Inagaki, M. (1988). R Curve Behaviour of a Polycrystalline Graphite: Microcracking and Bridging in the Wake Region, *J. Am. Ceramic. Soc.*, 71, [8], 609-616.

Sankar, N. G., Frederick, J. R. and Felbeck, D. K. (1970). Acoustic Emission from Metals During Unloading and Its Relation to the Bauschinger Effect, *Metallurgica Transactions*, 1, 2979-2980.

Scott, I. G. (1991). Basic Acoustic Emission, Nondestructive Testing Monographs and Tracts, Volume 6, Gordon and Breach Science Publishers.

Seldin, E. J. (1966). Stress-Strain Properties of Polycrystalline Graphites in Tension and Compression at Room Temperature, *Carbon*, 4, 171-191.

Slagle, O. D. (1967). Deformation Mechanisms in Polycrystalline Graphite, *Journal of the American Ceramic Society*, 50, [10], 495-500.

Smith, M. C. (1968). Relaxation of Tensile Stress in a Reactor Graphite at 2000 to 2700 °C, *Carbon*, 6, 503-516.

Srawley, J. E. and Gross, B. (1976). ASTM STP 601.

Stone, D. E. W. and Dingwall, P. F. (April 1977). Acoustic Emission Parameters and Their Intrepretation, *Non-Destructive Testing International*, 51-62.

Swindlehurst, W. E. and Wilshaw, T. R. (1976). Acoustic Emission in Brittle Solids, *J. Mater Sci*, 11, 1653-1660.

Tattersall, H. G. and Tappin, G. (1966). The Work of Fracture and its Measurement in Metals, Ceramics and Other Materials, *J. Mater. Sci.*, 1, 296-301.

Taylor, R., Brown, R. G., Gilchrist, K., Hall, E., Hodds, A. T., Kelly, B. T. and Morris, F. (1967). The Mechanical Properties of Reactor Graphites, *Carbon*, 5, 519-531.

Timoshenko, S. P. and Goodier, J. N. (1970). Theory of Elasticity, 3rd Ed., McGraw-Hill Book Company.

Tucker, M. O. (1992). Private Communication.

Tucker, M. O., Rose, A. P. G. and Burchell, T. D. (1986). The Fracture of Polygranular Graphites, *Carbon*, 24, [5] 581-602.

Tucker, M. O. and Wickham, A. J. (1990). Graphite Core Performance and Intregrity Assessment, In: The Commissioning and Operation of AGRs, a seminar organised by The Nuclear Energy Committee of the Power Industries Division at I.Mech.E. HQ, Westminster, SW1H 9JJ.

Vitovec, F. H., and Stachurski, Z. H. (1972). Effect of Environment on the Mechanical Anisotropy of Polycrystalline Graphite, *Carbon*, 10, 417-428.

Weibull , W. (1951). A Statistical Distribution Function of Wide Applicability, *J. of Applied Mechanics*, 293-297.

Wickham, A. J. (1990). Caring for the Graphite Cores, Private Communication.

Williamson, G. K. (1962). Lattice Defects in Graphite and Their Influence on Physical Properties, In:- Uranium and Graphite, The Inst. of Metals Monograph No. 27.

Woolley, R. L. (1965). The Yield Curve and the Compressive Strength of Polycrystalline Graphite, *Phil. Mag.*, 11, 799-807.

Youfa Yin, Cooke, R. G. and McEnaney, B. (1991). Radial Variations in Fracture and Acoustic Emission of a Thermic Graphite Electrode, *Carbon*, 29, [8], 1221-1225.

Ying, S. P. (Dec 1973). Characteristics and Mechanisms of Acoustic Emission from Solids Under Applied Stress. CRC CRIT REV SolidST Sci, 85-123.

Zukas, E. G. and Green, W. V. (1968). The High-Temperature Creep Behaviour of a Highly-Orientated Polycrystalline Graphite, *Carbon*, 6, 101-110.